Study and development of fluidic micro-oscillators for cooling electronic systems

Georges Saliba

THÈSE

En vue de l'obtention du
DOCTORAT DE L'UNIVERSITÉ DE TOULOUSE

Délivré par l'Université Toulouse 3 - Paul Sabatier

Présentée et soutenue par

Georges SALIBA

Le 31 mai 2022

Etude et développement de micro-oscillateurs fluidiques pour le refroidissement de systèmes électroniques embarqués

---

Ecole doctorale : **AA - Aéronautique, Astronautique**

Spécialité : **Dynamique des fluides**

Unité de recherche :
ICA - Institut Clément Ader

Thèse dirigée par
Lucien BALDAS et Vincent RAIMBAULT

Jury

M. Laurent KEIRSBULCK, Rapporteur
M. Gian Luca MORINI, Rapporteur
Mme Christine BARROT LATTES, Examinatrice
Mme Sandrine BERNARDINI, Examinatrice
M. Thierry CAMPS, Examinateur
M. Lucien BALDAS, Directeur de thèse
M. Vincent RAIMBAULT, Co-directeur de thèse
M. Nicolas MAZELLIER, Président

"Un troubadour arrive à la fête et montre ce qu'il a rapporté de ses voyages: des chansons graves ou joyeuses, et pour finir une danse. En vrai musicien, il brode et improvise autant qu'il peut. Cette histoire médiévale a servi de modèle à la composition"

Solo-Bratsche

Der Schwanendreher

I

„Zwischen Berg und tiefem Tal"

Paul Hindemith

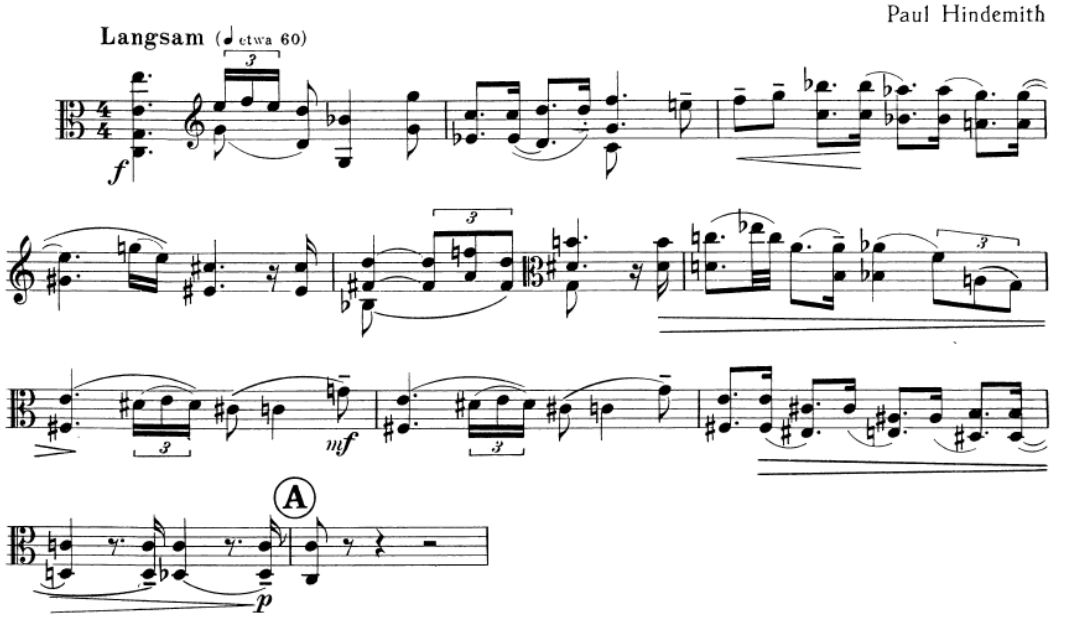

Remerciements

Les travaux présentés ci-après sont le résultat d'une collaboration entre deux laboratoires, l'Institut Clément Ader (ICA) et le Laboratoire d'Analyse et d'Architecture des Systèmes (LAAS). Durant cette thèse, j'ai côtoyé des chercheurs issus de nombreuses communautés distinctes et j'ai pu apprécier la diversité des démarches scientifiques qu'ils adoptent au quotidien. Sans s'en rendre compte, on est souvent limité par les outils, conceptuels et techniques, de notre propre discipline. Quand un problème se présente à notre esprit, nous tendons la main vers les outils les plus proches de nous pour le résoudre. Les outils que nous avons aiguillés, maîtrisés, par habitude ou par assiduité. Le jour où on se heurte à un écueil d'apparence insurmontable, plusieurs choix se présentent: persévérer avec les mêmes outils, abandonner, ou emprunter des outils à son voisin. Ces dernières années m'ont appris à voir au-delà des frontières fictives qui délimitent les différents domaines du savoir et à travailler avec des 'voisins' insoupçonnés...

Je voudrais donc remercier mes directeurs de thèse Pr. Lucien Baldas et Dr. Vincent Raimbault de m'avoir offert cette expérience édifiante et pour votre support scientifique, matériel et votre bienveillance. Je tiens aussi à remercier Pr. Thierry Camps, véritable *deus ex machina* de ma fin de thèse, dont l'enthousiasme, la créativité et la rigueur scientifique m'ont particulièrement marqué ces derniers mois. Un grand merci également à Stéphane Orieux, qui est probablement la personne la plus silencieusement efficiente que j'ai jamais connue et à Stéphane Colin pour son soutien scientifique. Je suis également redevable à Rémi Gilblas pour son soutien dans la partie thermique.

La fabrication des micro-oscillateurs et des plateformes instrumentées n'aurait pas eu lieu sans l'effort concerté de l'équipe technologique du LAAS que je remercie individuellement: Eric I. pour les LPCVD et les implantations ioniques, Jean-Christophe M. pour les PECVD, Aurélie L. pour les RIE, Ludovic S. pour les métallisations, Benjamin R. pour les FIB/MEB, Fabien M. de m'avoir formé (à plusieurs reprises!) au processus délicat de dépôt de films secs et Laurent M. qui m'a formé à l'art de la photolithographie et enfin Julia M. pour la découpe, soudure et enrobage des puces.

Je remercie ma soeur, Joëlle, âme tendre et révoltée, pour son soutien moral, et son courage qui fut une source d'inspiration pendant toutes ces années.

Enfin, je remercie mes parents, Charbel et Jamilé, qui, par leurs encouragements, leur éthique de travail, et leur foi inébranlable m'ont appris à persévérer, à croire que le meilleur est à venir et qu'il faut agir pour avancer. Vous méritez bien plus que ce que la vie vous a donné.

Résumé

Dans le domaine aéronautique, les contraintes sur le refroidissement sont multiples. L'efficacité d'un système de refroidissement ne se résume plus au simple taux de chaleur dissipée, mais englobe d'autres facteurs comme la compacité, le poids, la robustesse, le coût de maintenance ainsi que la durabilité. Une conception du système de refroidissement qui intègre ces aspects pourrait diminuer les coûts de fonctionnement, notamment la consommation de kérosène, et donc réduire l'impact environnemental du vol.

La multiplication de systèmes embarqués dans l'aéronautique amène des contraintes supplémentaires pour leur refroidissement. Dans ce contexte, les actionneurs fluidiques présentent un fort potentiel. Ces travaux portent plus précisément, sur l'utilisation de jets pulsés produits par des oscillateurs fluidiques pour refroidir une surface chauffée. Plusieurs travaux sur les jets d'impact ont montré qu'il était possible d'améliorer la dissipation thermique en introduisant des pulsations dans l'écoulement. Il manque cependant un consensus dans la littérature autour de l'ensemble des conditions opératoires propices à l'amélioration des performances. D'où la nécessité de mener une étude sur l'écoulement produit par ces dispositifs fluidiques et le refroidissement qui en résulte.

En amont de cela, il est nécessaire de se pencher sur l'effet de certains paramètres liés à la géométrie du l'oscillateur sur son mode de fonctionnement, en commençant par la caractérisation de l'écoulement pulsé produit par l'oscillateur. A cette fin, un prototype d'oscillateur est réalisé en fabrication additive puis caractérisé via une reconstruction spatiale 2D et 3D du champ de vitesse à l'aide d'un seul fil-chaud et d'une sonde de pression placée au niveau des canaux de retours. Cette méthode de mesure nous permet de mettre en évidence des structures cohérentes et suivre leur évolution. En marge de cette étude, un réseau de neurones artificiels profond, ayant des fonctions d'activations sinusoïdales atypiques, est utilisé pour créer une représentation implicite du champ de vitesse.

L'oscillateur ainsi caractérisé a alors été utilisé pour refroidir une plaque en verre chauffée , dont la température a été mesurée par thermométrie infrarouge. Des tests sont pratiqués sur des jets stationnaires et des jets pulsés de même débit massique moyen dans une large gamme de fréquences. Une amélioration considérable des performances est observée pour des faibles distances d'impact et des hautes fréquences de pulsation. Des simulations numériques sont ensuite réalisées pour mieux comprendre les phénomènes mis en jeu. Des méthodes statistiques en un point (dites RANS) et des modèles hybrides (alliant les méthodes RANS et les Simulations des Grandes Echelles, ou LES) ont été utilisés à cette fin.

En vue de concevoir un système de refroidissement compact et capable de cibler des composants de tailles sub-millimétriques, des versions micrométriques de ces mêmes oscillateurs ont été conçues et fabriquées ainsi qu'une instrumentation électronique à même de les

caractériser. Rares sont les études menées sur les microjets d'impact alors qu'aucune étude n'a pu être recensée à ce jour sur les microjets d'impact pulsés ni sur les micro-oscillateurs fluidiques gazeux. Le défi est donc double : de montrer que les micro-oscillateurs à gaz peuvent fonctionner à cette échelle et de les utiliser pour refroidir des composants dissipateurs de chaleur. À cela vient s'ajouter un problème non moins ambitieux, celui d'instrumenter l'oscillateur ainsi que la surface d'impact chauffée. Étant donné que la fréquence d'oscillation à cette échelle-là se mesure en kilohertz et que les fluctuations de température sont relativement faibles, des capteurs thermiques à base de couches de polysilicium fortement dopé ont donc été produits. Bien que leur haute sensibilité thermique ait été déjà démontrée, il est question ici d'améliorer leur temps de réponse. Pour ce faire, les capteurs ont été partiellement désolidarisés du substrat en silicium. Cette amélioration de la dynamique du capteur a été obtenue au prix d'une structure fragilisée qu'il a fallu prendre en compte dans les étapes technologiques suivantes.

Abstract

Thermal management in the aerospace industry is subject to a number of constraints. The suitability of a cooling system does not only depend on the heat flux that it can evacuate, but also includes such aspects as compactness, weight, sturdiness, cost of maintenance and durability. Taking these factors into consideration contributes to reducing fuel consumption, thus reducing the carbon footprint of the airplane.

With this in mind, fluidic actuators were developed for electronics cooling applications on-board airplanes. In other words, the aim is to cool heated surfaces using the periodic unsteady flow produced by no-moving-parts fluidic oscillators. Previous studies had shown the possibility of enhancing jet impingement heat transfer by introducing a periodic perturbation in the flow. Nevertheless, the exact experimental conditions that lead to this improvement remain somewhat inconsistent across different studies. For this reason, this study tackles both the flow features of the pulsed impinging jet as well as their effects on heat transfer.

In preparation, the oscillator is characterized by assessing its response to changes in design parameters and experimental conditions. This was followed by a two- and three-dimensional reconstructions of the velocity field outside the device using a hot-wire and a pressure transducer mounted onto one of the feedback loops. Using this technique, it was possible to deduce certain flow characteristics as well as detect and track the evolution of large coherent vortices produced by the pulsed jet. The data from these exhaustive measurements was then used to train a deep neural network that uses sinusoidal activation functions. The result is an implicit representation of the flow that could be useful to designers when the oscillator is only part of a larger system.

The oscillators were then used to cool a heated plate whose temperature was measured using an infrared camera. Both steady and pulsed jets were studied for a large range of frequencies, impact distances and flow rates. Remarkable enhancement was observed for small impact distances and high frequencies. Simulations where then performed using both RANS and hybrid LES/RANS approaches.

In the second part of this work, a miniaturized version of the oscillator was produced that can efficiently target small electronic components. Impinging microjets have rarely been studied, while little to no works could be found on pulsed microjets of air or no-moving-parts microfluidic oscillators. The goal of the present study is then twofold, to prove that functional microfluidic oscillators with air as working fluid can be produced and that they can efficiently cool a heated surface. From an experimental standpoint, this requires proper instrumentation capable of acquiring measurements at the spatial and temporal scales of the system. For this end, high-sensitivity thermal sensors were

implemented inside the microfluidic device as well as on the heated target surface. The current iteration of these sensing elements involves partially suspending them over the substrate on which they were built in order to reduce their thermal inertia. The carefully suspended structures were shown to withstand the subsequent fabrication steps despite undergoing high temperatures and pressures.

Contents

List of Figures

List of Tables

List of Symbols

*Note: symbols in **bold face** in the text represent tensors (vectors included)*

Latin Symbols

a	Scaling factor
c	Speed of sound
E	Property of solid/fluid interface in Navier's slip model
f	Frequency
f	Parallelizable fraction of a code
G	Slip coefficient in Maxwell's model
h	Convective coefficient
$\mathbf{I}$	Identity matrix
k	Thermal conductivity
L	Characteristic dimension
$\mathcal{M}$	Linear Momentum
n	Component normal to a surface
N	Number of processors
p	Static pressure
q	Heat flux per unit surface area
Q	Second invariant of the velocity gradient tensor
S	Rate of strain
t	Time
T	Temperature
$\mathbf{T}$	Viscous stress tensor
u	Local velocity
U	Freestream velocity
v, V	Velocity
w	Width of outlet channels of the oscillator
W	Width of a given channel
x	Distance along heated wall (or horizontal coordinate in general)
y	Vertical coordinate
z	Stand-off distance (outlet to wall)
Z	Speed-up (Amdahl's law)

Greek Symbols

α	Diffusion coefficient
δ	Thickness of boundary layer
ϵ	Viscosity in Navier's slip model
λ	Mean free path of fluid molecules
μ	Dynamic viscosity
ν	Kinematic viscosity
ρ	Density
θ	Deflection angle
χ	Arbitrary macroscopic quantity
Ω	Vorticity

Constants

R	Ideal gas constant
N_A	Avogadro's constant

Subscripts

a	Atmospheric
avg	Average value across heated surface
h	Hydraulic, as in hydraulic diameter
j	jet, as in jet temperature
s	Slip
t, N	Throat, Nozzle
T	Thermal
v	Vapor
w	Wall
x	Horizontal component
y	Vertical component

Turbulence Variables

k	Turbulence kinetic energy
ϵ	Turbulence dissipation
ν_t	Turbulence kinematic viscosity
κ	von Kármán constant
u_τ	Shear velocity
y^+	Dimensionless wall distance (y-plus)

Dimensionless Numbers

Re	Reynolds number, $\rho V L/\mu$
St	Strouhal number, fL/U
Pr	Prandtl number, α/ν
Nu	Nusselt number, hL/k
$\mathsf{Fö}$	Frössling number, $\mathsf{Nu}/\mathsf{Nu}_{\mathsf{NP}}$

Initialism/Acronyms

BOE	Buffered Oxide Etch
DMD	Dynamic Modes Decomposition
DNN	Deep Neural Network
LES	Large Eddy Simulation
PJA	Pulsed Jet Actuator
PFJA	Pulsed Jet Fluidic Actuator
PIV	Particle Image Velocimetry
POD	Proper Orthogonal Decomposition
RANS	Reynolds-averaged Navier–Stokes

"Merle nodded. "Something missing. He used to get so fired up about everything - we'd be designing something, run out of paper, he'd take his shirt collar off and just use that to scribble on."
"Lately he's been keeping those ideas pretty much to himself, like he's finally learned how much they might be worth. Seen that happen enough, Lord knows. This big parade of modern inventions, all spirited march tunes, public going ooh and aah, but someplace lurking just out of sight is always some lawyer or accountant, beating that 2/4 like clockwork and runnin the show."
"Anybody feel like dancing?" offered Chevrolette."

Against the Day, Thomas Pynchon

1 Introduction

When dealing with constraints on size and weight, simple cooling solutions are indispensable. It becomes even more pressing when peoples' safety depends on the reliability and robustness of these heat transfer systems. Although it does not pertain directly to the subject of the present work, the recent failure of lithium-ion batteries on a number of Boeing 787 commercial airplanes shows how the overheating of certain electrical components can be a serious liability. The difficulty is compounded when the elements prone to overheating are small and densely packed so that efficient cooling depends on targeting a specific area of the circuit. It is well known that efficient cooling is not tantamount to reducing the temperature of the whole circuit to a certain value, say room temperature. Rather, the aim is just to reduce the temperature of certain components safely below their thermal runaway thresholds; anything more would be wasteful.

In a bid to increase efficiency and reduce fuel consumption, the design concepts of a More Electric Aircraft (MEA) and an All Electric Aircraft (AEA) are becoming commonplace in the aerospace industry. This trend can be seen in both military (F-22, F-35) and civilian (Airbus A380, Boeing 787) aircraft. On a typical medium-range aircraft, such as the Boeing 737, the capacity of the electrical system is around 100 kW whereas the power level on the more recent Boeing 787 reaches 1 MW (Wheeler and Bozhko (2014)). Practically, a MEA is achieved by replacing pneumatic, hydraulic and mechanical power systems by electrical equivalents that rely on engine-driven generators (Figure 1.1). For instance, the thrust reversers on the Airbus A380 and A350XWB are electrically actuated while on older models, such as the A340, they rely on a hydraulic system (Swiderski and Guenzel (2006)). Each of the power transfer systems depicted in Figure 1.1 for a typical civilian aircraft also require specialized personnel and Ground Support Equipment. By shifting to a MEA, operational and maintenance can be significantly reduced. A projection from the

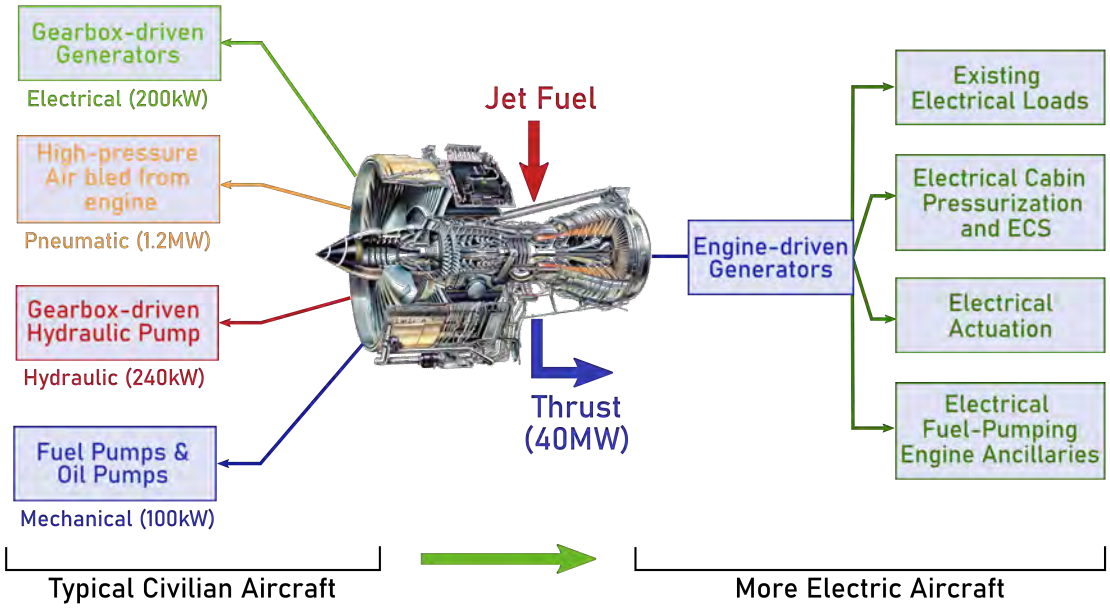

Figure 1.1: Power systems in a typical civilian aircraft versus a More Electric Aircraft (MEA). Abbreviation: ECS: Environment Control System. (Based information found in Wheeler and Bozhko (2014))

early 90's showed that a 2% reduction in fuel costs for a commercial airliner, primarily by reducing bleed air usage (Quigley (1993)).

However, these trends result in a higher demand on engines for power generation and a higher thermal load from the electrical/electronic components. While these demands continue to rise, the relative inefficiencies in aircraft systems have remained constant (Walters et al. (2010)). The Integrated Vehicle Energy Technology (INVENT) program was initiated by the US Air Force in order to tackle inefficiencies stemming from the propulsion system, electrical power systems and high-energy electronic devices. This initiative is based on a unified approach to military aircraft design where energy and thermal management systems are fully integrated and optimized. Thermal management also plays a key role in this perspective, since the efficiency and reliability of electronic components is dependent, to a large extent, on their operating temperatures.

Commercial aircraft also require integrated and compact electrical power systems and electronic devices in order to free up space, reduce weight and cut on fuel consumption. These are important factors for both economic and environmental reasons. A number of international entities have set ambitious goals in order to drastically reduce CO_2 and NO_x emissions. For instance, the Flightpath 2050 report from the European Commission sets a target reduction of 75% of CO_2 emissions per passenger kilometer, and a 90% reduction in NO_x emissions by the year 2050. As a consequence of the integration and miniaturization of on board systems, the effective surface for heat dissipation is significantly reduced. In military applications, heat flux densities can reach up to $10^2 - 10^3 \mathrm{W\,cm^{-2}}$ (Mahe-

fkey et al. (2004)). In addition to maintaining operating efficiency, cooling these densely packed systems is crucial in preventing heat-induced damage of surrounding components and structures. Possible failures include degradation of bonding wires, solder delamination, and current leakage. In highly integrated systems, such failures can be prohibitively expensive, or even impossible, to repair. A number of Thermal Management Systems (TMS) are at the aircraft designer's disposal, that rely on either single-phase flows, phase-changing materials (PCM) or even thermal drain. Compared to the other methods, single-phase cooling solutions remain more widely used for their simplicity and capacity to deliver relatively high cooling rates. A brief survey of their current applications are presented next.

1.1 Single-Phase Cooling

Single-phase thermal management systems rely on the sensible heat of the working fluid to evacuate waste heat. Single-phase cooling systems can be broadly divided into three categories: liquid cooling, spray cooling and air cooling. On board conventional aircraft such as the F-22, the Fuel Thermal Management System (FTMS) is an example of a liquid cooling system that uses fuel as its working fluid. On its way from the fuel tank to the engine, the fuel passes through a series of heat exchangers where waste heat is picked up from hydraulic and electro-mechanical actuation systems as well as the environment control system. In the same way, spacecraft rely on Mechanically Pumped Fluid Loops (MPFL) (Wang et al. (2020)) in order to transport waste heat from on-board devices through cold plates to be radiated out into space. Both these methods fall into the category of indirect cooling solutions since the fluid is separated from the heated components. On the other hand, direct cooling is characterized by the absence of a thermal resistance between the cooling fluid and the heated surface. Examples include air-cooled heat sinks and spray cooling. The following overview of some single-phase cooling methods is by no means exhaustive, but aims at presenting relevant developments in heat transfer technology, with a particular focus on aerospace applications. Some of the devices, such as heat exchangers and microchannels, fall under both liquid and air cooling and are only presented once for brevity.

1.1.1 Liquid Cooling

Heat exchangers Heat exchangers (HX) are conventional devices for indirect heat transfer. Despite their simplicity, they remain relevant today for the crucial role they play in both traditional and alternative power generation technologies. These devices can be classified according to flow arrangement and type of construction (Incropera et al. (2007)). One class of configurations, called *compact heat exchangers*, is often used in situations where space is scarce and the cooling demands are high. These can be further subdivided into *fin-tube* and *fin-plate* designs, shown in Figure 1.2. The fin-plate heat exchanger is the most common design in use for its high performance and low production cost. Possible flow arrangements are parallel flow, where both fluids have the same direction, and cross flow.

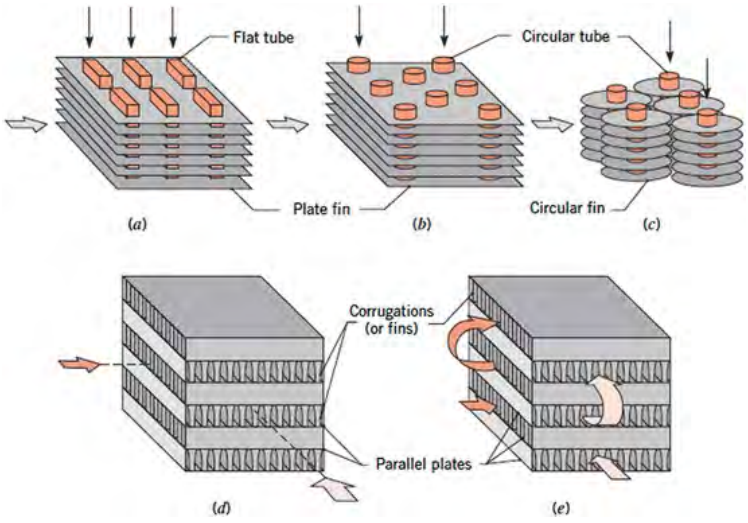

Figure 1.2: Compact heat exchanger designs (Incropera et al. (2007))

There is a large number of fin geometries to choose from, such as triangular, perforated or wavy fins among many more (Figure 1.3).

Heat exchanger design stands to benefit from recent developments in additive manufacturing. Novel geometries and materials can be incorporated into HX designs thanks to this technology. For instance, Saltzman et al. (2018) showed that an additively manufactured (AM) aircraft oil-cooler can increase thermal performance by 10% compared to a traditionally-manufactured HX. This comes at the cost of doubling the pressure drop. However, the authors attribute both effects to an increase in surface roughness. Another design, with small enhancement features, that takes advantage of the 3D printing technology was also tested. Its performance is comparable to that of the baseline AM HX design, which confirms again that surface roughness is the likely cause behind the performance boost, and that more work is needed to improve the manufacturing process. The additive manufacturing technique used in this case is the Selective Laser Sintering (SLS), that is known to offer relatively high roughness ($\geq 5\,\mu m$).

Honeywell Aerospace (Williams et al. (2008)) has been developing HX concepts that integrate new design features such as microchannels. Adding microchannels to the design increases the transfer surface area which leads to an improvement of heat transfer rates per unit volume. In this case, the hydraulic diameter of the flow passages falls in the range of 200 to 700 µm. Heat exchangers with low aspect ratio ($\alpha < 0.2$) flow cross-sections were tested. Flat rectangular microchannels were shown to perform significantly better than square or circular channels, judging by the Colburn factor (j) to Fanning friction factor (f) ratio which is higher for the same fluid pumping power. The small spacing between the fins can lead to several issues such as blockage due to contaminants in the fluid. Manufacturing constraints can also be problematic. Among the many manufacturing processes available, such as microelectomechanical (MEM), lithographie galvanoformung abformung (LIGA) or hollow polymer, the folded fins method was chosen due to the excellent formed shape and

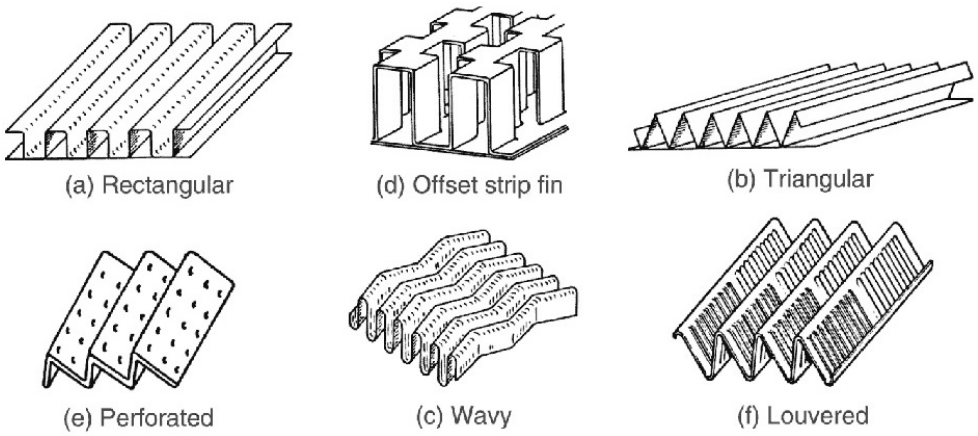

Figure 1.3: Fin-Plate exchanger surface geometries (Webb and Kim, 2005): (a) plain rectangular fins; (b) plain triangular; (c) wavy; (d) offset strip; (e) perforated; (f) louvered

tolerances of the fins as well as the low production cost. The choice of material determines the fin density and height that can be achieved. Furthermore, the brazing step in the heat exchanger fabrication process can lead to a number of issues when the fin-to-fin spacing is small:

- pooling of brazing alloy in the fin crowns
- buckling of tall fins during brazing
- the braze alloy can bend adjacent fins and bond them together, reducing the effective fin count

Both cases presented above show how heat exchanger design is not only driven by performance requirements, but also by manufacturing capabilities.

Cold-plate heat-sinks Cold-plates are extensively used in electronics cooling systems because of their simplicity and high heat transfer rates. The liquid flows through a tube that is mounted onto the plate as can be seen in Figure 1.4. Many factors come into play when designing a cold-plate, but perhaps the most crucial is the choice of coolant. As mentioned before, MEA's require high power density converters in order to run the different electrical components of the aircraft. These converters produce large amounts of heat that need to be efficiently dissipated. For this purpose, Sakanova et al. (2016) performed a numerical and experimental study of several cold-plate configurations. They changed the number of fluid passes in the system and evaluated the thermal and hydraulic performances of three working fluids: water, oil and fuel. They found that although water was the most efficient working fluid, it would require its own hydraulic system, and, as we have seen before, this goes against the idea of a MEA. On the other hand, the viscosity of the oil used induces large pressure drops across the channels, reducing the efficiency of the system. Finally, fuel was found to be the best candidate for the job, since it is readily available on-board, it meets the cooling requirements of the converters and finally induces

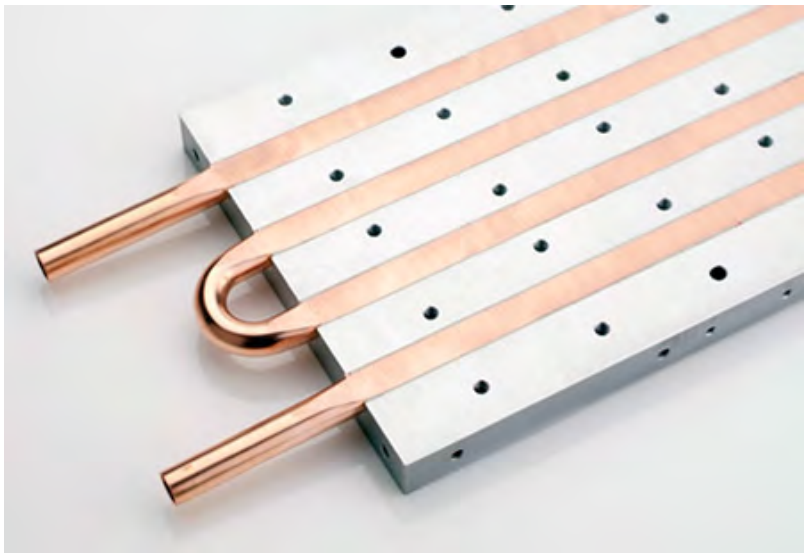

Figure 1.4: Exposed tube cold-plate design. (Wakefield-Vette)

lower pressure drops and so requires smaller and lighter pumps.

Microchannels Roughly speaking, the thermal performance of a cold-plate is inversely proportional to the hydraulic diameter of the tubing used. This has led to the idea of using microchannels, with hydraulic diameters ranging from 10 to 800 µm, as a novel cooling solution. However, the development of this technology is fraught with many challenges both practical and theoretical. For instance, if classical theories are applied, the reduction in size leads to a proportional increase in pressure drop.

In spite of the significant pressure drop (7 bar for a 12-millimiter-long heat exchanger, with a cross-section of 250 µm×320 µm), Alm et al. (2008) achieved heat transfer coefficients of up to 22 kW m^{-2} K, which can justify their use in certain applications where pumping power is not an issue. However, on-board airplanes, this would require large and heavy pumps that increase the load on the engine. The literature is sometimes divided on whether classical heat exchanger theory remain applicable at this scale. For instance, Alm et al. (2008) found that classical heat exchanger theory under-predicted heat transfer coefficients in microchannels when compared to their experimental results. In contrast, Koyama and Asako (2010) found good agreement between their experimental results and predictions from the Logarithmic Mean Temperature Difference (LMTD) method. And finally, making these devices is a technological challenge, since the choice of material and manufacturing process can affect their efficiency. For instance, by reducing the roughness of the walls, it is possible to reduce head loss across the channels, making microchannels a more attractive solution for a wider range of applications.

1.1.2 Spray Cooling

Spray cooling combines three possible functions of a liquid: heat carrier, impinging jet with high heat transfer coefficients and evaporation. The mechanisms by which heat is removed by spray cooling are complex and rely on a host of factors. Spray cooling relies on the break-up of a jet of liquid as it issues from a small orifice at the end of a spray nozzle. The droplets then impact the surface and remove heat both by convection and evaporation. A thin film of liquid can then form around the impact point and further cool the surrounding area. The breakup of the flow increases the surface area to volume ratio and results in lower surface temperature gradients and thus a more uniform cooling. The heat transfer response of a heated surface to spray cooling can change drastically depending on the difference between the surface and liquid saturation temperatures. This change is quantified using a *boiling curve* where heat flux q" is plotted against the temperature difference ΔT (Figure 1.5). The evolution of heat transfer goes through the following regimes:

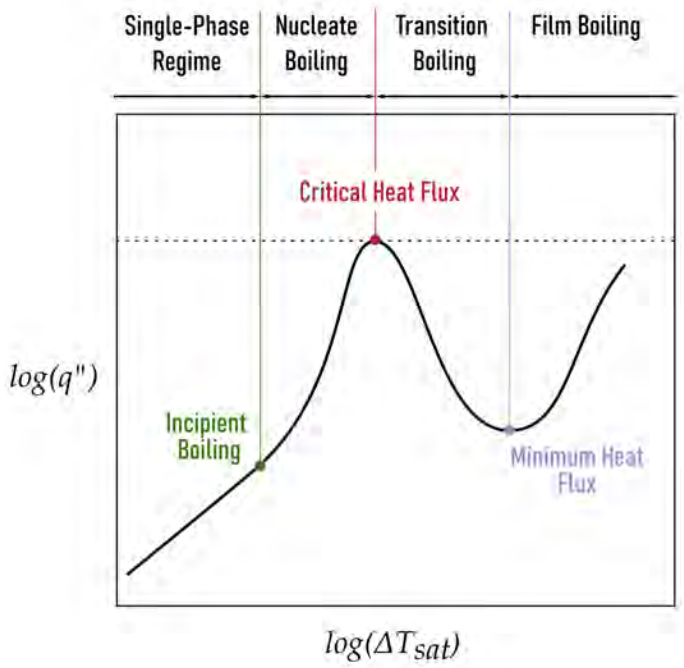

Figure 1.5: Boiling Curve

1. **Single-Phase Regime:** the droplets impact the surface and heat transfer occurs mainly by convection.
2. **Nucleate Boiling Regime:** Bubbles start to form when the droplets reach the surface and form a liquid film. This regime is associated with the highest heat transfer coefficients.
3. **Transition Boiling Regime:** As the temperature continues to rise, the volume of the vapor bubbles near the surface increases to the point where the surface is no longer

sufficiently wetted by the liquid phase. The heat transfer coefficient becomes zero at the point of critical heat flux.

4. **Film Boiling Regime:** Beyond this point, a continuous layer of vapor forms near the surface and a large temperature difference is needed in order to attain the same heat flux again.

The advantages of using this technique come at the price of a complex system that comes into difficulty both in design and during operation. For instance, small differences in nozzle shape (as a result of manufacturing imprecision, or because of wear) can lead to changes in spray patterns that can affect the heat transfer response, making the system unreliable. Furthermore, the liquid needs to be treated before impact to avoid clogging up the nozzle and it needs to be recovered afterwards. This leads to a significant increase of the weight and complexity of the system.

1.1.3 Air Cooling

Although liquids such as water have high heat capacities making them more efficient heat carriers than air, the systems that use them are inherently heavy, costly and require a hydraulic network (Bourdon et al. (2015)). This goes against the very idea of a More Electric Aircraft which aims at replacing hydraulic systems with more efficient electrical equivalents.Replacing liquid cooling with air cooling reduces maintenance costs by eliminating issues such as coolant leakage Morioka and Oyori (2014). Furthermore, there is a wide range of electronic components aboard the aircraft that have different energy requirements and produce heat at varying rates. Liquid cooling systems are often made of large circulation loop with pumps, tanks and coolers and so individual distribution is not possible without increasing the weight and volume of the system. This large loop cooling system cannot *efficiently* meet the requirements of all the various electronic components at once. However, according to Morioka et al. (2014), distributed air-cooling systems are capable of providing "cooling on demand" to the multitude of power electronics components without a significant increase in weight. Finally, distributed air-cooling is more reliable, since a failure in the system cannot propagate as easily as in a single loop system.

1.2 Research Questions and Thesis Structure

In spite of the simplicity and effectiveness of air-cooling systems, there is still room for improvement. A number of studies over the years have shown that jet impingement cooling can be enhanced by introducing periodic perturbations into the flow. These perturbations can be produced either acoustically or by pulsating the jet using mechanical devices. This, however, comes at the cost of adding moving parts that increase the complexity and weight of the cooling system all while decreasing its reliability. These new components require external control systems and are subject to degradation over time. A recent review on thermal management in the aerospace industry (Doty et al. (2015)) suggests the use of fluidic oscillators in order to simplify the fluid feed system. These fluidic oscillators induce

self-sustained instabilities that only rely on the device's fixed internal geometry. Depending on the design, these instabilities can be used to produce either sweeping or pulsating impinging jets. Unfortunately, studies on the heat transfer capabilities of these devices are scarce. The oscillator design considered herein produces pulsating jets, and is often confused with the well-known sweeping jet oscillator. The latter is often used in flow control applications to prevent flow separation on airplane wings (Ostermann et al. (2019) and Woszidlo et al. (2019)). In addition to producing pulsating, the present design has a particular frequency response to inlet pressure and can be scaled in size to accommodate the various needs of heterogeneous heat sources.

This thesis tackles these subjects from a number of vantage points, using both experimental and numerical methods. Its scope is not limited to the study of fluid and thermal phenomena but also extends into the realms of micro-fabrication and semi-conductor physics to develop and test microscopic versions of the device equipped with fast temperature sensors. So far, a brief overview of existing cooling systems has been presented with a particular focus on aerospace applications. The relevance of air cooling was emphasized in the context of a More Electric Aircraft, a concept that has gained traction in the industry over the years.

Chapter 2 is a survey on jet impingement cooling using pulsed jet. A clear distinction is made with synthetic jets that have a zero net mass flux and are produced by different means. The landscape of phenomena that occur in and around a pulsed impinging jet are presented first. The parameters affecting heat transfer performance of pulsed impinging jets are then discussed in detail. Some contrasting results in the literature are highlighted and the difficulty of optimizing performance is shown to stem from the large number of parameters affecting fluid flow and heat transfer. The chapter concludes with a presentation of emerging topics and some perspectives.

The following five chapters are grouped into two parts: the Original Design and the Microscopic Design. In the first part, the internal and external characteristics of the fluidic device are explored and its thermal performance assessed. More specifically, in **Chapter 3**, the response of the device to changes in operating and design parameters is presented along with flow field measurements performed using a moving hot-wire and conditional sampling. Flow features were brought out from the data by means of post-processing techniques such as vortex detection. In **Chapter 4**, results from thermal measurements using infrared thermometry are presented. Pulsed jets produced by fluidic oscillators are shown to be capable of improving heat transfer compared to steady jets having the same mass flow rate. In **Chapter 5**, a numerical study of the prototype that showed most promise in improving heat transfer is undertaken. A first set of simulations that explore the effects of inlet pressure and standoff distance was performed using Unsteady Reynolds Averaged Navier-Stokes (URANS) models. Although these simulations predicted some flow characteristics to a reasonable degree, a noticeable discrepancy in thermal aspects is noted. A second approach based on a hybrid LES/URANS, is then used. This technique only models part of the flow, allowing to simulate flow structures that are smoothed over by purely URANS models. Although it is less costly than Direct Numerical Simulations

(DNS) or pure Large Eddy Simulations (LES), it remains computationally intensive and so only a few cases were selected.

We then move on to the second part concerned with reducing the scale of the device. In **Chapter 6**, the manufacturing of micro-oscillator via polymer dry-film deposition on silicon wafer is presented. In **Chapter 7**, the development of polysilicon-based elements for rapid thermal sensing is presented. The microstructuring process is elaborated in great detail, along with the fine-tuning required in each step to obtain high-sensibility sensors with a short response time. Different doping levels were tested along with different sensor designs and sizes. In the previously studied version of the sensors, the polysilicon layer is in contact with the underlying substrate. In the present iteration, the sensing areas are suspended over the substrate via wet-etching of a sacrificial oxide layer underneath. This was done to reduce the thermal inertia of the sensor. A comprehensive test is then done to check that the process is repeatable, and that the elements are highly sensitive to temperature fluctuations and that their response time is sufficiently low. The micro-oscillators are then produced on the same wafers so that the microsensors are integrated inside the channels. A chip with a resistive heater and an array of sensors was also produced to act as the instrumented impingement surface for the pulsed jets.

We conclude in **Chapter 8** by summarizing the findings, providing directions for future work on the design of large scale prototypes and hinting at the numerous uses of the rapid thermal sensors in microfluidic applications.

"Face au réel, ce qu'on croit savoir clairement offusque ce qu'on devrait savoir. Quand il se présente à la culture scientifique, l'esprit n'est jamais jeune. Il est même très vieux, car il a l'âge de ses préjugés. Accéder à la science, c'est, spirituellement, rajeunir, c'est accepter une mutation brusque qui doit contredire un passé."

La Formation de l'esprit scientifique
Gaston Bachelard

2
Literature Review

2.1 Introduction

The simplicity of jet impingement cooling is deceptive. Although they might seem like the most straightforward way of cooling a heated object, impinging jets involve a host of interacting physical phenomena and depend on a multitude of experimental and technical factors, from the facilities used to produce the jet to the roughness of the impact surface. Introducing a periodic perturbation into the flow adds a layer of complexity both in terms of its effects on the flow and heat transfer and the devices that needed to produce it.

The following review is organized around three main axes:

- **Flow structures and phenomena:** an impinging jet is comprised of a number of canonical flows that feed into each other and interact.
- **Configuration parameters affecting flow and heat transfer**: in addition to well-known parameters such as impact distance and jet Reynolds number, pulsed jets introduce additional factors such as frequency, amplitude and waveform whose individual effects remain uncertain and inconsistent across different studies.
- **How to produce pulsed jets**: there are countless ways of producing consistently pulsating jets, such as electro-mechanical actuation, acoustical excitation, natural flow instabilities and self-excited fluidic devices. Each of these methods comes at a cost that must be compensated by heat transfer improvements compared to steady impinging jets.

Another complementary aspect is the use of numerical simulations to better understand the interaction between the flow and the solid interface. There are a number of approaches, from the fully resolved to the fully modeled, that be used to simulate impinging jets both with and without heat transfer. Unfortunately, there are only a few studies where a pulsed

impinging jet is simulated, and even less so using method that either fully or partially resolve the turbulence in the flow. Although more results on pulsed impinging jets can be found in experimental studies, investigators usually confine themselves to flat and smooth impact plate geometries and simple nozzle geometries. Moreover, the question of what device to use to perturb the flow is often considered as a technical or even secondary matter. But considering the variety of techniques available, it is worthwhile exploring some of them to highlight some of their key attributes and flaws in practical situations.

Following the three axes mentioned earlier, the following topics are considered in the present review:

- **A short history of pulsed impinging jets:** a brief timeline of the study of pulsed impinging jet is presented.
- **Coherent structure and the surface renewal effect:** since this review focuses on heat transfer applications of pulsed impinging jets, this section only serves as an overview of some key studies about coherent structures that pertain directly to the subject.
- **Pulsation waveform, amplitude and frequency:** since these three elements are presented together since they are closely related and have a direct influence on one another.
- **Two or more impinging jets:** in many applications, an array of jets is used to obtain a uniform heat transfer distribution. The flows from the jets may interact with each other, giving rise to, among other things, fountain flows and crossflows that influence heat transfer. In these cases, the phase angle between the pulsating jets becomes a determining parameter of the system.
- **Effect of standoff distance:** as with steady jets, the distance that separates the jet orifice from the target surface plays a crucial role in optimizing heat transfer from pulsed impinging jets. Its effects often differ change depending on other factors such as pulsation frequency and Reynolds number.
- **Characteristics of the target plate:** in order to further enhance heat transfer, passive and active additions to the target surface can be made. Surface roughness elements and heat sinks are passive methods often encountered in certain applications such as electronics cooling. Less common are active methods where certain parts of the surface are actuated. Finally, applications such as turbine blade cooling impose curved surface geometries that can be optimized for better heat transfer.
- **Simulating pulsed impinging jets:** compared to the work done on steady impinging jets, there are only a few studies where a pulsed impinging jet is simulated, especially using methods that resolve the entire flow (DNS) or part of it (LES or Hybrid LES/RANS).
- **Actuation methods:** in this section, a variety of devices are presented that are capable of producing pulsating flows. Some of them rely on moving parts and external control systems, while others are self-excited since they depend on flow instabilities.
- **Emerging topics:** recent developments in nanofluids and microfluidics have opened new pathways for studying pulsed jets.
- **Conclusion and perspectives:** some research gaps are highlighted in this section

along with a brief summary of the review.

2.2 A short history of pulsed impinging jets

> Soon after the music commenced, I observed that the flame of the last-mentioned burner exhibited pulsations in height which were exactly synchronous with the audible beats. This phænomenon was very striking to every one in the room, and especially so when the strong notes of the violoncello came in. It was exceedingly interesting to observe how perfectly even the trills of this instrument were reflected on the sheet of flame. *A deaf man might have seen the harmony.*

This is an oft-cited passage from an article by Leconte (1858) that describes the effect of musical sounds on the flame of a jet of coal-gas. This work, along with Plateau's study of liquid jets subjected to external vibrations (Plateau (1857)), are sometimes cited as the first to study periodically disturbed jets (Michalke (1984), Farrington and Claunch (1994)). However, it wasn't until a century later that pulsating jets were used for impingement heat transfer.

One of the earliest studies on pulsed jet impingement can be found in Burmeister (1959), where the heat transfer between air and a heated surface is evaluated for Reynolds numbers of around 2000, a Strouhal number $\mathsf{St} = fD/U$ (where f, D and U are the frequency, diameter and initial mean velocity of the jet) of 3.2×10^{-4} to 57.5×10^{-4} and a relative pulsation amplitude of 0.73 to 31%. The author showed that under these conditions, there was no appreciable difference in heat transfer, either enhancement or deterioration, when compared to a steady jet. However, they tempered this conclusion by noting that their results hint at the existence of a critical Strouhal number, outside of the range of values considered, beyond which the pulsations' effect becomes significant. Works from the same period (e.g. Nevins and Ball (1961)) supported these conclusions, with Cochrane and Nevins (1962) offering what is probably the first glimpse of pulsating jet impingement using a Schlieren apparatus. According to Ghadi et al. (2016a), these early explorations of the topic may have discouraged further work until the 80's and 90's. Since then, a number of studies were conducted that have looked at the problem from different perspectives. In what follows, we attempt to present significant developments from that last period up to the present day.

2.3 Coherent structures and the surface renewal effect

The formation of vortices around free submerged jets is a result of the Kelvin-Helmholtz instability that starts out in the shear layer between the potential core and the quiescent surroundings. These vortices are then carried by the flow and may undergo a number of transformations along the way, before the jet is completely dissipated. How these structures develop is of practical interest in applications ranging from Vertical Lift-Off and

Landing aircraft (VTOL) (Rizk and Menon (1988)) to cooling solutions for electronic circuits (Mladin and Zumbrunnen (2000)). These examples were not chosen at random; both involve interaction with a solid boundary and this adds a layer of complexity to the problem. In the first application, understanding and then inhibiting the formation of coherent structures is key to reducing the noise produced by the aircraft. In the latter, these same structures can influence the intensity of heat transfer between the cooling fluid and the solid boundary. One of the most promising methods for achieving this control, whether to curb or to intensify the phenomenon, is introducing a periodic perturbation to the jet.

This can involve a host of control parameters making pulsed jets more difficult to study than steady jets. The most notable of these parameters are the frequency, amplitude and waveform of the perturbation. Other factors, that are not directly related to the disturbance itself, can have a noticeable impact on the flow. For instance, the location of the target plate determines at which stage of their development the coherent structures impact the surface. However, the effects of these parameters, especially on heat transfer rates, are not consistent in the literature. Results are highly sensitive to the experimental facility used to conduct the study. For instance, variations in nozzle geometry and initial turbulence levels can influence measurements, leading to inconsistent results that depend on the experimental setup. The heated surfaces are also designed differently and the corresponding temperatures and heat fluxes are acquired using a variety of sensors and visualization methods. Furthermore, the ranges of the input parameters often do not overlap, precluding direct comparison between certain studies. Even though there is a common thread underlying these studies, especially in the phenomenological description of the flow, there remains a lingering ambiguity as to how these flow structures affect the heat transfer rates across the target surface and what combination of parameters are conducive to enhancement of heat transfer.

This section presents an overview of the work done on flow structures in both boundary-free and impinging jets, with special focus on the latter. The response of the flow to the previously mentioned input parameters will be discussed in more detail in later sections. We will limit ourselves here to describing the different parts of the flow. Impinging jets, whether steady or pulsed, produce a complex landscape of structures and regions that have different behaviors. The fluid crosses the nozzle orifice with a given velocity profile and gives rise to two distinct regions: the potential core and the shear layer. The first is a region of potential flow retaining the jet's inlet velocity. It is gradually eroded by the ever thickening shear layer that dissipates the jet's momentum. Growing instabilities in the shear layer can result in the formation of vortices that are transported by the jet. These can then merge in pairs and form larger structures that eventually collapse and become chaotic. When the flow reaches the plate, it can be separated into two regions: the stagnation region followed by the wall jet region. The vortices that form in the shear layer also reach the solid surface and their trajectories are deviated in the direction of the wall jet. These vortices can cause adverse pressure gradient along the solid boundary that can

provoke flow separation. The unsteady flow separation is sometimes associated with a local decrease in the Nusselt number on the heated surface (Liu and Sullivan (1996)) that can be explained by the Reynolds analogy (the separation point is where the friction coefficient $C_f = 0$). On the other hand, as a coherent vortex approaches the impact surface it can induce the formation of a secondary vortex. Together, they form a dipole and can depart from the surface because of auto-induction. This phenomenon, called vortex ejection, is associated with an increase in heat transfer (Varieras et al. (2007)) [1]

Didden and Ho (1985) investigated the flow structures resulting from a harmonically forced impinging air jet. The main focus was the mechanism of formation of secondary vortices and the ensuing separation of the flow from the impingement wall. The presence of the primary vortex in the inviscid region of the flow above the solid boundary causes an adverse pressure gradient in the viscous region, retarding the flow therein. On the other hand, the flow is accelerated in the inviscid region. A local shear layer then appears that has a vorticity of opposite sign to that of the primary vortex. This shear layer is unstable and a secondary vortex is formed. This vortex lifts up from the wall initiating the separation of the flow.

Kataoka et al. (1987) studied the heat transfer from a *steady* submerged water jet impinging on a heated plate. For liquids (in the asymptotic case where $\mathsf{Pr} \to \infty$), the Nusselt number resulting from a flow over a flat plate at either constant temperature or constant heat flux is proportional to :

$$\mathsf{Nu_{FP}} \sim \mathsf{Re}^{1/2}\mathsf{Pr}^{1/3} \tag{2.1}$$

For this reason, the investigators have chosen the Frössling number $\mathsf{Fö}$ – which is none other than the ratio $\mathsf{Nu}/\mathsf{Nu_{FP}}$ – as their criterion for evaluating the performance of the jet. The Nusselt number Nu is defined as hd/κ, where h is the convective heat transfer coefficient, d is the nozzle exit diameter and κ the thermal conductivity of the fluid. First off, they found that $\mathsf{Fö}$ always reaches its peak for a standoff distance of about $6d$. This result was interpreted by visualizing the jet (without an impact surface) using the hydrogen bubble method, thus revealing the following structure of the flow (Fig. 2.1):

1. At $z/d \approx 1$: vortex rings start to form due to instability in the shear layer.
2. At $z/d \approx 3$: vortices start to pair up and merge.
3. At $z/d \approx 4-5$: large eddies appear and are responsible for surface renewal effects that are tied to heat transfer enhancement.

The authors were also able to find a strong correlation between the Frössling number and

[1] For details on dipole vortex formation in planar wall jets see Conlon and Lichter (1995). Using a vortex ring generator, Hubble et al. (2013) conducted a simplified experiment whereby single vortices interact with a heated wall. A secondary vortex is produced at the heel of the impinging vortex after impact. Together, they form a vortex dipole that departs from the wall.

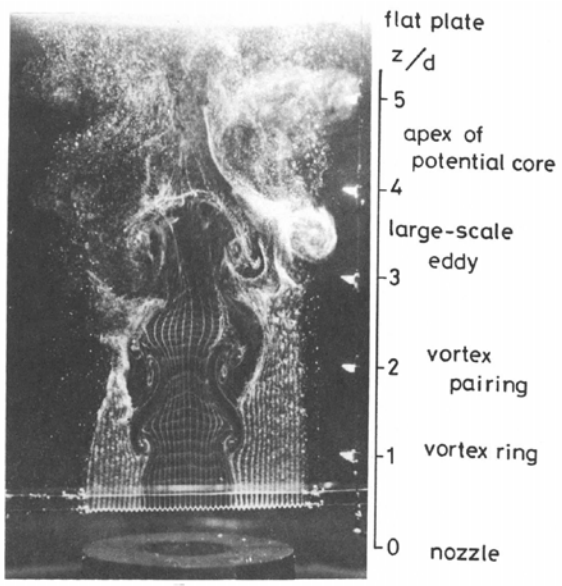

Figure 2.1: Cross-section view of the free jet flow patterns visualized by the hydrogen bubble method Kataoka et al. (1987)

the so-called surface renewal parameter, that they define as:

$$\mathsf{Sr} = \frac{\sqrt{\overline{u^2}}}{U_m}\frac{f_e d^2}{\nu} = \mathsf{Re}_{\mathsf{Turb}} \cdot \mathsf{St}_f \tag{2.2}$$

Here $\sqrt{\overline{u^2}}$ is the rms of the fluctuating velocity, f_e is a characteristic frequency of vortex formation (or passing frequency), ν is the kinematic viscosity of the fluid, U_m the velocity at the centerline, $\mathsf{Re}_{\mathsf{Turb}}$ is the Reynolds number based on the rms of the fluctuating velocity, and St_f is the Strouhal number based on the frequency f and the velocity U_m. The passing frequency is not the same in the transitional region ($2 < z/d < 4$) and the turbulent region ($z/d > 4$). In the transitional region, this frequency is equal to the dominant frequency of velocity fluctuations along the centerline of the jet. Beyond this region, the frequency is defined as the inverse of the characteristic time scale T defined as:

$$T(z) = \int_0^\infty R(z,\tau)d\tau \tag{2.3}$$

where $R(z,\tau)$ is the velocity autocorrelation function. The investigators thus conclude by plotting $\mathsf{Fö}$ versus Sr that the surface renewal effect of large eddies (same definition as Yule (1978)) is in large part responsible for the enhancement of heat transfer.

Popiel and Trass (1991), by use of a smoke-wire visualization technique, studied the flow structure of free and impinging *round* jets from vortex initiation at the nozzle, to pairing and merging. This investigation is particularly interesting because it considers small standoff distances ($H/D = 1.2, 2$) for a significant range of Reynolds numbers ($\mathsf{Re} =$

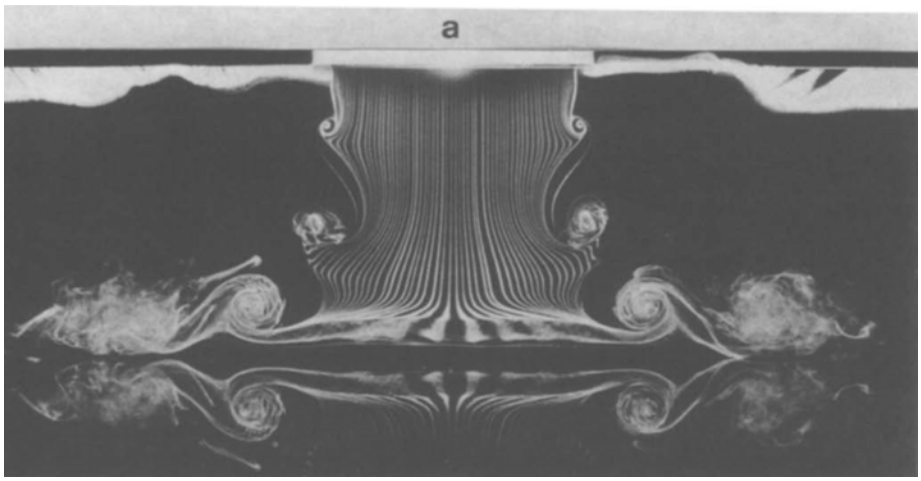

Figure 2.2: Round jet with $H/D = 1.2$ and $\mathsf{Re} = 20,000$ (Popiel and Trass (1991)). The investigators used the smoke-wire visualization method.

3500 to 20,000). At $H/D = 1.2$, as it approaches the plate, a large toroidal vortex stretches and loses its axial velocity component and starts diverging radially (Fig. 2.2). By placing the smoke-wire close to the plate, at the center of the jet, ring-shaped wall eddies, induced by the large toroidal vortices, were observed starting at the point where the latter reach the plate. At $r/D = 1 - 2$ these two structures merge and result in a turbulent wall jet. For $H/D = 2$ the vortices reaching the plate have larger characteristic dimension than in the previous case due to vortex merging. For $H/D = 2 - 4$ the instantaneous stagnation point is observed to oscillate around the mean stagnation point, and finally at $H/D > 4$, the flow reaching the plate is chaotic, and contains both large scale coherent structures, and fine scale turbulence. The authors note that the above-mentioned process involving wall eddies can lead to an enhancement of local momentum, heat or mass transfer.

Ghadi et al. (2016b) studied the development of vortex structures produced by externally excited unconfined impinging jets of air. The experimental setup was straightforward: two main flow channels were connected to a 100 mm diameter glass cylinder, equipped internally with a woven-wire screen and honeycomb flow-straightener. The temperature of the main flow was controlled via a heat exchanger system. Upstream from the two main channels, a loudspeaker was installed to excite the flow. In the first part of the study, the standoff ratio was set to $H/D = 2$ and flow visualization was achieved by the smoke-wire technique. The frequency of excitation was modulated from 1.5 to 9 Hz corresponding to a range of Strouhal numbers of $\mathsf{St} = 0.125 - 1.0$. First of all, the investigators found that, although they also appeared in steady state jets, vortex structures were far more noticeable in terms of size when external excitation was superposed onto the flow. Furthermore, increasing the frequency, up to a certain point, gave rise to large vortex structures which are the result of vortex interaction, pairing and finally merging. The vena-contracta phenomenon also occurs more prominently at Strouhal numbers between 0.25 and 5 and accelerates the flow before it impacts the surface. Nonetheless, for $f = 9$ Hz (or $\mathsf{St} = 1.0$), the vortices

were produced at such a high rate that they did not have the time to merge, and so formed a consistent row that was transported along the jet and along the plate. Although this study did not consider heat transfer at the solid surface, one can draw similarities with the results from Hofmann et al. (2007b) who found that heat transfer starts to improve above a Strouhal threshold of $\mathsf{St} = 0.2$. The difference here is that there might be an upper limit for frequency, above which it is not possible to improve heat transfer owing to the change in overall flow structure.

Farrington and Claunch (1994) studied free planar jets of air with low-frequency, high-amplitude disturbances. Their aim was to understand and improve mixing between the jet and the surrounding quiescent air. The planar jets were produced by a slot diffuser, commonly found in offices. Infrared imaging was used to extract temperature profiles and contours and deduce the spreading rate of the pulsating jet. Introducing pulsations increased the spreading angle of the jet while reducing its throw. This means that mixing was enhanced between the jet and the surrounding fluid. Furthermore, smoke-wire visualizations showed that for steady jets, the vortex structures are small and can be either symmetrical or antisymmetric and the jet boundaries are nearly vertical near the orifice, i.e. it does not spread significantly. On the other hand, when pulsations were introduced, large symmetrical pairs of vortices were observed. These vortices merged at the same location where the rate of decay of the axial velocity suddenly increases, at 6 to 8 nozzle width. The influence of pulsations on jet mixing can be one of the determining factors in heat transfer performance in impinging jets, as noted by Janetzke et al. (2008) and Zhou et al. (2019) (for sweeping jets).

2.4 Pulsation waveform, amplitude and frequency

The waveform of the area-averaged velocity profile at the jet orifice plays a significant role in the heat removal process. As we will see shortly, the production of vortices around the jet itself is dependent on how its characteristic velocity changes with time. We will also see that the relative time during which velocity stays at a certain value can affect the local intensity of heat transfer at the impact point.

Canonical Wave-forms

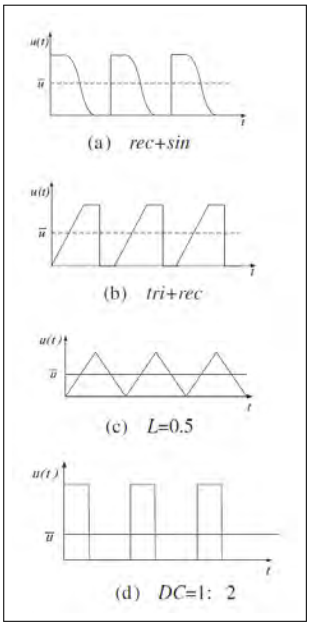

Figure 2.3: A sample of the periodic jet velocity signals used in Geng et al. (2015).

Experimental

Geng et al. (2015), in an experimental study, used a so-called mass flow rate controller (MFRC) in order to obtain nearly arbitrary velocity waveforms. Sinusoidal, rectangular and saw-tooth signals were used along with some of their combinations.

Combining two signals meant having a different waveform for each of the two halves of every period of pulsation. The saw-tooth signals were classified by the ratio $L = t_+/T$ where t_+ is the time during which velocity is increasing and T is the total length of a period. Five values of L were chosen between 0 and 1 (where $L = 0$, for instance, represents a waveform with a step increase in velocity followed by a linear decline). And finally, the rectangular signals were sorted by duty cycle $\mathsf{DC} = t_{\mathsf{on}}/t_{\mathsf{off}}$, i.e. the ratio of on- to off-time (see Fig. 2.3).

In addition, if the mass flow rate is set to a fixed value, we end up with higher peaks for greater duty cycles. In this study, the parameters quantifying performance were the time-averaged Nusselt number Nu, the stagnation point Nusselt number Nu_0 and the enhancement coefficient $\Delta\mathsf{Nu}/\mathsf{Nu}$. The standoff distance remained unchanged throughout the different tests at $H/D = 6$ (which is often considered to be the optimal standoff distance for steady jets). The time-averaged Reynolds number also remained unchanged at $\mathsf{Re} = 4500$. And finally, the frequencies considered ranged from 1.25 Hz to 20 Hz.

Among the five variants of triangular signals, the ones involving a step change in velocity outperformed the rest. Furthermore, the $L = 1$ case was shown to slightly surpass the $L = 0$. The authors speculate that positive step changes lead to the creation of coherent structures, whereas negative step changes destroy these same structures resulting in an

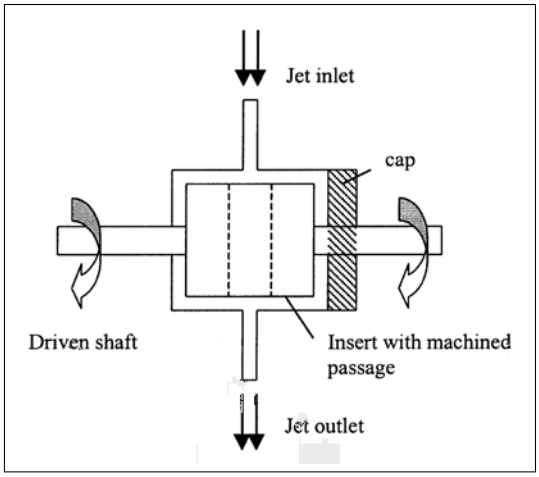

Figure 2.4: Rotating valve used in Sailor et al. (1999).

unstructured turbulent field. This explanation is in stark contrast to the conclusions arrived at by Chaniotis et al. (2003), who found that heat transfer enhancement is a signature of coherent structures rather than chaotic turbulence. They had reached this conclusion after simulating impinging jets using a remeshed Smooth Particle Hydrodynamics (SPH) methodology.

Nonetheless, the triangular signals were surpassed by an even larger margin by the rectangular signals. And among the latter group, smaller duty cycles (and so, higher velocity peaks) resulted in larger enhancement coefficients. This is a sign that the larger the velocity leaps, the better the heat transfer. It is worth noting however that the *exact* physical explanation behind this remains unclear.

Sailor et al. (1999) went a step further by investigating the effects of duty cycles (defined here as $t_{\mathsf{on}}/T_{\mathsf{tot}}$) on heat transfer rates. They were able to produce pulsed circular jets via a rotating valve that controlled the duty cycle (Fig. 2.4). The parameters of the experiments had the following ranges: $\mathsf{Re} = 21,000 - 31,000$, $\mathsf{DC} = 0.25 - 1$ and $f = 20 - 60\,\mathrm{Hz}$. Unlike Geng et al., Sailor et al. had a varying standoff distance ranging from 4 to 8 nozzle diameters and managed to show that lowering the duty cycle had much larger positive effect (resulted in larger *stagnation point* Nusselt number) at small distances than at larger ones. They also found that intermediate frequencies resulted in higher stagnation Nu. This, however, should be taken with a grain of salt seeing that the investigators studied a narrow gamut of frequencies, so that in reality there might be a more complex trend at work.

Numerical

Mohammadpour et al. (2014a), restricting themselves to sinusoidal and square-shaped waveforms, reached similar conclusions to Geng et al. They ran simulations of a submerged jet of air impinging on a concave surface using the renormalized group (RNG) $k-\varepsilon$ model.

The configurations studied had frequencies ranging from 20 to 80 Hz, Reynolds numbers (based on the hydraulic diameter of the orifice) from 4740 to 7200, nozzle-to-surface distances from 3 to 10 nozzle widths and amplitudes A from 0.2 to 1.0 for the sinusoidal wave:

$$u_{\text{jet}} = u_{\text{avg}} \left(1 + A \sin\left(2\pi f t\right)\right) \tag{2.4}$$

For a similar set of conditions (namely $\mathsf{Re} = 6000$, $f = 40\,\text{Hz}$, $H/B = 4.0$ and $A = 1.0$) the square-shaped waveform resulted in significantly higher time-averaged Nusselt number along the surface. This is attributed by the authors to the formation of larger coherent structures in the vicinity of the pulsed jet that are then transported downstream towards the exit.

In another numerical investigation, this time using the SST/$k-\omega$ turbulence model, Zhang et al. (2018) studied the effect of waveform on the heat transfer characteristics of *synthetic* impinging jets (i.e., having zero mean velocity). Their two-dimensional computational domain has a simple rectangular geometry. The inlet nozzle of the jet is simply modeled by an orifice in an adiabatic wall facing another solid surface whose mid-section is characterized by a constant heat flux while the rest is adiabatic. The turbulence intensity is set to 5% at the lateral exits. The waveforms are produced using a template function:

$$u_K(t) = \begin{cases} \dfrac{\sin\left[-K \arcsin(2\pi f t)\right]}{\arcsin\left(-K\right)} & -1 \leq K < 0 \\ \sin(2\pi f t) & K = 0 \\ \dfrac{\tanh\left[K \sin(2\pi f t)\right]}{\tanh K} & K > 0 \end{cases} \tag{2.5}$$

Three specific waveforms were considered, namely triangular T, sinusoidal S and rectangular R corresponding to $K = -1; 0$ and $10,000$ respectively (the value $10,000$ being a stand-in for $K \to \infty$). The following ranges were considered for each relevant parameter:

- $\mathsf{Re} = 1553 - 7766$
- Frequency $f = 10 - 400\,\text{Hz}$ (Strouhal $\mathsf{Sr} = 0.012 - 2.4$)
- Standoff distance $H/D = 2 - 8$

From a heat transfer point of view, a critical Strouhal number (above which performance enhancement can be seen) in the range $0.24 \leq \mathsf{Sr} \leq 0.48$ was detected. The turning frequency was found to depend on the Reynolds number and standoff distance in a non-monotonic way. The turning frequency also depends on the waveform of the inlet velocity signal. It seems that no clear, global trend transpires from this study regarding the effect of waveform and frequency on heat transfer rates. However, the main conclusion here is that, through a specific combination of parameters, it *is* possible to reach an enhancement as high as 74% compared to equivalent steady state cases.

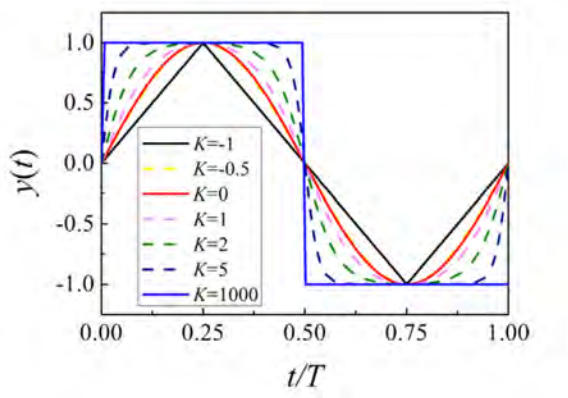

Figure 2.5: Plot of Eq. 2.5 for different values of the parameter K (Zhang et al. (2018)).

Going back to pulsating flows, Behera et al. (2007) also investigated the effects of waveform, frequency, Reynolds number and standoff distance on heat transfer. The heated wall was modeled as a no-slip boundary with constant heat flux. Reynolds numbers ranged from 5130 to 8560, frequency from 25 to 400 Hz and dimensionless standoff distance from 5 to 9. Both square and sinusoidal waveforms were considered with the latter having rms to mean ratios ranging from 18 to 53%. The standard $k-\varepsilon$ model was used with a two-layer zonal model for near wall treatment. Average radial velocity was computed along the wall, which showed that pulsating jets resulted in higher averaged velocity. The increase in radial velocity distribution was more readily seen for square-waves than sinusoidal ones. For square wave jets, increasing the frequency resulted in thinner boundary layers, meaning that resistance to heat transfer is reduced. The investigators found that square pulsations result in up to 12% enhancement in the stagnation region and 35% in the wall jet region, whereas sinusoidal pulsations led to 5 and 10% improvement respectively under the same operating conditions. The authors also noted that the amplitude of pulsation has a greater effect on heat transfer than does the frequency.

Although this is not mentioned by the authors, a critical Strouhal can be found for each combination of parameters for the square wave jet. This critical Strouhal number can go from 0.01 to 0.1, though most values are close to 0.02. This is a far cry from the $\mathsf{Sr}_{\mathsf{cr}} = 0.2$ found by Hofmann et al. (2007b) for sinusoidal wave jets, or even the range $\mathsf{Sr}_{\mathsf{cr}} = 0.24 - 0.48$ found by Zhang et al. (2018) for synthetic jets.

Frequency and Strouhal Number

Zulkifli et al. (2004), much like Azevedo et al. (2015) and Sailor et al. (1999), used a rotating cylinder valve in order to produce and study circular pulsed air jets as they impinge on a heated plated at frequencies ranging from 10 to 80 Hz (and $\mathsf{St} = 0.008 - 0.123$). The center-line velocity and the average velocity profile were measured using hot-wire anemometers at each frequency. Data from flush-mounted heat flux sensors and thermocouples were used to compute the Nusselt number on the cooled plate. The air jet was heated before it entered the rotating valve, while the target plate was a water-cooled aluminium block. Further-

more, the impact surface was covered in a Kapton sheet having the same conductivity as the heat flux sensor so that the latter's presence did not affect the heat distribution on the plate. The investigators found that the stagnation Nusselt number for pulsed jets remained smaller than for the steady jet all while exhibiting a complex, non-monotonous relation with frequency, which echoes the results obtained by Azevedo et al. (2015). However, unlike Azevedo et al. (2015), the present work also computed the local Nusselt number at different radial positions and found a noticeable enhancement in performance at $r/D > 1$. Furthermore, by averaging the Nusselt number distribution in space and in time, they were able to show that an improvement of up to 40% (compared to the steady case) was possible. This was obtained at $f = 70\,\mathrm{Hz}$ and $\mathsf{Re} = \mathsf{Re}_{max} = 32,000$. The authors posit that the improvement at $r/D > 1$ was due to the pulsation's ability to increase turbulence intensity.

Eschmann et al. (2015) used the same set-up to produce and compare steady and unsteady impinging jets. The set-up was comprised of a settling chamber, fed by a number of inlets, with a loudspeaker mounted on the side facing the jet orifice. This allowed the investigators to produce three types of jets at will: steady, pulsed (or hybrid-synthetic) or synthetic. The first is achieved by simply letting the inlet fill the chamber without turning on the loudspeaker, the second is produced by activating the speaker at a given frequency and pulsation amplitude while the third requires cutting off the inlet with the loudspeaker still on. Using a novel heat transfer coefficient (HTC) sensor, they were able to extract the radial distribution of Nusselt number along the impact surface. The jet Reynolds number ranged from 1600 up to 5600, the frequency from 30 Hz to 120 Hz and the amplitude from 20 % to 100 % (of mean velocity). Measurements from the steady case were found to be in good agreement with correlations from the literature for moderate Reynolds numbers and small standoff distances, while diverging significantly for larger values of these two parameters. For extremely narrow nozzle-to-plate spacing ($H/D < 2$), a typical Nusselt distribution was obtained: the primary peak is displaced downstream in the radial direction and is followed by a less prominent secondary peak. The former is attributed to the abrupt acceleration of the flow as it escapes the stagnation zone while the latter is tied to the vortex structures above the plate. While synthetic jets seem to lag behind the steady jets in terms of heat transfer performance for all the configurations considered, the pulsed jets had a slight edge over the steady cases, especially for the highest Strouhal number considered $\mathsf{St} = 0.27$. This enhancement is more marked for larger standoff distances.

Pakhomov and Terekhov (2013) performed numerical simulations of a round pulsed jet of air impinging on an isothermal plate[2]. A Reynolds-Averaged Navier-Stokes turbulence model was used along with the finite volume method to obtain the desired results. The average velocity was in the range $U = 3.5 - 35\,\mathrm{m\,s^{-1}}$ for both the steady and pulsed cases, which corresponds to a Reynolds number range of $\mathsf{Re} = 4600 - 46,000$. The pulsed inlet velocity had a rectangular waveform with a 50 % duty cycle (off time equals on time), and

[2]For complementary results from the same authors, see Pakhomov and Terekhov (2015)

frequencies ranging from 0 to 60 Hz. Finally, the standoff distance considered went from $H/D = 1$ to 10. The investigators found that heat transfer rates increase with standoff distance from $H/D = 1$ to 6 before steadily decreasing at larger distances. The gap width $H/D = 6$, as was mentioned before, corresponds to the length of the potential core of the jet. Increasing the frequency from 0 to 60 Hz at small impact distances led to a noticeably enhancement of stagnation Nusselt number. However, this was not the case at large gap widths where the trend was inverted. Part of the results (at $H/D = 3$ and $\mathsf{Re} = 7,500$) were compared with experimental data from Herwig and Middelberg (2008) and Middelberg and Herwig (2009). The enhancement ratios (ER) exhibited the same tendency whereby heat rates are suppressed at low frequencies (up to around 5 Hz) and then intensify as frequency increases.

In a thorough parametric study, Hofmann et al. (2007b) shed some light on how the frequency of a pulsed jet, among other factors, can influence heat transfer rates. They were able to identify a critical Strouhal number ($\mathsf{Sr} = fD/u = 0.2$) above which pulsed jets and their resulting heat transfer distributions depart from a quasi-steady behavior. They were able to produce a sinusoidally alternating jet by means of a rotating cage periodically opening and closing an orifice in a hollowed out cylinder. A laser-doppler-velocimeter was used to measure velocity at certain points in the flow. These measurements allowed the investigators to reveal the difference in flow structure between steady jets and low- and high frequency pulsed jets. For the high-frequency case, unlike the steady and low-frequency cases, the axial velocity is no longer distributed along a quasi-Gaussian curve and the turbulence intensity is more significant. The amplitude of pulsation is dampened along the jet for the high-frequency case, yet it remains the same for the low-frequency case. With regards to heat transfer, the researchers found that for low frequencies, ranging from 1 to 140 Hz, the Nusselt number distributions have the same form as in the steady configuration. Smaller standoff distances (precisely, $H/D = 2$) combined with larger pulsation intensities resulted in overall higher values of the Nusselt number, the form of the distribution remaining unchanged. On the other hand, for a standoff distance of 8.5 nozzle diameters, pulsating the flow resulted in a deterioration of performance for all Reynolds numbers, pulsation intensities and frequencies considered.

The authors argue that enhancing heat transfer rates can only be achieved when the frequency of pulsation exceeds that of the turbulence. In order to estimate the former, they posit that the period of a vortex first appearing at the boundary of the nozzle must have a period which is smaller than the time it takes to be convected from the base to the edge of the potential core. Keeping in mind that most of the literature agrees that the potential core is around 5 hydraulic diameter long, the residence time is then estimated as:

$$t_{\mathsf{res}} = \frac{5D}{u_0} \tag{2.6}$$

which then leads to the critical Strouhal number:

$$\mathsf{St}_{\mathsf{cr}} = \frac{f_{\mathsf{cr}} D}{u_0} = \frac{D}{u_0 t_{\mathsf{res}}} = 0.2 \tag{2.7}$$

These assumptions have been tested for $\mathsf{Re} = 34,000$ and $78,000$ and pulsation intensities ranging from 3.5 to 30%. This theoretical threshold proved to be more or less correct for standoff distances not exceeding the length of the potential core, namely $H/D = 5$. For larger distances, the effects of jet decay predominate and the overall performance plummets for all frequencies considered. In one of the cases, for a standoff distance of $H/D = 2$, the stagnation Nusselt number shot up from around 185 for the steady case to 240 for a jet pulsed at 750 Hz.

Xu et al. (2010) carried out a set of numerical simulations of a slot jet impinging on a surface. Each case is characterized by a combination of the following parameters: temperature difference between jet and surface (ΔT = 50 to 200 K), Reynolds number (Re = 2720 to 8200), standoff distance (H/D = 3 to 8) and frequency (f = 25 to 100 Hz. An intermittent (square) velocity signal was used at the inlet. It was found that the Nusselt number Nu increased with increasing frequency, increasing Reynolds number and decreasing ΔT. The intermittent jet, when compared to a steady case, resulted in thinner hydrodynamic and thermal boundary layers, which led to enhanced heat transfer.

By means of a semi-analytical model (similar to Karman-Pohlhausen), Mladin and Zumbrunnen (1994) investigated the nonlinear dynamics of laminar boundary layers subjected to periodic changes in velocity and heat flux. By rewriting the continuity, momentum and energy equations in a simplified dimensionless form, they were able to arrive at a set of three ordinary autonomous differential equations whose solution would yield the dimensionless hydrodynamic boundary-layer thickness $\Lambda = C\Delta^2/\nu$, the dimensionless surface temperature $\Theta_s = (T - T_\infty)/(T_{s0} - T_\infty)$ and the dimensionless thermal boundary-layer thickness $\Gamma = C\delta^2/\nu$. Sinusoidal forcing functions were used for both the velocity and heat flux.

For a constant heat flux, it was found that increasing the frequency above a certain threshold resulted in a non-linear response of the system along with a slight increase (2%) in overall Nusselt number. Nonetheless, for all remaining frequencies, the time-averaged Nusselt number was found to decrease significantly more compared to the steady case (more than 15% decrease). Similar results were subsequently found by Mladin and Zumbrunnen (1995), where the effect of pulse shape was considered. It is worth noting here that these two studies were limited in frequency due to the stability criteria of the mathematical model employed. A complementary experimental study on submerged planar jets was conducted by the same researchers Mladin and Zumbrunnen (1997) which reached similar conclusions solely in the stagnation region.

Zumbrunnen and Aziz (1993) in an experimental study looked for a critical frequency

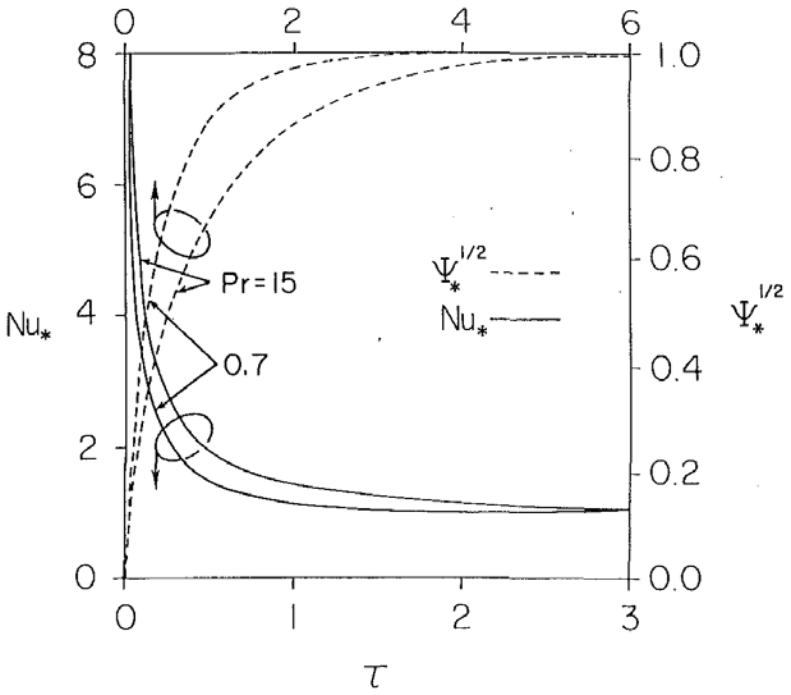

Figure 2.6: Unforced transient response of the thermal boundary layer (TBL) and Nusselt number. $\Psi_* \propto \Delta^2$ where Δ is the thermal boundary layer thickness (Zumbrunnen and Aziz (1993)) .

(in terms of the Strouhal number) above which heat transfer enhancement is achieved for a non-submerged water jet. The idea of a threshold frequency came from observing the unforced response of a laminar boundary layer studied analytically in Zumbrunnen (1992) (see Fig. 2.6), where little enhancement was found for the dimensionless time $\tau > 3$ [3]. With this reasoning in mind, an approximate critical Strouhal number was defined as:

$$\mathsf{St} = \frac{fw}{v_j} = \frac{1}{3/C}\frac{w}{v_j} = \frac{C^*}{3} \tag{2.8}$$

where w is the width of the jet, v_j is the jet velocity, and $C^* = Cw/v_j$ is the dimensionless velocity gradient. For planar jet with of constant velocity profile $C^* = \pi/4$. This would mean that the Strouhal number should be greater than 0.26 in order to see enhancement in heat transfer. The flow intermittency was achieved by means of blades on a large rotating wheel that periodically deflected the water jet off of the plate's path. However, this technique resulted in jet distortion and hence a Nusselt profile skewed in the direction of the moving blade. The experimental results showed that a minimum Strouhal number was required in order to enhance heat transfer, at the stagnation point and downstream along the plate. This critical Strouhal number is close to the approximate criterion previously mentioned. Another factor, the ratio of on- to off-time Γ, helped show that the primary

[3] τ is defined as $\tau = Ct$ where C is the constant (Schlichting (2017)) free-stream velocity gradient.

reason for enhancement is the boundary layer renewal and not increased turbulence. Plotting the dimensionless stagnation Nusselt number against Γ showed a rapid increase in enhancement relative to the steady case as Γ was decreased. A twofold enhancement was found for $\Gamma = 2$ (which was the lowest value considered).

Mladin and Zumbrunnen (2000) sought to show the link between flow structures and time variation of heat flux by use of the coherence function [4]. The following experimental conditions were considered:

- $\mathsf{Re} = 1000, 5500$ and $11,000$
- Frequency $f = 0$ to $82\,\mathrm{Hz}$ ($\mathsf{St} < 0.13$)
- Pulse amplitude $A_N = 0$ to 50% of mean velocity
- Standoff distance $H/w = 3$ to 10

for a planar jet of air impinging normally on a heated surface. By analyzing the velocity signals measured at different axial distances from the nozzle they have shown the occurrence of the vortex pairing process. Small scale structures having the same frequency as the pulse were identified within the fluctuating velocity signal, as well as larger structures having half of that frequency (indicating the merging process). As in other studies, it was found that increasing both the Strouhal number and the amplitude of oscillations results in a marked enhancement in cooling reaching up to 80% in certain regions of the plate.

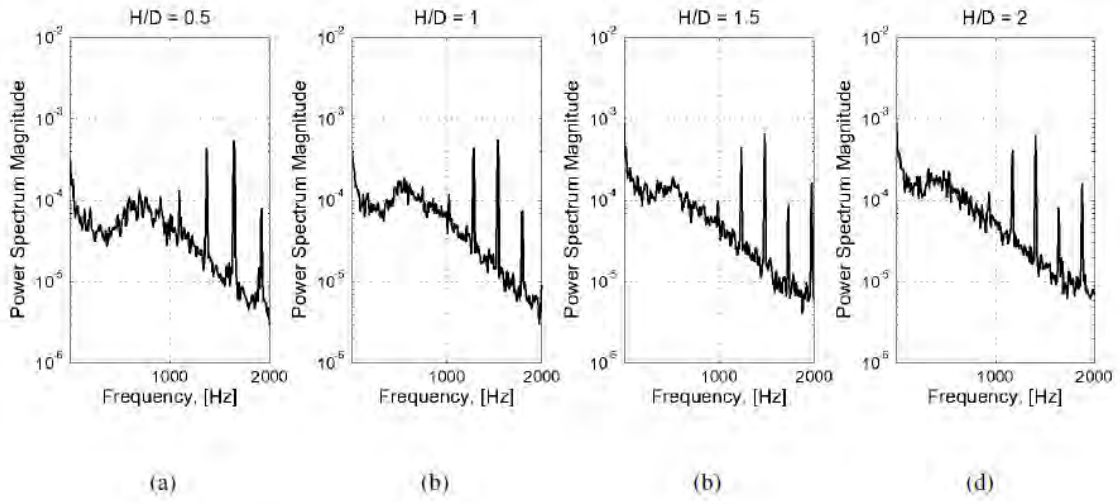

Figure 2.7: Heat transfer spectra for $\mathsf{Re} = 10,000$, $f_e = 0\,\mathrm{Hz}$ and $r/D = 1.3$ in O'Donovan and Murray (2007a)

Control of vortex development and behavior can be achieved by changing the excitation frequency. In an experimental study conducted by O'Donovan and Murray (2007a), this influence was made evident in the response of the secondary peak of the Nusselt number distribution to acoustic perturbation of the jet. The investigators observed that exciting

[4] More precisely, the *mean-squared coherence*, which is the ratio of the squared amplitude of the complex cross-spectral density to the product of the auto-spectral densities of the signals considered.

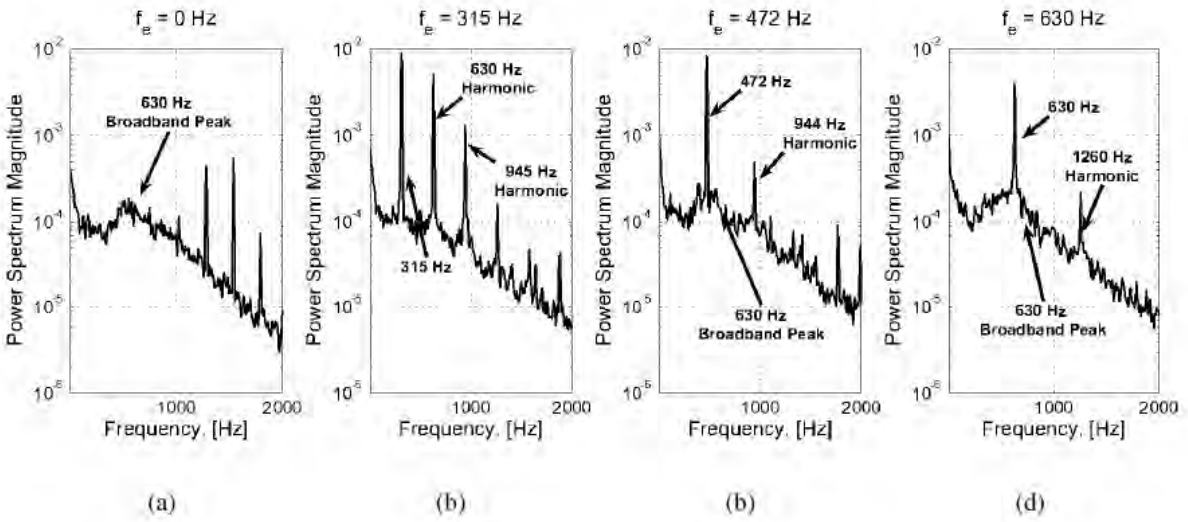

Figure 2.8: Heat transfer spectra for $\mathsf{Re} = 10,000$, $H/D = 1.0$ and $r/D = 1.3$ in O'Donovan and Murray (2007a)

the jet at frequencies below $f_j = 630\,\mathrm{Hz}$ (natural frequency of the jet) leads to a suppression of the secondary peak (that manifests itself at low impact distances, here $H/D < 2$). As H/D is increased up to 2, the fluctuating Nusselt number in the unexcited case is enhanced in the stagnation region and reduced near the secondary peak. A similar behavior is observed for excitation frequencies less than the natural frequency, except that two secondary peaks are present instead of one. As the excitation frequency nears f_j, the fluctuating and time-averaged Nusselt profiles approach those of the steady case. It is worth noting that locations other than the stagnation point and the secondary peak were less affected by the acoustic perturbations. As already shown in O'Donovan and Murray (2007c), there is a link between the passing frequency of the vortices in the wall jet and the prominence of the secondary peak. As mentioned above, for $f < f_j$ in the excited case and by increasing H/D in the unexcited case, similar trends can be observed in the fluctuating and average Nusselt number distributions. In both cases, the effect on the secondary peaks is attributed to a lower vortex passing frequency. For increasing H/D, the nascent vortices have more time to merge, reducing their passing frequency (see Kataoka et al. (1987) and Popiel and Trass (1991)). By exciting the jet at $f < f_j$ (especially at a subharmonic frequency $f = 315\,\mathrm{Hz}$), vortex merging is also favored even at smaller values of H/D. These links are based on the response of the heat transfer spectra to different values of H/D (steady case, Fig. 2.7) and excitation frequency (Fig. 2.8). For more details, the reader is referred to the following studies by the same authors: O'Donovan and Murray (2007b) and O'Donovan and Murray (2007c).

Using an experimental setup akin to that of O'Donovan and Murray (2007a), Roux et al. (2011b) investigated the impact of exciting the flow at different harmonics of the

natural frequency of the steady jet. The only difference in the setup is that the nozzle exit is surrounded by a confining plate. Three excitation frequencies, corresponding to the first ($\mathsf{St} = 0.26$), second ($\mathsf{St} = 0.51$) and third harmonics ($\mathsf{St} = 0.79$) of the preferred mode of the unexcited jet, were considered along with two impact distances $H/D = 3$ and 5. A reference case $\mathsf{St} = 0$ was also studied for comparison. PIV measurements of the impinging jet were taken along with average temperature field measurements using an infrared camera. For $H/D = 3$ a prominent secondary peak can be seen in the Nusselt distribution for the $\mathsf{St} = 0$ case which is then stamped out by exciting the jet at $\mathsf{St} = 0.26$. By switching to the second harmonic ($\mathsf{St} = 0.51$), the Nusselt profile starts to resemble that of the steady case, especially near the stagnation point (for $r/D < 1$) where they nearly overlap. Further downstream, the secondary peak reappears but remains less prominent than in the steady case and closer to the stagnation point (at roughly $r/D = 1.6$). It was observed that this secondary peak in the Nusselt profile corresponded to an uptick in turbulence level. For $\mathsf{St} = 0.79$, the rate of heat transfer is more important than in the steady case for $r/D < 2$ and the secondary peak like in the previous case, stands at $r/D = 1.6$. For $H/D = 5$, the Nusselt number remains higher than in the reference case for all frequencies considered up to $r/D = 2$ where all the profiles start to converge. However, it was noted that the frequency of excitation did not have a noticeable effect on heat transfer. According to the authors, this may be due to lack of interaction between the frequency-sensitive coherent structures and the impact plate. The vortex rings are seen diverting from the jet without directly impacting the plate. [5]

Hwang et al. (2001) attempted to control the vortex pairing process by two means: secondary flow (blowing and suction) and acoustic excitation ($\mathsf{St} = 1.2$, 2.4, 3.0 and 4.0). The natural Strouhal number of the jet was identified as $\mathsf{St} \approx 1.2$ by observing the formation of vortices in the steady jet. The flow excitation was shown to suppress the vortex pairing process and reinforce the primary frequency of the flow. This dominant (vortex) frequency was affected by the flow conditions, and exhibited a stronger relation to the sub-harmonics of the excitation frequency than to the excitation frequency itself. For $\mathsf{St} = 1.2$, vortex pairing was enhanced which led to a shorter potential core and a slight improvement of stagnation Nusselt number over the steady case. For $\mathsf{St} = 2.4$ and 3.0 the pairing process was suppressed and the vortices' shape and frequency were preserved over a longer distance so that the potential core was elongated. This resulted in a noticeable improvement of stagnation Nusselt number at larger standoff distances ($H/D > 12$). Finally, for $\mathsf{St} = 4.0$, the vortex pairing process was initiated again and the jet behaved like the steady and $\mathsf{St} = 1.2$ cases.

In a follow-up study, Hwang and Cho (2003) investigated the influence of excitation frequency and level on the heat transfer performance of an impinging submerged jet of air. In the first part of the study, the excitation source was located upstream from the nozzle

[5] for more information of the causes behind the secondary peak, refer to Uddin et al. (2013)

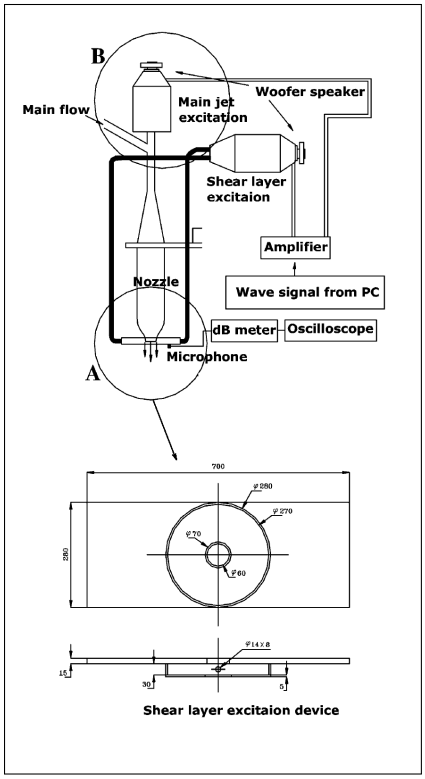

Figure 2.9: Experimental setup for shear layer excitation in Hwang and Cho (2003)

exit so as to excite the main jet. It was subsequently moved towards the nozzle exit to cause shear layer excitation (see Fig. 2.9). The frequencies applied were the same as in the previous study, namely $\mathsf{St} = 1.2,\ 2.4,\ 3.0$ and 4.0. However, this time the excitation level (sound pressure level) was set to different values ranging from 0 to 100 dB. The investigators mainly relied on mean velocity, fluctuating velocity, and the Nusselt number for evaluating and interpreting the performance of the jet under a variety of conditions. Having reached the same conclusions as before with regards to the Strouhal number, they focused on the influence of the excitation level. They found that, for both the favorable and unfavorable configurations, increasing the sound pressure level intensified the effects of excitation. For instance, as already shown, the heat transfer performance for $\mathsf{St} = 1.2$ at large gap distances is less than that for $\mathsf{St} = 0$; increasing the excitation level resulted in a further deterioration of performances. On the other hand, for $\mathsf{St} = 2.4$ and large standoff distances, performance was superior to the steady case and kept improving as the excitation level was increased.

Liu and Sullivan (1996) set out to compare the heat transfer performance of unexcited and excited jets under a variety of operating conditions. Special attention was given to the roles of organized vortices and random turbulence in the enhancement or deterioration of heat transfer between an impinging jet and a heated solid boundary. The investigators used a smoke visualizing technique in order to observe the nascent and coalescing vortices.

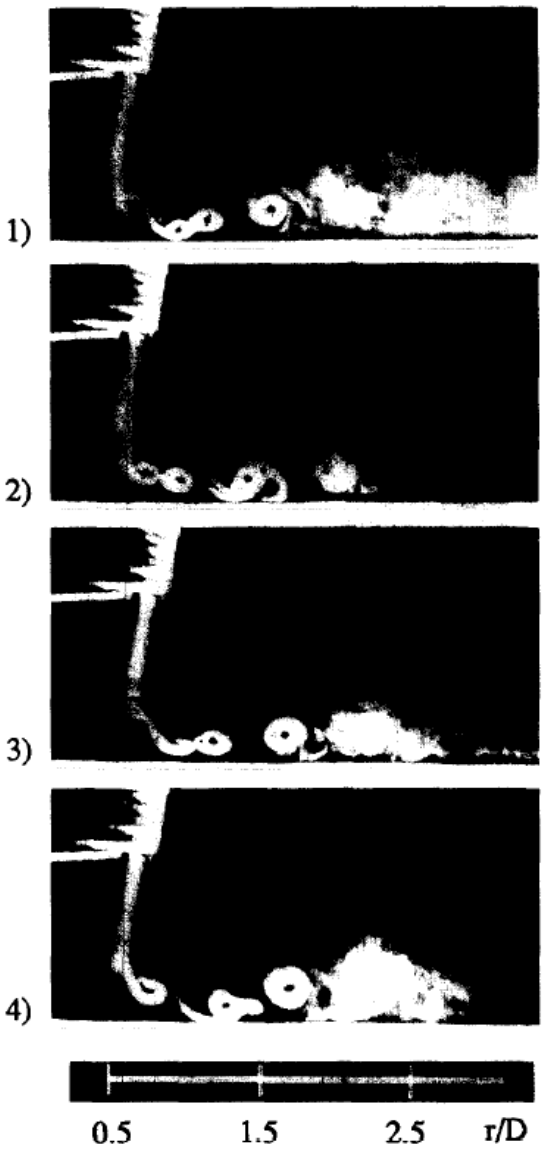

Figure 2.10: Successive photos of stable vortex pairing in excited impinging jet at $f_e = 950\,\mathrm{Hz}$ with $H/D = 1.125$ and $\mathsf{Re} = 12,300$ (Liu and Sullivan (1996)).

Flush-mount hot-film sensors were used to measure the fluctuating heat flux Q' and hot-wire probes for fluctuating velocity u'. The jet was excited by means of a loudspeaker mounted onto the settling chamber upstream from the exit nozzle. After performing some measurements on an unexcited jet and validating their findings against results from the literature, the investigators were able to deduce the natural frequencies of the free and confined jets. For a spacing of $H/D = 1.125$, the authors noted that, on one hand, the monochromatic excitation had little to no effect on the heat transfer in the stagnation region ($|r/D| < 1$), and on the other hand, that it could improve or worsen performance in the wall jet region ($1 < |r/D| < 2$) depending on the excitation frequency f_e. When f_e was close to the natural frequency f_n of the jet, the Nusselt number in the wall-jet

region was noticeably higher than in the unexcited case. The smoke visualization revealed that for this frequency, the vortex pairing process was intermittent and produced random turbulence in the flow. For f_e close to the first sub-harmonic of the natural frequency, vortex merging became more stable and induced an adverse gradient near the wall at around $r/D = 1.8$ (leading to the formation of secondary vortices, see section 2.3, and Fig. 2.10), which corresponds to a dip in the Nusselt number distribution under these conditions. The authors point out that the heat flux is made up of three components:

$$Q = -k\partial\overline{T}/\partial y + \rho c_p \overline{v_c' T' c} + \rho c_p \overline{v_{ic}' T_{ic}'} \tag{2.9}$$

Namely, and in order, the mean heat flux, the coherent part of the turbulent heat flux and the incoherent part. As already mentioned, large coherent structures draw cold fluid from the ambient to the wall while ejecting hot stagnant fluid from the boundary layer, thus improving heat transfer. However, they also decrease the mean shear rate by mixing low momentum fluid into the boundary layer. Random turbulence on the other hand increases the mean shear rate and thus can only enhance heat flux. For $f_e = f_n/2$, the coherent vortices cause the flow to separate and thus diminish heat flux in the wall jet region, whereas for $f_e = f_n$, the small scale turbulence produced by the intermittent vortices prevents the flow from separating all while augmenting the incoherent heat flux. The spectra of heat transfer fluctuation obtained from a flush mounted hot-film sensor further supported the claim that random flow structures are behind heat flux improvement.

Vejrazka et al. (2005) studied acoustically excited jets impinging on a solid plate for small standoff distances. The spectrum of the velocity signal measured for an unexcited jet showed a wide range of frequencies corresponding to the irregular vortices passing by the probe. However, two frequencies appear to dominate, $\mathsf{St} = 1$ and to a lesser extent $\mathsf{St} = 0.5$. When the flow is excited up to $\mathsf{St} = 0.3$, the spectrum remains unaffected. Above this threshold, and specifically in the range $\mathsf{St} = 0.6 - 1.1$, the flow starts behaving more regularly, as witnessed by the appearance of a sharp peak in the spectrum at the excitation frequency. Above $\mathsf{St} = 1.1$, the peak near the sub-harmonic becomes more prominent which is explained as an irregular frequency switching between f_e and $f_e/2$. In other words, irregular vortex pairing dominates the flow. This goes on until $\mathsf{St} = 1.45$ where vortex pairing becomes regular and the flow exhibits a periodic behavior at $f = f_e/2$. This periodic behavior begins to wane at $\mathsf{St} = 2.1$ until it completely disappears at around $\mathsf{St} = 3$ and a spectrum resembling that of the unexcited case manifests itself again.

The root-mean-squared velocity was then obtained from the velocity signals that were bandpass-filtered to remove all fluctuations that did not correspond to either f_e or $f_e/2$. It became apparent by plotting the RMS velocity against frequency that fluctuations in the first periodic regime (corresponding to f_e) were noticeably higher that those in the second ($f_e/2$) while they were strongly suppressed above $\mathsf{St} = 2.25$. In other words, the flow near the wall mainly consists of small-scale chaotic vortices. Through phase-averaging techniques the investigators were able to reconstruct the flow field under specific conditions in

order to obtain a clearer image of the vortex dynamics at play. One case worth mentioning in detail is when a polychromatic excitation (consisting here of two different frequencies) was applied to the jet. Vortex triplets were observed to interact and subsequently merge into larger structures. For this case, five parameters were required, the two frequencies, their respective amplitudes as well as their phase difference. In conclusion, the authors note that the influence of these different flow structures on heat and mass transfer remains unclear.

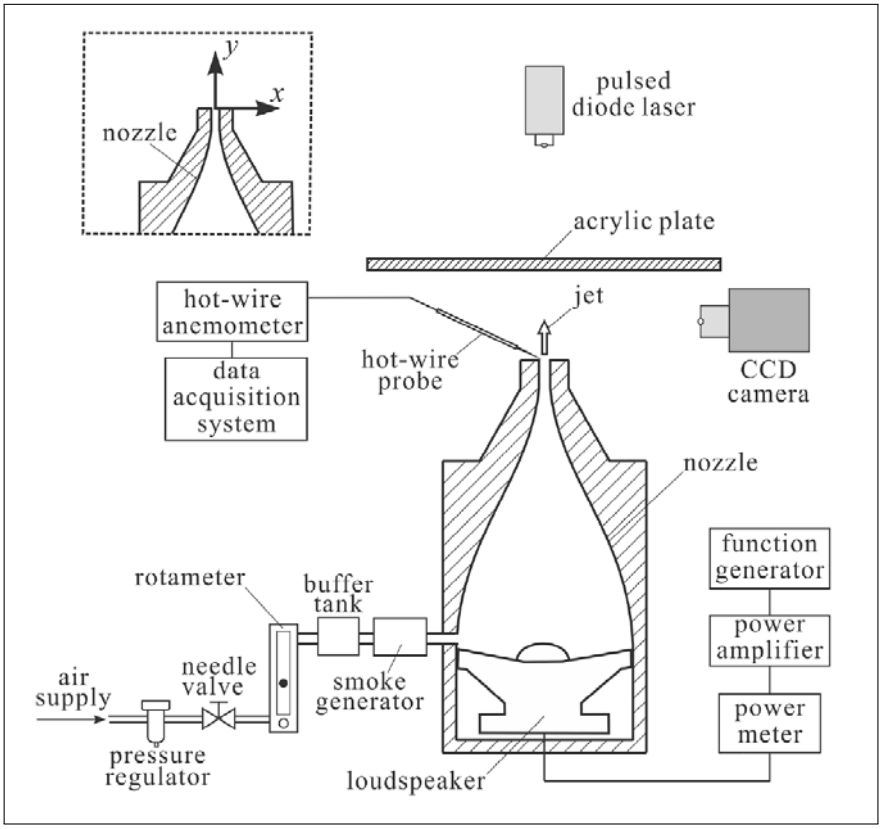

Figure 2.11: Typical rig for an acoustically excited impinging jet (Hsu et al. (2019)).

Hsu et al. (2019) sought to reveal the flow structures of pulsed impinging jets and how they could affect heat transfer. The jet was excited by means of a loudspeaker (Fig. 2.11) which allowed the investigators to modulate the frequency as well as the pulsation amplitude of the exit velocity. The flow visualization was achieved with a PIV setup while the heat transfer at the heated plate was measured on the wall using an infrared camera. Two different modes prevailed depending on pulsation amplitude (or intensity I_p defined as the ratio of fluctuating to mean velocity): a coherent vortex mode and a vortex break-up mode, the first being achieved at low $I_p = 0.5, 1.2$ and the second at relatively high $I_p = 2.0, 5.0$. Contrary to much of the results mentioned thus far, the investigators did not observe a clear correlation between the Strouhal number and the Nusselt number averaged over the plate (for a given I_p). They however noted a strong influence of the pulsation

intensity on heat transfer. Indeed, the occurrence of vortex break-up at large pulsation amplitudes led to a greater boost in performance compared to when coherent structures dominated the flow. In this regard, the authors put forth evidence that coherent structures behave in a laminar fashion after impingement whereas, predictably, incoherent structures exhibit greater velocity fluctuations in the impingement region as well as downstream in the wall jet region. The following correlation was found:

$$\frac{\mathsf{Nu}}{\mathsf{Pr}\cdot\mathsf{Re}_j} = 0.125 I_p^{0.209}\mathsf{St}_{\text{exc}}^{0.0196} \tag{2.10}$$

for $\mathsf{Re}_j = 325$, $H/D = 10$, $\mathsf{St}_{\text{exc}} = 0.2 - 1$, and $I_p = 0.5 - 9$.

2.5 Two or More Impinging Jets

Rizk and Menon (1988) performed large-eddy simulations (LES) of a pair of steady and periodically forced jets (supposed to represent an infinite row of jets). This configuration is supposed to represent the flow field of vertical take-off and landing (VTOL) aircraft hovering near the ground. More specifically, the goal of this study was to understand the effect of external excitation on an array of impinging jets. Two main cases were considered, one where the two simulated jets are in-phase and another where they are not. For each case, two regions are described in detailed: the outflow (where the wall jet is expelled laterally) and the fountain region (where two wall jets collide, see Fig. 2.12). By inspecting the former, the investigators reached similar conclusions to Didden and Ho (1985) with regards to the impingement of the primary vortex, the formation of a secondary vortex to adverse pressure gradients and the convection of both downstream towards the outlet. The authors note however that the convection velocity of these vortices is smaller than for a single jet (about $0.3U$ versus $0.65U$, where U is the initial velocity of the jet). This is attributed to the lifting and subsequent deformation of the primary vortex ring by the fountain flow which holds back the train of convected vortices.

The second region – the fountain flow – behaves differently depending on the setup. If both forced jets are in-phase, the two wall jets collide and are lifted up until they reach the upper wall. Two secondary counter-rotating vortices appear at the base of the fountain but are not convected upwards. The flow structures in this area remain relatively simple.

When the two jets are out of phase (with the phase difference $\phi = \pi$ for instance) the spatial symmetry between the colliding wall jets is broken and the cores of the lifted vortices on either side are offset by a half-wavelength. As the left vortex is being lifted, the secondary vortex at the heel of the fountain vanishes. The right vortex then approaches and part of the associated secondary flow is entrained by the left vortex. The reverse then occurs as the right vortex is lifted.

One last situation is considered where one jet is steady and the other is forced. The fountain flow is no longer smoothly ascending towards the upper wall and a prominent flap-

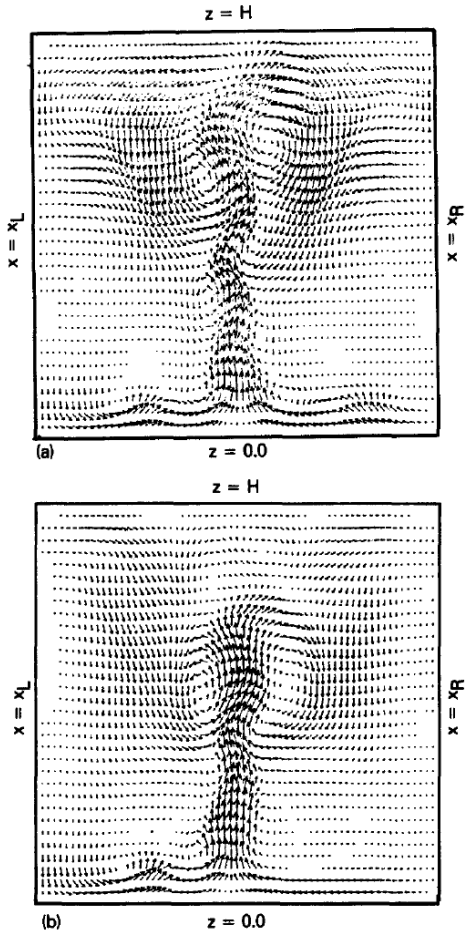

Figure 2.12: Velocity vector diagram showing the fountain region where wall jets collide for (a) a phase difference of $\pi/2$ and (b) a single forced jet. Rizk and Menon (1988).

ping motion can be seen. Although the heat transfer was not evaluated in this study, the knowledge gained from this simulation about the interactions between different parts of the flow allows us to better understand how they can affect heat transfer with a solid boundary.

In spite of the possible interaction between their effluents, the convective heat distributions resulting from a jet array is nonuniform and thus prone to the formation of hot/cold spots. Motivated by previous work that showed that pulsating jets produce relatively even distributions of heat, Sheriff and Zumbrunnen (1999) conducted an experimental study on a 3-by-3 array of pulsating jets. Velocity measurements obtained from a hot-film revealed an increase in turbulence intensity due to the pulsations. Moreover, the amplification and subsequent attenuation of the pulsation amplitude along the jet centerline signaled the formation and dissociation (respectively) of coherent vortex structures in the flow. Temperature and heat flux measurements on the heated surface revealed a slightly more uniform distribution for pulsating jets than for the steady jets. This is linked to a noticeable reduction in performance at the stagnation point. Further reduction was observed as

the pulsation amplitude was increased to 60%. These results are in agreement with the findings of Mladin and Zumbrunnen (1994). The authors conclude that the nonlinear behavior of the boundary layer in response to pulsation can offset any possible improvement brought about by coherent structures and/or increased turbulence.

Chaniotis et al. (2003) performed a numerical study of single and double slot jets of air using the so-called *Smooth Particle Hydrodynamics* SPH approach in order to gauge the effects of frequency, pulsation amplitude and phase difference between two jets on the temperature distribution on a constant heat flux plate. For both cases (single and double jets), a parabolic inlet velocity profile was used that varied sinusoidally in time. The Reynolds number was defined as:

$$\mathsf{Re} = \frac{\overline{V} D_h}{\nu} \tag{2.11}$$

where the hydraulic diameter D_h is twice the jet width. The width of the single jet was chosen to be $w = 2D$, twice that of each jet in the other case $w = D$. Most of the simulations had the following geometrical configuration: standoff distance $H = 5D$, the distance between the two jets $L_T = 5D$ and flat plate length $L = 20D$. The authors chose the maximum plate temperature T_{max} as the performance gauge of the system (the lower, the better).

They started by simulating steady single and double jet impingement. The maximum temperature was higher in the latter case because convection is very weak in the region between the two stagnation points. By increasing the Reynolds number, they also found that the relative efficiency of the double jet tends to decrease. Moving on to a pulsating pair of jets, the investigators ran simulations for difference phase angles φ. For $\varphi = 0$, they found no significant difference with the steady case. As φ was increased, the maximum temperature started to diminish until, at $\varphi = 2$, it became comparable to that associated with the steady single jet. At maximum phase angle $\varphi = \pi$, the double pulsating jets were observed to outperform the single steady jet. Maximum temperature was found to have a non-monotonic relation to frequency [6]. With regards to amplitude of pulsation, increasing it to 100% entailed a reduction in maximum temperature by 11% compared to the steady pair-jet and 6% compared to the steady jet. This remains true for increasing value of the Reynolds number.

In order to gain insight into the dynamic behavior of the flow in response to the different configurations, the researchers measured the velocity signal at an arbitrary point in the vicinity of the stagnation point, just over the plate, for different values of the Reynolds number. Based on these data, the power spectrum, time-delay [7] reconstruction of the phase space and Lyapunov exponents [8] were computed. For low values of the Reynolds number

[6] The graphs showing maximum temperature for different phase angles and different frequencies are the same, probably due to an error in editing, so cannot provide further comment on the results. The authors however do not mention any critical frequency like many of the studies previously cited.

[7] Taken to be one-tenth of the forcing period.

[8] In fluid mechanics, the Lyapunov exponent λ_2 is used as a Lagrangian method of vortex identification. In short, the value of λ_2 at a given point represents the rate of separation between two infinitesi-

($\mathsf{Re} = 133$), the phase portrait shows a limit cycle behavior and a dominant frequency f_0, equal to the forcing frequency, was observed in the power spectrum. As the Reynolds number is increased, sub-harmonics, that do not follow the frequency-halving bifurcation scheme, start to appear one after the other, while the phase portrait exhibits multiple corresponding limit cycles. At the largest Reynolds number considered $\mathsf{Re} = 533.3$ the system is deemed fully chaotic owing to its relatively large Lyapunov exponent $\lambda_2 = 0.37 \pm 0.01$ bits per orbit. As predicted by bifurcation theory, a chaotic system can exhibit discontinuous behavior. In this case, it means that brief windows of periodic behavior can arise within the chaos. This was observed for values of Re ranging between 280 and 333.3 and resulted in lesser mean and maximum value of T_{max}.

Mohammadpour et al. (2014b) used the RNG-$k - \varepsilon$ turbulence model to simulate the two-dimensional fluid flow and heat transfer resulting from an array of four slot jets of width w and separation S between successive jets, impinging on an isothermal surface at a distance H. Each configuration was a different combination of steady, intermittent and sinusoidal jets. This allowed the investigators to control the flow patterns arising in the development region and thus enhance the uniformity of the Nusselt number distribution and the overall heat transfer rates. The combination of intermittent and steady jets surpassed the rest in those regards. The frequency of pulsation, for cases involving intermittent and sinusoidal pulses, played a crucial role in determining the morphology of the Nusselt distribution. Lower frequencies resulted in more uniform distributions, especially in-between stagnation points, whose heat transfer rates plummet significantly when frequency is increased. Increasing the amplitude of pulsation, as has been noted for other works already discussed, lead to better overall performance as well.

Janetzke et al. (2008) conducted tests on an array of three identical jets pulsating at the same frequency with no phase difference. The actuator used to achieve this configuration is comprised of two parts: a chamber with three orifices and a set of vertical bars mounted on a disc. A DC-motor rotates the disc so that the orifices are successively open and shut thus producing a pulsating discharge of air. A stainless steel plate, covered in Type K thermocouples, acts as the target surface and is heated by a steam heater. The input parameters of interest here are the frequency and amplitude of pulsation whereas performance is evaluated by the cooling effectiveness ϵ defined as:

$$\epsilon = \frac{T_{hot} - T_{wall}}{T_{hot} - T_{cool}} \tag{2.12}$$

where T_{hot} is the temperature inside of the steam heater, T_{cold} is the temperature of air in the settling chamber and T_{wall} is the wall temperature. A reference case at $f = 0\,\mathrm{Hz}$ was conducted. For the pulsating jets, the Reynolds number and standoff distance were kept constant at $\mathsf{Re} = 7280$ and $y/d = 2$, respectively. In a nutshell, the results showed

mally close particles initialized in the neighborhood of that point.

that high frequencies coupled with high amplitudes resulted in the best enhancement ratio compared to the steady case. On the other hand, at low frequencies and high amplitudes a deterioration of performance is observed. For large pulsation amplitudes, the threshold for performance enhancement lies at around $\mathsf{St} = 0.28$ (which is close to the thresholds $\mathsf{St} = 0.2$ and $\mathsf{St} = 0.26$ found by Hofmann et al. (2007a) and Zumbrunnen and Aziz (1993), respectively). Furthermore, if amplitude is reduced, this threshold is pushed higher until it reaches $\mathsf{St} = 0.6$ for the lowest amplitude considered. This situation is reminiscent of Mladin and Zumbrunnen (2000) whose results made clear the importance of increasing the product $\mathsf{St} \times A_N$. This observation seems to have theoretical underpinnings in the work of Reynolds and Hussain (1972). In order to gain deeper insight regarding the fluid structures, Particle Image Velocimetry (PIV) was used to extract the velocity and vorticity fields. Three values of Strouhal number were chosen $\mathsf{Sr} = 0.136, 0.42$ and 0.82, based on the heat transfer results that showed a decrease in performance in the first case, and enhancement peaks in the remaining two. For $\mathsf{Sr} = 0.136$, the main features of the jet could still be observed, and puffs of high velocity fluid – so-called, "velocity packets" (v) – were periodically produced and seen traveling along the jet axis until they hit the target surface. These velocity packets result in toroidal vortices in the shear layer region. Increasing the Strouhal number to $\mathsf{Sr} = 0.41$ caused an increasing in the velocity of the velocity packets and intensified the vorticity in the shear layer. Pairs of successive vortices that appear around the jet began to rotate around one another and reach the target plate without fulling merging. And finally, at $\mathsf{Sr} = 0.82$, the structure of the jet was completely altered, whereby its familiar shape, consisting of a potential core surrounded by a shear layer, was replaced by the velocity packets. The vorticity is intensified as well, resulting in more prominent coherent structures that impinge on the target plate.

Turbine blades require enhanced cooling systems in order to withstand the high inlet temperatures required for peak efficiency. Arrays of steady impinging jets are usually used to cool the blades from the inside. Berthold and Haucke (2020) attempted to improve this configuration by pulsating the inlet mass flow rate of the jets, effectively creating square-wave velocity signals. A 7×7 array of jets was placed in a cross flow in order to imitate the flow coming from other jets further upstream in an actual cooling system. The effects of pulsation frequency $f = 0 - 1000\,\mathrm{Hz}$, Reynolds number $\mathsf{Re}_D = 3200, 5200, 7200$, impingement distance $H/D = 2, 3, 5$, phase shift $\Phi = 0 - 90°$ and duty cycle $DC = 35 - 65\%$ were explored. It is worth noting from the start that the pulsed cases outperformed the steady reference cases regardless of configuration. In response to a change in frequency, the ratio of the time/space-averaged Nusselt number for the pulsating case and the spatially-averaged Nusselt number of the equivalent steady case $\overline{\mathsf{Nu}}/\overline{\mathsf{Nu}_0}$ (improvement ratio) exhibited a complex behavior; depending on standoff distance and Reynolds number, two or three peaks in enhancement were observed. The most prominent peak occurred when $f = 700\,\mathrm{Hz}$ for all value of H/D and Re_D considered. The maximum improvement was obtained for $H/D = 5$ and $\mathsf{Re}_D = 5200$. Next, the velocity signal of each row of jets was shifted by Φ with respect to the previous, adjacent row. This resulted in higher improvement ratios, regardless of

the value of Φ for $f = 300$ and 500 Hz and lower improvement ratios for $f = 700$ Hz except for $\mathsf{Re}_D = 7200$ and standoff distances $H/D = 2$ ($\Phi < 75\%$) and $H/D = 3$ ($\Phi < 70\%$). To conclude, the duty cycles over 50% were shown to reduce the efficiency of pulsed jets for large Reynolds number ($\mathsf{Re}_D = 7200$), $f = 700$ Hz and $H/D = 2, 3, 5$. For the remaining Re_D, peak performance is reached at $DC = 50\%$ and plummets below the steady case for smaller and larger values of DC.

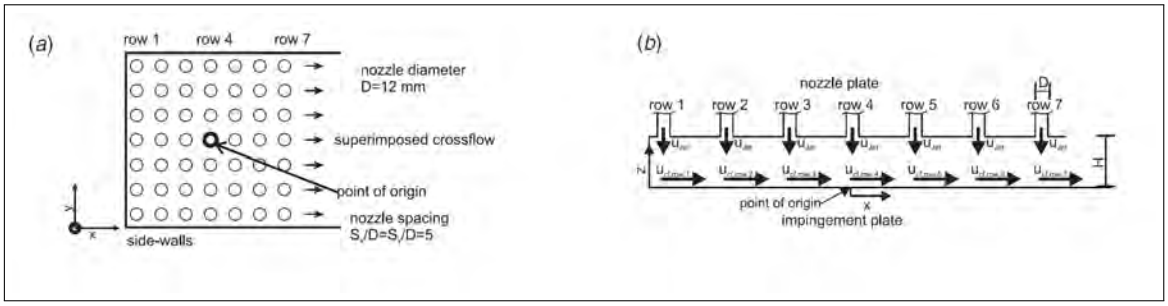

Figure 2.13: Experimental setup used in Berthold and Haucke (2020) showing (a) the array of jets and (b) the cross flow.

Berthold et al. (2020) then performed PIV measurements to understand the phenomena underlying the complex behavior described above. Contours of mean velocity $|U|$ showed that the pulsed jets were less sensitive to the cross flow than the steady jets. The pulsations significantly reduced the deviation angle of the downstream jet so that the impact of the jet on the plate was not as subdued as in the steady case. Furthermore, for the same jet Reynolds number, increasing the frequency of pulsation from $f = 0$ to 500 then to 700 Hz resulted in higher vorticity levels (and thus more stable vortex rings) especially for the downstream jets that are the most affected by the cross flow. The investigators invoked the Reynolds analogy in order to predict heat transfer performance from shear stress values near the impact wall. They found that the increased jet velocity and the stronger vorticity lead to greater shear stress and hence more efficient heat transfer for the same mass flow rate. Finally, the pulsations were shifted by $\Phi = 20\%$ for each successive jet. For $\mathsf{Re}_D = 7200$ and $f = 500$ Hz, a so-called "wave-packet" was seen to travel along the flow in the cross flow direction. Without phase-shifting the fluid is discharged at the same time from all the nozzles and the vortices move at the same axial position from the nozzle lip to the impact plate where they are swept away by the ever-increasing cross-flow. In other words, "In-phase actuation generates velocity distributions with a uniform vortex propagation". On the other hand, when the pulsations are shifted with respect to another, the spatial distribution of cross flow velocity is altered and a downstream-traveling wave is induced. The minimum local cross flow velocity reaches $0\,\mathrm{m\,s^{-1}}$ and allows for stronger vortices to interact with the surface.

2.6 Effect of standoff distance

The width of the space that separates the jet orifice and the target plate has an important impact on both flow structures and heat transfer. For instance, Varieras et al. (2007) studied the stability of an impinging jet with steady inlet condition in response to changing gap width and found that beyond certain thresholds the jet starts oscillating.

Alimohammadi et al. (2014) investigated experimentally and numerically, among other factors, the effect of standoff distance on heat transfer from an *unconfined* intermittent jet, where the term unconfined refers to the absence of a confining wall around the nozzle, facing the plate. The performance of each configuration is measured by the enhancement factor, defined as follows:

$$\delta\overline{\mathsf{Nu}} = \left(\frac{\overline{\mathsf{Nu}_{\mathsf{pulsed}}}}{\overline{\mathsf{Nu}_{\mathsf{steady}}}} - 1 \right) \times 100 \tag{2.13}$$

Experimentally, for H/D ranging from 1 to 6, $\delta\overline{\mathsf{Nu}}$ was mostly negative except for the highest frequency considered $f = 65\,\mathrm{Hz}$ for which $\delta\overline{\mathsf{Nu}} > 0$ for $\mathsf{Re} = 1300$ over the entire range of standoff distances (reaching a maximum at $H/D = 2$ of 30% enhancement), and only positive for $H/D = 2, 3$ and 5 for $\mathsf{Re} = 2800$ but with significantly smaller peaks (the highest (15%) being at $H/D = 2$).

Numerically, at $H/D = 1$, $\mathsf{Re} = 6000$, $\delta\overline{\mathsf{Nu}}$ was seen to increase monotonically with frequency from about 10 to 18% while for a larger impact distance $H/D = 6$, the increase was more significant, going from about 58 to 63%.

On the other hand, Esmailpour et al. (2015) studied a similar configuration, with the only difference being the presence of a confining wall and a sinusoidal forcing function, and ended up with contrasting results. For $\mathsf{Re} = 5500$ (nearly the same value mentioned above) and $H/D = 6$ the steady jet consistently outperformed the pulsed jets. Only at $f = 100\,\mathrm{Hz}$ did the researchers observe an enhancement, and even then it was a measly 2%. However, for $H/D = 1$, enhancement was observed for all but three combinations of frequency and amplitude, and reached up to 30%.

Marcum et al. (2015) investigated a similar range of Reynolds numbers $\mathsf{Re} = 866 - 3776$ and standoff distances $H/D = 0.5 - 6$ as Alimohammadi et al. (2014) but with lower frequencies $f = 5 - 10\,\mathrm{Hz}$. Prior to thermal measurements on the impingement plate, the free jet was characterized using a hot wire anemometer. An estimated power spectral density (PSD) was computed for each case at different axial and lateral positions in the jet. They found that the highest PSD peak occurs at $x/D = 3$ (axial distance) $f = 5\,\mathrm{Hz}$ so they assumed that heat transfer enhancement should be obtained under these conditions. Thermal measurements proved otherwise since optimal enhancement occurred at $H/D = 6$ and $f = 10\,\mathrm{Hz}$. The authors note that further investigations are needed to pinpoint the standoff distance between $H/D = 3$ and 6 that will result in optimal heat transfer and flow characteristics.

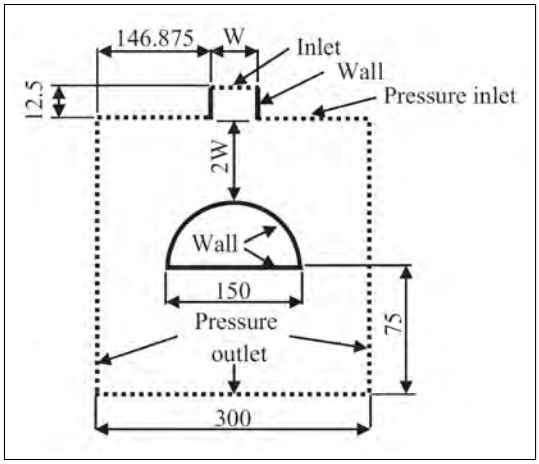

Figure 2.14: Problem configuration and boundary conditions in Kharoua et al. (2017)

In an attempt to scale the enhancement factor for a pulsed axisymmetric jet, Persoons et al. (2013) proposed two modified Strouhal numbers, one of which depends on the standoff H/D and is defined as $\mathsf{Sr} \times (H/D) = fH/U_m$ while the other $\mathsf{SrRe}^{0.5}$ does not. These modified Strouhal numbers were able to collapse the stagnation point and area-averaged enhancement factors, respectively (the power laws obtained using these two dimensionless groups collapsed the entire investigated range with a coefficient of determination $R^2 = 0.8$). Furthermore, it was found that the stagnation point enhancement factor increases with the first modified Strouhal number $\mathsf{Sr} \times (H/D)$ in the stagnation region. In other words, large standoff distances coupled with high pulsation frequencies induced significant enhancement in heat transfer compared to an equivalent steady jet. However, the overall heat transfer enhancement did not depend on the standoff distance for the configuration considered.

2.7 Characteristics of the target surface

2.7.1 Curved Surfaces

Kharoua et al. (2017) conducted a LES study of a heated pulsating jet that impinges on a convex surface and focused on the vortex structures generated in the flow. They showed that the interaction between a single vortex and the solid boundary does not entirely capture the dynamics of the flow and that other phenomena such as vortex merging and dipolar ejection must be considered.

Rajabi Zargarabadi et al. (2018), in an effort to study the cooling of the leading edge of a turbine blade, simulated a jet impinging on a concave surface. This surface is split into two parts having different relative curvatures D/B (here B is the width of the jet nozzle, see Fig. 2.15). Both steady and pulsating jets were considered. A sinusoidally pulsating velocity was imposed at the inlet having the same average velocity as the steady jet. By comparing the steady and periodic jets' thermal performance in a number of configura-

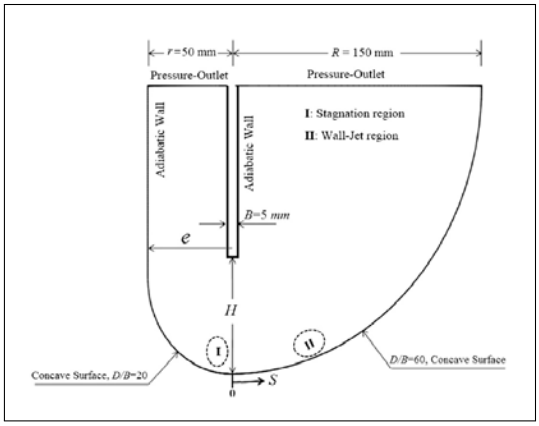

Figure 2.15: Computional domain and boundary conditions in Rajabi Zargarabadi et al. (2018).

tions, it was consistently noted that the latter under-performed in the stagnation region while enhancing heat transfer in the wall jet region. Increasing the frequency from 40 to 160 Hz resulted in an overall increase in Nusselt number, albeit remaining below the steady level in the stagnation region. On the other hand, increasing the amplitude of pulsation from $A = 0.4$ to 1 again improved the wall jet performance while further deteriorating it near the impact point. Overall improvement was also observed when the standoff distance was decreased from $H/B = 8$ to $H/B = 2$ (where H is the distance between the nozzle orifice and the impact surface). Regarding the shape of the target surface, the side with lower relative curvature ($D/B = 20$) performed better than the other side ($D/B = 60$) regardless of the configuration. Furthermore, moving the jet position towards the higher curvature side resulted in an enhancement in average Nusselt number compared to a reference pulsating case where $A = 0.4$, $f = 40$ Hz and $H/B = 4$.

2.7.2 Obstacles and Surface Roughness

For steady impinging jets, it has been found that increasing surface roughness tends to enhance heat transfer performance. The roughness elements can protrude into and hence disturb the thermal boundary layer, improving heat transfer for single (Sharif and Ramirez (2013)) and dual (Xu et al. (2016)) steady jets. The effects of roughness or the presence of an obstacle on the wall on unsteady impinging jets, was, however, rarely been explored.

Rakhsha et al. (2020) studied, both numerically and experimentally, the effects of flow pulsation on a "pinned" surface, in light of previous studies that have only dealt with steady jets. In the experimental part, a metal disk rotates above the orifice of a steady jet. The disk is perforated in a such a way that it blocks and releases the air flow twice in a cycle and for an equal amount of time. This results in an approximately square-wave velocity profile which is replicated in the numerical simulations. Three versions of the $k - \varepsilon$ turbulence model (Standard, Realizable and RNG) as well as the $k - \omega$-SST model

were tested and compared to experimental data. The $k-\varepsilon$ RNG model resulted in good agreement with experiments in both the steady and pulsed ($f = 100\,\text{Hz}$) cases. A combination of low impact distance, large Reynolds number and large pulsation frequency led to optimal performance when compared to the steady case. Numerically, the average Nusselt number remained higher for the pulsating case than the steady case within the ranges $f = 50-100\,\text{Hz}$, $\mathsf{Re} = 7000-15000$ and $H/D = 2-5$. And finally, the presence of pins on the target plate were shown to lower the surface minimum temperature by as much 20 K when compared to the steady, smooth surface case. This is attributed to increased turbulence in the vicinity of the pin and modification of the velocity profile in the wall jet region.

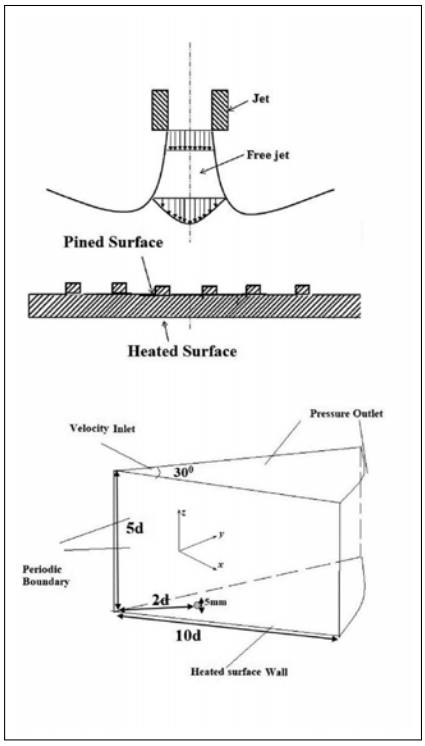

Figure 2.16: Geometry and computational domain used in Rakhsha et al. (2020)

It is a tacit assumption of most studies on pulsed impinging jets that the impact surface is smooth and that the same conclusions thus obtained are applicable to rough surfaces. Zhou et al. (2009) attempted to test this assumption by placing a ring (of variable height h, see Fig. 2.17) around the impact point of a circular jet (diameter $D = 15\,\text{mm}$). Both sinusoidal and rectangular velocity profiles were used with frequencies ranging from 1.25 to 40 Hz. For relatively small values of h ($= 1-2\,\text{mm}$), the Nusselt number distribution was nearly identical to the smooth surface case. For $h = 3\,\text{mm}$ the Nusselt number distribution was drastically altered since the obstacle deflected the flow from the wall, reducing heat transfer performance. In light of this, the investigators consider the first set of cases as representing local roughness while the $h = 3\,\text{mm}$ case as an outright change in geometry. The $h = 2\,\text{mm}$ ring was then used to explore the effect of frequency on heat transfer. A

clear reduction in performance with respect to the smooth case, and even, in certain situation to the steady case was observed. The presence of the ring caused the unsteady jet to under-perform regardless of frequency and radial position.

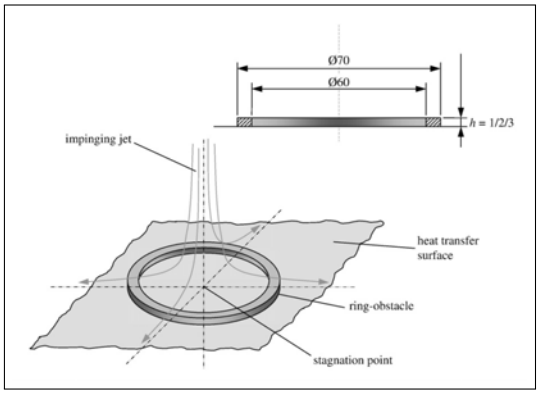

Figure 2.17: Ring-obstacle used in Zhou et al. (2019) in order to emulate either a large obstacle or surface roughness.

Heat sinks play a central role in electronics cooling, so it is of practical interest to optimize their heat transfer rates, using pulsating jets. For this reason, Sanyal et al. (2009) performed a numerical study of steady and pulsating jets that impinge on a pin-fin heat sink where they consider the effects of pulsation frequency, duty cycle, fin height, standoff distance and, of course, Reynolds number. The first part of the study only deals with laminar jets. For these cases, the base-area heat transfer coefficient is at its peak for the lowest frequency considered $f = 50\,\text{Hz}$. Beyond this frequency and up to $f = 200\,\text{Hz}$, the heat transfer coefficient exhibits a complex behavior, either increasing or decreasing, but remaining below the value at $f = 50\,\text{Hz}$. As for the duty cycle, the authors noted that the heat transfer coefficient reaches its peak for duty cycles of 35% and 25% for the unfinned and finned laminar flow cases, respectively. It is worthwhile noting that previous studies (mentioned in Section 2.4) had shown that the optimal duty cycle is 50% and that it is the main factor influencing the performance of turbulent jets. Finally, when the authors considered turbulent flows at larger Reynolds number, the enhancement in heat transfer was marginal. To conclude, pulsed laminar jets might have a greater potential for improvement than turbulent ones since it was found that pulsating the flow increases performance by up to 35% compared to the finned steady case, and by 200% compared to the unfinned steady case. This is an indication that the use of pulsating microjet arrays (see Section 2.10.2) can lead to substantial heat transfer improvement.

2.7.3 Reciprocating target surface

Most experiments and simulations in the literature operate using a basic set of elements: a jet of fluid issues from a nozzle (circular or rectangular), impinges on a heated plate (flat, curved, dimpled or finned) and is either confined or not by a wall that surrounds its

base. Nevertheless, some works considered variations, such as reciprocating confinement walls (Chang et al. (2000)), a stagnation region that is actuated against the jet (Klein and Hetsroni (2012)) or even changing the geometry of the setup upstream of the jet nozzle (Roux et al. (2011a) and Tang et al. (2019)). These additions, both passive and active, modify the behavior of the flow and can result in an enhancement of heat transfer or a change in heat transfer distribution across the heated surface.

Klein and Hetsroni (2012) studied steady microjets (220 µm wide) that impinge on a slab that can slide forward and backward along the jet axis. Although this method of actuating the flow is different from what was presented so far, it can lead to the same phenomena, namely the perturbation of the hydrodynamic and thermal boundary layers and the production of vortex structures between the confining walls and the part of the impact surface that surrounds the slab and does not move. The periodic movement of the slab has frequencies of up to 400 Hz. In addition to frequency and Reynolds number, the authors also investigated the effects of actuation height, i.e., the maximum distance crossed by the slab. They found that increasing these three parameters leads to an enhancement in heat transfer. A maximum enhancement ratio of 34% was attained for a Reynolds number of 1260, an actuation height equal to 75% of the standoff distance, and a Strouhal number of 0.032. They attributed the improvement to three factors: the disruption of thermal boundary layer, the improved mixing between the boundary layer and the bulk fluid and the vortices that are convected along the surface.

On the other hand, in the experimental setup of Chang et al. (2000), the air jet impinges the inside of a reciprocating enclosure. Their study was performed in the context of cooling pistons in a marine propulsive diesel engine. Thermocouples were mounted onto the rib-roughened target surface inside the enclosure in order to find the Nusselt number distribution. First, nonreciprocating tests were conducted as a reference to which the reciprocating results were then compared. Compared to a smooth target surface, the authors found that the addition of ribs reduces heat transfer near the stagnation region while enhancing it further downstream. This effect can be observed for small impact distances, e.g., $H/D = 4$ and is due to the formation of high pressure regions in the space between successive ribs surrounding the stagnation point. The flow does not penetrate into these regions and so the heat transfer is reduced. Further downstream, the flow becomes turbulent and the presence of the ribs enhances the formation of vortical structures that in turn promote heat transfer. In the reciprocating case, the enclosure was actuated using a crankshaft mechanism. The Nusselt number distribution was then evaluated for different pulsation numbers, defined as $\mathsf{Pu} = \omega r / W_m$ (where ω is the angular velocity of the crank, r its radius, and W_m the mean through-flow velocity). The authors found that the heat transfer rates deteriorated by 80% for small pulsation numbers of around $\mathsf{Pu} = 0.00365$ while a remarkable improvement of 240% was attained for the largest pulsation number considered $\mathsf{Pu} = 0.014$.

2.7.4 Transmission chamber/nozzle shape

Unlike the two previous studies in which an active actuation method was used to enhance heat transfer,Tang et al. (2019) adopted a passive strategy that consisted in adding a transmission chamber ahead of the jet exit. They performed experimental and numerical tests on a confined impinging jet configuration for different frequencies, standoff distances and Reynolds numbers. Transmission chambers of different sizes and aspect ratios were studied in order to determine the optimal configuration. In the experimental part, a mass flow control device produced the pulsating jets and a thin stainless steel sheet placed on infrared-transparent glass constituted the heated plate. The surface temperature was monitored using an infrared camera on the obverse of the plate (so that the foil, on which the jet impinges, is seen through the glass). The investigators were able to show both the numerically and experimentally that the presence of a transmission chamber resulted in an enhancement of Nusselt number. The radially averaged Nusselt number (around the stagnation region $x/d < 2$) was between 8 and 16% higher than the reference case (without transmission chamber). The cause of this enhancement is attributed to the vena contracta phenomenon which manifests itself in the presence of a transmission chamber. More precisely, this phenomenon produces an increase in local velocity, leading to a more forceful impact of the jet on the plate. With regards to the other flow parameters, performance was observed to increase with increasing frequency (in the limited range considered here $f = 20 - 40\,\text{Hz}$, and to plummet for larger standoff distances ($H/d = 2 - 10$, $f = 10\,\text{Hz}$) with either $H/d = 2$ or $H/d = 4$ taking the lead, depending on the dimensions of the transmission chamber.

However, a crucial piece of information is missing in Tang et al. (2019): the initial mean velocity profile of the jet. Roux et al. (2011a) also compared two jet nozzle configurations: a plenum followed by a contraction with an area ratio of 10.8, and a plenum with a long tube. The axisymmetric jet issuing from the contraction has a flat initial profile while the long tube allows the flow to develop and to produce a laminar parabolic profile with a clear peak at its center. Thermal measurements showed that the long tube configuration offered better results since the maximum impact velocity of the jet is significantly higher than for the contraction nozzle.

2.8 Simulating pulsed impinging jets

RANS

A number of studies that have used RANS methods for simulating pulsed impinging jets were already cited earlier. In this section, we only focus on a single study that used several RANS models to simulate the same pulsating flow. Hofmann et al. (2007a), using the commercial CFD software FLUENT 6.0, first simulated a steady axisymmetric impinging jet with different turbulence models including on one hand the standard $k-\varepsilon$ model and its variants (and the Low-Reynolds option) and on the other hand the standard $k-\omega$ model and the SST-$k-\omega$ model coupled with the Transitional Flow option. Two Reynolds numbers

34,000 and 124,000 and two normalized distances $H/D = 2.5$ and 10 were considered. The Nusselt number profile along with the radial velocity profile were extracted and compared to experimental work done by the same authors. The investigators found that the $k-\omega$ models outperformed the rest in terms of accuracy. Interestingly, the SST $k-\omega$ model was the sole model able to predict the secondary peaks in Nusselt number associated with close impingement. In light of this, the $k-\omega$ models were chosen for simulating the pulsed impinging jets. Two cases were considered, one at large standoff distance using the standard $k-\omega$ model and the other at small standoff distance with the SST $k-\omega$ model, both having the Transitional Flow option activated. For the former configuration, a drop of 30% of heat transfer rates was found and is consistent with the cited experimental work. However, the characteristics of the jet differed. For instance, the simulation was found to overestimate the width of the jet. When the standoff distance was set to $H/D = 2.5$, the investigators noticed stability problems, since the simulation predicted unreasonably high values of the Nusselt number. For instance, at $f = 40\,\text{Hz}$, the distribution of heat transfer nearly coincides with that of the steady case. However, by lowering the frequency to 10 Hz, the peak of the Nusselt number profile was slightly more than double its steady state value.

As a side note, Viskanta (1993) had already noted the inadequacy of high Reynolds number $k-\varepsilon$ models at predicting the enhancement of heat transfer at small standoff distances for steady jets.

Large Eddy Simulation (LES)

Olsson and Fuchs (1998) studied the sensitivity of mean and turbulence quantities to different sub-grid scale models in a perturbed impinging circular jet. The forcing signal has a Strouhal number and amplitude equal to 0.28 and 0.028, respectively. This forcing frequency roughly corresponds to the average "puff" formation frequency found experimentally by Crow and Champagne (1971). Four cases were considered:

- Case I: reference case, no subgrid scale (SGS) model, fine grid (128^3)
- Case II: no SGS-model, coarse grid (96^3)
- Case III: dynamic Smagorinsky model, coarse grid (96^3)
- Case IV: stress-similarity model (Liu et al. (1994)), coarse grid (96^3)

Since applying SGS-models means that non-local energy transfer is neglected, the choice of model, or lack thereof, should not have a *significant* effect on the mean field value; indeed, the mean velocity profiles for cases II through IV correlate well with the reference case. The turbulence intensity profiles, however, were visibly different, although the maximum difference did not exceed 10% for any of the cases. On one hand, cases III and IV correlate better than case II with the reference case and on the other hand, the similarity-stress model (case IV) correlates better than case III. The gain in accuracy comes at an increase in computational cost (100% for case III and 50% for case IV).

By simulating a forced plane impinging jet with a span-wise disturbance, Xu et al. (2013) attempted to elucidate the formation mechanisms of secondary flow instabilities

that stem from the main Kelvin-Helmholtz instability (which manifests itself as a pair of counter-rotating span-wise rollers). The frequency of the primary instability, the *spanwise rollers*, was half of the forcing frequency. The investigators observed that a nascent vortex pair is stretched by the spanwise rollers directly downstream into a braid region, halting their development.

The secondary structures (Figure 2.18) inventoried in this study are:

- successive ribs (SR): structures that partially envelop the lower part of a roller pair having streamwise ($z-$)vorticity.
- cross ribs (CR): zones of lateral ($x-$)vorticity underneath a roller pair, connecting the two sides.
- wall ribs (WR): lateral ($x-$)vorticies near the wall that are periodically intensified by the convected cross ribs.

The number of vortex pairs in the SR and CR structures is dictated by the wavenumber of the initial spanwise disturbance. Of particular interest to heat transfer applications is the interaction between the cross ribs and the wall ribs. As mentioned above, the wall ribs are periodically excited by the impinging cross ribs thus increasing the turbulence intensity near the wall. The capacity to manipulate these fine flow structures by tuning inlet conditions should allow us to better control heat transfer rates around the stagnation region.

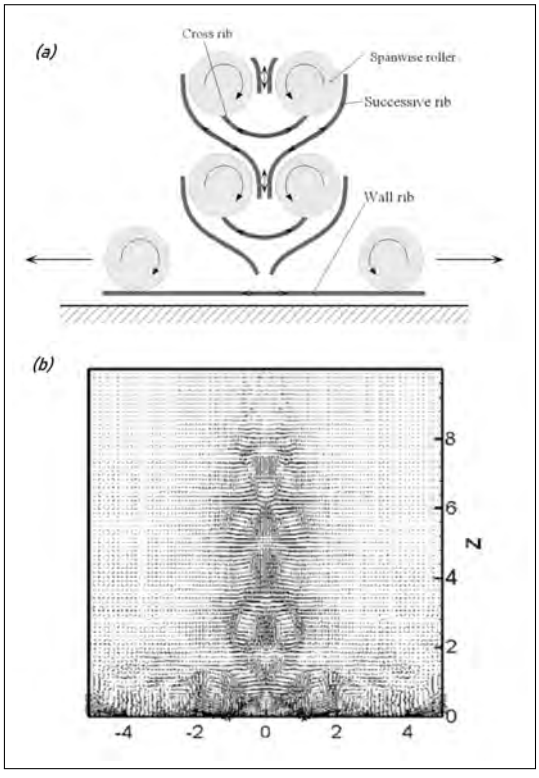

Figure 2.18: (a) Schematic of coherent structures and (b) relative velocity field in Xu et al. (2013)

Uddin et al. (2016) simulated steady and excited impinging jets using LES with the Dynamic Smagorinsky subgrid model. The following inlet velocity condition was used for the excited jets:

$$U_{\mathsf{in}} = U_{\mathsf{b}} + A_N \sin(2\pi f t) \tag{2.14}$$

where the amplitude A_N is set to 50% the average bulk velocity U_{b}. The preferred mode f_n of the jet was found from the unexcited reference case, and its corresponding Strouhal number based on pipe diameter and average bulk velocity was $\mathsf{St} = 0.36$. The jet was then excited at the subharmonic $f_{n/2}$ and second harmonic f_{2n} of the preferred mode which correspond to $\mathsf{St} = 0.16$ and 0.6 respectively. The results from the steady case using two different grids were compared to existing experimental results in order to determine the most adequate mesh resolution. The excited cases were then simulated and compared to the steady case. Enhancement of heat transfer was observed for both the subharmonic and second harmonic excitation frequencies. The stagnation point peak and secondary peak in the Nusselt profile were more prominent and sharp than in the reference case. The increase in Nusselt number in the secondary peak region was also noted by Roux et al. (2011b) in their experimental work, although their secondary peak was relatively flatter in the excited cases, and could have more aptly been described as an inflection point. In Uddin et al. (2016), the secondary peak becomes higher and sharper in the excited cases, and unlike Roux et al. (2011b), it remains roughly in the same position as in the reference case. The increase in average Nusselt number over the target plate, compared to the reference case, was 7% for the subharmonic excitation and 12.5% for the harmonic excitation.

In a work cited earlier in Section 2.7.1, Kharoua et al. (2017) studied the heat transfer characteristics of a heated jet of air impinging on a convex semi-cylinder at relatively low impact distances (two times the width of the plane jet nozzle). The simulations were performed using the FLUENT commercial code. The investigators validated their results against experimental work in which the impact surface is flat due to the scarcity of studies using convex surfaces that can be found in the literature.

Direct Numerical Simulation (DNS)

Performing Direct Numerical Simulations of impinging turbulent jets -that are steady on average- is in itself a computationally arduous task. Adding a periodic forcing into the mix makes it all the more daunting to achieve. This explains why only few have undertaken such an endeavor. Tsubokura et al. (2003) ran direct numerical simulations as well as large eddy simulations with the specific aim of understanding the flow structure in and around the stagnation point of weakly excited impinging jets (both plane and circular). In the DNS, at $\mathsf{Re} = 2000$, plane jets with disturbances of different waveforms at the inlet were considered. Beside the roll-up vortices shed from the jet's shear layer, a host of counter-rotating vortices were observed around the stagnation region. For the circular jets,

no discernible coherent structures were seen in stagnation zone. The same configurations were used for large eddy simulations at a larger Reynolds number $\mathsf{Re} = 6000$. For plane jets, the same structures reappear albeit muddled by the increased turbulence. In light of the knowledge gained from this study, the authors note the possibility of controlling heat and mass transfer in the stagnation region by tuning the forcing parameters at the flow inlet.

2.9 Methods of Jet Excitation

2.9.1 Conventional Methods

An experimentalist working on impinging jets can resort to a number of techniques to introduce a periodic component into the flow. The most widely used technique is acoustic excitation. A loudspeaker (Vejrazka et al. (2005), Roux et al. (2011b), Hsu et al. (2019)) is mounted on the settling chamber that feeds the nozzle and a tone having a certain combination of frequency, amplitude and waveform is produced. A number of studies employed mechanical devices to produce more forceful pulsations. Two devices stand out, rotating valves and mass flow rate controllers (MFRC). The first consists of a cylinder with a hole in the middle that rotates inside a casing (Azevedo et al. (2015)). The flow passes through the casing when its inlet and outlet orifices are completely aligned with the cylinder hole. A variation exists for set-ups with multiple jets (Janetzke et al. (2008)) where a number of plates mounted on a rotating disk successively block and unblock the passage of air out of the orifices of the plenum chamber. On the other hand, MFRC's (Middelberg and Herwig (2009)) are comprised of a controller that receives data from a mass flow meter and regulates a linear valve. They enable the production of a variable mass flow rate at their outlets.

2.9.2 Fluidic Oscillators

A family of fluidic devices, called fluidic oscillators, have been used in the past to produce pulsating jets for heat transfer applications. The literature on this specific topic is scarce as was noted in a review by Doty et al. (2015). Nevertheless, some of these studies have proven that it is indeed possible to improve heat transfer using these devices. Most (but not all) fluidic oscillators rely on an interplay of strength between the Coandă effect and a certain feedback mechanism. The Coandă effect deviates the main jet laterally towards one of two solid boundaries inside the oscillator. This then activates the feedback mechanism that after some time forces the jet to detach itself from the boundary and switch to the other side. This mechanism then repeats itself ad infinitum. The feedback mechanism can either be feedback loops (Warren, 1960), vortex chambers (Peszynski et al., 2016) or a resonance chamber (Spyropoulos, 1964), just to name a few. The reader is referred to Tesař (2017) for more detailed information on fluidic oscillators, their designs and working principles.

In what follows we will focus on the very few heat transfer studies done using these devices.

Herwig et al. (2004) employed three types of nozzles in order to produce unsteady jets: a Karman jet nozzle, a flip-flop nozzle (sonic oscillator) and a precessing nozzle (Fig. 2.19). The Karman nozzle exploits the formation of vortex streets in the wakes of bluff bodies, here a ring whose axis is parallel to the flow direction. The flip-flop nozzle is a fluidic oscillator with its control ports connected to one another via loop in which compression waves travel. It produces two pulsating exit jets instead of one sweeping jet. And finally the precessing nozzle consists of a small orifice that widens slightly, allowing for the jet to attach itself to the slanted walls by virtue of the Coandă effect . Since the set-up is axisymmetric, the jet turns around in the azimuthal direction, or more concisely, it precesses. Improvements in heat transfer were only observed for the Karman nozzle. The authors posit that in the other cases, the increased mixing between the jet and the surrounding fluid led to a dissipation of the momentum of the jet which led to deterioration of performance. They then point out the importance of finding out which kinds of unsteadiness are conducive to enhancement.

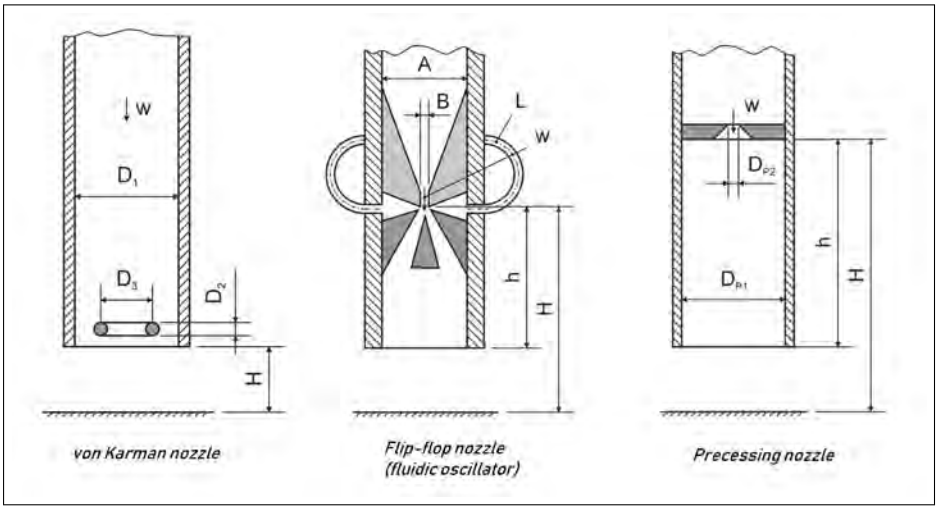

Figure 2.19: Nozzle designs used by Herwig et al. (2004). The flow direction is indicated with an arrow w.

Pulsating Jets

Ten and Povey (2019) used a fluidic oscillator with two pulsating exit jets (see Fig. 2.20) for a turbine cooling application. The investigators first attempted to optimize the design of the oscillator by changing the dimensions of the interaction chamber, the inlet, the splitter edge and the feedback loops. After numerically simulating the system, calorimeter tests were performed that showed an improvement of 20% over the steady reference case. Thin film heat gauges revealed that local enhancement was most noticeable in the region between the two stagnation points, the Nusselt number elsewhere being comparable to the

reference case. The authors used a range of high pulsation frequencies of 10 to 20 kHz.

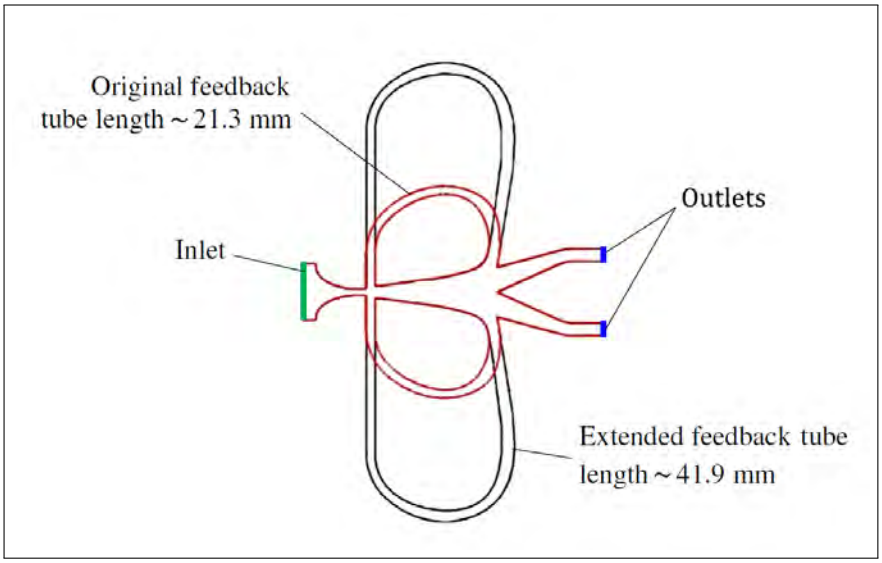

Figure 2.20: Design of the fluidic oscillator used in Ten and Povey (2019).

A jet impingement heating device was studied by Tesař (2009) consisting of a plane fluidic oscillator and annular exit nozzles. The oscillator resembles that of Ten and Povey (2019), but with a splitting edge that is much closer to the main jet, resulting in a different frequency response to inlet pressure. The frequencies ranged from 5 to 50 Hz. A typical improvement of $180 - 200\%$ over the steady case was observed and enhancement remained noticeable for different impact distances.

Sweeping Jets

Camci and Herr (2002) studied the heat transfer performance of an oscillatory jet issuing from a fluidic oscillator. They carried out experiments with Reynolds numbers ranging from 7500 to 14,000, standoff distances from $H/D = 24$ to 60 and frequencies from 10 to 100 Hz. They were able to show that improvements of 20 to 70% ($\mathsf{Re} = 14,000$ and $H/D = 24$) were possible using this configuration.

For a given mass flow rate, Narumanchi et al. (2008) noted an improvement of up to 30% in heat transfer for an oscillating jet compared to its steady counterpart. On the other hand, Zhou et al. (2019) have noted that at the same mass flow rate, the increase in turbulent kinetic energy no longer compensates for the decreased average velocity before impact, meaning that introducing a deterministic oscillatory component to a steady flow does not in fact improve heat transfer rates. It is worth noting that although producing similar sweeping jets, the oscillators in the two studies have different jet exit dimensions (the first has an area of 1.1 mm × 1.1 mm while the second has an exit aperture that is 10 mm wide) and different internal geometries.

Hewakandamby (2009) conducted a numerical study of an array of impinging oscillatory (sweeping) jets and compared their heat transfer performance with that of equivalent steady jets. Different frequencies (1 to 500 Hz), Reynolds numbers (250 to 1000), stand-off distance ($H/D = 2.5$) and nozzle separation ($S/D = 3$ to 8, where S is the distance separating the axes of successive nozzles) were considered. The performance was enhanced for lower S/D and higher Reynolds number. The highest frequency considered resulted in the best performance overall. The investigators have reported a possible improvement over steady jets of around 100% in some cases. This result, however, is nuanced by the fact that only low Reynolds numbers were considered and so the comparison was made with inefficient laminar jets.

More recently, Wen et al. (2020) proposed an oscillator design with an adjustable sweeping angle. The design had two plates: the master plate and the exit plate (see Fig. 2.21). The first contains the throat, interaction zone, splitting-edge and the feedback loops without exit channels. The second plate consisted of a throat (with a separate inlet), a diverging exit and two control channels connected to the primary plate. The jet in the second plate is then pushed from one side to the other by the fluid flow coming from the oscillator through the control ports. The proportion $P_{I/II}$ of flow from the primary plate with respect to that of the secondary plate determines the sweeping angle. The sweeping angle went from 0° at $P_{I/II} = 0$ to 100° at $P_{I/II} = 1$.

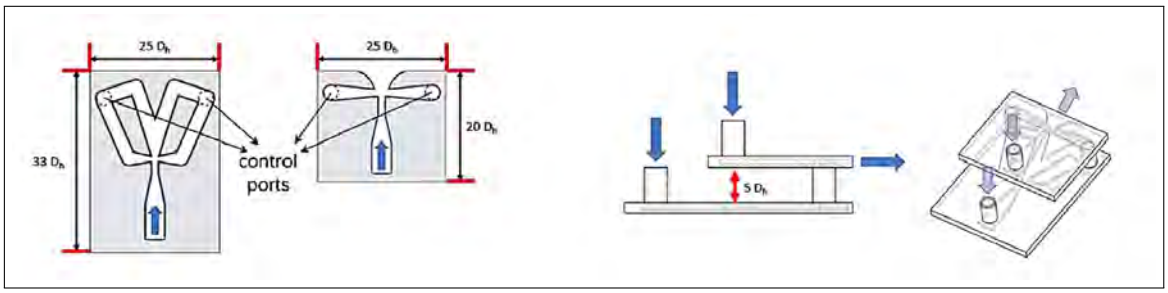

Figure 2.21: Variable sweep-angle fluidic oscillator used in Wen et al. (2020).

Using concave, convex and flat target surfaces, Kim et al. (2019) conducted an experimental study to determine the heat transfer performance of an oscillator's sweeping jet (Figure **??**). Concave surfaces resulted in higher Nusselt numbers along the wall than did the flat surface. Moderate values of curvature led to the best improvement rate. Convex surfaces also resulted in enhancement over the flat surfaces, albeit to a lesser extent. The improvement seen for concave surfaces were partly attributed to steeper velocity gradients at the surface in the wall jet region.

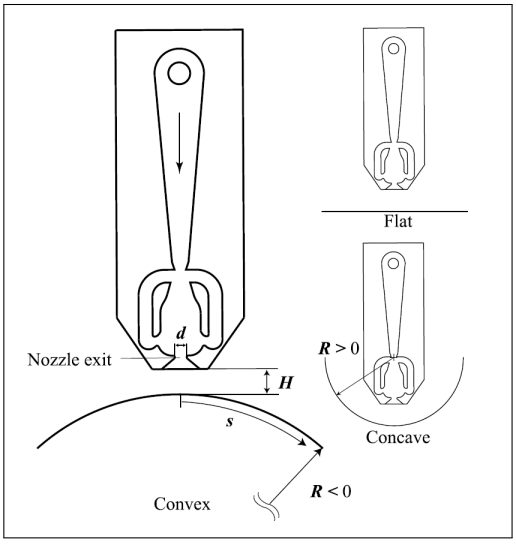

Figure 2.22: Experimental model of a fluidic oscillator and a convex surface. Right:flat and concave surfaces (Kim et al. (2019)).

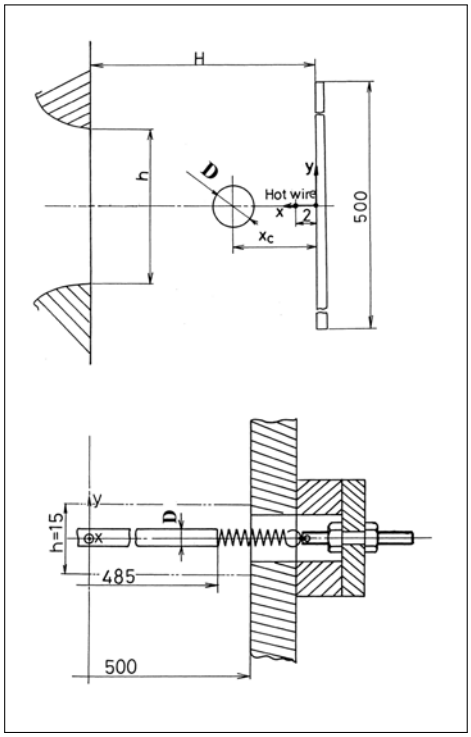

Figure 2.23: Top: Jet nozzle, cylinder and target surface. Bottom: Cylinder suspension system (Haneda et al. (1998)).

2.9.3 Miscellaneous Methods

Other, more exotic, methods can be found in the literature. Haneda et al. (1998) placed a spring-mounted cylinder between a steady jet and the impact plate (Fig. 2.23). Very rigid springs were used to prevent the cylinder from vibrating. As the air flowed around the

obstacle, an unstable wake manifested itself before impinging on the solid surface. Looser springs were then used to allow the cylinder to vibrate on its own due to interaction with the flow. This gave rise to a feedback mechanism between the cylinder and the now excited flow. On the other hand, Klein and Hetsroni (2012), instead of pulsating the (micro-)jet itself, used a movable target surface in such a way that the *relative velocity* between the fluid and the solid was perturbed.

2.10 Emerging topics

2.10.1 Nanofluids

A nanofluid consists of a base fluid, such as water or ethylene glycol, to which nano-sized particles are added to enhance its heat transfer characteristics. Recent developments (see Manca et al. (2011)) have shown that, given the right conditions, these nanofluids can improve steady jet impingement heat transfer by up to 18% compared to the base fluid. In addition to the usual parameters such as the Reynolds number and standoff distance, enhancement in this case also depends on the volume fraction of nano-particles. To our knowledge, only two studies have looked into periodically unsteady impinging jets of nanofluid, one of which uses synthetic jets (Li et al., 2019) while the other uses pulsed jets (Selimefendigil and Öztop, 2014). Both studies numerically simulate a submerged water/aluminum oxide nanofluid jet using a single-phase model. The low volume fraction of nano-particles in the base fluid justifies the assumption that the nanofluid behaves as a single non-Newtonian fluid.

Li et al. (2019) tested both rectangular ('R-wave') and triangular ('T-wave') zero-mean velocity profiles. They found that for all values of the Reynolds number and volume fractions of nano-particles, the T-wave fluctuations produces higher average Nusselt numbers. The difference becomes even greater for higher frequencies (in this case, $f = 10-50\,\mathrm{Hz}$). In contrast, Zhang et al. (2018), who simulated synthetic air jets, could not find a conclusive link between velocity waveform and heat transfer enhancement.

Selimefendigil and Öztop (2014) simulated a submerged jet of nanofluid with sine-wave pulsations and presented a comparison with an equivalent steady jet. Although the performance of the steady nanofluid jets was higher than that of the base fluid jets, the addition of nano-particles to the pulsating flow did not consistently improve heat transfer relative to the steady cases. The stagnation point Nusselt number decreased when the nanofluid jet was pulsated at relatively low frequencies. The time-averaged global Nusselt number decreases with increasing frequency from $f = 1-6\,\mathrm{Hz}$. As in the synthetic nanofluid jet study, performance was positively correlated with the volume fraction and the Reynolds number of the flow.

2.10.2 Micro-jets

Microjets, and microflows in general, are finding more applications in the fields of flow control (for instance, Choi et al. (2006)) and heat transfer. In most cases, heat transfer application involve a steady jet (Chang et al. (2013)) or an array of steady jets (Browne et al. (2010)), that impinge on flat or finned surface. In addition, many studies have also used synthetic jets in heat transfer applications and are listed in a comprehensive review by Arshad et al. (2020). To date, pulsatile microflows have mostly been studied in the context of drug delivery (e.g., Wang et al. (2012)). As for jet impingement cooling, one study by Klein and Hetsroni (2012) has reported some results from heat transfer measurements on a actuated slab cooled by a steady microjet. Although the jet itself is steady, the periodic movement of the slab induced flow phenomena akin to what is observed in pulsed jets (refer to section 2.7.3). Their results have shown that improvement is possible when the flow is actuated. In addition, certain works in the literature (e.g., Sanyal et al. (2009), mentioned earlier), have pointed out that heat transfer improvement is relatively better for laminar jets as compared to turbulent ones.

Almost all studies concerned with unsteady impinging microjets have used synthetic jets produced by vibrating membranes to produce zero-net mass flow microjets. However, a very recent numerical work by Huang et al. (2022) has demonstrated that by using pulsed impinging microjets in microchannel heat sinks can significantly improve heat transfer. Their configuration combines a number of elements evoked so far in this literature review, to wit: the use of multiple jets pulsed with a phase difference $\Delta\phi$, the inclusion of surface modifications in the form of eccentric ellipsoid protrusions, and the sub-millimetric dimensions of the jet. The main focus of the study was finding the ideal value of the phase difference $\Delta\phi$ that would reduce the negative effects of the crossflow on heat transfer and was found to be $\Delta\phi = 0.75\pi$. This study being entirely numerical, the practical implementation of this configuration is not discussed. In this thesis, the development and production of a working microfluidic oscillator capable of producing pulsed microjets is presented and may represent a way of reproducing experimentally this numerical configuration.

2.11 Conclusion and Perspectives

A survey on pulsed jet impingement cooling was presented, which was motivated by the variety of experimental and numerical setups in the literature that often led to somewhat contrasting conclusions. The parameters affecting heat transfer are not only confined to the jet characteristics, such as its Reynolds number or pulsation frequency, but can also involve the characteristics of the pulsed jet actuators used, the geometry of the impact surface and the type of nozzles used. Whether tuning one parameter can improve heat transfer is often dependent on other factors that can alter its effects. For instance, depending on the value of the Reynolds number or standoff distance, increasing the frequency can either deteriorate or enhance cooling. Of particular interest are the flow characteristics that can be controlled by the pulsations in conjunction with other geometric factors. Depending

on the waveform, frequency and amplitude of pulsation, large vortex structures can either be produced or broken down into small scale, incoherent turbulence. Other factors related to the experimental setup, e.g. surface roughness or adding a transmission chamber, have also been explored and in certain cases tangible improvements in heat transfer performance were obtained. In spite of this, certain aspects call for more exploration such as:

- **The impact angle** (O'Donovan and Murray (2008)) which has a strong influence on heat transfer distribution.
- **The addition of water droplets** to the pulsating flow, as Pakhomov and Terekhov (2010) had shown this can significantly increase heat transfer in the vicinity of the stagnation point.
- **Polychromatic forcing** which consists in exciting the flow at two or more frequencies simultaneously. Vejrazka et al. (2005) has shown that it can induce phenomena such as the merging of vortex triplets.
- **The use of new hybrid LES/RANS methods** to simulate the unsteady slot jet and observe the dynamics of the vortex structures induced by the pulsed flow. The hybrid approach can drastically cut down on computational costs all while resolving part of the flow
- **The use of fluidic devices** to produce unsteady jets in heat transfer applications.
- **Pulsed microjets:** there are almost no studies on the heat transfer from pulsed impinging microjets. A very recent study by Huang et al. (2022) has shown the potential of pulsed impinging jets in improving the heat transfer of microchannel heat sink.

In the present work, we attempt to give some answers to these last three points by assessing the heat transfer of an impinging pulsed jet produced by a fluidic oscillator, which is then simulated using several methods, among which the hybrid LES/RANS approach and finally a scaled down version of the device is produced, instrumented and used to produce pulsed impinging microjets.

Part I

Original Design

"Nous avons autant à apprendre des fluides que des solides. Nous devrions nous apprendre à penser les solides à partir de l'expérience primitive des fluides, ne serait-ce que pour contre-balancer le mouvement épistémologique inverse suivi par la tradition."

La Formation de l'esprit scientifique
Gaston Bachelard

3
Characterizing the Oscillator

A study of the behavior of the oscillator was conducted in preparation for the thermal measurements that will be presented later on. This includes both the internal mechanisms and design parameters that determine the pulsation frequency of the device as well as the characteristics of the produced pulsed flow. Although the aim of the present work is not to offer detailed design guidelines for a pulsed jet fluidic oscillator, some design aspects were touched on.

The present embodiment of the fluidic oscillator can function in different ways depending on the geometry of its parts. Two parameters considered here were the length and channel width of the feedback loop. It was shown that the device can switch between two different pulsation modes depending on both the width of the feedback loops and the inlet pressure. Some two-dimensional simulations were performed in an attempt to explain this phenomenon. Even though the results were inconclusive, they hinted at the probable role of capacitive elements placed ahead of the control ports of the device. The frequencies of a number of prototypes, differing only in feedback loop lengths, were measured and used to deduce the switching and wave travel times of the device as a function of inlet pressure. This was done by fitting the data to a model that takes into account both the switching mechanism and wave propagation in the feedback loops.

In the second part of this study, measurements of the flow field near the exits of the device were performed. It is complicated to use high-end visualization methods such Particle Image Velocimetry (PIV), seeing the range of pulsation frequencies considered here. High-speed CCD cameras that are commonly used for PIV can reach frame rates in the order of 1000 frames/s while CMOS cameras can attain frame rates of a few thousand frames per second at the cost of a lower image resolution. In this study, a much simpler measurement technique, that uses a hot-wire anemometer, was deemed sufficient to gather

information from the flow field. Pressure data inside the oscillator's feedback loops were acquired along with the hot-wire measurements in order to perform a conditional reconstruction of the flow field. From this data set, the expansion rate and velocity decay were computed for different operating conditions. The presence of lateral instabilities such as puffing and flapping was detected for certain cases. The jets pulsating at lower frequencies were shown to produce vortex dipoles whose convection velocity changes with jet Strouhal number. This part is concluded with three-dimensional measurements of the jet that better revealed the structures of these dipoles. Due to the limited space between the jet orifice and the impingement plate, it was not possible to perform the measurement in the confined configuration, so only free pulsed jets were considered here. The information obtained from these measurements remains relevant when the jet impinges onto the target plate, since a large part of the flow before impact remains relatively unaffected by the presence of the solid boundary.

Seeing as fluidic oscillators are usually integrated into larger systems, the ability to construct a model of the pulsed flow (that takes into account such parameters as the input pressure of the device) and to use it during the design process may be of great utility in a number of applications. This topic is explored in the appendix to the present chapter. Several data-driven methods were used to achieve this. Two of these methods, Proper Orthogonal Decomposition and Dynamic Mode Decomposition, can be classified as modal decomposition techniques. The third method relies on Deep Neural Networks using an (unusual) sinusoidal activation function. It was shown that, although a truncated POD reconstruction of the flow can reproduce the flow relatively well, DMD is not capable of consistently capturing the salient features of the flow. For the DNN approach, a grid search was first performed to determine the optimal number of neurons per layer that is needed to construct an adequate representation of the flow. Several widely used activation functions were then tested. The sinusoidal activation function, with the appropriate initialization scheme, resulted in the most accurate representation of the flow with the shortest training time.

3.1 The Warren Oscillator

Fluidics was born in 1957 in the fireplace of an American physicist in Washington, D.C. (McKetta Jr (1997)). Instead of going up the chimney, the smoke from his fireplace flowed into the living room. To remedy this, he used a small bellow to redirect the flow up the chimney. The word *small* is the key to this story. Billy M. Horton, the physicist with a now smoke-free living room, put this observation to practical use: the small signal from the bellow could set the flow direction of a larger flow. This is the basis for the fluid amplifier, which is at the heart of many fluidic devices. One embodiment of the fluid amplifier consists of a plenum from which the main jet issues into an interaction zone (Figure 3.1). This jet is flanked by a pair of control port by which it can be deflected in the desired direction. The presence of a side wall gives rise to a depression region between the jet and the solid boundary, causing the jet to attach to one side, even after the control flow deflecting the

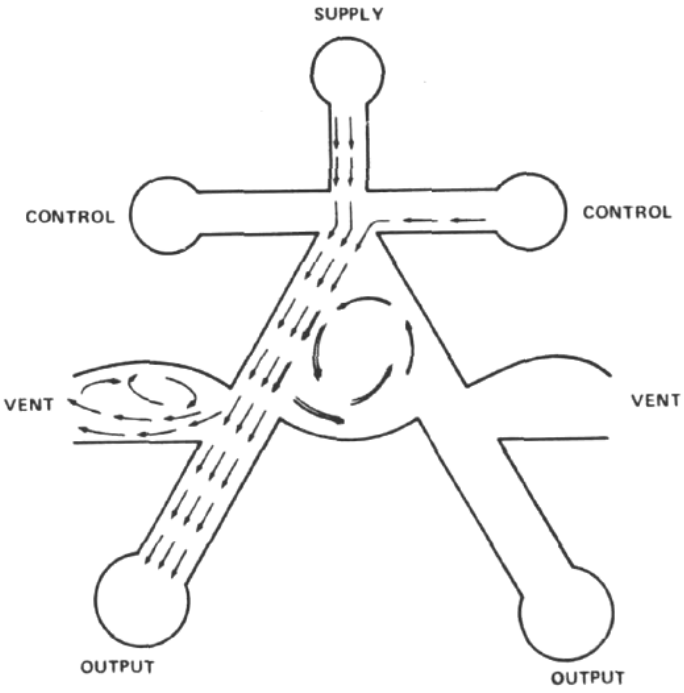

Figure 3.1: Example of a fluid amplifier switched to the left.

jet is turned off. Additional elements can also be added, such as vents, or a sharp splitter.

Other devices that act as logic elements were proposed earlier, such as the Tesla valve (leaky fluid diode) in 1920 and the turbulence amplifier (inventor R.E. Hall) in 1922. However, the field of fluidics really took off in the late 1950's at the Harry Diamond Laboratory where Horton worked. Sensing as well as control and logic tasks were performed using fluidic devices. At that time, they offered many advantages over electrical and electromechanical systems, such as resistance to shocks, vibration and nuclear radiation. In addition, the absence of moving-parts made them immune to harsh operating environments and to wear over time. Unlike electrical devices performing similar tasks, fluidic devices did not dissipate heat, and so did not run the risk of thermal runaway. However, with the miniaturization and increased complexity of electronic circuits, fluidic devices could not keep up and eventually became obsolete.

Nevertheless, interest in fluidic devices re-emerged in recent decades, especially in the fields of active flow control and heat transfer. Much attention has been given to a particular device: the fluidic oscillator. In the present study, a design based on a patent by Warren (1964) is studied. This design is often overshadowed by the sweeping jet oscillator which has been successfully used in flow control on airplane wings (Woszidlo et al. (2019), (Ostermann et al., 2019)). The Warren oscillator is built around a fluid amplifier with a splitting edge placed in front of the main jet. Each branch connected to the interaction zone is split into two channels, one that leads to the output, and another that is connected to a control port through a feedback loop. In this configuration, the amplifier is self-excited, i.e. the main jet switches between the two sides continuously, without external input. The flow returning

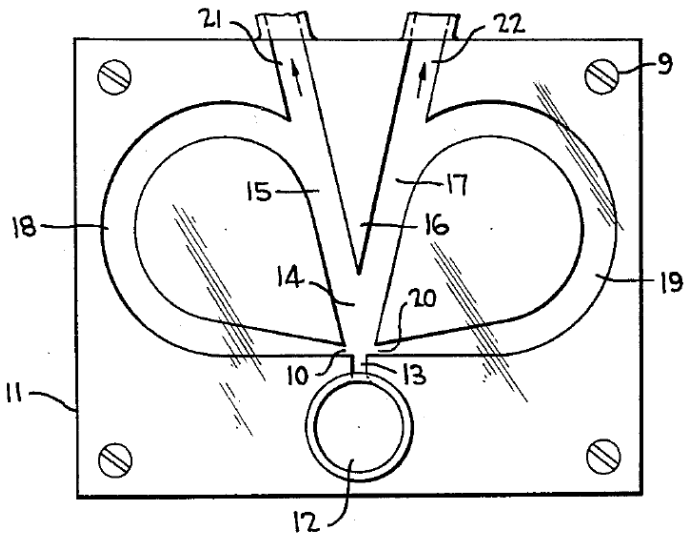

Figure 3.2: Illustration of the negative feedback oscillator from Raymond Warren's patent (Warren (1964)).

through the feedback loop deflects the attached main jet, allowing it to switch. The outputs of the device are then a pair of pulsed jets. More recent studies of this device, scarce as they may be, have shown that certain design parameters and operating conditions can give rise to different operating modes. For instance, Wang (2017) showed that the deflection of the main jet by the control flow is not enough to cause switching. A pressure wave has to travel from the feedback loop inlet to the control port and back in order for switching to occur.

3.2 Materials and Methods

3.2.1 Prototypes

The design of pulsed jet oscillators can be fine-tuned according to the demands of any given application. The main design factors that can affect the behavior of the device are:

- **the length and volume of the feedback loops:** in Wang et al. (2016), it was found that the feedback loop length was the predominant factor affecting the frequency of the oscillator. For the particular design used, they identified the pressure waves traveling back and forth along the feedback loops as the primary feedback mechanism. This meant that the period of oscillation can be estimated by the time it takes the pressure wave to travel across the loop, twice on each side. Löffler et al. (2021) arrived at a similar conclusion, for a slightly different oscillator design, that the length of the feedback loop has a stronger effect on frequency than does its volume.
- **the control ports:** depending on the design, the switching mechanism can depend entirely or partially on the pressure difference between the control ports.
- **the inlet, exit and feedback ports:** the relative areas of these ports can drastically

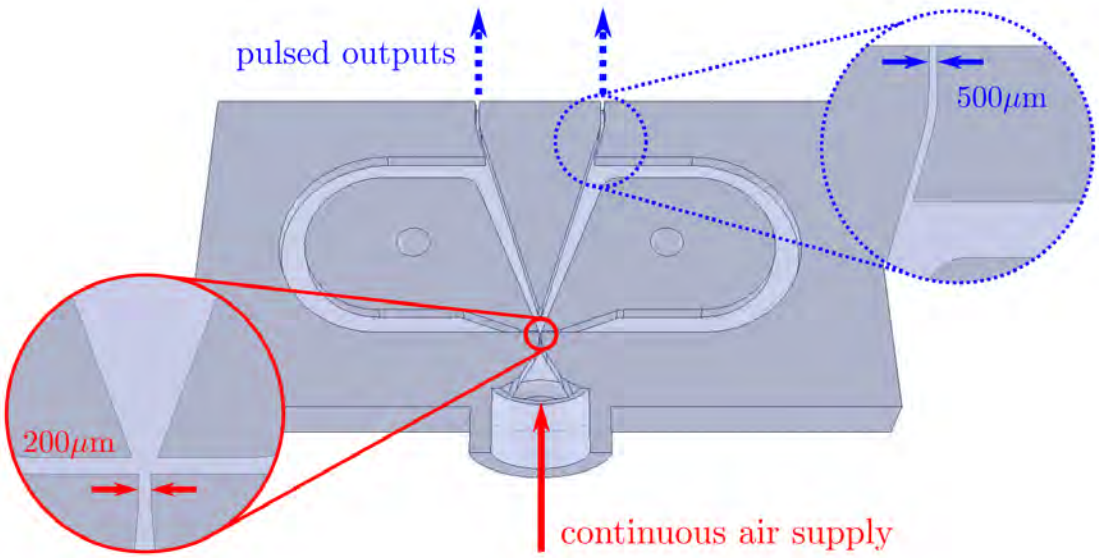

Figure 3.3: CAD drawing of the Lg0 prototype with detailed views of the input and output channels.

change the behavior of the oscillator as was demonstrated by Löffler et al. (2021). They showed that it was possible to change the frequency response of the device to mass flow rate by changing the throttling ratio T_{OP} [1]. The ratio of the outlet section to the feedback section was found to have a small effect on frequency.

- **the shape and placement of the splitting edge:** if we compare the designs used in Ten and Povey (2019) and Wang et al. (2016), respectively, we can see that the main difference is the placement of the splitting edge. In Ten and Povey (2019), the flow is split far downstream from the inlet, on the same level as the feedback ports whereas in Wang et al. (2016) the edge is placed within the interaction zone. This has a clear effect on the frequency response since in the first case the frequency keeps increasing with inlet mass flow rate whereas in the second it eventually reaches a plateau.
- **the lateral attachment walls:** more particularly the angle between them and possible modifications such as curvature (Ten and Povey, 2019) or secondary attachment walls (Löffler et al., 2021).

In the present work, only the length and width of the feedback loops were changed in order to understand their effect on the behavior of the actuator. Due to the limited space inside the 3D-printer, two of the prototypes were printed with integrated feedback loops and a fluidic amplifier was made whose feedback and control ports are connected externally using flexible tubes. One of the prototypes with integrated loops, Lg0, is shown in Figure 3.3. The second prototype with integrated loops, Lg1, has the same geometry as Lg0 but with slightly longer feedback lines (not shown here). The L- and Ls-configurations are achieved using the same fluidic amplifier shown in Figure 3.4.

The devices studied herein have a wide range of frequencies, going from 185 Hz for L7

[1] defined as the ratio of inlet area A_{PJ} to outlet area A_O.

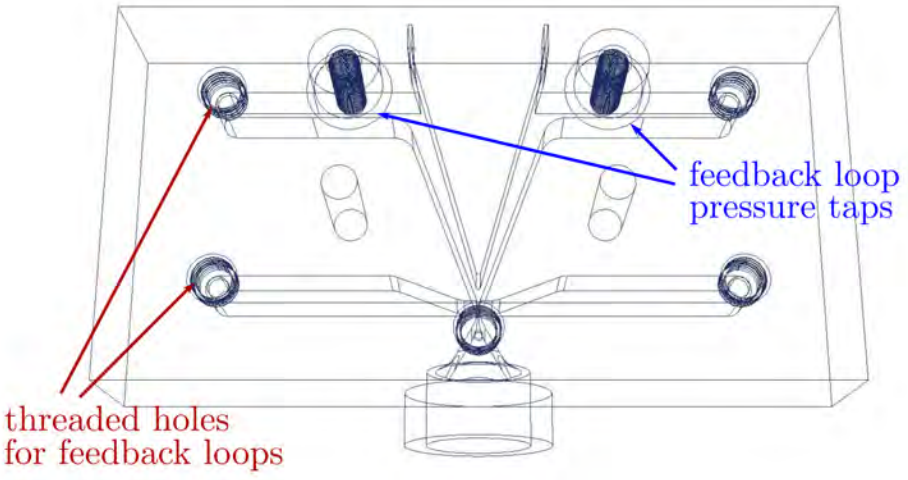

Figure 3.4: CAD drawing of the fluidic amplifier used for the L- and Ls-series configurations.

up to 1240 Hz for Lg0 (refer to Table for device nomenclature). For cases L3 to L7, the same device was used whose frequency was modulated by externally connecting tubes of different lengths. The pneumatic fittings and the pressure taps in the device impose a minimum loop length corresponding to a maximum frequency of 740 Hz. To overcome this issue, two additional compact prototypes Lg0 and Lg1 were produced with fixed, integrated feedback loops, with Lg0 having a peak frequency of 1240 Hz and a saturation frequency of 990 Hz. A final part was printed that produces a pair of steady jets having the same dimensions as the pulsed jets (Figure 3.5). All the prototypes were 3D printed using a medical-grade printer and they include ports for pressure sensors that are flush-mounted onto the feedback loops.

3.2.2 Experimental Setup

Instantaneous velocity signals were measured using a Dantec hot-wire probe (type 55) with a diameter of 5 µm and a length of 1 mm and Mini Constant-Temperature Anemometer (CTA, Model 54T20). Calibration was performed using a jet of air exiting a 1 m-long cylindrical settling chamber with a diameter $D = 58$ mm. The exit orifice had a diameter of $d = 10$ mm. Assuming that the air is under isentropic conditions and applying the energy equation between the settling chamber and the exiting flow, velocity can be deduced from the *integrated Bernoulli equation*:

$$\frac{1}{2}U^2 + \frac{\gamma}{\gamma-1}\frac{p_0}{\rho_0}\left(\frac{p}{p_0}\right)^{(\gamma-1)/\gamma} = \frac{\gamma}{\gamma-1}\frac{p_0}{\rho_0} \tag{3.1}$$

where U is the average velocity at the exit of the settling chamber, p the ambient pressure, p_0 and ρ_0 the pressure and the density of air inside the chamber. The pressure p_0 was measured using a manometer while the density ρ_0 was deduced from the ideal gas

Table 3.1: List of prototypes used for the present study. L^* and W^* are the dimensionless feedback loop length and width and are defined as L/w and W/w, respectively, where L is the feedback loop length, W its width and w the actual width (see the next section) of the exit channel.

Prototype	FBL length L^*	FBL width W^*	Frequency range (Hz)
Lg0	77	4.6	$985 - 1240$
Lg1	107	4.6	$771 - 940$
L2	136	2.4	$618 - 723$
L3	183	2.4	$510 - 643$
L4	244	2.4	$438 - 561$
L5	353	2.4	$346 - 439$
L6	670	2.4	$234 - 288$
L7	1007	2.4	$177 - 213$
Ls3	183	1.1	$484 - 950$
Ls4	244	1.1	$432 - 824$
Ls5	353	1.1	$386 - 1288$
Ls6	670	1.1	$277 - 998$
Ls7	1007	1.1	$200 - 1130$

law and temperature measurements using a K-type thermocouple. The average velocity was also estimated using a mass flow meter (MFM, Mass Stream Model D6270) having the following technical specifications:

- Accuracy (based on air calibration): ± 3 % FS (Full Scale) including non-linearity
- Repeatability: ±0.5% FS
- Range (Turn-down-Ratio): 5…100 % (1 : 20)

For most of the calibration range, the velocity estimations from the mass flow meter remained within 2% of those from the integrated Bernoulli equation. Since the second method is more practical, it was used for all subsequent calibrations. The pressure inside the chamber was gradually changed and the resulting velocity was plotted against the average voltage measured by the hot-wire probe. The data were then interpolated using a fourth-order polynomial whose coefficient of determination R^2 remained around 0.9999 for all calibrations performed for this study.

A Parker model G9 XPD filter was placed between the air service and the settling chamber in order to avoid particulates from entering the system and possibly colliding with the hot-wire. Miniature pressure sensors from Kulite (model XT-140M) were flush mounted on the channel walls of the feedback loops. The width of the channels is 3.2 mm while the diameter of the sensing area over which the pressure is averaged is 2.6 mm. The measurements were acquired from the hot-wire probe and the pressure sensors using a National Instruments Multifunction I/O device model USB-6221.

The time-averaged and phase-averaged velocity fields were reconstructed from hot-wire measurements at points on a predefined grid in the midsection plane at the exit of the

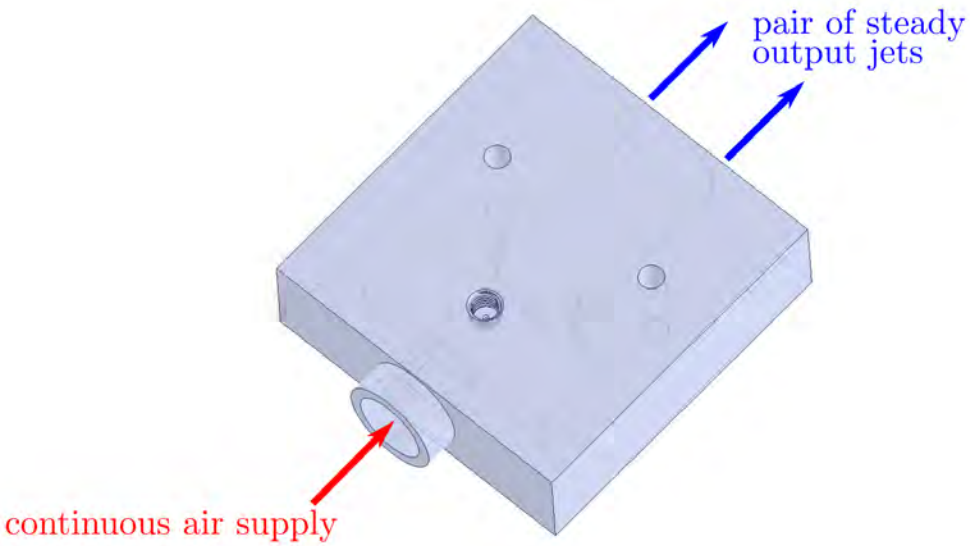

Figure 3.5: Printed part used to produce steady jets.

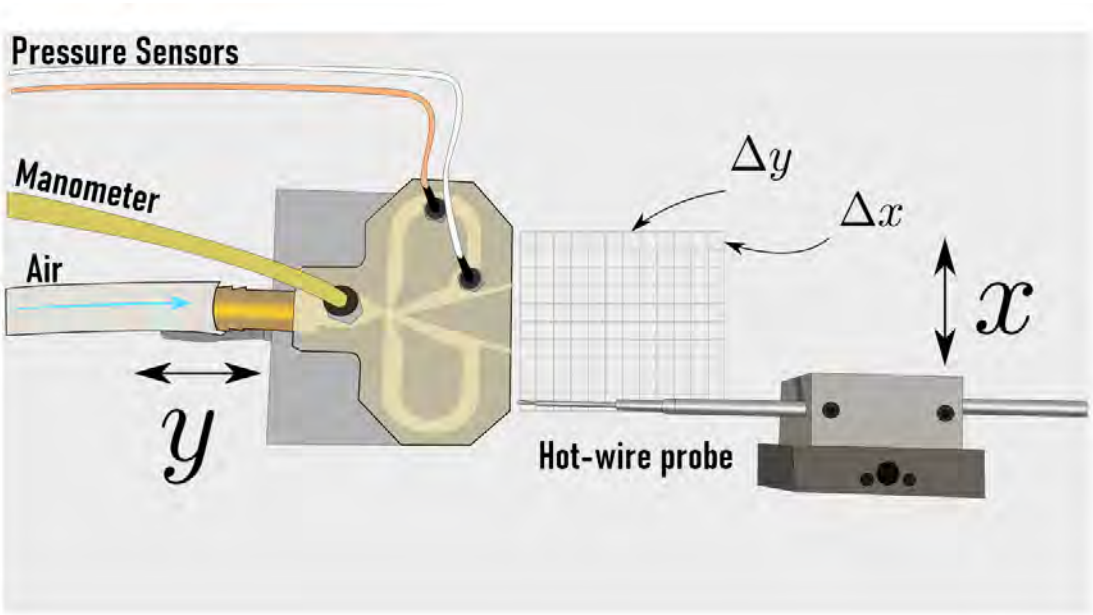

Figure 3.6: Illustration of the experimental setup used to measure the velocity field.

oscillator (see Figure 3.6). Two ball-bearing linear stages, with mounted step-motors, were used to move the hot-wire and oscillator prototypes with respect to one another. The minimum lateral and axial spacings were $\Delta x = \Delta y = 100\,\mu\text{m}$.

The oscillator prototype used by Wang (2017) consisted of several metallic parts that had to be mechanically assembled. This led to several issues, namely misalignment, causing an asymmetrical internal geometry, and leakage, both of which strongly affect the functioning of the oscillator. To avoid dealing with the same issues, the prototype studied

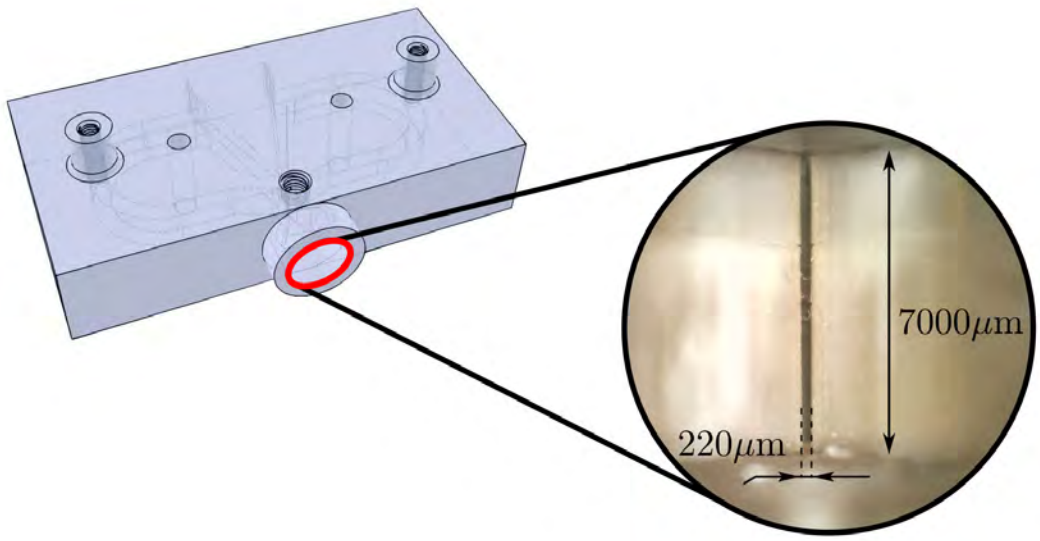

Figure 3.7: Microscope image of the inlet section of the fluidic oscillator which shows the high dimensional accuracy of the 3D-printer used.

here were produced by stereolithography. We had access to the MultiFAB platform at the Laboratoire d'analyse et d'architecture des systèmes (LAAS) which is a unique technology platform in France equipped with high resolution SLA printers, among other things. The most suited 3D-printer for our devices in terms of dimensional accuracy and surface quality was the DW 029J+ from DWS Systems which uses a proprietary resin dubbed DS3000. Due to the limited working area of the printer ($150 \times 150 \times 100\text{mm}^3$) the span of the feedback loops had to be reduced compared to the prototypes in Wang (2017). The inlet slot of the oscillator of width $W \approx 200\,\mu\text{m}$ is shown in Figure 3.7. The aspect ratio of the inlet is about 1:35, which is difficult to achieve using other production methods, with the advantage here being a monolithic part that does not require assembly. The average slot width was around 700 µm (Figure 3.8). The effective slot width w at the measurement position (refer to section 3.5.1) is also approximately equal to 700 µm. This was confirmed by first dividing the mass flow rate at the exit (measured using the MFM) by the mean velocity and the density of air to get the effective area of the slot. This area was then divided by the slot length (Figure 3.8) to get the effective slot width. Since the material used to produce the prototypes by stereolithography can undergo warping over time, the dimensions of the slots were checked before each test and no significant change was noticed during the time it took to perform all the measurements.

Hot-wire anemometry and compressibility effects

As the inlet pressure is increased, the peak Mach number of the jet might occasionally exceed $\mathsf{Ma} = 0.3$, the value below which the flow can be treated as incompressible. This mainly occurs for $p_{\text{IN}} = 3\,\text{bar}$ when the velocity reaches its peak value before rapidly

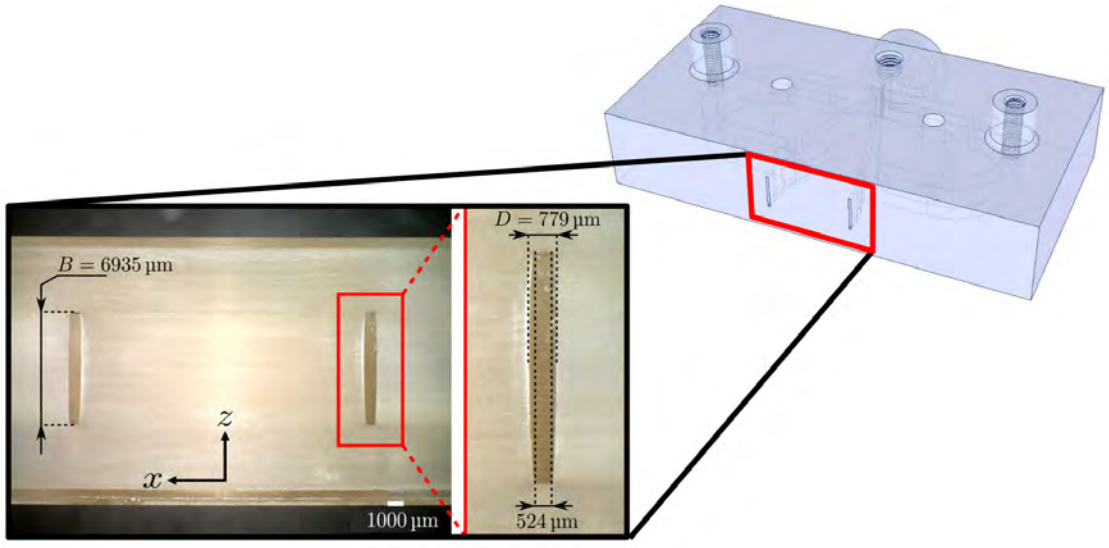

Figure 3.8: Detailed view of the exit plane of the Lg0 prototype showing the two output slots.

decreasing. This results in the Mach number momentarily reaching the value $\mathsf{Ma} = 0.36$ at the center of the jet. The average Mach number for all cases remains below the limit of $\mathsf{Ma} = 0.3$. According to Morkovin (1956), neglecting compressibility effects for $\mathsf{Ma} = 0.3$ leads to an underestimation of U/U_{mean} of about 11.5%. Seeing as the flow occasionally crosses this threshold only for $p_{\text{IN}} \geq 3$ bar, we will forgo the complex calibration procedures usually used for high subsonic flows in favor of the standard calibration described above. To obtain the correction factors that would account for compressiblity effects, a specialized facility capable of varying ρU, M and T_t [2] independently is needed. The increase in precision does not justify the use of a high subsonic calibration procedure for the reasons cited above and since most of this study focuses on flow characteristics and instabilities downstream from the exit slots where the velocity has already begun to decay.

3.3 Data Processing

The frequency of the pulsed jet is determined from the pressure measurements inside the feedback loop. The periodic character of the flow requires a triple decomposition (Reynolds and Hussain (1972)), as follows:

$$u = \langle u \rangle + u' = \overline{u} + \tilde{u} + u' \tag{3.2}$$

where u is any given field quantity, $\langle u \rangle$ its phase average, $\overline{u}$ its average value, $\tilde{u}$ the fluctuating part of the phase average and u' the incoherent remainder. The phase-averaging process is locked-in with the pressure signal because it is consistent across pulsations. The

[2] the stagnation temperature

phase average is obtained by:

$$\langle u(t)\rangle_i = \frac{1}{N}\sum_{k=1}^{N} u(t_i + kT) \tag{3.3}$$

where T is the period of oscillation obtained from the pressure signal and i is a given phase position. Turbulent kinetic energy is obtained from the standard deviation of the fluctuating component $u' = u - \langle u\rangle$ (with a large enough sample, this is equivalent to a reordering of the data because it was not measured at the same time everywhere, see Lumley (2007)).

The reference signal is the pressure data measured in one of the feedback loops. The pressure recording starts when the edge of the signal reaches a certain threshold on a rising slope. Although this assured that a large part of the data was acquired at the same phase of oscillation of the device, unwanted noise was seen to trigger acquisition at the wrong instant. This was corrected in post-processing by choosing a reference pressure signal at an arbitrary location in the flow and finding the sample cross-correlation between it and the pressure signal at every other location. The cross-correlation for a discrete function:

$$\Gamma\{p, p_{\mathsf{ref}}\}(m) = p * p^*_{\mathsf{ref}} = \sum_{m=-\infty}^{+\infty} p(n+m)\overline{p_{\mathsf{ref}}(m)} \tag{3.4}$$

is estimated by:

$$\hat{\Gamma}\{p, p_{\mathsf{ref}}\}(m) = \frac{1}{N-|m|}\sum_{0}^{N-|m|-1} p(n+m)p^*_{\mathsf{ref}}(n) \tag{3.5}$$

The factor $1/(N-|m|)$ is included so that the expected value of the estimator becomes equal to the actual cross-correlation:

$$\begin{aligned} E\left[\hat{\Gamma}\{p, p_{\mathsf{ref}}\}(m)\right] &= \frac{1}{N-|m|}\sum_{0}^{N-|m|-1} E\left[p(n+m)p^*_{\mathsf{ref}}(n)\right] \\ &= \frac{1}{N-|m|}\cdot(N-|m|)\,\Gamma\{p, p_{\mathsf{ref}}\} \\ &= \Gamma\{p, p_{\mathsf{ref}}\} \end{aligned} \tag{3.6}$$

To simplify things, the Fourier transforms of the pressure signals were computed and multiplied by one another:

$$\hat{G}(s) = \mathcal{F}\left[p\right]\cdot\mathcal{F}\left[p_{\mathsf{ref}}\right]^* \tag{3.7}$$

The cross-correlation is finally obtained by computing the inverse Fourier transform of the above product. The delay between the signals corresponds to the lag at which the sample cross-correlation reaches its first peak. The velocity signal is offset accordingly

before the phase averaging process starts.

3.3.1 Proper Orthogonal Decomposition

The Proper Orthogonal Decomposition attempts to extract, in a way, structures that typify the behavior of the flow as a whole. Originally, these modes are referred to as 'characteristic eddies' (Lumley (2007)). However, the procedure in itself does not attach any a priori physical interpretation to each mode. In other words, these modes do not necessarily correspond one-by-one to the phenomena underlying the physical data. So we cannot directly jump to conclusions based on the modes alone. In what follows, the now commonly used variant called Snapshot POD is used. The data consists of the phase-averaged velocity field $\mathbf{U}(\mathbf{x}, t)$ obtained using a hot-wire. The POD is performed on the fluctuating field $\mathbf{U}_f(\mathbf{x}, t) = \mathbf{U}(\mathbf{x}, t) - \overline{\mathbf{U}}$:

$$\mathbf{U}_f(\mathbf{x}, t) = \sum_{n=1}^{\infty} \mathbf{A}_n(t)\mathbf{\Phi}_n(\mathbf{x}) \tag{3.8}$$

The data matrix $\mathbf{U}_f$ is constructed by filling each row with the p samples measured at each of the q grid points. First, the $q \times q$ correlation matrix is constructed:

$$\mathbf{C} = \frac{1}{p-1}\mathbf{U}_f\mathbf{U}_f^T \tag{3.9}$$

The eigenvectors $\mathbf{\Phi}_n(\mathbf{x})$ and eigenvalues λ_n of the above correlation matrix represent the spatial functions and the energy contained in the corresponding mode, respectively. The time coefficients can be found by projecting the data matrix onto the corresponding spatial function:

$$\mathbf{A}_n(t) = \mathbf{\Phi}_n(\mathbf{x})\mathbf{U}_f \tag{3.10}$$

Finally, as mentioned before, each mode is the product of the time coefficient and the spatial mode:

$$\tilde{\mathbf{U}}_n = \mathbf{A}_n(t)\mathbf{\Phi}_n(\mathbf{x})^T \tag{3.11}$$

The eigenvalues are sorted in descending order, so that the fluctuations associated with the first modes are more significant than the rest from an energy standpoint. In other words, the eigenvectors represent the principal components of the data, also called the directions of maximum variance.

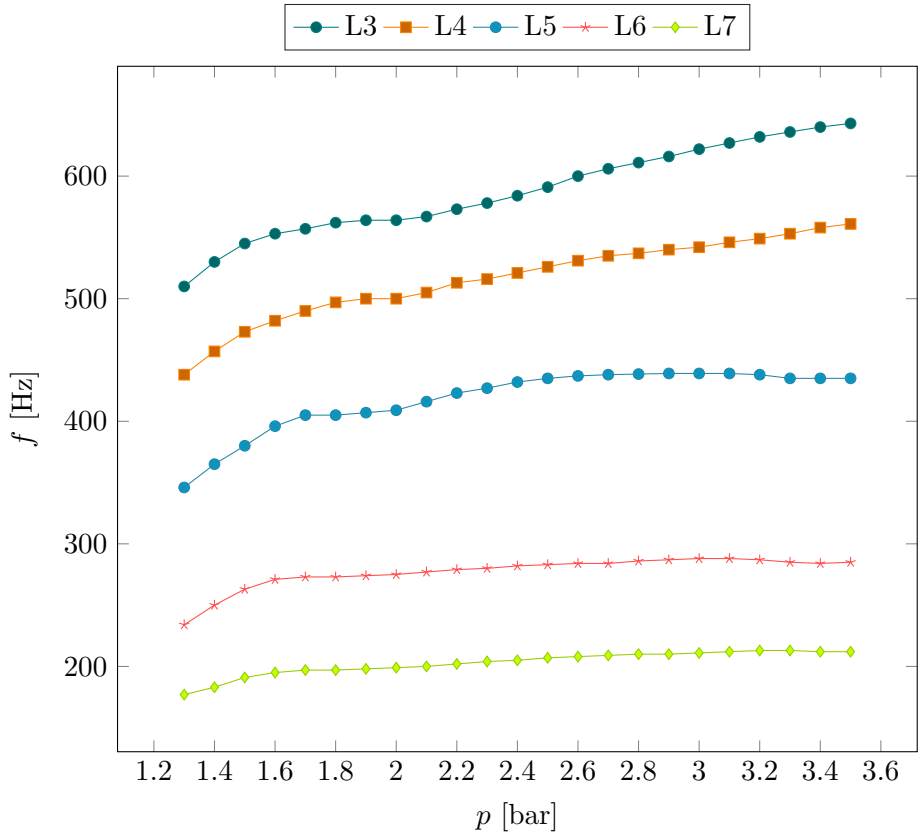

Figure 3.9: Frequency response of the L-prototypes to different inlet pressures.

3.4 Results I: Characterizing the PJAs

3.4.1 Frequency vs. inlet pressure

For the purposes of this section, the different cases are divided into three sets:

- First set: L3 through L7 (Figure 3.9)
- Second set: Ls3 through Ls7 (Figure 3.10)
- Third set: Lg0, Lg1 and L2 (Figure 3.11)

For the first set of cases, L3-L7, a relative supply pressure of 0.1 bar is enough to trigger jet switching inside the device. The frequency then increases steadily with inlet pressure up to around $p_{in} = 3.5$ bar then begins to level out. For cases L3-L5, the increase in frequency slows down at $p_{in} \approx 2$ bar before continuing its rise. The same occurs for L6 and L7 but is less noticeable.

For the second set, the feedback loop width W^* is less than half that of the first, which leads to a completely different frequency response. In Figure 3.10, the grey shaded area corresponds to the absence of pulsations. These prototypes require a pressure difference of at least 0.7 bar between the inlet and exit in order to function. Between the grey- and red-shaded area, cases Ls5-Ls7 have the same frequencies as cases L5-L7, respectively. Although the frequencies of Ls3 and Ls4 are lower frequencies than those of L3 and L4, they increase

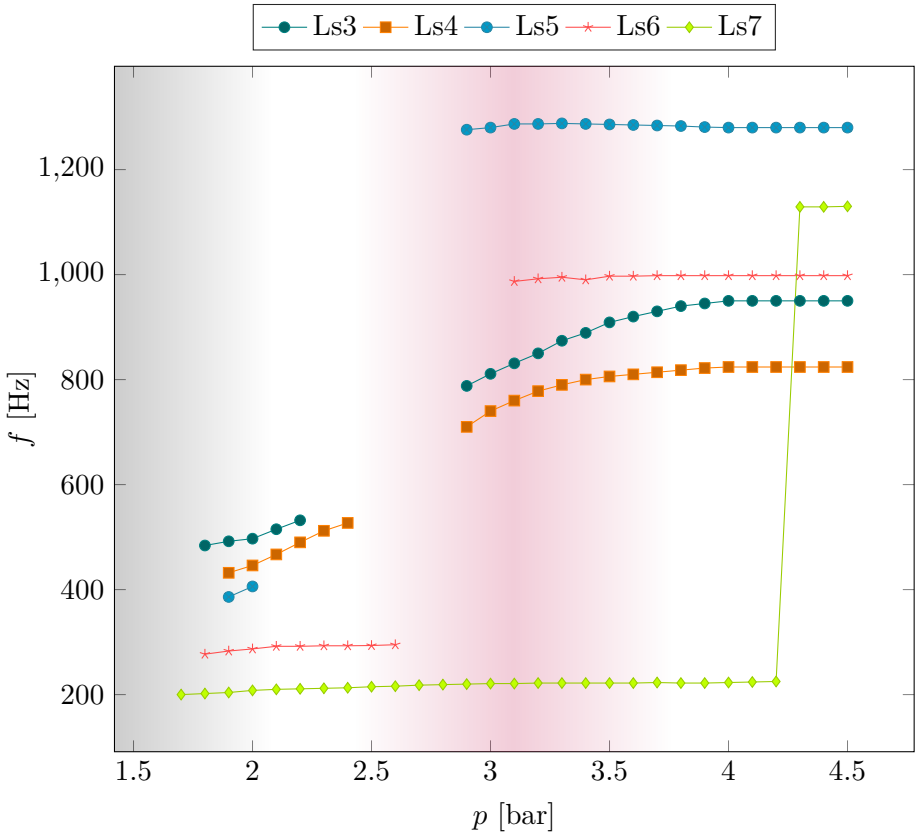

Figure 3.10: Frequency response of the Ls-prototypes to different inlet pressures.

at higher rate in this range of pressures. Right out of the red-shaded area, cases Ls5 and Ls6 reach constant frequencies that are about 3 times their values entering the red region. For cases Ls3 and Ls4, the frequencies continue to increase beyond the red region before reaching their respective final, constant values at around $p_{in} = 4\,\text{bar}$. Up to $p_{in} = 4.2\,\text{bar}$, Ls7 has the same frequency response as L7, meaning that at large FBL length L^*, the FBL width W^* does not significantly change the behavior of the device. At $p_{in} = 4.2\,\text{bar}$, Ls7 suddenly switches to a frequency that is around 5 times its value before that point. In the aforementioned red-shaded area, the prototypes erratically switch between the initial and final frequency in this region. Unlike Löffler et al. (2021), the transition between two pulsation regimes occurs irregularly, over a range of pressures, the only exception being Ls7. Furthermore, the response of the device is different after the transition. Although the frequencies of Ls5 and Ls6 are lower than those of Ls3 and Ls4 entering the red-shaded area, they become noticeably higher leaving it.

For the third set, the value of W^* for Lg1 is twice that of L2, while their FBL lengths are close. Although the frequency curves of Lg1 and L2 eventually converge for large enough supply pressures, there is a marked difference for lower pressures. Prototype L2 behaves similarly to cases L3-L7 in that its frequency increases with pressure, with a slight inflection point at around $p_{in} = 2\,\text{bar}$. On the other hand, the frequency curve of Lg1 peaks at around $p_{in} = 1.5\,\text{bar}$ with a frequency around 50% higher than that of L2 at

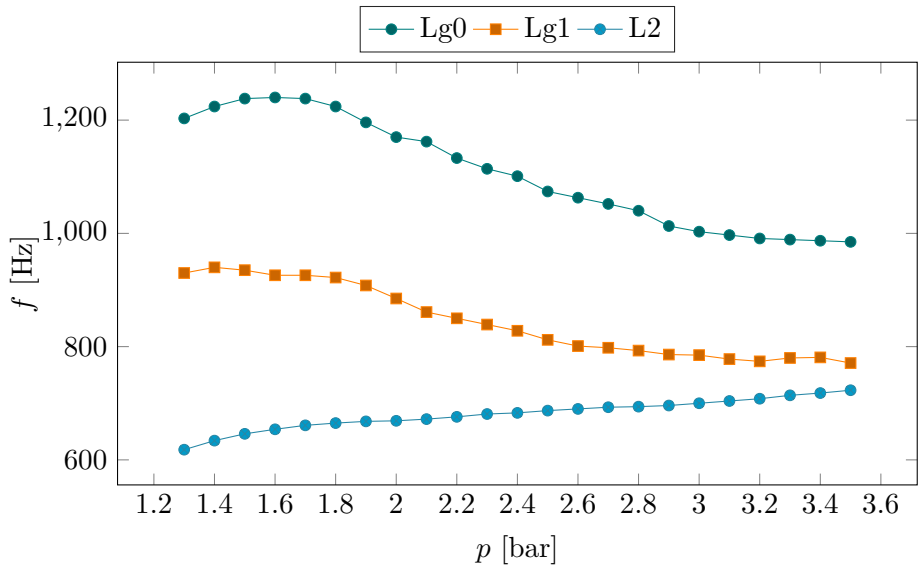

Figure 3.11: Frequency response of the L-prototypes to different inlet pressures.

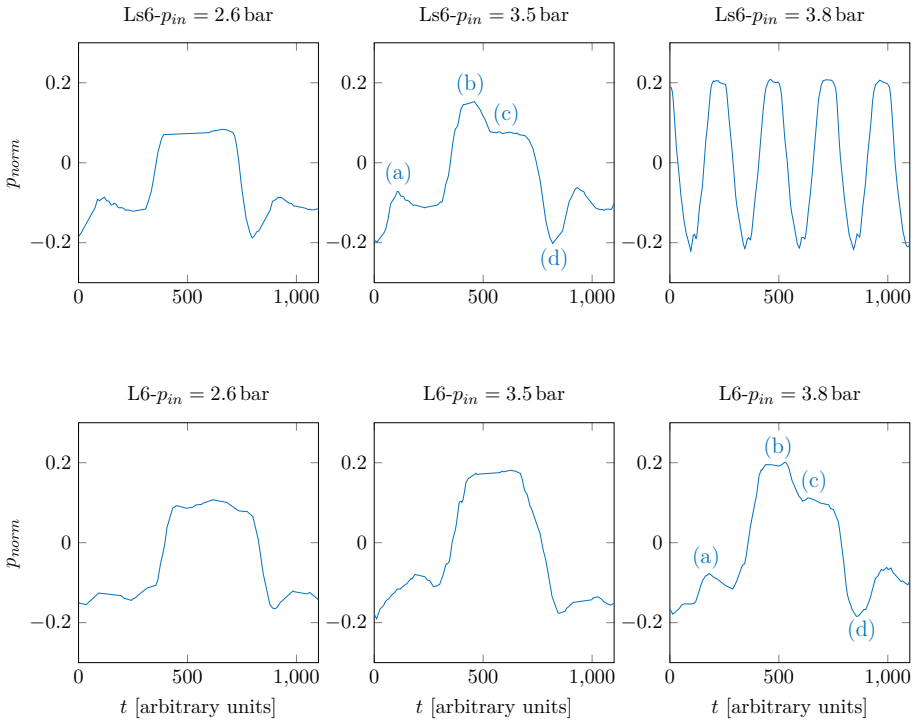

Figure 3.12: Pressure signal at the inlet of left feedback loop for two different models, Ls6 and L6

the same pressure. The frequency then decreases, approaching the value of L2 at high pressures. Finally case Lg0 exhibits the same behavior of Lg1 but at higher frequencies, which is expected considering that the only difference between these two cases is the value of L^*.

In Figure 3.12, the pressure fluctuates between two levels during which the corresponding side of the oscillator is on (high pressure) or off (low pressure). At $p_{in} = 2.6\,\text{bar}$, both models have the same frequency, the sole difference between the two pressure signals being a marked pressure peak for Ls6 during the off-time and a slightly lower pressure level during the on-time compared to L6. For a supply pressure of 3.5 bar, the frequency of the L6 increases slightly but remains stable. However, a peak in pressure during the off time can be seen. For Ls6, the high pressure level is no longer flat: pressure first rises to its maximum value (b) before decreasing to a lower plateau (c) and then plummets to its minimum (d) during the off-time. The passage from levels (b) to (c) on one side of the device corresponds to the pressure reaching (a) on the other. Although this was not verified experimentally, features (a) and (c) are assumed to be due to the interaction between the curved main jet and the splitter. The reattachment point is pushed downstream along the wall so that part of the main jet begins to feed into the other side before it completely switches. Features (a) and (c) appear progressively with increasing supply pressure while (b) becomes narrower. At this point, the frequency becomes unstable with short bursts of high frequency pulsations. These bursts become more predominant as we approach $p_{in} = 3.8\,\text{bar}$ when the device switches to a different pulsation mode where only features (b) and (d) remain. Although it remains to be verified, it seems that in this mode, the jet switches between the two branches of the device without attaching to either side.

At high enough values of p_{in}, the pressure signals from the L6 model begin to show the same features (a) and (c) described above, but the frequency remains stable as these feature evolve. No transition was observed in the pressure range available.

Early work on fluidic amplifiers have shown the role that the control-line impedance [3] plays in determining the switching time of the jet. For instance, Muller (1964) increased the flow gain of the amplifier [4] by increasing the impedance of the control-line *opposite* to the attachment side. Fluid entrainment by the attached supply jet results in a greater depression at the opposite control port when the corresponding control-line impedance is increased. This then lowers the minimal value of the attached-side control port flow rate needed for jet switching. This can be easily verified with the amplifier used in this study as the base model for the L-prototypes (Figure 3.4) by blocking the FBL entry ports and then alternatively blocking and releasing the control-lines. Blocking a control-line corresponds to having a resistance $R \to \infty$ while leaving it open corresponds to a low resistance. If one side is blocked while the other is free, the jet switches to the high-impedance side. Constricting the feedback loop, as is the case with the L- and Ls-prototypes, leads to an increase in control-line impedance. The precise effects of this increased impedance on the switching mechanism inside the present devices remains to be shown.

As mentioned before, the switching mechanism in the present model of the oscillator depends on both the returning flow at the control port and the pressure wave that travels back through the feedback loop and increases the pressure in the attachment branch. The design parameters of the feedback loops have an effect on both phenomena.

[3] in the present case, the feedback loop impedance

[4] defined as the ratio of the supply rate to the minimal control flow needed to cause jet switching.

3.4.2 Switching and travel time: L2-L7

The period of pulsation is determined by two quantities: the main jet switching time and the travel time of the pressure waves in the feedback loops. The switching time depends on the geometry of the interaction zone, in particular the aspect ratio of the main jet, the position, shape and angle of the splitter edge and reattachment walls as well as the inlet mass flow rate. It is also affected by the pressure in the control ports and the branches leading to the outlet. Both the strength of the pressure surge and its duration can determine the switching time (Muller (1964)). One variable aspect of main jet switching is the size of the recirculation bubble and the jet reattachment position during the attachment phase. The stronger the relative depression in the control port on the attachment side, the stronger the Coanda effect holding it to the wall. If the recirculation bubble is large enough, the main jet can interact with the splitter and part of it can be deflected to the off-side (as described earlier).

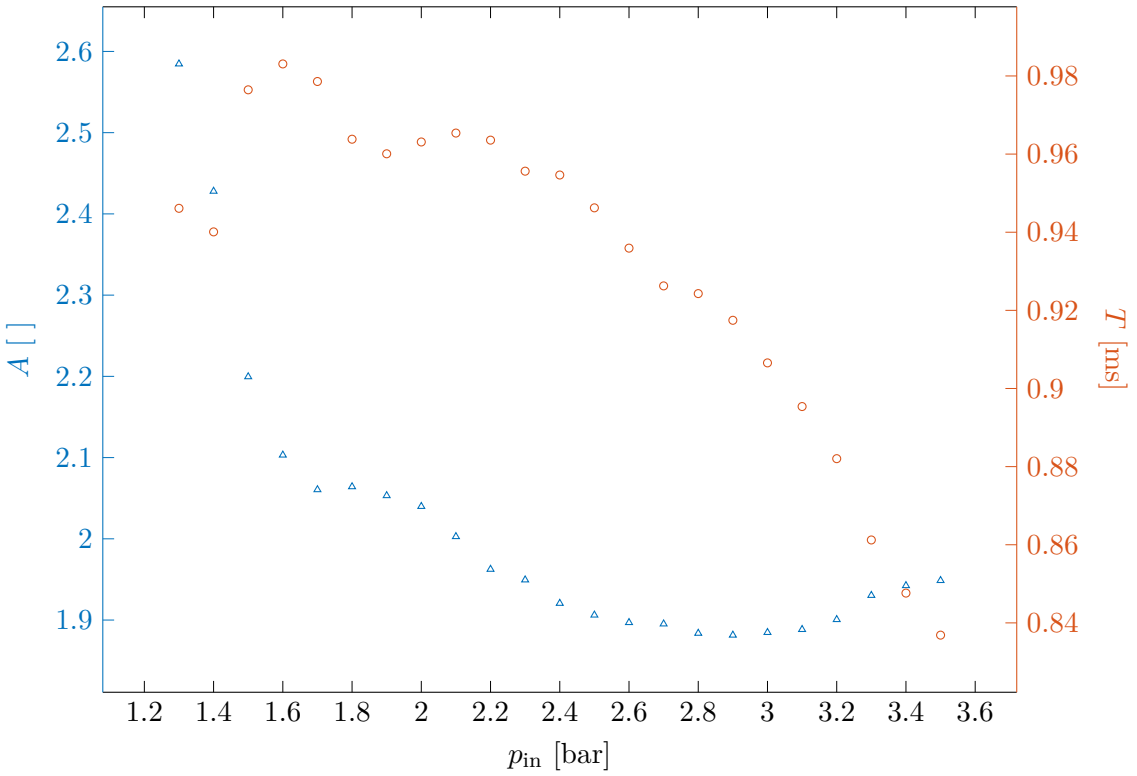

Figure 3.13: Travel length A (triangles) and switching time τ_{switch} (circles) versus supply pressure.

Wang (2017) showed that switching occurs after the pressure waves had traveled forwards and backwards through the feedback loops. The pressure at the control port is not enough to induce switching. The reflected wave must again reach the interaction, creating a pressure difference between the two branches that finally pushed the main jet to the other side. As a consequence, the period of pulsation of the device is equal to the time needed for the pressure wave to travel four times the feedback loop length L_f plus the switching time.

By neglecting the switching time (which in their case was around 1% of the period) and assuming that the speed of sound c remains roughly constant, they were able to estimate the frequency using:

$$f = \frac{c}{4L_f} \tag{3.12}$$

Löffler et al. (2021) used a modified Strouhal number $\mathsf{St}_{\mathrm{FBL}}$ based on the outlet jet velocity and feedback loop length, and the outlet jet Mach number $\mathsf{Ma}_{\mathrm{jet}}$ to scale their data. Their model is noticeably different from the ones used here and in Wang (2017), as it includes a secondary attachment wall, bent control lines and a sharp splitter between the feedback loop inlets and the outlet channels. They were able to collapse their data using the following expression:

$$\mathsf{St}_{\mathrm{FBL}} = a\mathsf{Ma}_{\mathrm{jet}}^{b} \tag{3.13}$$

without any underlying physical argument. The coefficients a and b depend on the pulsation mode of the device.

In the present work, we will adopt a general expression for the frequency that takes into account the variable switching time (Muller (1964)) and the possibility that, unlike Wang (2017), the jet switches before the reflected pressure wave travels back through the feedback loop. The frequency can be expressed as:

$$f = \frac{1}{\tau_{\mathrm{wave}} + \tau_{\mathrm{switch}}} = \frac{1}{AL_f/c + \tau_{\mathrm{switch}}} \tag{3.14}$$

where τ_{wave} is the total travel time of the pressure waves in both feedback loops and τ_{switch} the total switching time, which is the time required by the main jet to go from one branch to the other and then back during the second phase of the pulsation .The data from the previous section was fitted using this expression, with A and τ_{switch} as the model parameters (R^2 was consistently greater than 0.992). The value of A is close to 2 for inlet pressures greater than $1/0.527$. The switching time is close to 0.96 ms for low pressures, then starts to decrease for $p_{\mathrm{in}} \geq 1/0.527 \approx 1.9$ bar, reaching 0.84 ms for $p_{\mathrm{in}} = 3.5$ bar.

Nevertheless, without further information, it may not be possible to interpret the values of A for $p_{\mathrm{in}} \leq 1.9$ bar. If these values are correct, it could mean that the pressure at the control port must be maintained for a certain duration, allowing the recirculation bubble to grow and eventually detach the jet, before the reflected wave reaches the interaction zone. The fact that the value drops to 2 at around the point where the flow at the throat becomes choked may also be a hint. Most studies on jet switching, especially those performed during the fluidics era, only involve subsonic jets. To our knowledge, the transition to sonic and supersonic has not been explored as a topic in its own right.

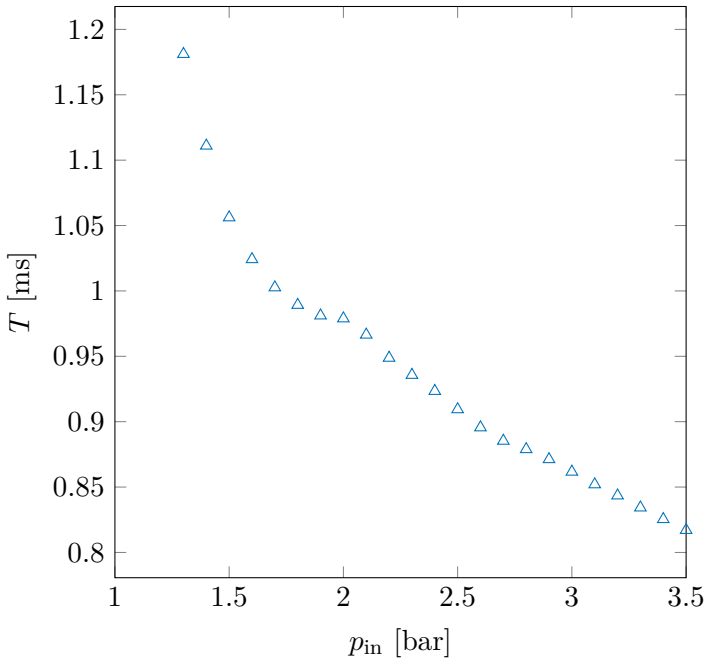

Figure 3.14: Switching time for case L2/L7 assuming $A = 2$.

Avoiding any speculation, a second fitting was attempted with A set to 2. The switching time decays for low pressures and seems to reach a plateau for $p_{\text{in}} \leq 1.9\,\text{bar}$ before taking an almost linear decline for higher pressures. Here again the coefficient of determination remains relatively high ($R^2 \geq 0.97$).

3.4.3 Numerical results: frequency

Numerical simulation were performed using a 2D URANS approach to supplement the experimental data. The details of the numerical simulations are elaborated in Chapter 5.

The peak in the Lg0 frequency curve The frequency curve of the Lg0 prototype presents a peak of 1240 Hz at $p_{in} = 1.6\,\text{bar}$ before reaching a stable value of around 970 Hz for $p_{in} > 3.5\,\text{bar}$. This peak can be attributed to a change in switching time which depends on the ratio of the control port pressure to the supply pressure p_c/p_s (Müller (1964)). In previous work on similar prototypes Wang et al. (2016), this peak did not appear since the switching time was negligible compared to the time needed by the pressure waves to travel across the feedback loops.

In Figure 5.4, the frequency curves of the Lg0 prototype simulated using two different turbulence models are compared to experimental data. Both turbulence models were able to capture the final frequency (corresponding to $p_{in} \geq 3.5\,\text{bar}$) to within 5% of the experimental value. At lower pressures, the gap between the numerical and experimental results becomes more evident as the simulations fail to reproduce the frequency peak at $p_{in} \approx 1.7\,\text{bar}$.

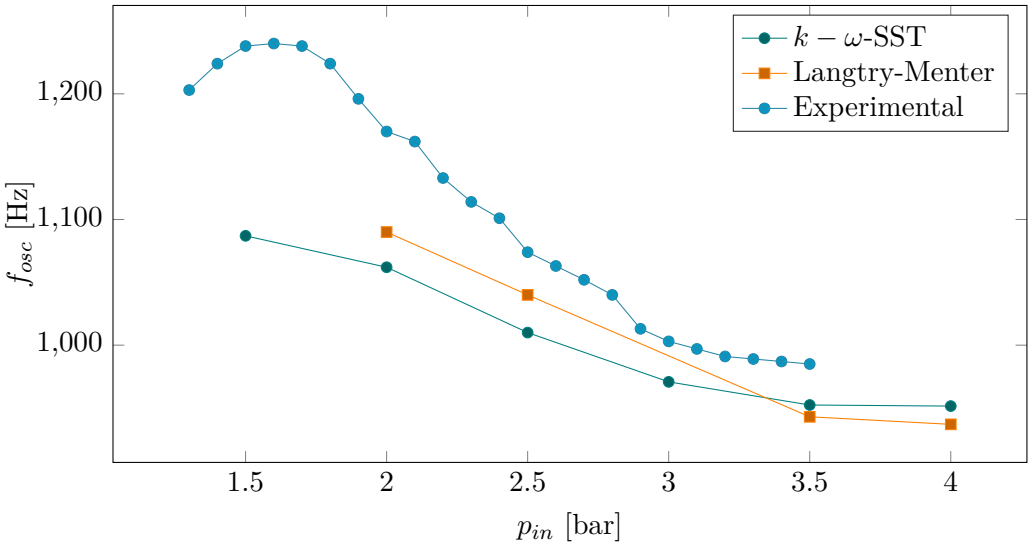

Figure 3.15: Frequency response of Lg0 from numerical results (2D $k-\omega$ SST and Langtry-Menter) and experimental results.

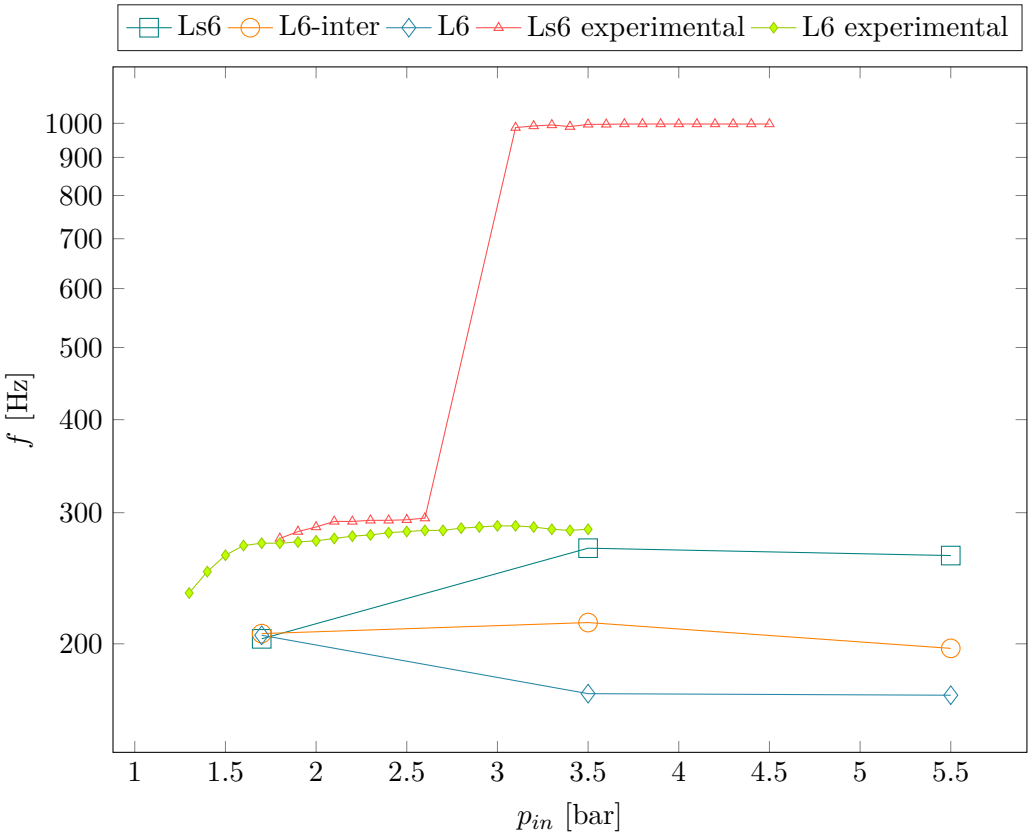

Figure 3.16: Frequency of the oscillator from numerical results ($k-\omega$ SST) as a function of inlet pressure p_{in} and dimensionless FBL width W^*

Figure 3.17: Detail of the model (Ls6) used for the simulations.

Dependence of frequency on the FBL width W^* Two-dimensional models corresponding to L6 and Ls6 were simulated for three inlet pressures $p_{in} = 1.7$, 3.5 and 5.5 bar along with an additional case, L6-inter, with an intermediate value of W^*. For $p_{in} = 3.5$ and 5.5 bar, constricting the feedback loop leads to an increase of up to 50% in frequency between cases L6 and Ls6 (Figure 3.16). The change in frequency is not comparable to what was observed experimentally. Regardless, to explain the increase in frequency in the numerical simulations for Ls6, we have looked at the pressure fluctuations at the control ports and along the control line (Figure 3.18). As the width of the feedback loop is decreased, the pressure fluctuations at the control port and in the wide channel ahead of it decrease significantly with the nondimensional standard deviation going from 0.33 to 0.245 for L6 and Ls6 respectively. As a consequence, the difference in pressure between the left and right control ports is diminished, thus weakening the attachment of the main jet, by virtue of the Coanda effect, to the lateral walls of the interaction zone. A slight increase in pressure is also observed, which further prevents the main jet from fully attaching to the wall. This then results in a decrease in the switching time and an increase in oscillation frequency. The reason for the weakened pressure fluctuations can be found in the wide channel preceding the control port (Figure 3.17). This part of the feedback loop starts to act as a capacitance the more its inlet and exit are constricted, making it possible to leverage it as a new design parameter that would allow us to shape the frequency response of the oscillators.

We can also compute the time during which the recirculation bubble grows before switching occurs as well as the maximum reattachment length on the side wall (Figure 3.19). As W^* decreases, both the switching time $\tau_{\text{switch}}/2$ and the reattachment length decrease. For $p_{\text{in}} = 5.5$ bar, the frequency increases from 170 to 268 Hz when W^* is reduced from 16 to 8 (Figure 3.16). This can be attributed solely to the change in switching time. Between Ls6 and L6, the total switching time increases by $\Delta\tau_{\text{switch}} = 2.28$ ms. By subtracting this duration from the period of pulsation of L6, we get $1/f - \Delta\tau_{\text{switch}} = 1/170 - 0.00228 = 3.6$ ms which roughly equals the pulsation period of Ls6, i.e. $T_{\text{Ls6}} = 1/268 = 3.7$ ms.

In spite of the large value of p_{in}, the simulated model did not switch to the second pulsation mode identified earlier. In addition, the values of the frequency in the primary

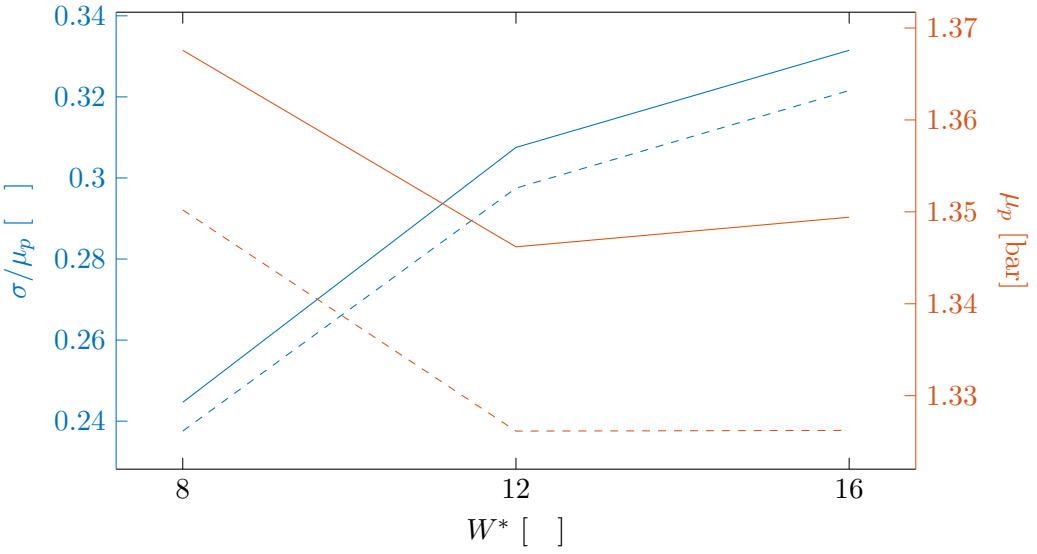

Figure 3.18: Nondimensional standard deviation σ/μ_p and mean value μ_p of pressure inside the large channel ahead of the control port (solid lines) and at the control port (dashed lines) for $p_{in} = 5.5\,\text{bar}$.

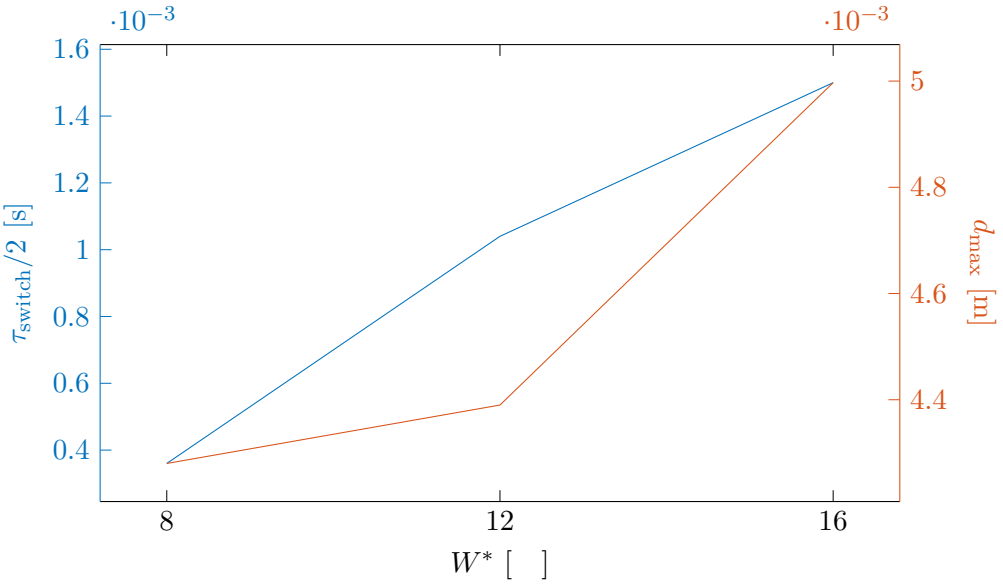

Figure 3.19: Switching time $\tau_{\text{switch}}/2$ and maximum attachment distance for different values of W^* (L6, $p_{\text{in}} = 5.5\,\text{bar}$).

mode do not match experimental values, as was the case with Lg0. This leads to the conclusion that, even though the physical model has an aspect ratio of 35, a 2D URANS model is not suited to predict the complex behavior of the oscillator in response to certain design parameters. More specifically, the dynamics of jet switching cannot be replicated with these models.

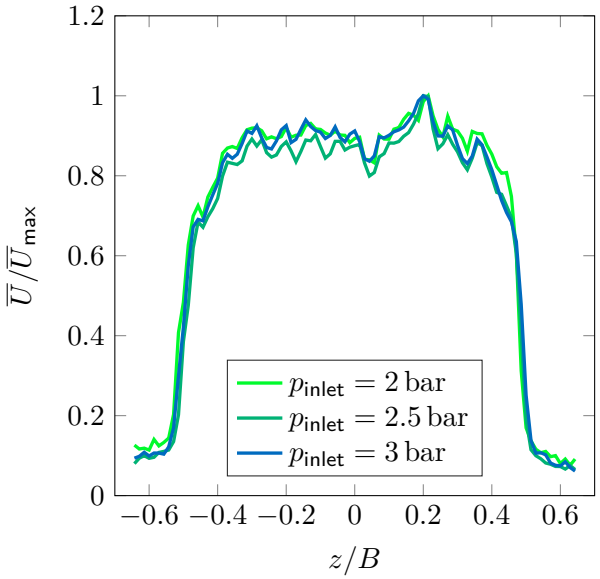

Figure 3.20: Velocity measurements along the length of the exit slots for different inlet pressures at $y/D = 0.5$ and $x/D = 0$ (in this case, Lg0). ($z/B = 0$ corresponds to the center of the slot in the z direction).

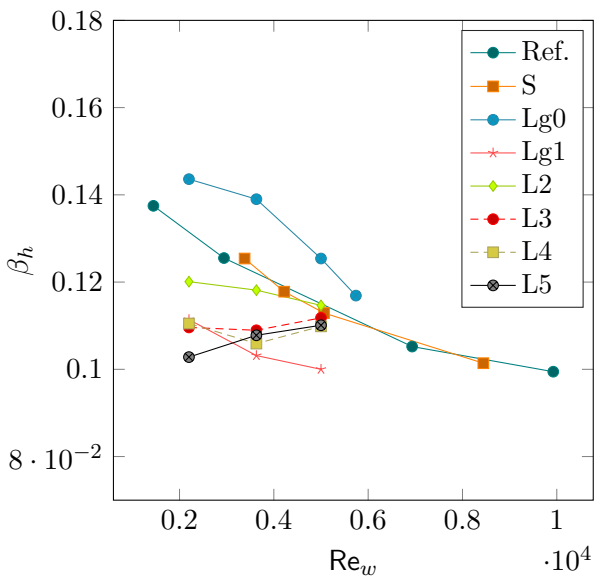

Figure 3.21: Expansion ratio as a function of Reynolds number (based on the exit jet width w) for different pulsation frequencies. Data from an equivalent steady case and a reference study (Deo et al. (2008)) are also included.

3.5 Results II: Flow field characteristics

3.5.1 Length-wise hot-wire measurements

Before performing measurements on the pulsed jets produced by the devices, velocity measurements were taken along the length of the exit slots. The hot-wire was placed along the z-direction in a position where the length-wise velocity profile is relatively uniform. As an example, the normalized velocity profile for the Lg0 is shown in Figure 3.20 (where U_{max} is the maximum velocity for each inlet pressure). These profiles obtained at different inlet pressures have the same form. Noticeable deviations from the ideal flat profile (roughly in the region $0.1 < z/B < 0.3$) are attributed to printing defects inside the exit channels of the oscillator. The left side of the profile shows less fluctuations and so the 1 mm-long hot-wire was kept between the positions $z/B = -0.4$ and $z/B = 0$ for this particular case. A similar procedure was also applied for the other configurations.

3.5.2 Average velocity field and jet development

Based on dimensional arguments and self-preservation assumptions regarding the lateral velocity profiles of free turbulent jets, it can be shown that a lateral characteristic length scale of the jet ℓ grows linearly with axial distance y from the jet orifice (Tennekes and

Lumley (1972)):

$$\frac{d\ell}{dy} = A \tag{3.15}$$

for the self-similar solution of a plane jet with constant mean velocity. The authors take $A = 0.078$ based on experimental results from the literature. Rajaratnam (1976) defines the width of the jet b as the distance from the jet axis at which the average velocity is half the centerline velocity. From the Tollmien and Goertler solutions of the moment equation of the average velocity, the author shows that the ratio $C_2 = b/x$ is equal to 0.097 and 0.114 respectively. Furthermore, Lee and Chu (2003) cite experimental work that placed the expansion ratio (also called spreading rate) β_G of the jet between 0.1 and 0.154. It was assumed that the velocity profile $u(x)$ has a Gaussian shape, and that its width corresponds to the Gaussian curve's standard deviation (hence the subscript G).

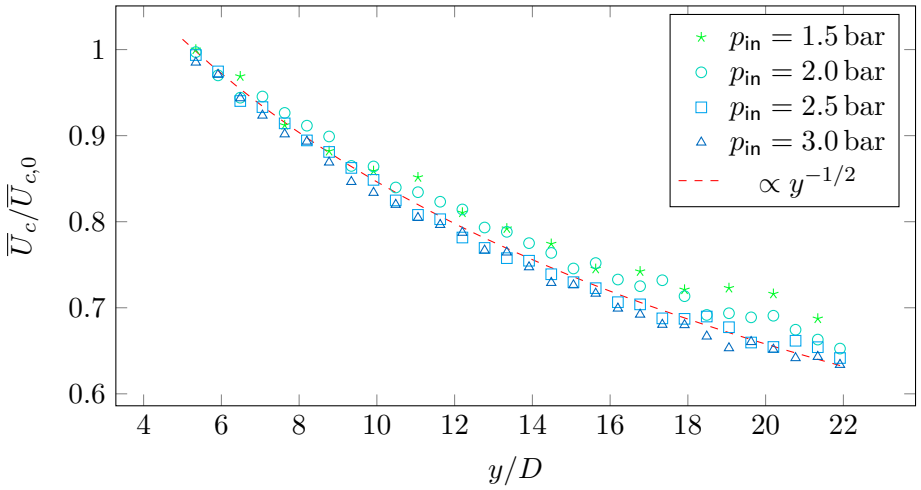

Figure 3.22: Normalized centerline velocity as a function of axial distance for Lg0. $\overline{U}_{c,0}$ is the initial average centerline velocity.

Kotsovinos (1976) notes that, based on previous findings, the spreading rate does not depend on the aspect ratio of the slot. Furthermore, the investigator shows that the growth of the half-width is not linear at large axial distances which explains the disparate results found in the literature. The author also notes that the range of axial distances considered are not usually the same. However, the author does not offer a concrete justification for this increase of spreading rate, but hypothesizes that it may be due to relaminarization of the flow at large downstream distances. Bradshaw (1977) rejected this suggestion, showing that background turbulence due to the recirculating flow of the jet, rather than natural draught, is likely the culprit. In addition to background turbulence, Ribeiro and Whitelaw (1980) attributed disparity in jet spreading rate to the flapping motion of the jet.

The hot-wire measurements allow us to reconstruct the average velocity field and to deduce the spreading rate of the jet. The width of the jet, defined as the width of the average velocity profile at half the peak height changes along the jet axis. The measure-

ments start out at a distance of $5D$ from the slot. At around $y = 8D$ the jet starts to expand linearly and so the expansion ratio β_h, based on the half-height width of the velocity profile, is found by performing a linear fit of the data starting at this point. The results are presented in Figure 3.21 for the steady and pulsating jets along with results from Deo et al. (2008) for steady jets. The spreading rates for the steady jet nearly overlap with the values found in the reference paper. The slight discrepancies can be explained by the fact that the experimental setups are noticeably different, especially with regards to the aspect ratio of the slot, being equal to $AR = B/D = 60$ in Deo et al. (2008) and $AR = 10$ in the present study. By pulsating the jets, the expansion ratio decreases by about 15 to 20%, except for the Lg0 case where it increases.

For all of the cases, the centerline velocity, because of self-similarity and conservation of momentum, decreases at a rate proportional to $y^{-1/2}$ for sufficiently large axial distances as shown in Figure 3.22. However, studies such as Béra et al. (2001) found an inflection point in the velocity decay curve for pulsed jets which were attributed to vortex pairs. This phenomenon was not observed in any of the cases presented here.

3.5.3 Lateral instabilities: puffing and flapping motion

The boundaries of a plane jet can move either simultaneously (both outwards or inwards with respect to the jet center) or opposite to one another. In the first case 'puffs' of air (or 'velocity packets' Janetzke et al. (2008)) can be seen in the flow traveling downstream from the jet orifice. In the latter, a 'flapping' motion can be observed which causes the center of the jet to move back and forth in the lateral direction. A study by Goldschmidt and Bradshaw (1973) was one of the first to show that steady plane jets can exhibit this flapping motion.

In the present study, the centerline of the jet was found by detecting the lateral position of the center of the velocity profile of the jet at each axial location. In Figure 3.23 two representative cases were chosen to illustrate the behavior of the jet centerline. In Figure 3.23a, the centerline position of the Lg0 at $p_{\mathsf{in}} = 3.0\,\mathrm{bar}$ remains nearly the same for $y/w = 5 - 26$. This is also the case for the remaining Lg0 configurations considered here. On the other hand, for the L3 case with $p_{\mathsf{in}} = 2.0\,\mathrm{bar}$ (Figure 3.23b), a clear back and forth motion of the centerline can be detected starting at $y/w = 10$ and having a maximum amplitude of two jet widths at around $y/w = 20$. This flapping motion is also found in the L3 at $p_{\mathsf{in}} = 1.5\,\mathrm{bar}$ and becomes less prominent as the inlet pressure or jet Reynolds number is increased.

On the other hand, puffing can be detected as a peak in centerline velocity that travels along the jet axis. This phenomenon was only observed for the Lg0 at $p_{\mathsf{in}} = 1.5\,\mathrm{bar}$ and the L3 at $p_{\mathsf{in}} = 1.5$ and $2.0\,\mathrm{bar}$. To illustrate this, the centerline velocity distribution at different phase angles during a single pulsation is shown in Figure 3.24. In the first few frames, the velocity of the Lg0 at $y/w = 5$ starts to increase until $\phi = 130°$. As the initial velocity decreases, a wave is seen traveling from left to right until its peak is outside the measurement domain at $\phi = 330°$. For all the other cases, where no puffing

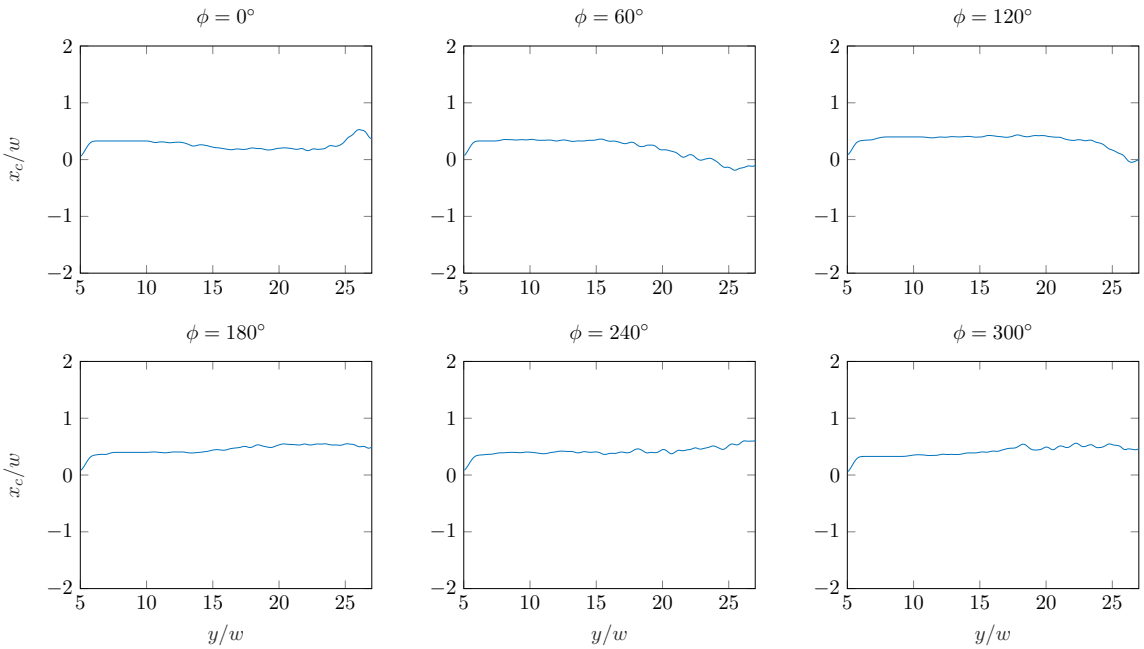

(a) Lg0 oscillator jet $p_{\text{in}} = 3.0\,\text{bar}$

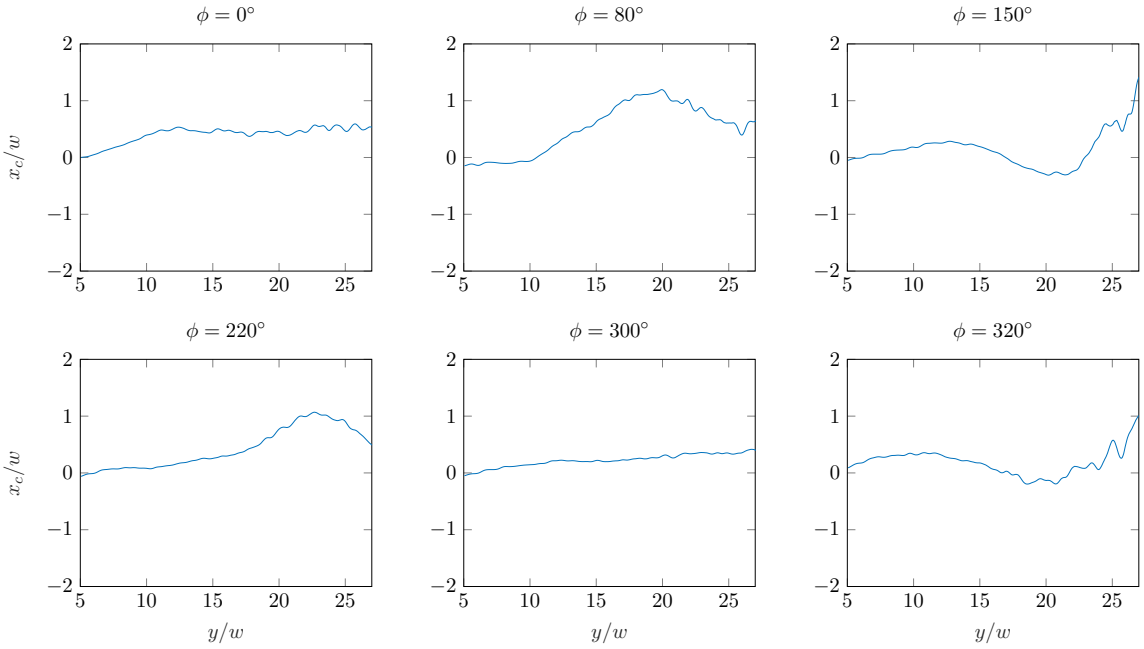

(b) L3 oscillator jet $p_{\text{in}} = 2.0\,\text{bar}$

Figure 3.23: Position of the center of the velocity profile as a function of axial distance for various values of phase angle ϕ. In (a) the axis of the jet produced by Lg0 is relatively stable whereas in (b) the axis of the jet moves about the centerline with an amplitude of up to one initial jet width w.

was detected, the centerline velocity decreases monotonically with distance from the jet orifice and remains so throughout each pulsation.

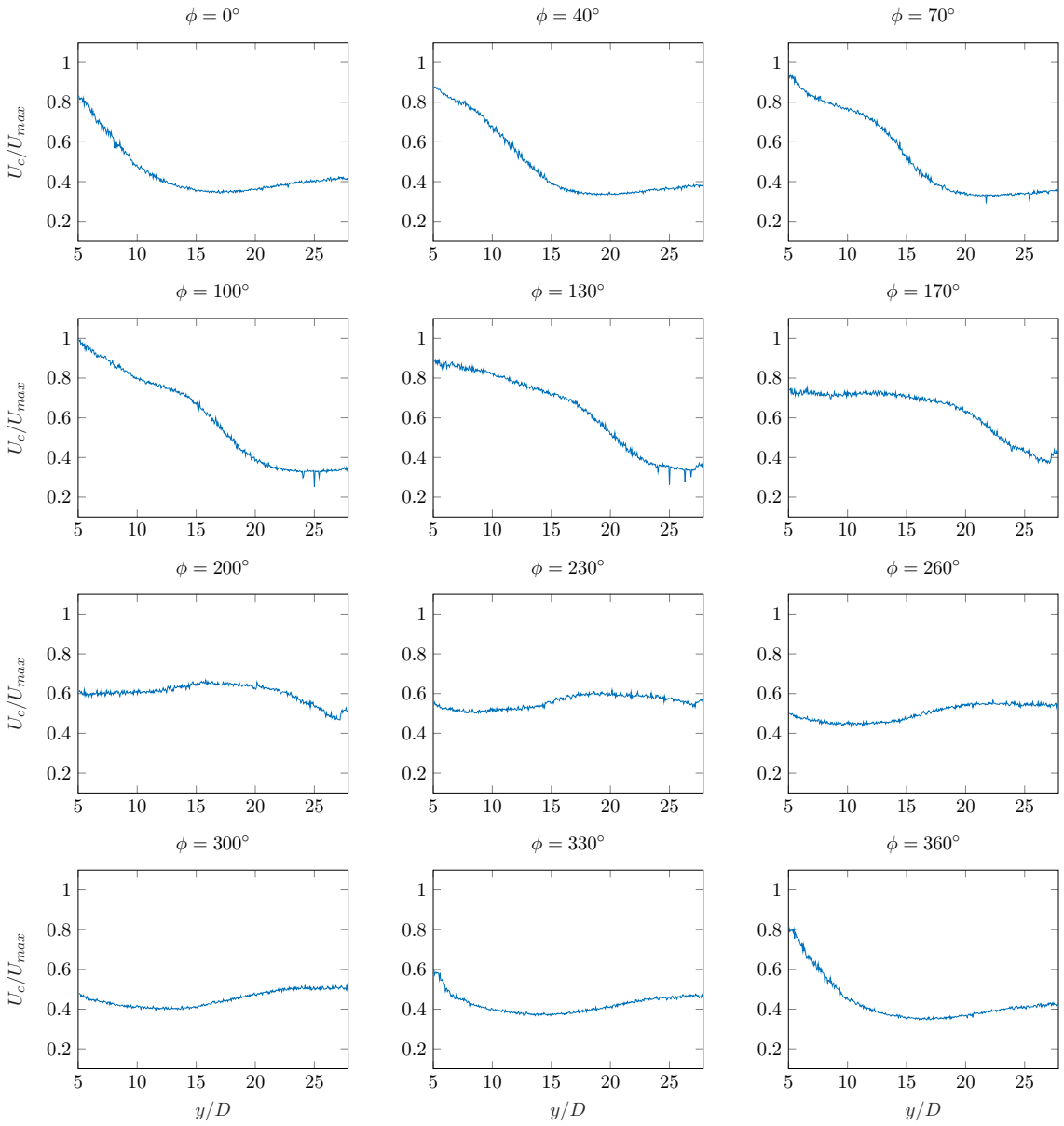

Figure 3.24: Centerline velocity along axial distance y/w at different phase angles for the Lg0 at $p_{\mathsf{in}} = 1.5\,\mathrm{bar}$

3.5.4 Evolution of vortex dipoles

Vortices in the flow, either coherent or incoherent, have an influence on jet impingement heat transfer. Using the conditional sampling method (phase-averaging), it is possible to spatially reconstruct the flow and deduce some of its vortex structures. Using the aforementioned measurement method, we were able to detect large vortex pairs that develop as they are convected along the jet axis. Finding the size, convection velocity and trajectories of these vortex pairs and how they change with both frequency and jet velocity is crucial to understanding heat transfer results later on in this work.

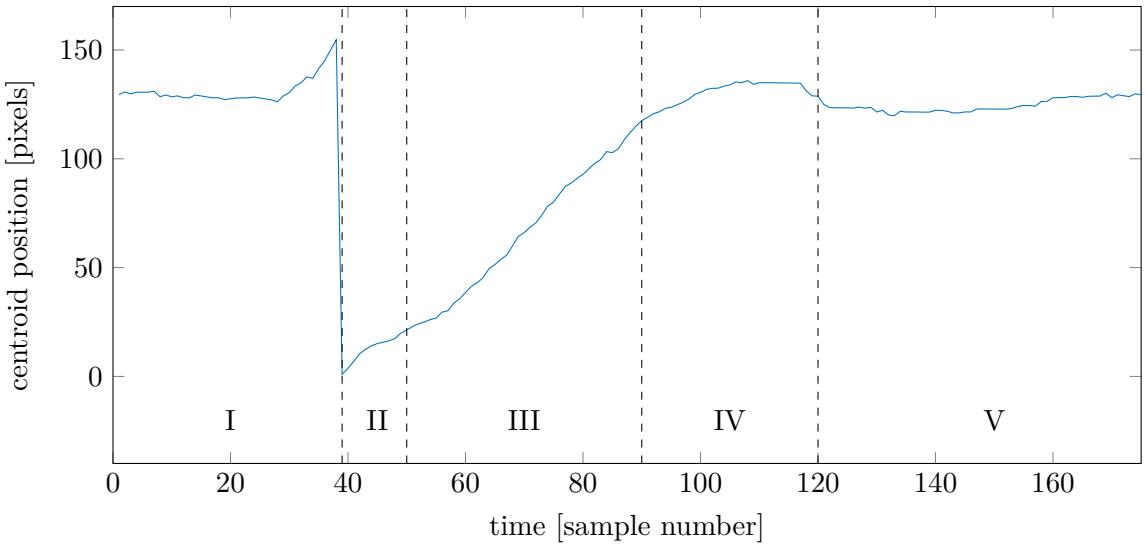

Figure 3.25: Axial location of the centroid of the 'detected' vortex dipole during a pulsation period. I: no ellipse is detected, II: ellipse detected, partially outside the frame, III: ellipse detected, entirely inside the frame, IV: the ellipse begins to leave the frame, V: ellipse outside the frame. The data used to produce this example is from the L3 case with $p_{\text{in}} = 2\,\text{bar}$.

Vortex rings, which are the axisymmetric equivalent of vortex dipoles, are of interest to a number of scientific communities. In their review on the subject, Shariff and Leonard (1992) mentioned the utility of this phenomenon in engineering applications such as underwater drilling, fighting oil well fires and understanding aircraft downbursts. In biology, some sea creatures depend on vortex rings for locomotion whereas dolphins blow vortex rings and swim through them for mere amusement. Studying vortex rings often depends on finding their formation time, the volume of surrounding fluid that they entrain and their convection velocity. Although vortex rings can appear naturally as a consequence of flow instability, it is often the case in engineering applications that we need to produce them at will. As mentioned by Steinfurth and Weiss (2020), most studies use a piston-cylinder assembly to produce starting jets. This sudden injection of fluid induces the formation of vortex rings that are accompanied by a trailing jet. The nascent ring continues to develop until it separates from the trailing jet (a phenomenon called 'pinch-off') at which point its size remains stable.

In two-dimensional flows, applying a force to the fluid produces vortex dipoles, i.e., a pair of counter-rotating vortices, that are analogous to vortex rings but have been shown to behave differently. For instance, Afanasyev (2006) showed that unlike vortex rings, the vortex dipoles do not separate from the trailing edge for the range of stroke lengths considered, although the author does not preclude the existence of a "pinch-off time" beyond which separation occurs. They also set up a simplified model that describes the growth and subsequent translation of a 2D dipole. The dipole begins by expanding through absorption of the injected fluid from the nozzle. The dipole then starts translating with a

speed $U_f = U_{\text{jet}}/2$. This result was then confirmed experimentally by the authors.

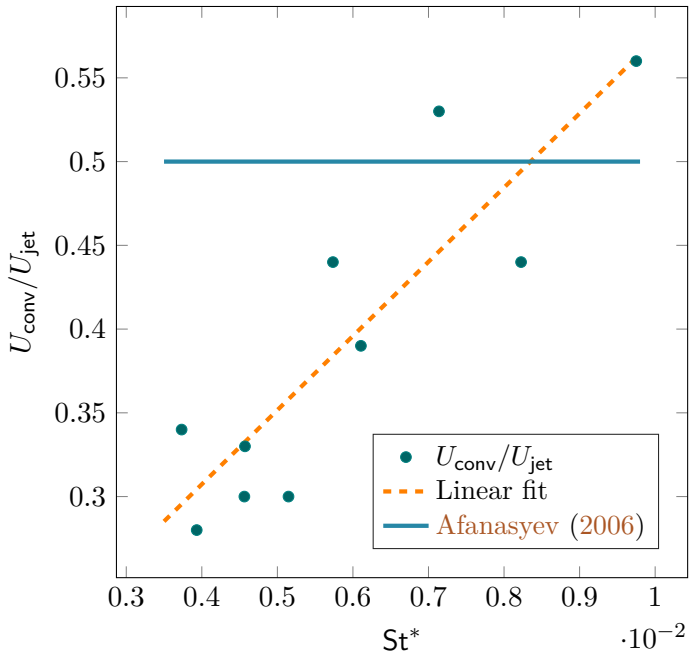

Figure 3.26: Normalized convection velocity of vortex dipoles as a function of jet Strouhal number

In the present study, the reconstructed velocity field is used to detect the vortex dipoles which manifest themselves as elliptical regions of non-zero velocity that appear during the injection phase of the pulsation. Basic image processing is used to detect the elliptical shape and track the position of its center and its major and minor axes. This procedure is applied to the entire pulsation period and the position of the ellipse is plotted against time; an example is shown in Figure 3.25. When the vortex dipole is in the frame, the position of its center increases linearly with time (region III). A linear regression is done on part III of the data in order to deduce the convection velocity of the dipole. The remaining data cannot be used since the dipole is partially outside the frame and so the algorithm cannot properly detect the elliptical shape. The computed convection velocity is then divided by the average velocity of the exit jet and plotted against the Strouhal number $\mathsf{St} = fw/U_m$(Figure 3.26). Although the number of points available is relatively small, the non-dimensional convection velocity seems to increase with the Strouhal number, beginning with $U_{\text{conv}}/U_{\text{jet}} = 0.28$ and reaching about 0.55 which is close the value found by Afanasyev (2006).

3.5.5 Three-dimensional view of vortex dipoles

Impulsively started jets and pulsed jets are often produced by a piston-cylinder configuration. Steinfurth and Weiss (2020) noted that pulsed jet actuators, such as a solenoid valve or a fluidic oscillator, have a larger over-pressure at the jet outlet plane than do the piston-cylinder configurations. This leads to a highly nonparallel flow.

The evolution of the flow field during a single pulsation is presented for L4 (Figure 3.27). The remaining configurations for which dipole formation occurs exhibit a similar behavior, so for the sake of brevity only the flow field pertaining to L4 is shown. The flow field is shown as a set of isosurfaces of velocity magnitude. Warmer colors and higher opacity indicate higher values of the velocity. The origin of the jet outlet plane is at $(x/w, y/w, z/w) = (0, 0, 0)$, and is not shown here. The velocity of the jets starts by decreasing (Figures 3.27a-3.27c) as the main jet inside the oscillator switches to the other branch. This sudden change produces a lump of relatively high velocity which persists after the jet switches off and travels axially until it exits the measurement domain (Figures 3.27d-3.27f). As noted earlier, during the off-time, the deflected main jet leaks into the unattached side, slightly raising the pressure at the inlet of the feedback loop and prematurely increasing the velocity of the corresponding jet. This increase results in a small puff of air, of indeterminate shape, that travels along the jet axis before briskly dissipating into the surrounding fluid (Figures 3.27g-3.27i).

As the main jet inside the device starts to switch, the velocity begins to rise (Figures 3.27j-3.27l). A lateral bulge (along y/w) can be seen as the jet is impulsively started, especially in the outer isosurfaces (Figures 3.27m-3.27o). This feature travels along the jet axis before exiting the measurement domain (Figure 3.27p). The jet finally reaches its maximum velocity (Figure 3.27q and 3.27r) before the whole process repeats itself. The lateral bulge described above is a manifestation of the vortex dipole described earlier in the chapter. It is possible to isolate this feature from the flow using Proper Orthogonal Decomposition (*cf.* appendix to this chapter, Figure 3.28). Unlike Steinfurth and Weiss (2020) who observed a vortex ring at sufficiently long distances from the jet outlet plane (approximately 40 jet widths downstream), the two vortices here remain distinct on each side of the jet, at least within the current measurement window.

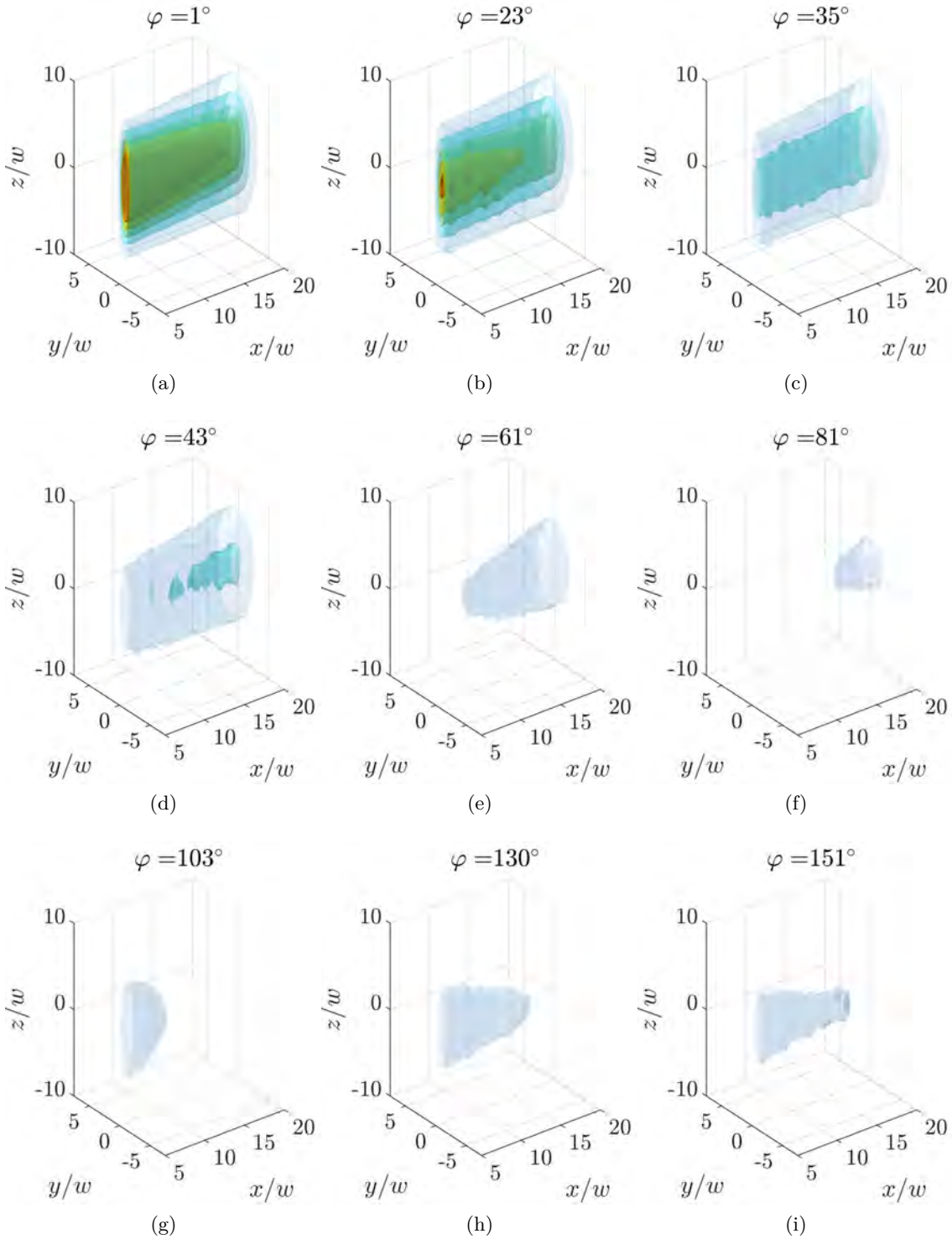

Figure 3.27: Velocity isosurfaces of the pulsed jet produced by L4 for $p_{\text{in}} = 2\,\text{bar}$. The opacity of the isosurfaces is proportional to the corresponding value of the velocity magnitude.

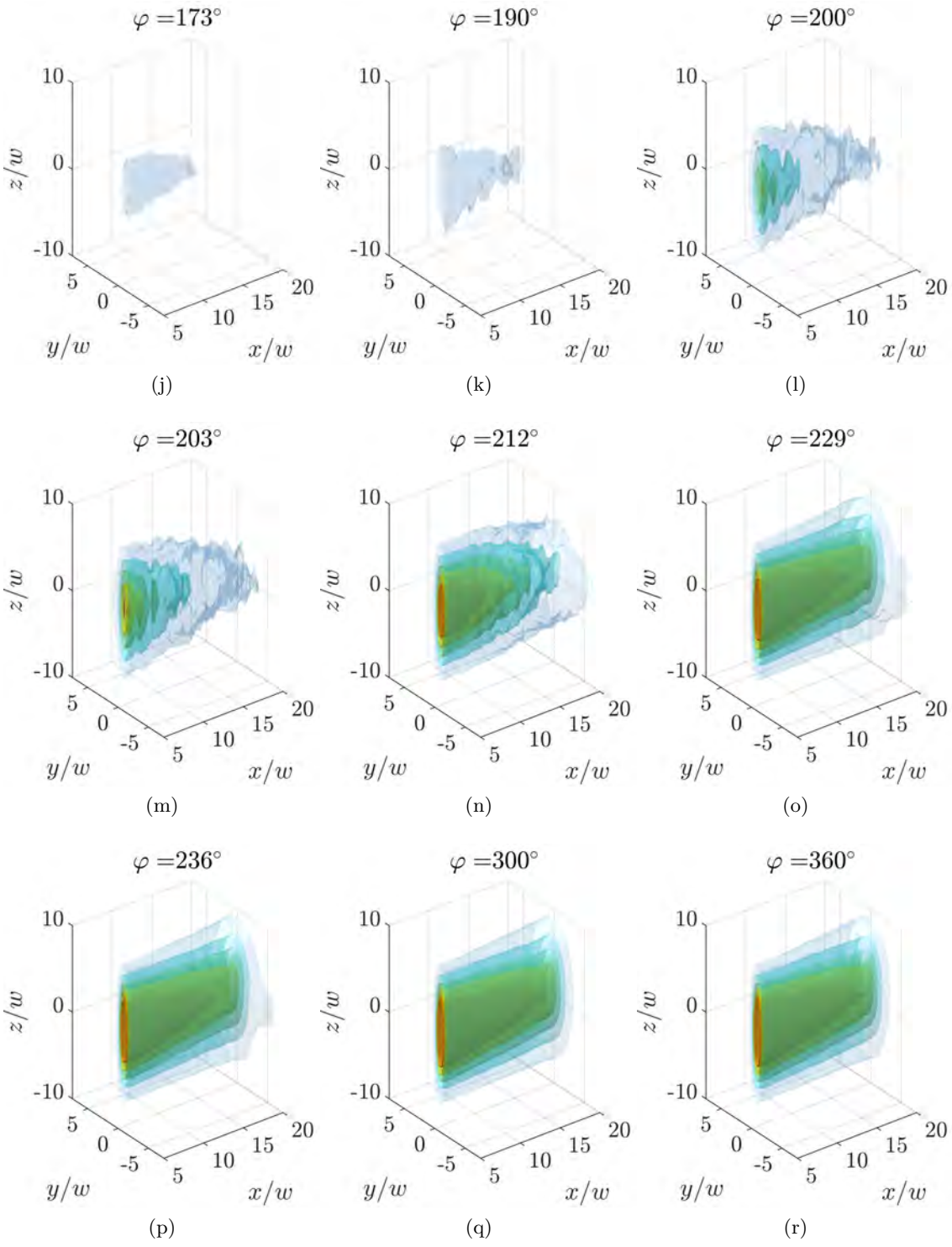

(j) (k) (l)

(m) (n) (o)

(p) (q) (r)

Figure 3.27: (cont'd)

3.6 Concluding remarks

This chapter has dealt with the characteristics of the Warren fluidic oscillators and the pulsed flow that they produce. The response of the device to changes in design parameters was assessed. It was found that the pressure wave traveling from the interaction zone, through the feedback loop and to the control port was enough to provoke main jet switching. This was not the case for a similar device studied by Wang (2017) in which the pressure waves have to travel twice across each loop thereby doubling the total travel time. For the devices studied in the present work, the switching time was found using the frequency data as a function of inlet pressure. It was observed that the switching time rapidly decreases for low pressures, seeming to reach a constant value just before $p_{\text{in}} = 2\,\text{bar}$. Beyond this point, however, the switching time continues to drop linearly.

In addition, it was found that narrower feedback loops allowed the device to switch to a different pulsation mode which is characterized by a significantly higher frequency. The transition between the primary mode and the high frequency mode seems to be chaotic and occurs over a range of inlet pressures.

Following this assessment, the external flow field at the outlets of the device was examined using hot-wire anemometry. Using pressure transducer flush-mounted onto the feedback loops, the phase-averaged velocity field was reconstructed via conditional sampling. Classical jet characteristics were computed, such as the jet expansion rate and the velocity decay profile, for both the pulsating cases and a reference steady case. Jet flapping was only observed in lower frequency cases, while the higher frequency cases exhibited a puffing motion along their axes.

The same data was also used to detect vortex dipoles in the flow. These were observed for cases L2-L7 and their convection velocity was shown to depend on the jet Strouhal number, whereas a previous study (Afanasyev, 2006) had shown that the convection velocity remains equal to half the average jet velocity at the jet exit plane. Finally, 3D measurements were performed that showed that the two vortices remain separate on each side of the jet and do not coalesce into a vortex ring within the measurement window which extends about 20 initial widths downstream from the exit plane of the oscillator.

3.7 Epilogue: Modeling the flow using data-driven methods

Data-driven methods for decomposing the velocity field into its constituent phenomena are presented next. The theoretical development behind these methods are deferred to Appendix B.

Data-driven modeling, under its many guises, is gaining ground in physical sciences. The ability to gather large amounts of data from experiments or even simulations and the development of powerful processing machines have enabled the use of these methods. Modal decomposition is one such class of techniques that is widely used in fluid mechanics, and finds one of its earliest expressions in the Proper Orthogonal Decomposition (POD, Lumley (2007)). POD decomposes the data into constituent modes and orders them by

energy content. Although a large number of modes can coexist, it is often the case that only a small subset dominates the flow dynamics and can be used to reconstruct the whole system. Nevertheless, the energy containing modes are not necessarily the most important ones.

Dynamic Mode Decomposition is a more recent development that also attempts to extract meaningful information from measured data. This technique assumes that the dynamical system is approximately linear for a large enough sample of data, such as snapshots of a flow fluid evolving in time. In other words, that the Nth snapshot is a linear combination of the $N-1$ previous ones for a sufficiently large value of N. A number of works were dedicated to applying these two techniques to measured or simulated data, and to even comparing them for their abilities to distinguish flow features. However, it must be stated that neither technique contains a priori knowledge about the physics of the flow, and so the resulting modes have to be validated. Leask and McDonell (2019) noted that no systematic validation procedure was available that could facilitate the interpretation of these modes. To remedy this, they adopt a hierarchical approach by first studying canonical flows (in their case, a liquid jet) whose characteristics are well known and can be used to interpret adequately the POD or DMD modes. They then check if the knowledge gained from these simple flows is transferable to flows of more practical interest.

The availability of large sets of measured data and the increase in computational capabilities made possible the use of Machine Learning in the field of fluid mechanics. Flow modeling usually relies on governing equations or conservation laws (such as the Navier-Stokes equation). However, the problem of performing scale-resolved simulations quickly becomes intractable for Reynolds numbers that are of practical interest. In these cases, closure models based on simplifying assumptions (such as local isotropy) are often used. Machine Learning provides new possibilities through dimensionality reduction and reduced-order modeling. In the present work, the aim is to obtain a reduced-order model of the flow by producing a parameterized dynamical system (a neural network) capable of describing the spatial and temporal development of the flow.

3.8 Modeling the flow using POD, DMD and DNN

3.8.1 POD: two-dimensional

Two oscillators were used in order to showcase different flow behaviors and the ability of the modal decomposition methods to separate them. In the first configuration, dubbed Lg0, the pulsation frequency is around 200 Hz and can slightly change when the inlet pressure of the oscillator is increased. The resulting velocity waveform is similar to a square signal with a minimal value nearing $0\,\mathrm{m\,s^{-1}}$. In the second configuration L4 the waveform is more sinusoidal in the sense that velocity switches between its maximum and minimum values less abruptly than in Lg0. The frequency of pulsation for L4 is around 1100 Hz. In each case, the measurements were performed for four different jet Reynolds numbers. The color map used was specifically chosen to highlight the prominent features of the POD modes. Its range goes from $-C$ (blue) to C (red), where C is the maximum absolute value of a given POD mode, i.e.

$$C = \max_{x_i, y_i} \{\mathbf{\Phi}(x_i, y_i)\}$$

The specific values of each spatial mode are not important per se in the forthcoming analysis since what we hope to obtain from these modes are correlated structures in the flow. Regions having the same color, either red or blue, are well correlated among themselves. Blue and red zones are negatively correlated to each other, while white regions are neutral.

Having subtracted the mean field from the data before performing the decomposition, the first mode represents the principal pulsation of the jet for all Reynolds numbers (Figure 3.28). In other studies, the mean field may not have been subtracted, in which case the first mode would be equal to the mean field with a constant time coefficient (zero frequency). The first four modes for the first Reynolds number (Fig. 3.28a) contain similar structures to those of the second Reynolds number (3.28b). A nearly symmetrical two-lobed structure can be seen in modes 2,3, and 4 at different y/w positions. These structures, in all likelihood, correspond to a counter rotating vortex pair transported by the jet along its axis. These structures can be gleaned from the raw data as an indistinct 'halo' around the jet during part of the pulsation period. The last mode in Fig. 3.28b is mostly noise while the same mode in Fig. 3.28a, while not as noisy, does not have any orderly structures similar to the previous modes. The first mode contains most of the energy of the system as can be seen in the modal energy distribution (Figure 3.29) for the first jet (Figure 3.28a). The successive modes contain decreasing portions of the total energy. As the Reynolds number increases, the flow becomes more turbulent, hindering the development of large coherent structures. The incoherent part of the flow that becomes more predominant with increasing Reynolds number, cannot be captured with the present measurement and reconstruction technique. The disappearance of coherent structures can be seen in modes 2 through 5 in Fig. 3.28c and 3.28b, that mostly contain noise.

The modal energy distribution (Figure 3.29) is nearly the same for the four configurations of Figure 3.28. The first mode, that represents the main pulsation of the jet,

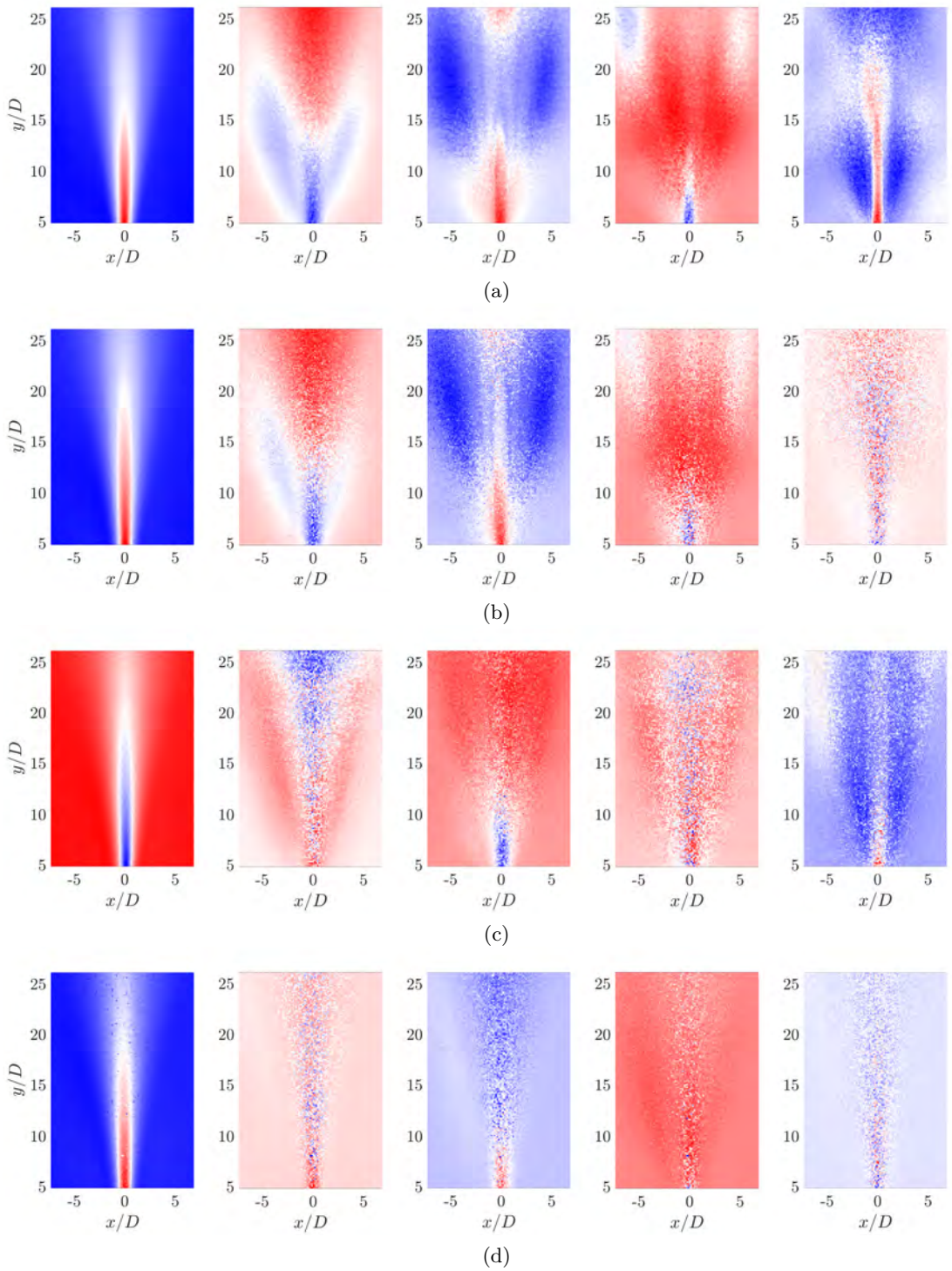

Figure 3.28: First five POD modes for the Lg0 case with (a) $p_{\text{in}} = 1.5\,\text{bar}$, (b) $p_{\text{in}} = 2.0\,\text{bar}$, (c) $p_{\text{in}} = 2.5\,\text{bar}$, and (d) $p_{\text{in}} = 3.0\,\text{bar}$

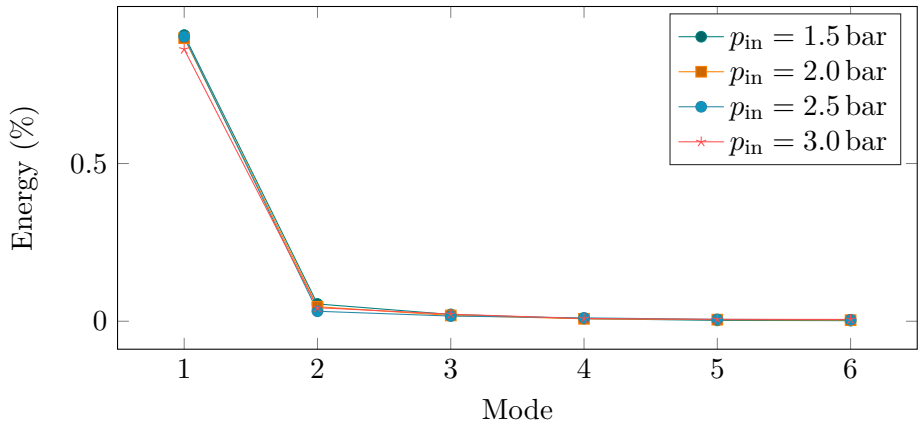

Figure 3.29: Modal energy distribution for the cases presented in Figure 3.28

consistently monopolizes around 90% of the energy of the system. The second modes in Fig. 3.28a and 3.28b contain 5.5 and 4.6% of the energy, respectively, which drops to around 3.5% for the remaining Reynolds numbers. Each remaining mode contains 2% or less of the system's energy. In light of this, it can be said that the correlated structures are not predominant from an energy standpoint when compared to the main pulsations, but remain present in the flow and detectable by the present measurement technique. Nevertheless, the energy distribution is often less biased toward a single mode as will be seen in the next configuration.

In the L4 configuration, the jet pulsates at around 1100 Hz and the velocity waveform is smoother than that of the previous case and has a narrower amplitude. The POD modes (Figure 3.30) reveal a different set of correlated structures. The first mode for all Reynolds numbers still represents the main pulsation of the jet, and its structure curves slightly to the left when compared to the first modes in Lg0. In Fig. 3.30a, 3.30b and 3.30c, the second mode is dominated by two negatively correlated regions stacked side by side along a sloped line. This can be interpreted as an asymmetrical flapping or whipping motion. In Fig. 3.30a, modes 3 and 4 contain structures that are periodically spaced along the jet axis. The spatial periodicity in these modes could be associated to a repeated ejection of a high-velocity parcel of fluid during each pulsation of the jet. This is often referred to as puffing motion (Goldschmidt and Bradshaw (1973)). These structures also appear in modes 3 and 4 of Fig. 3.30b, but with a wider spacing in between. The last mode in Fig. 3.30a also has periodic structures, but slightly tilted compared to the previous modes. This seems to be a combination of mode 2 on one hand and modes 3 and 4 on the other. The last in mode in Fig. 3.30b is mostly noise, with indistinct structures. The modes in Fig. 3.30c are less diverse, with only the main pulsation and the flapping motion in modes 1 and 2 respectively. Modes 3 and onward are mostly noise. In Fig. 3.30d, the second mode is different than in the previous cases and cannot be clearly associated with any of the previously described motions of the flow. The third mode seems to capture some spatial periodicity comparable to modes 3 and 4 of Fig. 3.30a, but less distinct, suggesting a weak puffing motion.

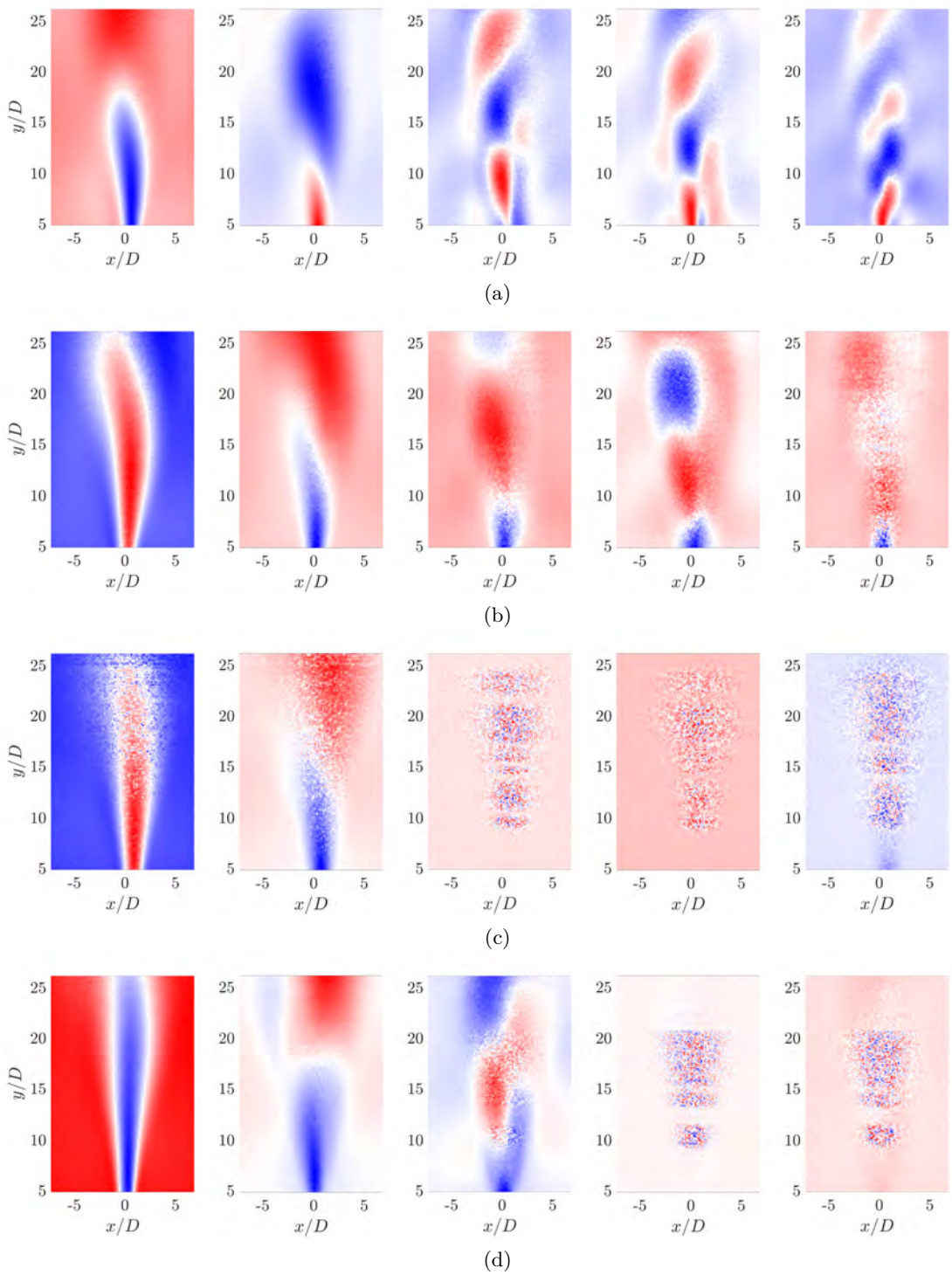

Figure 3.30: First five POD modes for the Lg0 case with (a) $p_{\text{in}} = 1.5\,\text{bar}$, (b) $p_{\text{in}} = 2.0\,\text{bar}$, (c) $p_{\text{in}} = 2.5\,\text{bar}$, and (d) $p_{\text{in}} = 3.0\,\text{bar}$

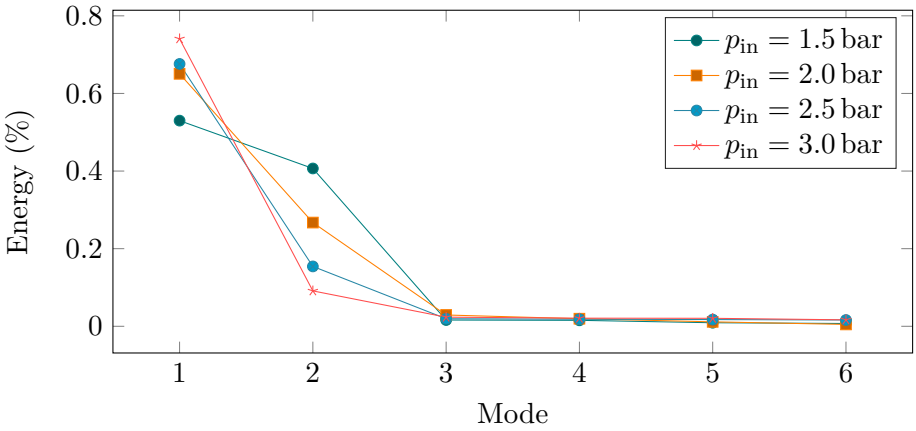

Figure 3.31: Modal energy distribution for the cases presented in Figure 3.30

Turning to the modal energy distribution (Fig. 3.31), it can be seen that the first mode is not relatively as energetic as it was in Lg0. For Fig. 3.30a, modes 1 and 2 capture 52 and 40% of the total energy, which demonstrates the significance of the flapping motion described earlier. The remaining three modes, that are associated to puffing, only contain about 1.5% of the total energy each. As the Reynolds number is increased, the first mode captures more of the energy at the expense of the second mode that becomes increasingly less prominent.

These dynamic features, that evolve in both time and space, can be seen in the raw data. It would then seem that the flow can be represented in a low-dimensional space comprised of the relevant modes. For the Lg0 case, where the jet pulsates at 200 Hz and the velocity fluctuates like a square-wave, the first two modes are enough to reconstruct the velocity along the centerline of the jet (Figure 3.32). Adding more modes does not significantly improve the reconstruction, except around the small secondary peak at $t^* = 0.7, 1.7, \ldots$ where a slight improvement can be seen. Moving into the shear layer at $x/w = 2$ and $y/w = 12$ (Fig. 3.33), the same observation can be made that the first 3 modes are sufficient to represent the velocity, even though some features, such as the peaks at $t^* = 0.7$ and 1.33 were underestimated. The same observations can be made for the L4 case, where the velocity field can be represented well enough using the first few modes.

3.8.2 POD: three-dimensional

A 3D data set was compiled by stacking 2D field measurements, corresponding to Lg0, at different depths z. The same synchronization technique, based on feedback loop pressure signals, was used to reconstruct the 3D velocity field. The purpose of including these results here is simply to reveal the full spatial form of the lobes observed in Figure 3.28. Unsurprisingly, these traveling structures (Taira et al. (2017)), cannot be captured in a single spatial mode since these modes are real valued. They appear shifted in two modes just like modes 2 and 3 in Figures 3.28a and 3.28b. Having identified the corresponding modes from the decomposition of the 3D field, they can be used to reconstruct the lobed

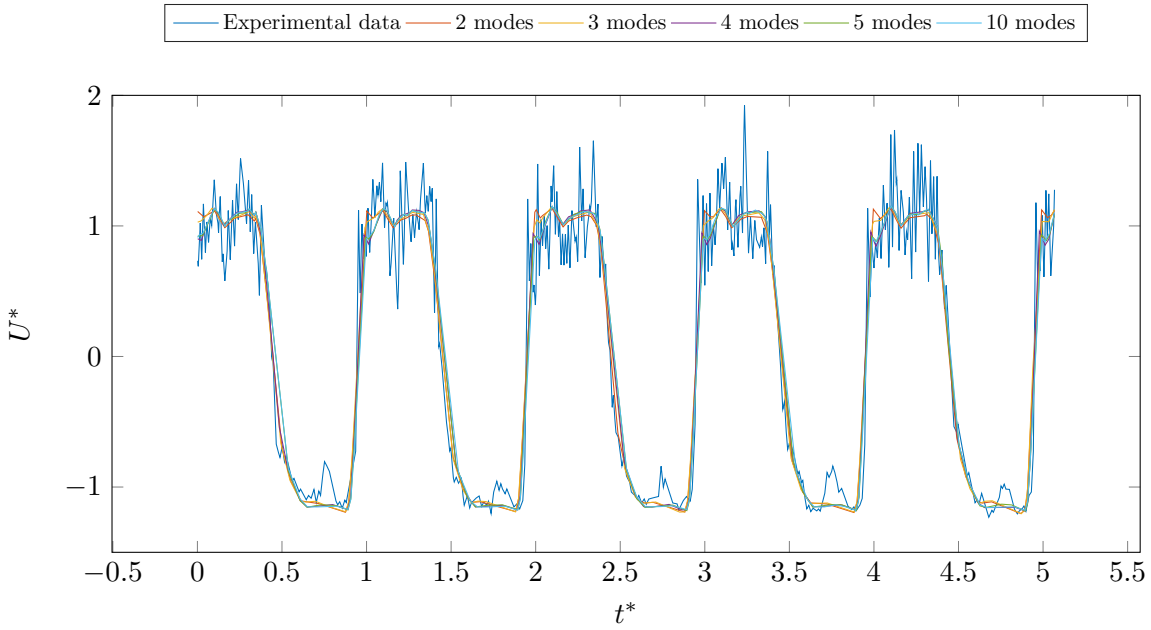

Figure 3.32: Normalized velocity for case Lg0 at $x/w = 0$ and $y/w = 12$ ($p_{\mathsf{in}} = 2\,\mathrm{bar}$)

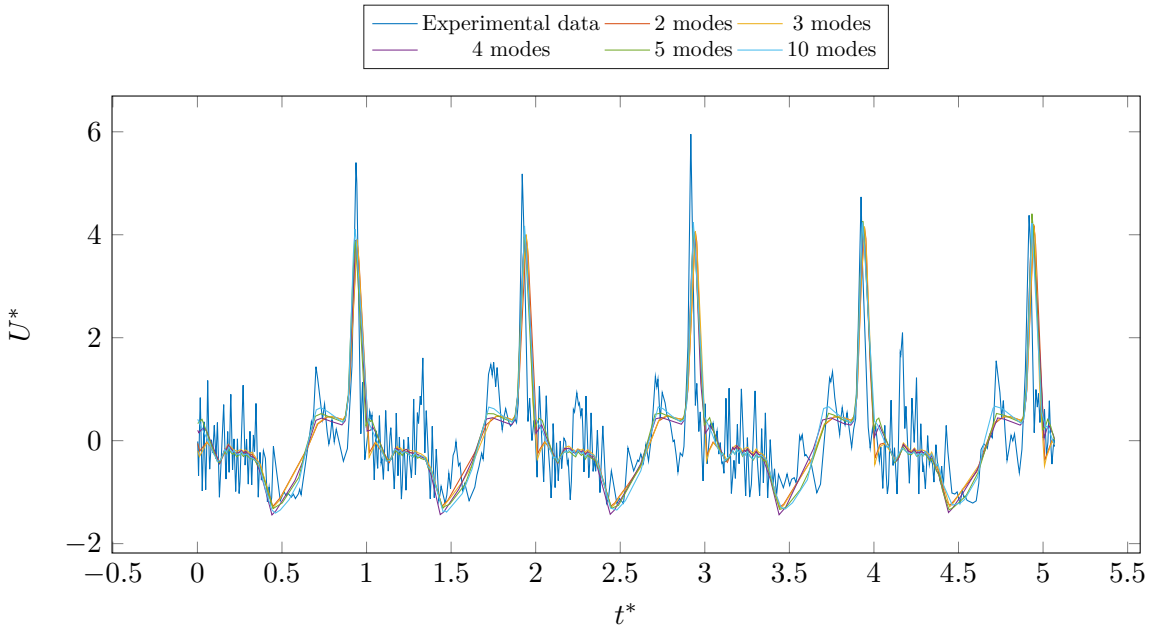

Figure 3.33: Normalized velocity for case Lg0 at $x/w = 2$ and $y/w = 12$ ($p_{\mathsf{in}} = 2\,\mathrm{bar}$)

forms described earlier (Figure 3.34). These structures are only observed during a pulsation when the jet velocity suddenly increases, in this case, between the phase angles $\phi = 207°$ and $\phi = 237°$.The elongated form may be due to the decomposition method itself. In the next section, we will see that these same structures present themselves under a slightly different shape.

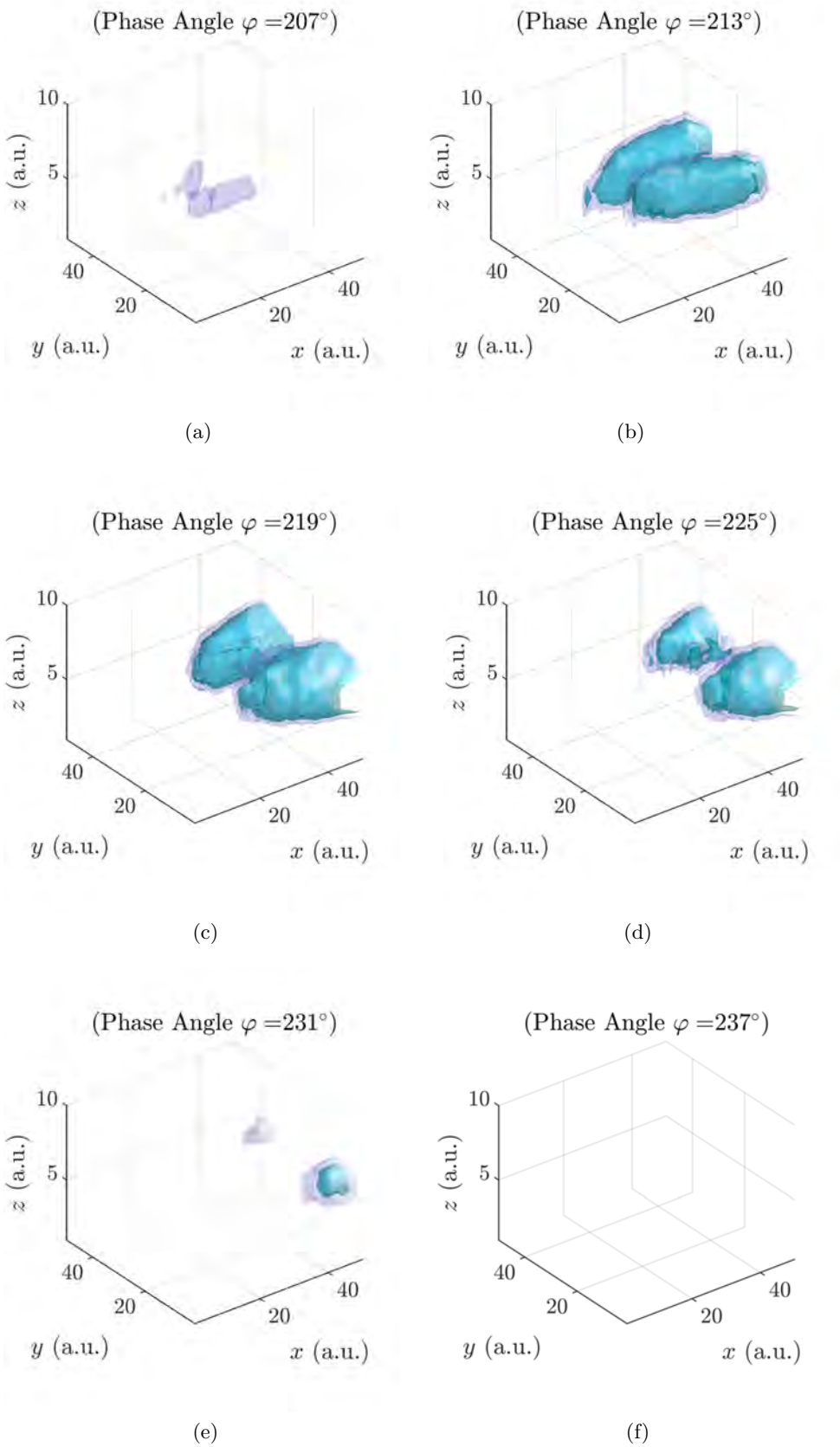

(a) (b) (c) (d) (e) (f)

Figure 3.34: Reconstruction of the flow field using only POD modes 3 and 5 isolates the lobe structures convected by the jet during part of the pulsation period.

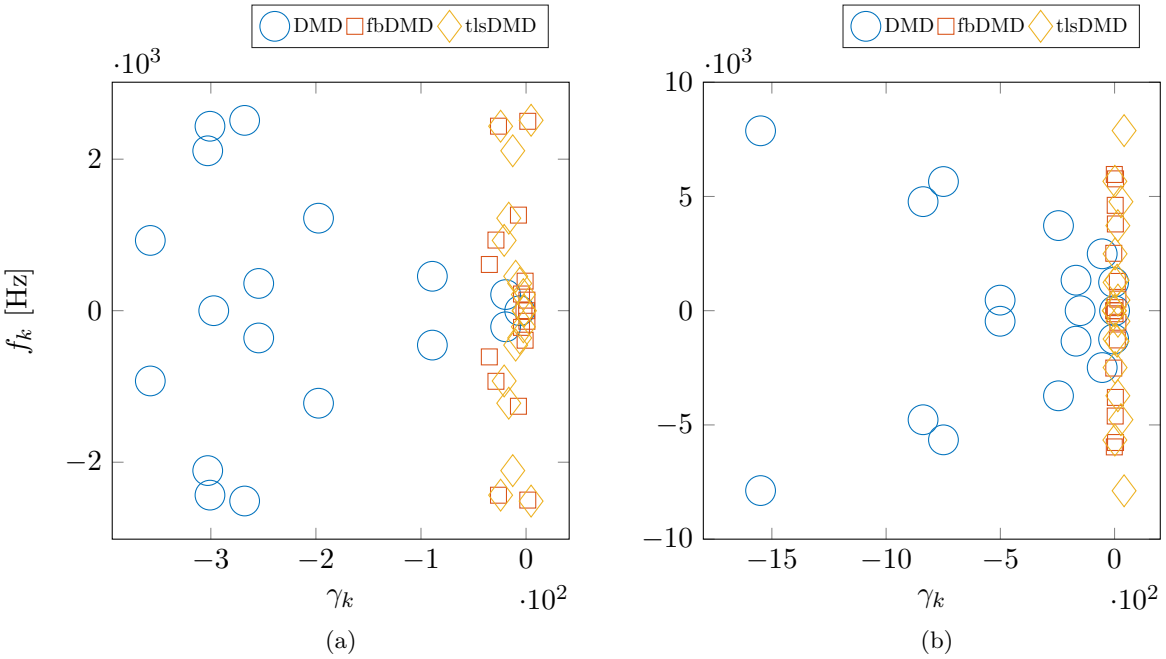

Figure 3.35: Eigenvalues $\omega_k = \gamma_k + 2\pi i f_k$ from three DMD variants (standard, forward-backward and total least-squares) for (a) Lg0 at $p_{\text{in}} = 2.0\,\text{bar}$ and (b) L4 at $p_{\text{in}} = 1.5\,\text{bar}$.

3.8.3 DMD: two-dimensional

Eigenvalues ω_k

When performing a DMD, the data set is used without subtracting the mean field (e.g. Dawson et al. (2016) or Leask and McDonell (2019)). However, by doing so with the present data, we were not capable of correctly finding the time characteristics of the flow. As a consequence, it was not possible to correctly reconstruct the velocity field with the resulting decomposition. And so, the data sets were constructed in the same way as for POD, that is, by subtracting the temporal mean of the data at each point in the field. Through trial and error, it was found that a decomposition of rank $r = 18$ is sufficient to capture the main features of the flow for both cases Lg0 and L4. Before examining the spatially-dependent modes, we begin by comparing their growth rates and frequencies for the three variants considered (Fig. 3.35): the standard formulation, the forward-backward DMD (fbDMD) and the total-least-square DMD (tlsDMD). Although the data was low-pass filtered before the decomposition, part of the noise from the incoherent part of the flow (that can still interact with the coherent part) was kept. Since the flow is periodic in time, it is expected that the growth rate of the DMD modes should be close to 0. However, the distribution of ω_k for the original DMD follows a parabolic form that extends into the left half plane (Figure 3.35b). This shift in growth rates is due to process noise. Although the fbDMD and tlsDMD were designed to reduce sensor noise, Dawson et al. (2016) showed that they also eliminated process noise by using the algorithms on numerical and experimental data from simple flows (e.g., an unstable cylinder wake). This seems to be the case for the

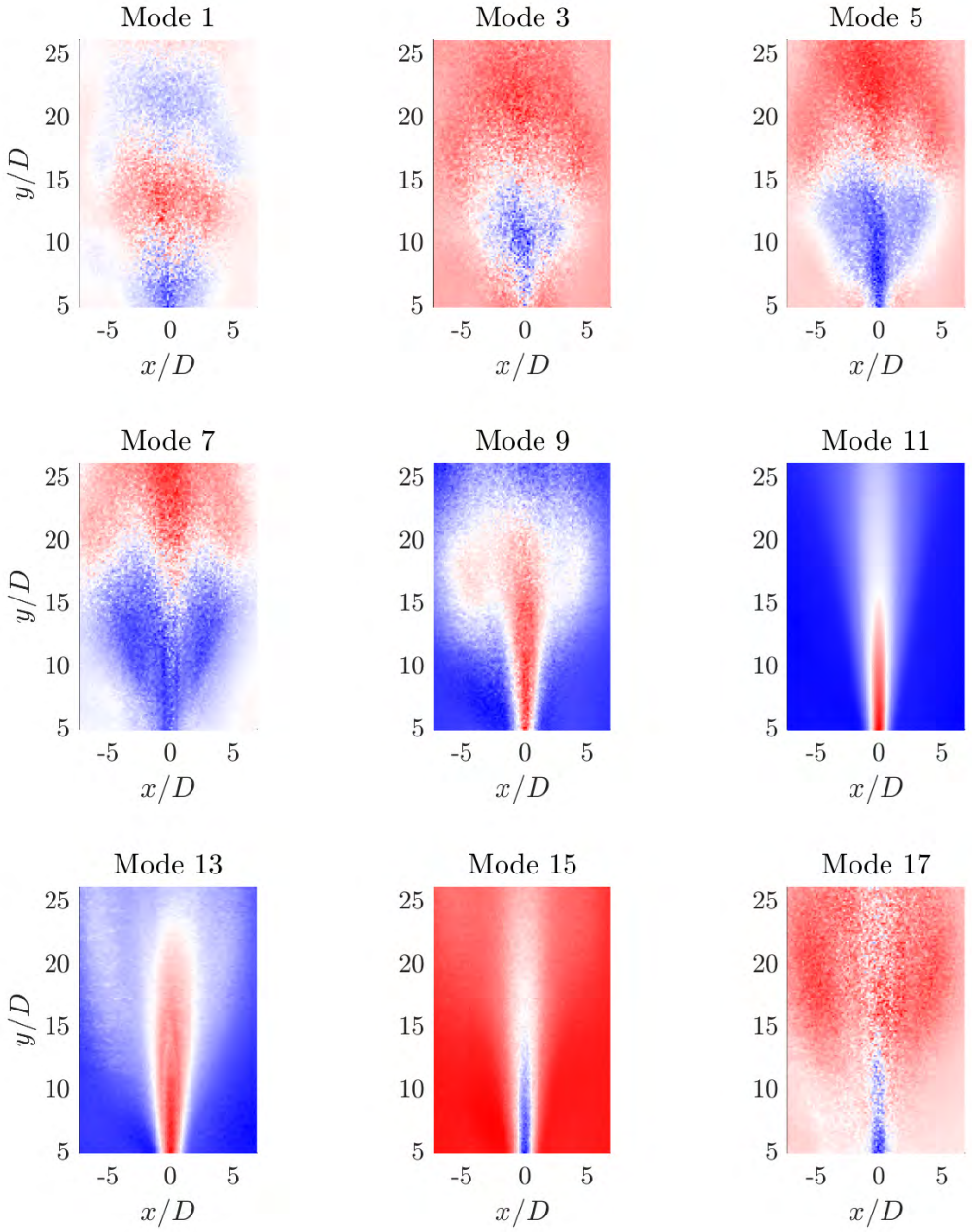

Figure 3.36: DMD spatial modes ($r = 18$) for Lg0 at $p_{\mathsf{in}} = 2.0\,\mathrm{bar}$

present data where both variants result in growth rates that are closer to the $y-$axis for Lg0 and L4 (Fig. 3.35a and 3.35b, respectively).

Spatial Modes

For the sake of brevity, only two sets of DMD spatial modes are presented that correspond to Lg0 at $p_{\mathsf{in}} = 2.0\,\mathrm{bar}$ (3.36) and L4 at $p_{\mathsf{in}} = 1.5\,\mathrm{bar}$ (3.37). The spatial modes, as already noted by Dawson et al. (2016), do not change significantly between DMD variants

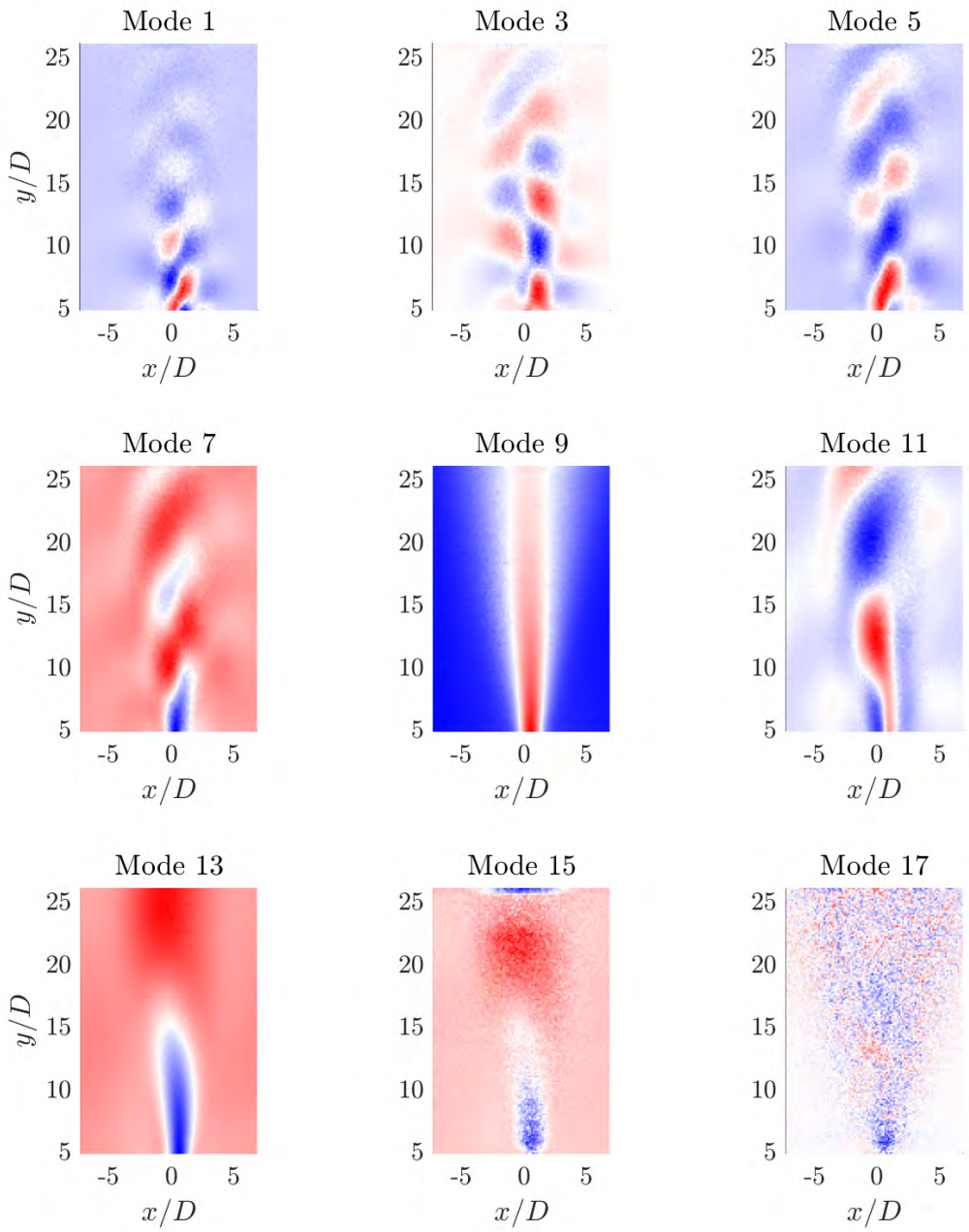

Figure 3.37: DMD spatial modes ($r = 18$) for Lg0 at $p_{\mathsf{in}} = 1.5\,\mathrm{bar}$

so Figures 3.36 and 3.37 were computed using the standard algorithm. Furthermore, unlike POD, DMD produces spatial modes in conjugate pairs so only one of each is presented here. Certain motifs gleaned from the POD modes re-emerge here but with some differences. For instance, Modes 5, 7 and 9 in Figure 3.36 can be associated with the second and third POD modes for the same case (Fig. 3.28b) and represent a pair of counter-rotating vortices convected along the jet axis. However, in the DMD modes, these structures standout from their surroundings and have a more compact form, whereas in the POD modes they are

elongated in the axial direction and seem less distinct. Similarly, POD modes 1, 3 and 5 in Figure 3.30a can be associated with DMD modes 13, 11 and 5 in Figure 3.37. The DMD modes do not seem to offer any additional information about the flow structures that wasn't already deduced from the POD modes.

Reconstruction

The ability of the DMD algorithms to capture the constituent spatial structures, frequencies and growth rates of the flow should mean that they can be used to reconstruct the velocity field. This is not the case for Lg0 (Figure 3.38). As expected, the velocity signal reconstructed from the standard DMD decays with time since most of the corresponding eigenvalues are shifted into the left half plane (Figure 3.35). The forward-backward DMD seems to correct the growth rate, but the resulting signal is not well aligned with the experimental data. The total-least-square algorithm produces the least convincing reconstruction since the velocity quickly decays with time although the growth rate of the modes are closer to zero relative the standard algorithm (Figure 3.35). It was possible to marginally improve the reconstruction by selectively removing certain modes, however this would make the reconstruction impractical and not worthwhile.

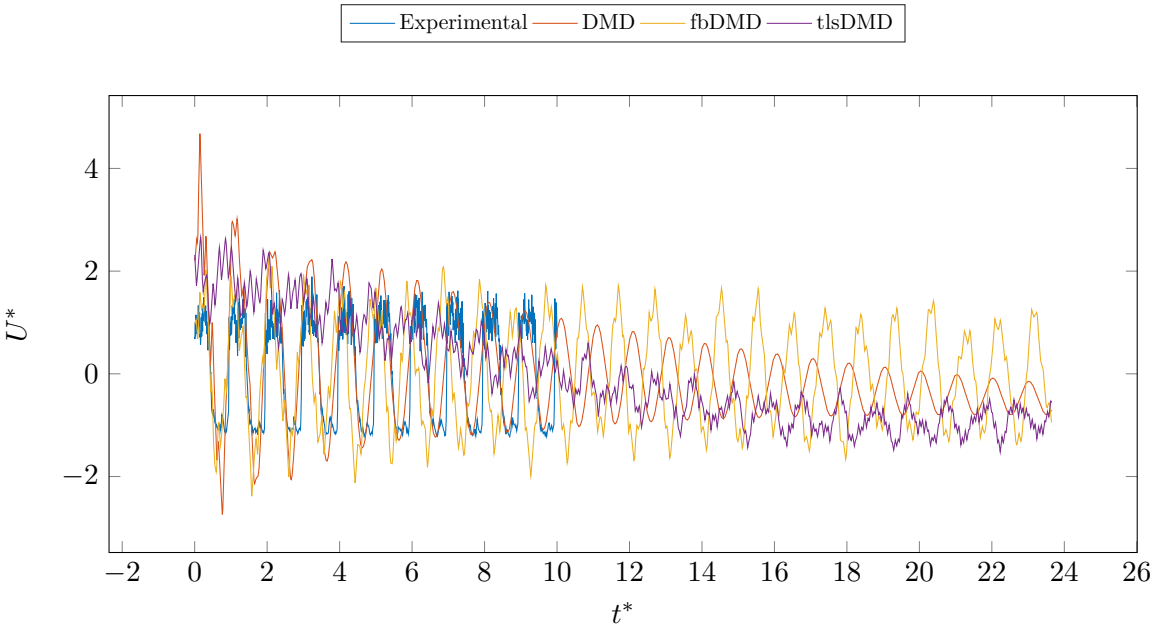

Figure 3.38: Normalized velocity at $x/w = 0$ and $y/w = 12$ reconstructed from the standard, forward-backward and total-least-square DMD algorithms (Lg0 at $p_{\mathsf{in}} = 2.0\,\mathrm{bar}$). The experimental plot is intentionally cut at $t^* = 10$ for clarity's sake.

For L4, the standard algorithm does not show significant decay and correctly captures the fundamental frequency of the flow, however the reconstructed signal (Figure 3.39) smooths out most of the small fluctuations (for instance, the small peaks that occur at $t^* = 0.6, 1.6, \dots$). The forward-backward algorithm also correctly captures the fundamental

frequency of the flow and its growth rates are closer to zero than the standard algorithm. However, the reconstructed velocity signal does not resemble the input data. Finally, the signal reconstructed from the tlsDMD modes is well aligned with the original signal and captures more temporal details of the waveform (such as the previously-mentioned small peaks). It is also possible to improve the model by selectively removing certain modes, but again this makes the reconstruction process impractical.

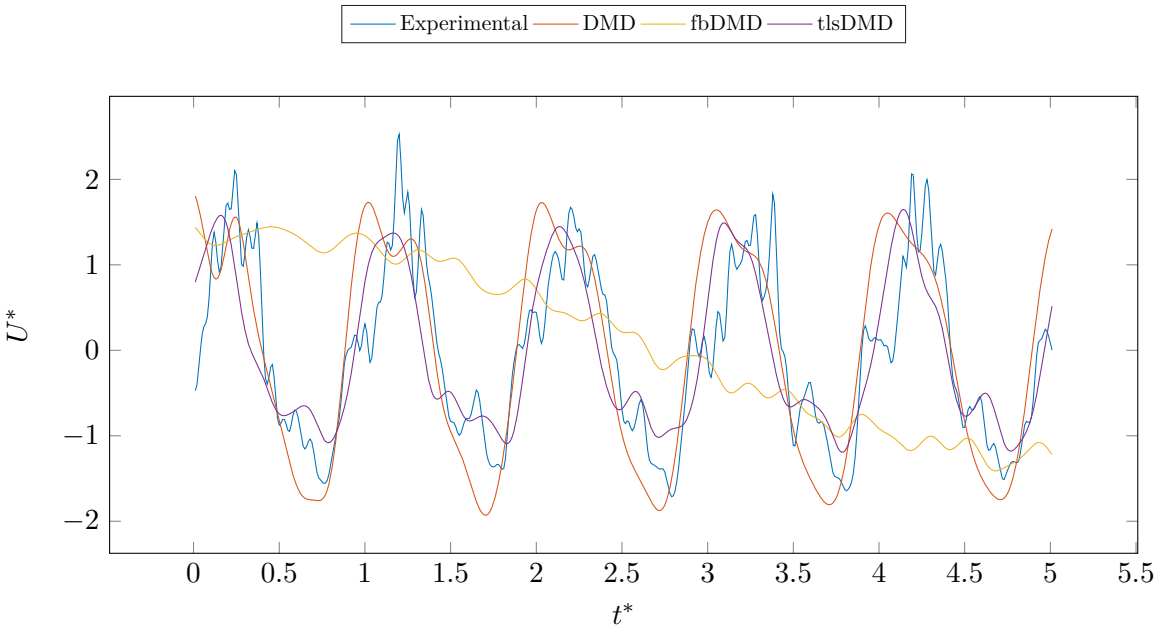

Figure 3.39: Normalized velocity at $x/w = 0$ and $y/w = 12$ reconstructed from the standard, forward-backward and total-least-square DMD algorithms (L4 at $p_{\text{in}} = 1.5\,\text{bar}$). The experimental plot is intentionally cut at t^* for clarity's sake.

3.8.4 Deep Neural Networks

The final approach to modeling the flow is by training deep neural networks (DNN) using the position in space $\mathbf{x}$ and time t as input parameters and the velocity U as the output. A dense structure is chosen with 3 hidden layers containing the same number of neurons N each. This means that each network requires $N_P = 2N^2 + 7N + 1$ parameters in total. Several well-known activation functions were used, such as ReLU and ELU, along with a sinusoidal activation that requires a specific initialization scheme presented earlier (Sitzmann et al. (2020)). We begin by setting a number N of neurons per layer and then train the networks for different activation functions. When the training is over, the velocity is reconstructed at two points $(x/w, y/w) = (0, 12)$ and $(-4, 12)$ and compared to the raw data. The sigmoid activation function was used with two 3-layered dense neural networks with 20 and 40 neurons per layer, respectively. The reconstructed velocity profile is well aligned with the original data, but smooths out many of the small dynamic features such as the peak at $t^* = 0.7, 1.7, \ldots$. This peak corresponds to a weak puff of air produced

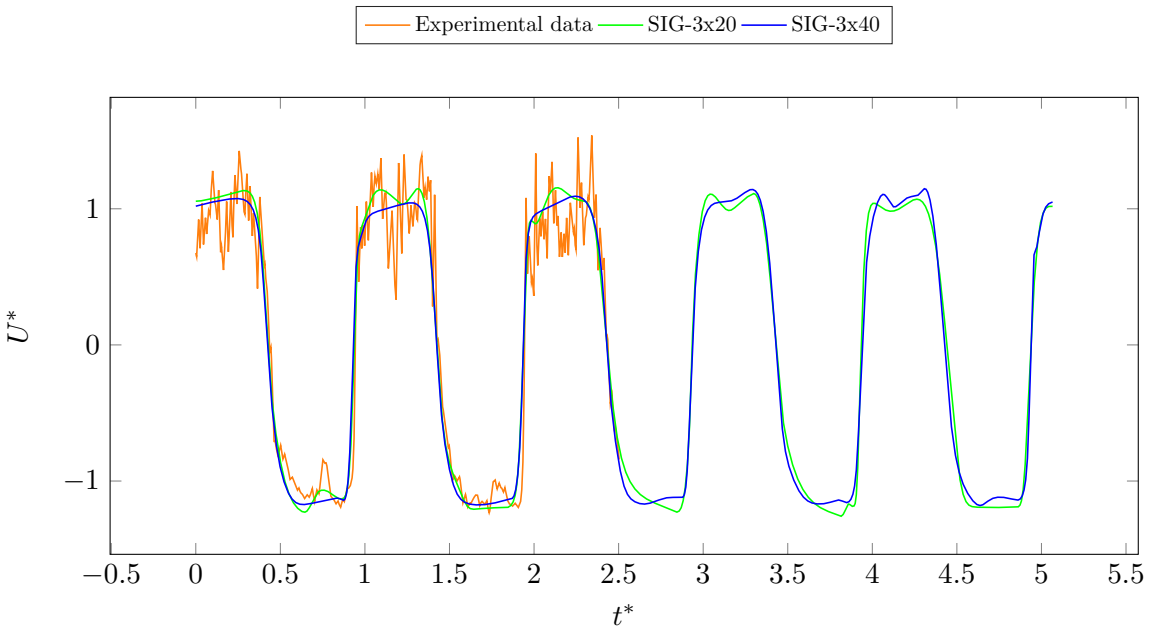

Figure 3.40: Normalized velocity at $x/w = 0$ and $y/w = 12$ as estimated by the neural networks SIG-3x20 and SIG-3x40

by the oscillator during each pulsation's off-time. During the on-time, both structures inconsistently model the local maxima: for SIG-3 $\times$ 40 and $t^* \in [1, 1.4]$, the velocity profile is nearly flat, whereas a few pulsations later, for $t^* \in [4, 4.4]$ fluctuations in velocity can be seen. The same observation can be made for SIG-3 $\times$ 20 for $t^* \in [0, 0.4]$ and $[1, 1.4]$. In addition, training these networks required over 1000 epochs before reaching convergence, which is relatively long compared to the other networks.

Neural Network	Number of epochs	Activation function
SIG-3 $\times$ 20	1500	sigmoid
ReLU-3 $\times$ 20	400	ReLU
ELU-3 $\times$ 20	1430	ELU
SINE-3 $\times$ 20	230	sinusoidal
SIG-3 $\times$ 40	800	sigmoid
ReLU-3 $\times$ 40	580	ReLU
ELU-3 $\times$ 40	630	ELU
SINE-3 $\times$ 40	90	sinusoidal
ELU-3 $\times$ 60	200	ELU
SINE-3 $\times$ 60	90	sinusoidal

Table 3.2: Deep Neural network structures and activation functions tested.

Using the same two structures, but with the ReLU activation function, the reconstructed velocity profile exhibited ragged, sharp fluctuations that deviate from the original experimental data (Figure 3.41). Although doubling the number of neurons per layer leads to a better approximation of the velocity fluctuations, it still fails to consistently capture

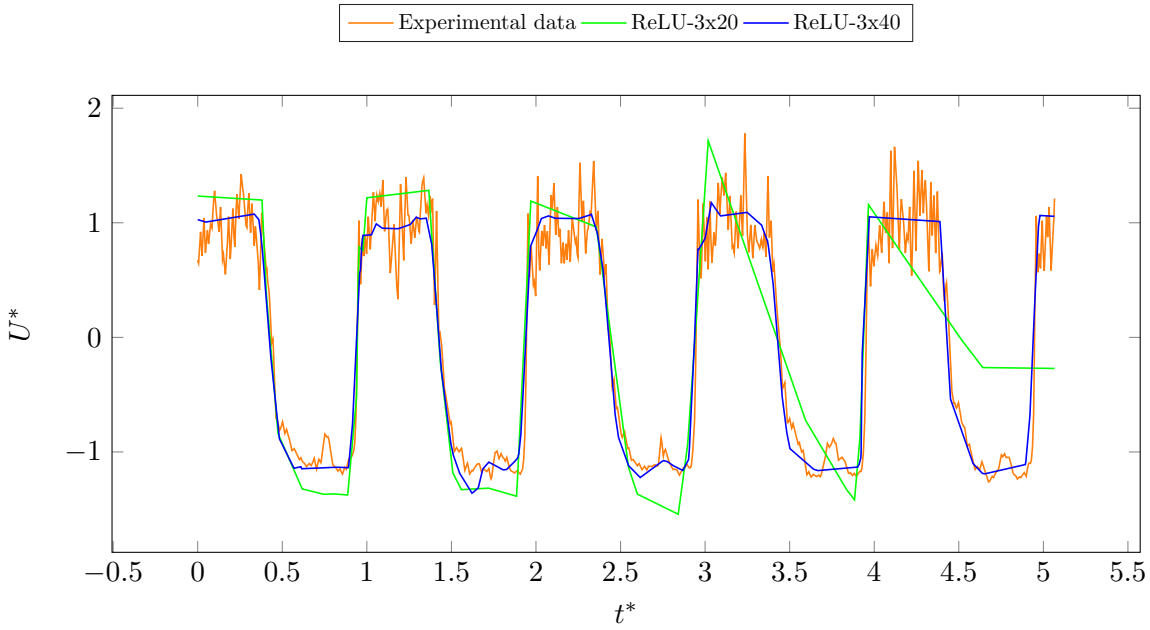

Figure 3.41: Normalized velocity at $x/w = 0$ and $y/w = 12$ as estimated by the neural networks ReLU-3x20 and ReLU-3x40

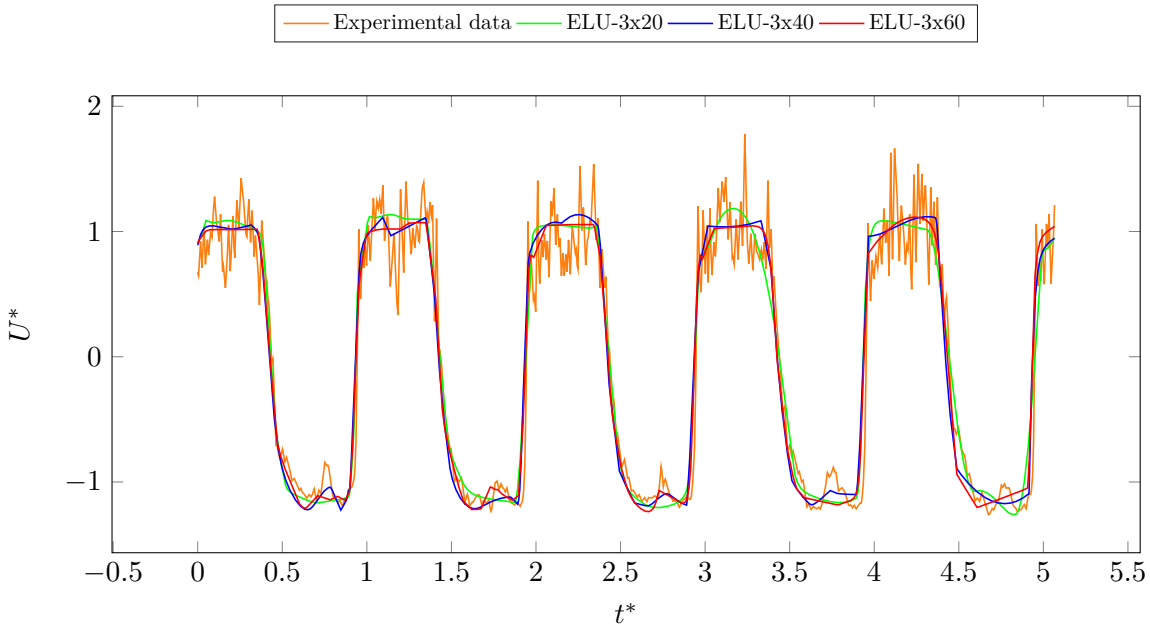

Figure 3.42: Normalized velocity at $x/w = 0$ and $y/w = 12$ as estimated by the neural networks ELU-3x20, ELU-3x40 and ELU-3x60

the previously mentioned dynamic features such as the off-time peak.

Replacing the ReLU with an ELU activation function significantly improves the reconstructed fields even for the 3×20 structure. In addition, increasing the number of neurons per layer seems to enhance the temporal resolution of the velocity profile. How-

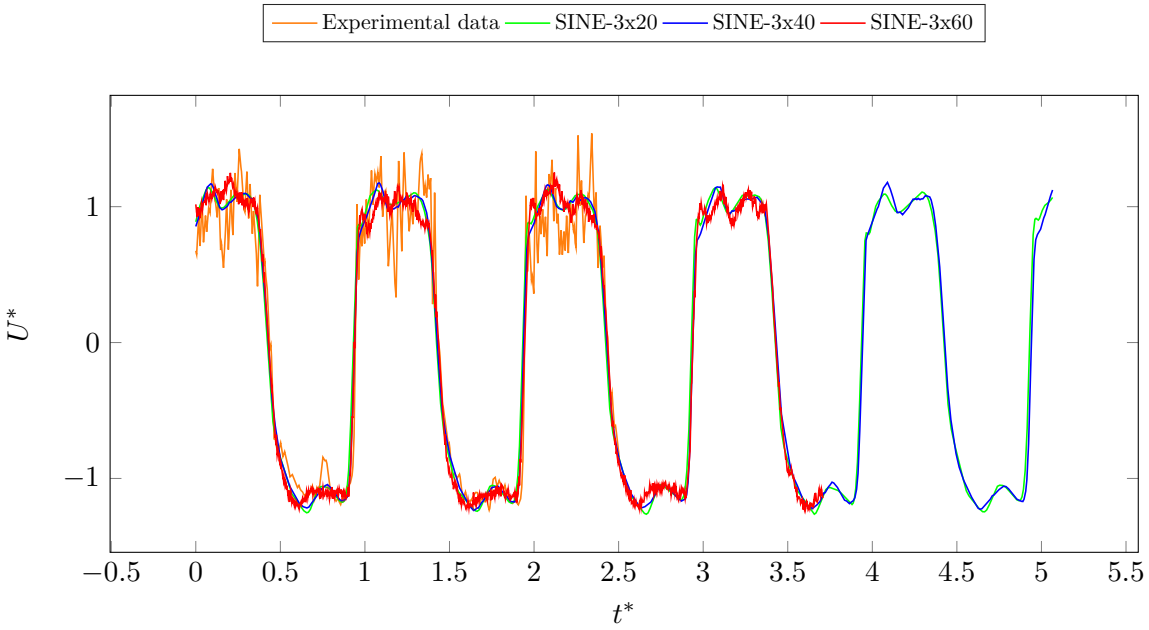

Figure 3.43: Normalized velocity at $x/w = 0$ and $y/w = 12$ as estimated by the neural networks SINE-3x20, SINE-3x40 and SINE-3x60. (The experimental and SINE-3x60 plots were cut at $t^* = 2.5$ and 3.7 in order to better compare the remaining two plots).

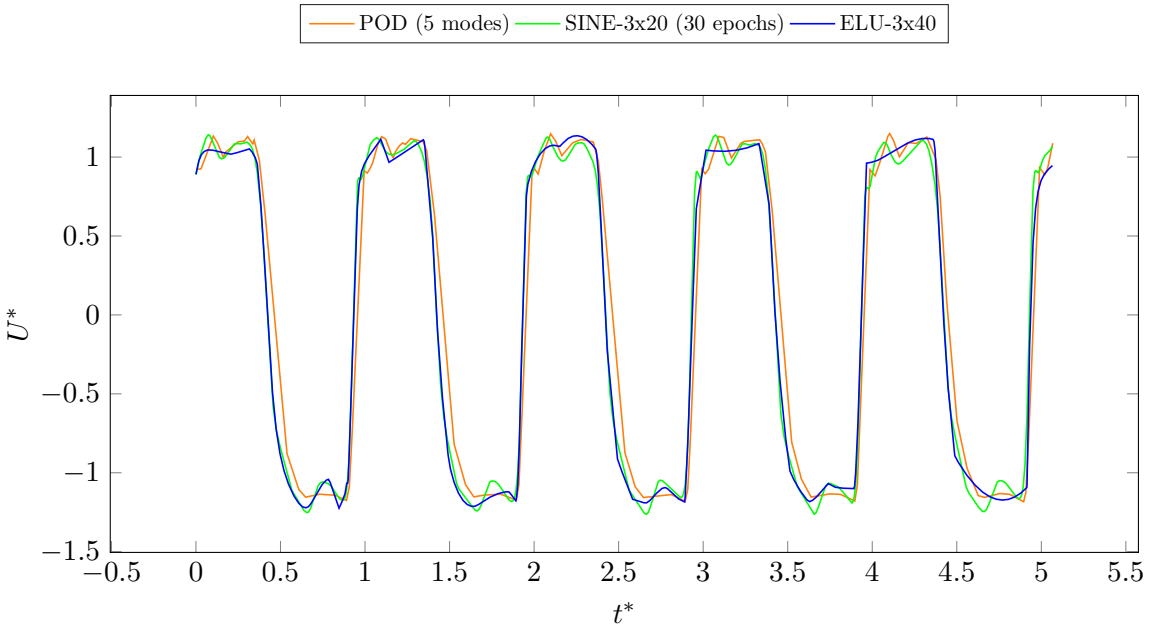

Figure 3.44: Comparison of normalized velocity at $x/w = 0$ and $y/w = 12$ as estimated by POD, SINE-30x20 and ELU3x40.

ever, the fluctuations during the on-times are clearly not consistent across pulsations even for ELU-3 $\times$ 60.

The neural networks with sinusoidal activation functions required the least amount of training for any given network size (3.2). With only 20 neurons per layer, SINE-3x20 is

able to reproduce the salient features of the velocity fluctuations (3.43). Increasing the number of neurons per layer to 40 only marginally improves the model and increasing it to 60 neurons results in small unrealistic fluctuations.

Finally, comparing the velocity estimation from the POD reconstruction and the SINE-3x20 and ELU-3x40 neural networks, it is clear that that the most energetic POD modes fail to capture certain features such as the small velocity peak during the pulsation off-time.

3.9 Conclusion

In this study, different data-driven methods are used to model an unsteady velocity field measured using a single hot-wire probe. Pressure signals from inside the fluidic actuator that produces the pulsed jets are used to synchronize the velocity signals measured on a uniform spatial grid. This enables a spatial reconstruction of the velocity field. The first two data-driven methods, Proper Orthogonal Decomposition (POD) and Dynamic Mode Decomposition (DMD) are based on a modal decomposition of the experimental data. POD yields spatial modes and their corresponding temporal coefficients and classifies them according to their energy content. A limited number of the most first, most energetic modes can be used as a reduced-order model of the original data. This energy-optimality of POD is not always desirable since lower energy modes can contain features of the flow that are dynamically significant. It was shown that the first POD modes were not enough to adequately reproduce all the features of the velocity fluctuations. Next, three DMD versions were used with the same data: the standard, forward-backward and total-least-square algorithms. The forward-backward and total-least-square algorithms build on the standard version but correct the bias error due to sensor noise. The DMD spatial modes were similar to the POD modes and the fbDMD and tlsDMD algorithm were effective in correcting bias error. However, it was not possible to adequately and consistently reconstruct the velocity field.

Neural networks were also used to model the flow. Different network sizes and activation functions were tested. The assessment of these networks was based on the number of training epochs required before convergence and their ability to accurately reproduce the velocity field. In addition to the well-known sigmoid, ReLU and ELU activation functions, a sinusoidal activation function was also considered. Although using a sinusoidal activation function is not in itself a novel idea, the initialization scheme proposed by Sitzmann et al. (2020) allows it to compete with the other activation functions, even surpassing them in terms of training time and accuracy.

In the present work, the neural networks were trained on velocity fields of pulsed jets at a given average velocity and pulsation frequency. The data set can be extended by measuring velocity for different conditions. It can then be used to train a model of the fluidic actuator. This can prove invaluable in situations where the actuator is only a component in a much larger system. It would obviate the need to simulate or measure the complex flow inside the actuator whenever design specifications are altered.

"And yet, there is Murphy's law to consider, that brash Irish proletarian restatement of Godel's Theorem - when everything has been taken care of, when nothing can go wrong, or even surprise us, ... something will"

Gravity's Rainbow, p. 328
Thomas Pynchon

4
Thermal Measurements

In this chapter, the pulsed jets produced by the fluidic oscillators are used to cool a surface with a constant heat flux. The performance of the jets are quantified using the time-averaged Nusselt number. Steady jets having the same mass flow rates were used for comparison. In spite of the numerous studies concerned with pulsed jet impingement heat transfer, some of which were discussed in the Literature Review, we believe that it is not possible to draw general conclusions that are applicable to the present configuration. The combination of geometry, scale, frequency range and pulsation method used here, among other factors, do not have clear equivalents in the literature, and so a new set of thermal measurements are needed to evaluate the performance of fluidic oscillators as cooling devices.

One of the earliest studies on pulsed jet impingement can be found in Burmeister (1959), where the heat transfer between air and a heated surface is evaluated for Reynolds numbers of around 2000 (based on the diameter of the round nozzle), a Strouhal number of 3.2×10^{-4} to 57.5×10^{-4} (based on the frequency of pulsation, initial mean velocity and nozzle diameter of the jet) and a relative pulsation amplitude of 0.73 to 31%. The author showed that under these conditions, there was no appreciable difference in heat transfer, either enhancement or deterioration, when compared to a steady jet. However, they temper this conclusion by noting that their results hint at the existence of a critical Strouhal number, outside of the range of values considered, beyond which the pulsations' effect becomes significant. Works from the same period (e.g., byNevins and Ball (1961)) supported these conclusions, with Cochrane and Nevins (1962) offering what is probably the first glimpse of pulsating jet impingement using a Schlieren apparatus. According to Ghadi et al. (2016a), these early explorations of the topic may have discouraged further work until the 80's and 90's. Since then, a number of studies were conducted that have

looked at the problem from different perspectives.

In spite of the numerous studies that were conducted in the past, and because of the many parameters involved, it remains unclear under what conditions can pulsating an impinging jet improve heat transfer. Many results in the literature seem at times contradictory. Azevedo et al. (2015) used a rotating valve to produce pulsating impinging jets with frequencies going from 0 (steady) to 200 Hz. The steady and pulsed jets were compared for the same values of the Reynolds number (based on the time-averaged flow rate). Although the stagnation Nusselt number varied with frequency when the jet was pulsed, its value remained around 25% lower than in the corresponding steady case. In this study, the duty cycle (DC) was only set to 50% (that is, the on-time is equal to half the pulsation period), although it can have a significant effect on heat transfer performance. Marcum et al. (2015) studied a narrower range of frequencies (0−10 Hz) but tried two values of DC, 50% and 75%. They concluded that the duty cycle has a more significant effect on heat transfer than frequency and that it was possible to improve performance, compared to a steady jet, for a frequency $f = 10$ Hz and a duty cycle $DC = 50\%$. Pakhomov and Terekhov (2013) conducted a numerical study on pulsed jets at frequency of 0 to 60 Hz and found that, for standoff distances H/w less than 6, increasing the frequency led to an enhancement of stagnation point Nusselt number compared to the steady case. At lower frequencies, pulsating the jet led to a degradation of heat transfer performance. This trend was inverted for larger standoff distances. A similar behavior was observed in another study by Pakhomov and Terekhov (2010), where a larger range of frequencies ($0 - 500$ Hz) was considered.

Simulations by Behera et al. (2007) showed that the pulsation amplitude A_N and waveform had a greater effect on heat transfer than frequency. Increasing A_N from 23% to 47% led to a consistent enhancement of average Nusselt number, compared to the steady case, for all frequencies ($f = 25 - 400$ Hz) and standoff distances ($H/w = 5 - 9$) considered. Their results also hinted at an improvement for rectangular over sinusoidal waveforms. This conclusion is supported by Geng et al. (2015) who found that waveforms containing step increases in velocity led to better heat transfer performances when compared to smoother waveforms. They used a mass flow rate controller (MFRC) to produce pulsed jets with $f = 1.25 - 20$ Hz, $\mathsf{Re} = 4500$ and $H/w = 6$. Herwig and Middelberg (2008) confirmed this conclusion by showing that improvement due to square-wave pulses is more substantial than for sinusoidal or triangular waveforms with $H/w = 6$, $\mathsf{Re} = 7500$ and $1.25\,\text{Hz} < f < 40\,\text{Hz}$. In contrast, Zhang et al. (2018) found that, in the case of synthetic jets, triangular and sinusoidal waveforms were more efficient than rectangular waveforms at increasing heat transfer. So it seems that rectangular waveforms are only efficient when the time-averaged velocity of the jet is greater than zero. They also noted an increase in performance with frequency up to a Strouhal number of around $0.26 - 0.48$. Beyond this range, performance rapidly deteriorated.

It is clear that the literature is replete with conflicting conclusions on how to improve pulsed jet impingement heat transfer. The main reason for this is the number of parameters involved and their interactions. In response, Persoons et al. (2013) used two modified

Strouhal numbers $\mathsf{Sr} \times (H/w)$ and $\mathsf{SrRe}^{0.5}$, to scale the heat transfer in the stagnation and wall jet regions, respectively. They successfully collapsed their data using these new parameters, and showed, among other things, that there is a strong positive correlation between heat transfer enhancement and pulsation frequency.

The question remains as to what advantages can be gained from using fluidic oscillators over other methods of producing pulsed jet. In an experimental setting, using rotating valves (e.g., Azevedo et al. (2015)) or loudspeakers (Roux et al. (2011b)) to introduce unsteadiness into the flow seems practical since these methods enable a direct control of certain parameters such as frequency or even pulsation waveform in the case of loudspeakers. However, for industrial applications, they suffer from two flaws: moving parts and external control systems. Having moving parts makes these solutions vulnerable over time to wear and tear, especially under harsh operating conditions. In addition, external control systems incur additional installation and operating costs. The fluidic oscillator offers an alternative since it produces a self-excited periodic flow by virtue solely of its internal geometry. In this chapter, we attempt to identify the operating conditions of the oscillator that can lead to heat transfer enhancement compared to steady jets having the same average mass flow rate.

4.1 Overview of the experimental setup

The average temperature on the impact surface can be measured indirectly on the other side of the plate. The plate is made out of borosilicate glass with a coating of Indium Tin Oxide (ITO) on the oscillator's side. When a current crosses the ITO coating, through copper tape with conducting adhesive, Joule heating occurs across the surface. As shown in Figure 4.1, the prototype is mounted on a linear stage and the distance between the jet exits and impact surface can be adjusted with a micrometer (20 µm step). The oscillator's inlet mass-flow rate is monitored since it can change for a given pressure at small impact distances H/w. The pressure inside the feedback loops is also measured to check for possible changes in frequency due to extreme confinement of the oscillator's exit slots. On the other side of the plate, a FLIR SC235 infrared camera is placed slightly off-center relative to measurement zone in order to avoid surface reflection that would be difficult to filter out. The resulting distortion of the image is negligible and was not taken into account while processing the data. The experiments were performed in a temperature-controlled room and the area around the IR camera was cleared in order to minimize unwanted reflection on the glass surface. This particular camera was chosen because it operates in the $[7.5, 13]$µm range which is best-suited for the temperature range we expect to measure (i.e., roughly between 20 and 50 °C). The complete specifications of the camera are given in the appendices.

Before performing the measurements, the optical properties of the glass surface must be known. Usually, the surface is coated with high-emissivity paint in order to avoid problems with reflection and enhance the quality of the measurements. This option was ruled out since laying the paint can result in a textured surface, making it difficult to extract features

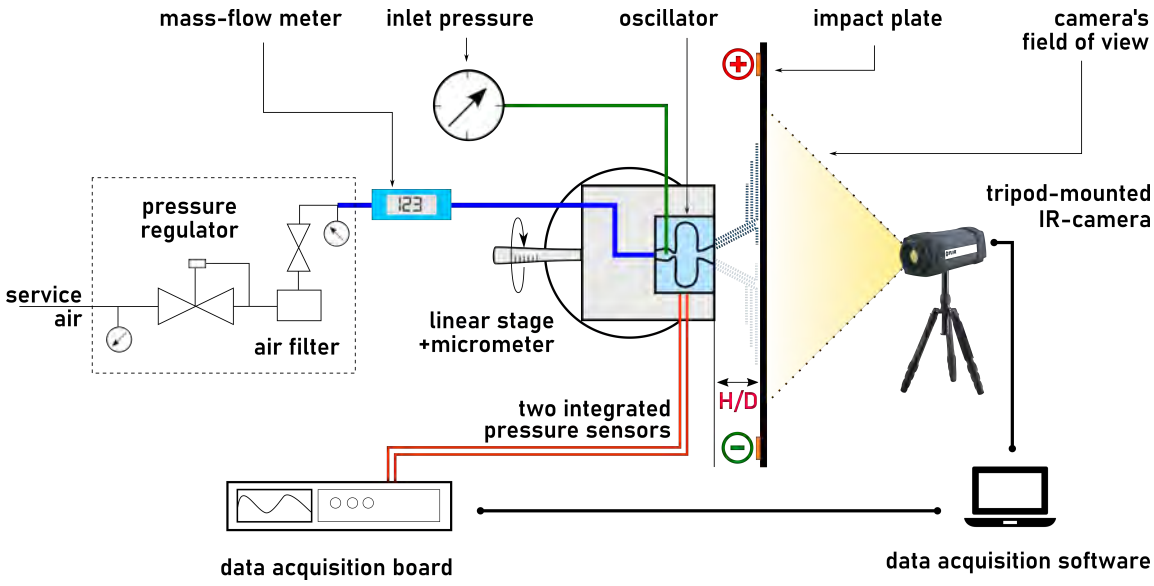

Figure 4.1: Experimental setup for the measurement of the temperature field on the impact plate.

of the temperature field having dimensions of the order of a millimeter. Instead, the optical properties of the glass are obtained by Fourier-transform spectroscopy and an optical model is chosen that minimizes temperature errors (Section 4.2).

Next, we look into the impact of the jet Reynolds number, pulsation frequency and standoff distance on heat transfer performance by finding the distribution of the Nusselt number Nu on the impact plate. Other parameters mentioned earlier, such as the waveform of the velocity pulsations, cannot be independently controlled. Computing Nu requires measuring the temperature field, for each combination of parameters, while changing the heating rate of the glass plate. The slope of the convective heat flux as a function of surface temperature gives us the convection coefficient h needed to compute Nu. The detailed procedure is presented in Section 4.3. Having done this, the Nusselt profiles along a central axis on the surface are plotted and the evolution of salient features, such as secondary peaks, is studied. The maximum and mean values of the Nusselt number are also compared for different configurations. Certain parameters, such as pulsation frequency, can not only reduce or enhance the overall performance of the impinging jets, but also significantly alter the response of the Nusselt number to other parameters, such as standoff distance. These results are compared to a steady configuration with jets having the same initial dimensions and time-averaged Reynolds numbers as the pulsed jets.

4.2 Optical properties of the ITO-coated glass

4.2.1 Spectrometer

A VERTEX 70, Bruker spectrometer (shown in Figure was used to find the optical properties of the glass samples. It is a Fourier Transform (FT)-IR type spectrometer capable

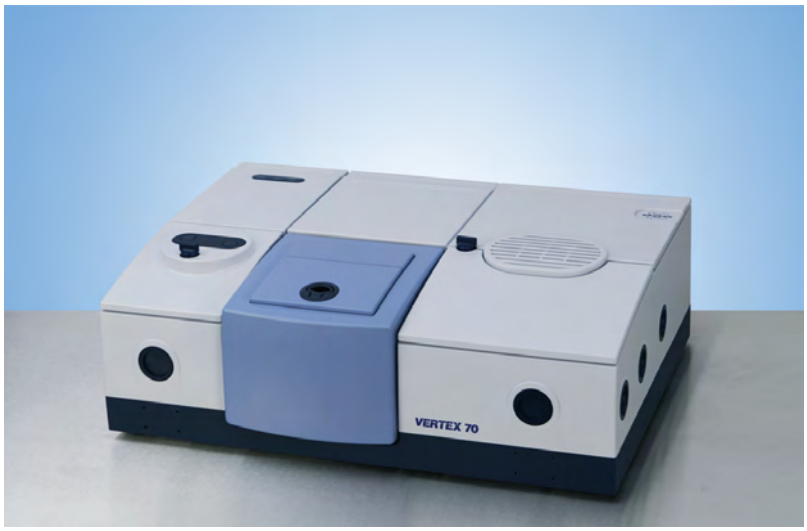

of performing measurements in a 0.5 to 20 µm range. To achieve this, the device contains three different detectors (Si-diode $[0.5-0.9]$µm, InGaAs $[0.9-2]$µm and DLaTGS $[2-20]$µm) and two sources (halogen $[0.5-2]$µm and globar $[2-20]$µm).

For the present study, the spectrometer is operated in three different modes:

- Directional transmission: measurement of the transmitted flux in a given direction (best suited for non-diffusing materials),
- Integrating sphere: measurement of directional hemispherical reflectivity (best suited for rough surfaces), and
- External module enabling the measurement of emission spectra for temperature starting from ambient and up to 450 °C.

4.2.2 Ambient Temperature Measurements

In order to measure the temperature field, the optical properties of the glass sheet and ITO coating must be determined. Measurements obtained by Fourier-transform spectroscopy were used to choose an appropriate emissivity model. We begin by measuring, at ambient temperature, the fraction of incident energy transmitted (T) and reflected (R) by glass samples. The fraction A of absorbed energy can be computed from the energy balance:

$$A + T + R = 1 \tag{4.1}$$

The fraction E of emitted energy is equal to A when the system is in thermodynamic equilibrium, so that:

$$E + T + R = 1 \tag{4.2}$$

The transmittance T_i and reflectance R_i are related to the transmissivity τ_i and reflectivity ρ_i of the material via:

$$R_i = \rho_i + \frac{(1-\rho_i)^2 \rho_i \tau_i^2}{1-\rho_i^2 \tau_i^2} \tag{4.3}$$

$$T_i = \frac{(1-\rho_i)^2 \tau_i}{1-\rho_i^2 \tau_i^2} \tag{4.4}$$

In the case of two parallel, adjoined layers, the total transmittance and reflectance are given by:

$$T = \frac{T_1 T_2}{1-R_1 R_2} \tag{4.5}$$

$$R = R_1 + \frac{R_2 T_1^2}{1-R_1 R_2} \tag{4.6}$$

where indices 1 and 2 correspond to the first and second layers encountered in the incident ray's path, respectively. It must be noted that the order in which the layers are stacked relative to the incident ray affects the total reflectance since its constitutive terms are not interchangeable. This is important when it comes to the ITO-coated samples where R changes depending on which side is studied.

Uncoated glass

We begin by measuring R and T for a sample of uncoated borosilicate glass in order to compute the reflectivity and transmissivity of the material. Unsurprisingly, the transmittance of glass drops at $\lambda = 2.7\,\mu\text{m}$, plateaus up to $\lambda = 4.17\,\mu\text{m}$ before reaching a value of zero beyond this point (Figure 4.2). This means that the glass is completely opaque for $\lambda \geq 5$, which is convenient since the spectral range of the camera used is between 7.5 and 13 µm. Another typical characteristic of glass is the Christiansen point, at $\lambda \approx 8\,\mu\text{m}$ where the reflectivity is nearly zero [1].

ITO-coated glass (ITO side)

The transmittance curve preserves some of the features found for the uncoated glass, particularly the cutoff at $\lambda \approx 5\,\mu\text{m}$. The values in the region of maximum transmittance (for $\lambda \leq 2.7\,\mu\text{m}$), and at the plateau ($2.7\,\mu\text{m} < \lambda = 4.17\,\mu\text{m}$) are slightly lower because of the ITO coating. The reflectivity on the other hand increases with wavelength, with a peak at around 9.5 µm. The properties of the ITO layer can be deduced from Equations 4.5 and 4.6 (Figure 4.3). The monotonic rise of reflectance is characteristic of metallic surfaces, while the high value of transmittance can be explained by how thin the coating is (25 nm).

[1] cf. refractiveindex.info

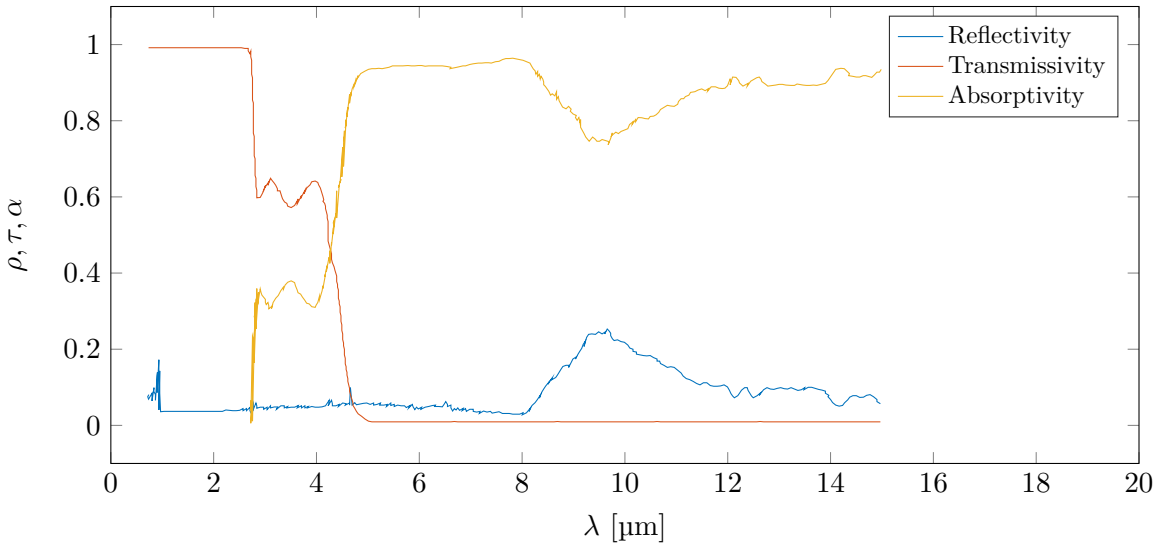

Figure 4.2: Reflectivity, Transmissivity and Absorptivity spectrum for the ITO-coated side.

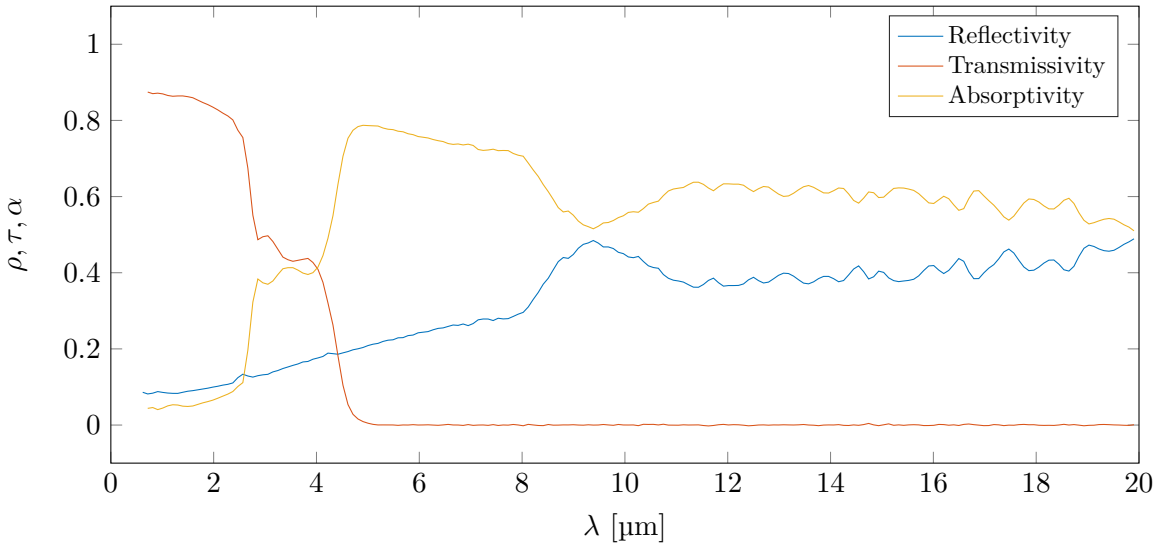

Figure 4.3: Reflectivity, Transmissivity and Absorptivity spectrum for the ITO-coated side.

ITO-coated glass (glass side)

As stated before, the transmittance remains the same for a two-layered sample (Figure 4.4), regardless of which side is exposed to the incident light. The reflectance curve is slightly altered, compared to that of the uncoated glass, for $\lambda \leq 5\,\mu m$, since the glass remains relatively transparent in this region. Beyond this point, the glass is opaque, and so the properties are the same as those of the uncoated sample.

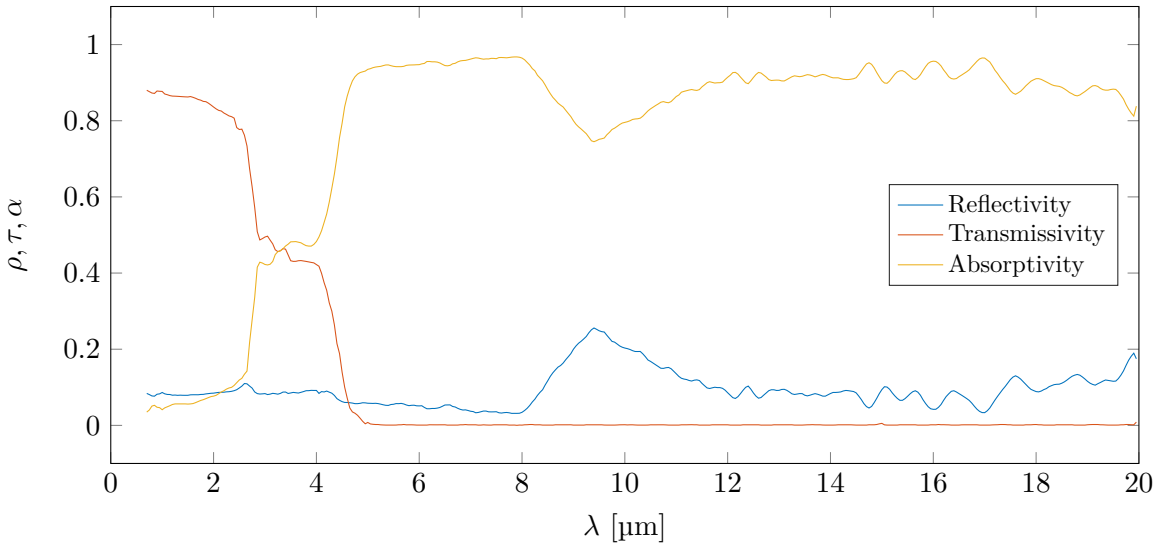

Figure 4.4: Reflectivity, Transmissivity and Absorptivity spectrum for the glass side.

4.2.3 Emissivity as a function of temperature

We now turn to studying the emissivity of the glass sheet and how it changes with temperature. In light of these results, an appropriate model is constructed that reduces the error in temperature measurements. The samples are heated inside the spectrometer and the spectral emitted flux $\phi_{\mathsf{sample}}(\lambda, T)$ is measured at different temperatures. The emissivity is computed relative to a reference (a bar painted in black that is inside the spectrometer) via:

$$\epsilon_{\lambda,\mathsf{sample}} = \frac{\phi_{\mathsf{sample}}(\lambda, T)}{\phi^0_{\mathsf{ref}}(\lambda, T)} \epsilon_{\mathsf{ref}} \tag{4.7}$$

where $\epsilon_{\mathsf{ref}} = 0.94$ is the emissivity of the black paint (assimilated to a gray-body) and $\phi^0_{\mathsf{ref}}(\lambda, T)$ the flux that it emits. The resulting spectrum is then integrated in the spectral range $[\lambda_1, \lambda_2]$ of the IR camera:

$$\epsilon_{\Delta\lambda} = \frac{\int_{\lambda_1}^{\lambda_2} \epsilon_\lambda L^0(\lambda, T) d\lambda}{\int_{\lambda_1}^{\lambda_2} L^0(\lambda, T) d\lambda} \tag{4.8}$$

where L^0 is the luminance of a black body. The range $\Delta\lambda$ is between 8 and 12 µm since the IR camera operates in the long-wave infrared (LWIR) band.

Spectral Emissivity of the ITO coated glass plate

The spectral emissivity is plotted for different temperatures in Figure 4.5 for the ITO-coated side. The emissivity hardly changes with temperature between 40 and 100 °C. As a reminder, the transmissivity is equal to zero in this spectral band, meaning that reflectance and emittance are related by $R + E = 1$.

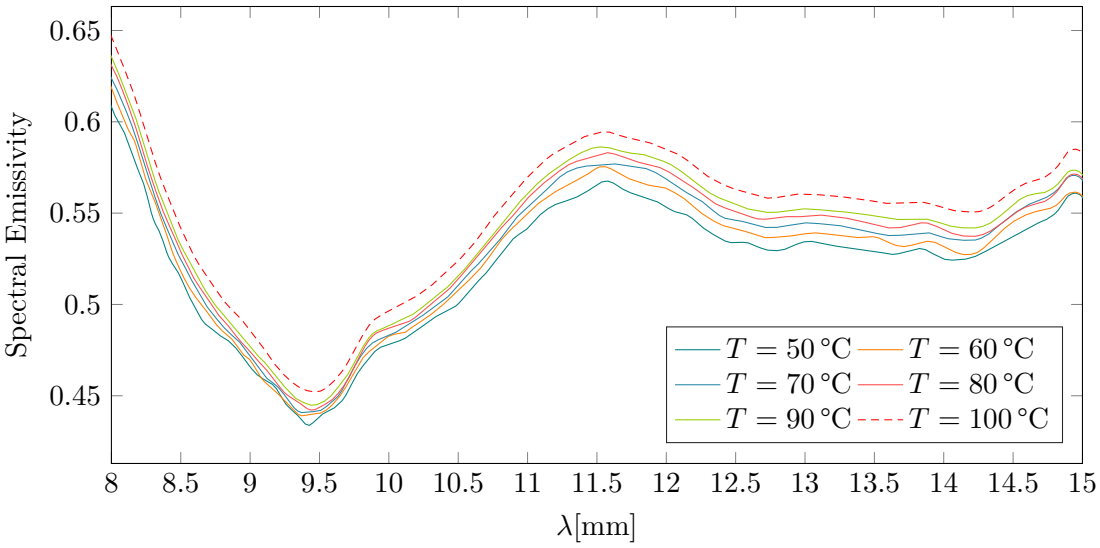

Figure 4.5: Spectral emissivity of the ITO-coated side of the plate for different values of the temperature T.

The integrated emissivity (Figure 4.7) decreases at $T = 40\,°\text{C}$ and increases afterwards. Polynomials of degrees 0, 1 and 2 are used to fit the variation of emissivity and their absolute error over the temperature range is given by:

$$\Delta\epsilon = |\epsilon - \overline{\epsilon}| \tag{4.9}$$

The zero-order polynomial gives the highest value of $\Delta\epsilon/\epsilon$ at 8% for low temperature, and quickly decreases thereafter. Practically, we also need to assess the error in temperature measurements. It can be computed using $\Delta\epsilon$ and Planck's Law:

$$\frac{\Delta\epsilon}{\epsilon} = \left|\frac{c_2/\lambda T}{\exp\left(-c_2/\lambda T\right) - 1}\right| \frac{\Delta T}{T} \tag{4.10}$$

The constant model, $\epsilon = 0.53$, gives the highest value of $\Delta\epsilon$ at 8% for low temperature, and quickly decreases thereafter. The low value of emissivity was expected since the coating is a metallic oxide. The first-order polynomial produces a peak error of 5% at $T = 55\,°\text{C}$ while the second-order polynomial reaches 3% at $T = 40\,°\text{C}$. The deviations of the respective polynomials fits from the experimental data lead to discrepancies in temperature of around 7 to 10 °C. If this side of the plate were to be used, a smoothing spline would have been a more appropriate that these polynomials, as it produces deviations of less than 0.7 °C over the range of temperatures. However, the emissivity on this side is relatively low at $\epsilon = 0.53$, which means that most of the measurement errors will be caused by reflection from the surroundings.

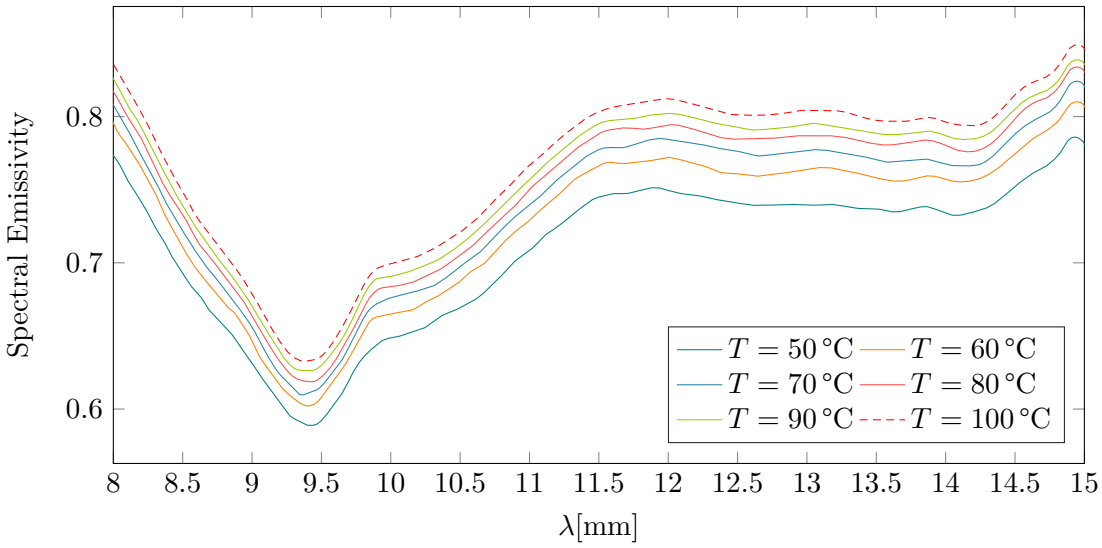

Figure 4.6: Spectral emissivity of the uncoated side of the plate

ITO Glass, uncoated side

The same analysis is performed on the uncoated side of the glass sheet. The zero ($\epsilon = 0.8$), first and second order fittings also fail to accurately represent emissivity variations with temperature. In this case, a smoothing spline is used in order to reduce the errors stemming from the dependence of surface emissivity on temperature. Considering the relatively high value of ϵ, the temperature measurements will be performed on the uncoated side of the plate.

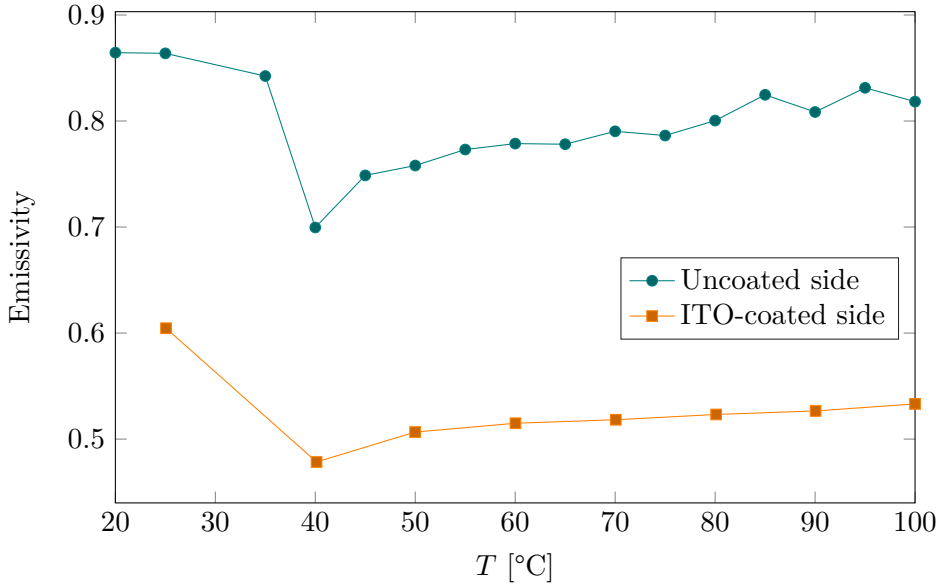

Figure 4.7: Integrated emissivity in the band of the infrared camera for the coated and uncoated sides of the plate.

4.3 Computing the heat transfer coefficient h

The local heat transfer coefficient h is deduced from Newton's cooling law:

$$\phi_{\mathsf{c,osc}} = h\,(T_{p,\mathsf{osc}} - T_f) \tag{4.11}$$

where $\phi_{\mathsf{c,osc}}$ is the heat flux of forced convection, $T_{p,\mathsf{osc}}$ the local temperature of the cooled surface, and T_f the temperature of the fluid. The only quantity that is directly measurable is T_f. The ambient temperature T_∞ is equal to T_f. Since the aim is to compute the time-averaged Nusselt number, thermal equilibrium is assumed. In order to find ϕ_{conv} we begin by applying energy conservation on the heated plate (see Figure 4.8):

$$\sum \Phi_{\mathsf{in}} = \sum \Phi_{\mathsf{out}} \tag{4.12}$$

$$\phi_{\mathsf{elec}} = \phi_{\mathsf{c,osc}} + \phi_{\mathsf{c,nat}} + \phi_{\mathsf{rad,osc}} + \phi_{\mathsf{rad,cam}} \tag{4.13}$$

where

- $\phi_{\mathsf{elec}} = U^2/RA$: electrical heat flux, where U is the applied voltage, R the electrical resistance of the ITO layer, and A the effective area of the heated surface.
- $\phi_{\mathsf{c,osc}} = h\,(T_{p,\mathsf{osc}} - T_f)$: heat flux due to forced convection
- $\phi_{\mathsf{c,nat}} = h_{\mathsf{nat}}\,(T_{p,\mathsf{cam}} - T_f)$: heat flux due to natural convection on the other side of the plate, the Churchill/Chu correlation (Incropera et al. (2007)) was used to estimate h_{nat}.
- $\phi_{\mathsf{rad,osc}} = \epsilon_1\sigma(T^4_{p,\mathsf{osc}} - T^4_\infty)$: heat flux due to radiation on the oscillator's side, where $\epsilon_1 \approx \mathsf{const.} \approx 0.56$ is the emissivity of the ITO layer, and σ the Stefan-Boltzmann constant.
- $\phi_{\mathsf{rad,cam}} = \epsilon_2\sigma(T^4_{p,\mathsf{cam}} - T^4_\infty)$: heat flux due to radiation on the camera's side, where $\epsilon_2 \approx \mathsf{const.} \approx 0.79$ is the emissivity of the borosilicate glass.

The emissivities ϵ_1 and ϵ_2 were assumed to be constant for convenience, the uncertainty due to this assumption is taken into account in the uncertainty analysis.

Next, in order to find $T_{p,\mathsf{osc}}$ from the temperature measured on the camera's side, we use Fourier's law, supposing that the plate is made out of a homogeneous material of thermal conductivity k:

$$T_{p,\mathsf{osc}} = T_{p,\mathsf{cam}} - \frac{e}{k}\,(\phi_{\mathsf{rad,cam}} + \phi_{\mathsf{c,nat}}) \tag{4.14}$$

where e is the thickness of the glass plate. To accurately compute h, we find the values of $T_{p,\mathsf{osc}}$ for arbitrary values of $\phi_{\mathsf{c,osc}}$ (by changing ϕ_{elec}). It is clear from Equation 4.11 that h is none other than the slope of the line $\phi_{\mathsf{c,osc}} = f(T_{p,\mathsf{osc}})$. Which means that we have to find a linear fit for the data $\phi_{\mathsf{c,osc}}$, whose slope is equal to h.

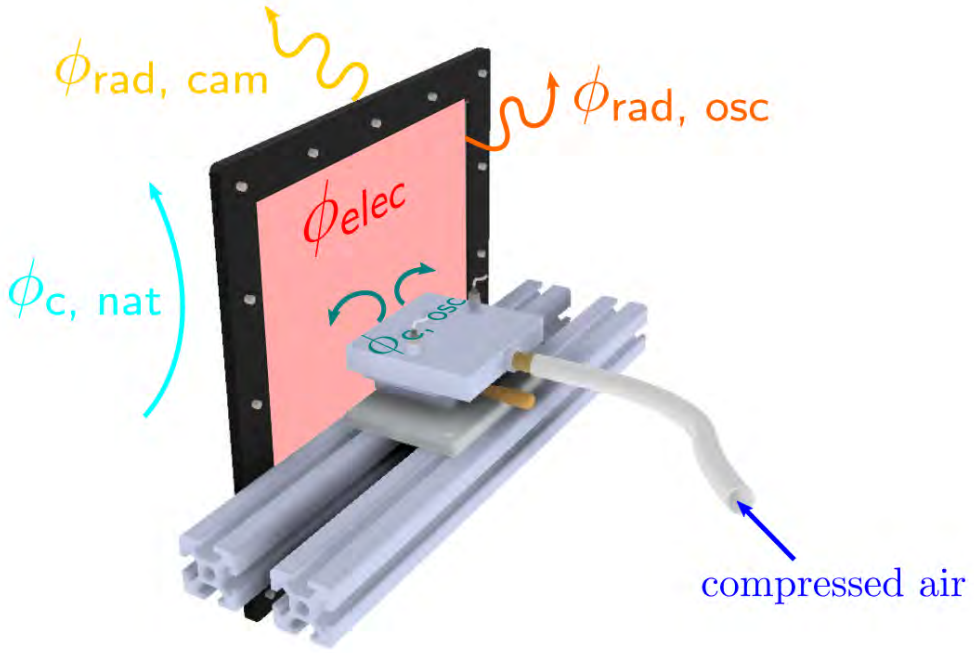

Figure 4.8: Illustration of the heat flux densities in Equation 4.13.

Finally, having found h, the Nusselt number can be computed:

$$\mathsf{Nu} = \frac{hD_h}{k_{\mathsf{air}}} \tag{4.15}$$

where D_h is the hydraulic diameter of the exit slots ($\simeq 2w$) and k_{air} is the thermal conductivity of the impinging flow of air.

4.3.1 Uncertainty estimation

The uncertainty propagation method as outlined in Kline and McClintock (1953), was used here to find the uncertainty interval w_{Nu} of the Nusselt number from the uncertainty intervals w_{x_i} of its constitutive independent variables xi:

$$w_{\mathsf{Nu}} = \left[\sum_i \left(\frac{\partial \mathsf{Nu}}{\partial x_i} w_{x_i}\right)^2\right]^{1/2} \tag{4.16}$$

For the sake of clarity, error bars are not included in the forthcoming plots of the Nusselt number. Values of the uncertainty for the Nusselt number are around 5 to 10% which is typical for this type of measurements.

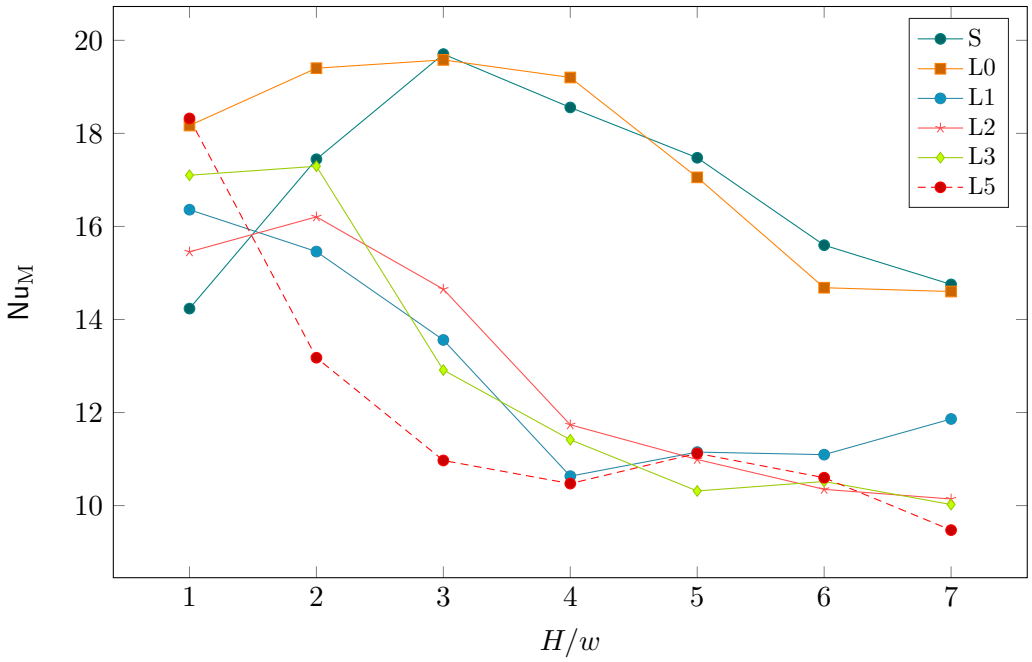

Figure 4.9: Peak Nusselt number as a function of standoff distance H/w for the steady and pulsating case at $\mathrm{Re}_w = 3200$

Table 4.1: List of prototypes used for the thermal study with the corresponding frequency ranges

Prototype	Frequency range (Hz)
L0	985 – 1240
L1	771 – 940
L2	618 – 723
L3	510 – 643
L4	438 – 561
L5	346 – 439

4.4 Results

4.4.1 Peak Nusselt Number

We begin by looking at the peak Nusselt number for steady and pulsed jets for different impact distances H/w, pulsation frequencies f and average velocity Reynolds number Re_w. The frequency range of the different prototypes is given in Table 4.1.

For the smallest Reynolds number considered, $\mathrm{Re}_w = 3200$ ($p_{in} = 1.5\,\mathrm{bar}$), the different curves (Figure 4.9) follow two distinct behaviors. On the one hand, the curves corresponding to S and Lg0 present a peak for $H/w \approx 3$. This behavior was expected for the steady case, and was demonstrated early on by Gardon and Akfirat (1966). The authors explained that this phenomenon is a result of how velocity and turbulence intensity change along the

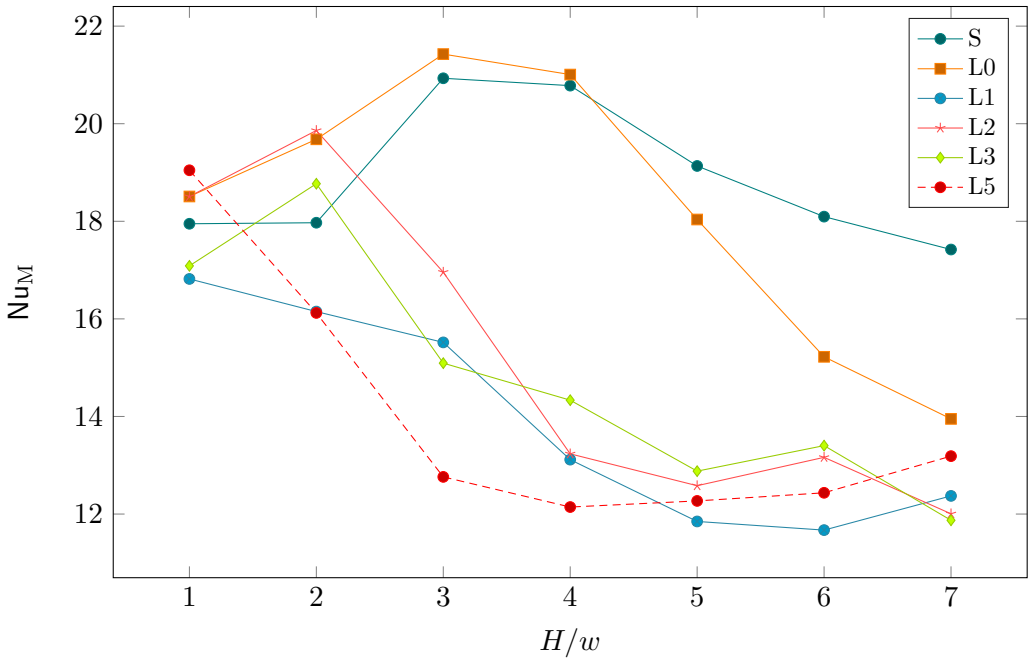

Figure 4.10: Peak Nusselt number as a function of standoff distance H/w for the steady and pulsating case at $\mathsf{Re}_w = 5200$

axis of the jet. From the base of the jet to the tip of the potential core, which is typically at 4 to 6 jets widths downstream from the orifice, the velocity along the jet axis remains constant while the turbulence intensity increases. The net result is an increase in stagnation Nusselt number up to the potential core length. Beyond that point, the turbulence intensity continues to rise, but is offset by the rapidly decaying velocity, which results in a decrease in peak Nusselt number beyond the potential core. In the same study, the authors showed that increasing the turbulence level at the nozzle exit promoted heat transfer for standoff distances shorter than the length of the potential core.

The remaining cases, Lg1 through L5, nearly overlap (within the error margins) and do not exhibit a distinctive peak at $H/w = 3 - 4$. Only in cases L2 and L3 can a local maximum be seen for $H/w = 2$. Nearly all the pulsating cases outperform the steady case for small standoff distances of one to two initial jet widths.

Increasing the Reynolds number up to 5200 ($p_{in} = 2.0\,\mathrm{bar}$), the peak Nusselt curves (Figure 4.10) can still be sorted into categories: the S and Lg0 cases that have prominent peak at $H/w = 3 - 4$ and the lower frequency cases either decrease monotonically or have a peak at $H/w = 2$. However, for this value of the Reynolds number, the Nusselt number decreases rapidly for the Lg0 compared to S for standoff distances greater than the potential core length (i.e., for $H/w > 4$). This is a departure from Gardon and Akfirat (1966) who found that increasing initial turbulence levels led to an increase in peak Nusselt number over a range of H/w going from 0 to 25.

And finally, for $\mathsf{Re}_w = 6700$ ($p_{in} = 2.5\,\mathrm{bar}$), nearly all of the pulsating cases improve heat transfer for values of H/w less than 2 (Figure 4.11). For Lg0, the enhancement

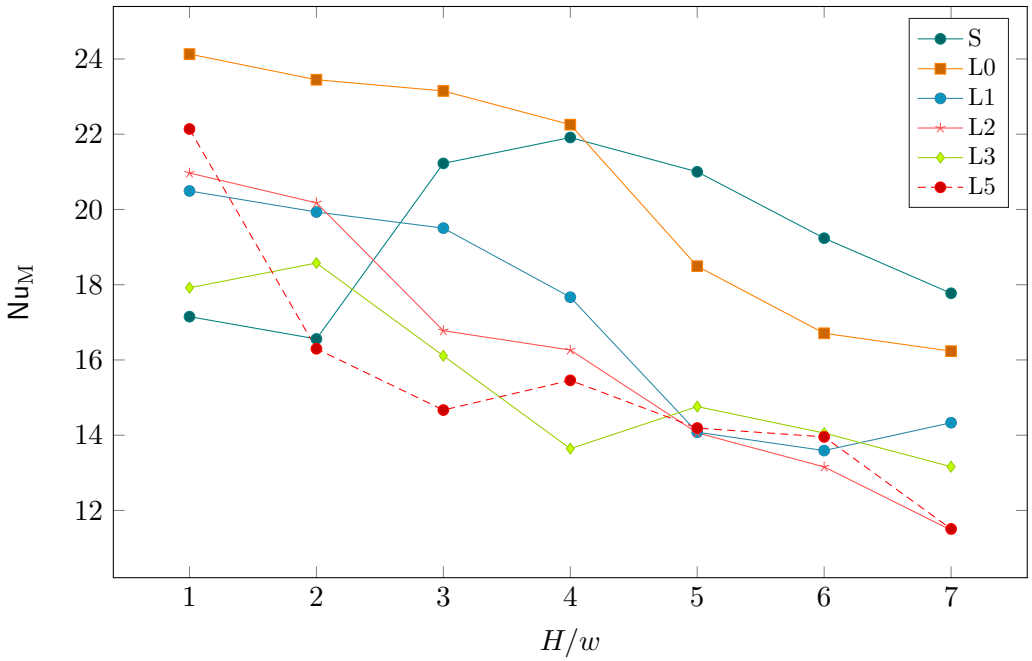

Figure 4.11: Peak Nusselt number as a function of standoff distance H/w for the steady and pulsating case at $\mathsf{Re}_w = 6700$

relative to the steady case is further amplified, even reaching values of up to 40%. The only noticeable difference compared to the lower Reynolds number cases is the slow decrease of the Lg1 curve for small values of H/w. The Lg0 and Lg1 curves seem to parallel one another but at different levels.

4.4.2 Mean Nusselt Number

The average of the Nusselt number is performed over a line which encompasses both impinging jets produced by the device and the surrounding space. The mean Nusselt curves resemble, qualitatively, the peak Nusselt curves presented earlier. The major difference worth mentioning is the further improvement of heat transfer, relative to the steady case, for small impact distance. Pulsating the jets at lower frequencies seems to have a greater effect on the mean Nusselt number than it does on the peak for $H/w \approx 1-3$. Here again, for $\mathsf{Re}_w = 6700$, the Lg1 curve departs from the other low frequency curves, decreasing at a slower rate in the interval $H/w = 2-4$.

4.4.3 Scaling of convective heat transfer enhancement

In order to make sense of these results, we have attempted to find a scaling law between an enhancement ratio $\delta\mathsf{Nu}_0$ and the relevant parameters of the experiments, to wit, the frequency, the impact distance and the average velocity of the jet. Persoons et al. (2013)

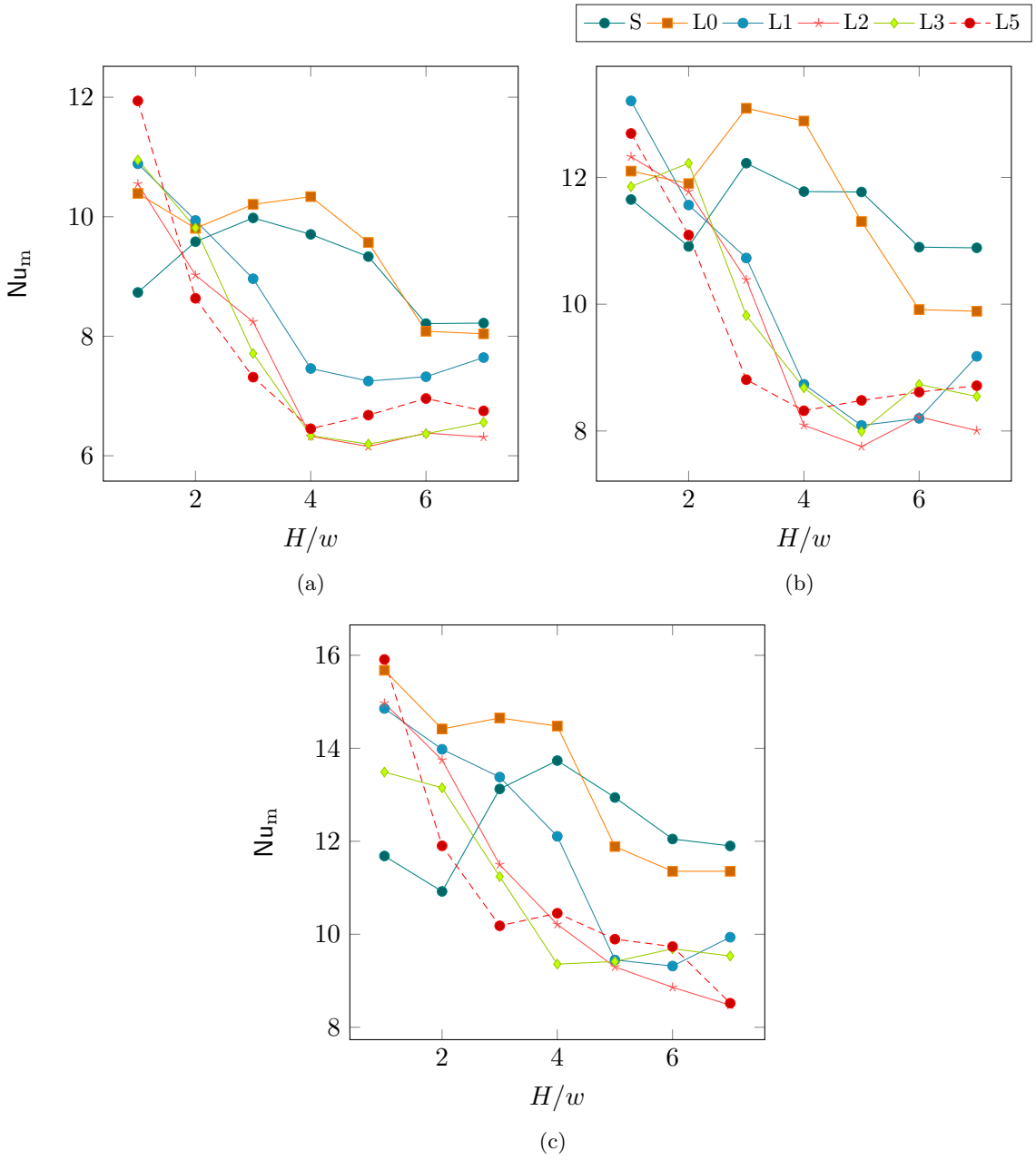

Figure 4.12: Mean Nusselt number versus standoff distance H/w for Re_w = (a) 3200, (b) 5200, and (c) 6700

used the following general power law:

$$\delta\mathsf{Nu} = b + a\left(\frac{fH^p}{U_m^n}\right)^q \tag{4.17}$$

to identify the appropriate scaling parameters for heat transfer enhancement of pulsed round jet. The enhancement parameter is defined as

Table 4.2: Coefficients of the general power law (Eq. 4.17) for peak and overall mean Nusselt numbers from Persoons et al. (2013) and the data in the present study.

Source	Dependent variable	Independent variable	Coefficients b	a	q	p	n	R^2
Persoons et al. (2013)	$\delta\mathsf{Nu}_\mathrm{M}$	fH^p/U_m^n	−0.071	0.27	1.06	0.78	0.71	0.81
Persoons et al. (2013)	$\delta\mathsf{Nu}_\mathrm{M}$	$\mathsf{Sr}(H/w)$	−0.079	0.805	0.836	1	1	0.80
Persoons et al. (2013)	$\delta\mathsf{Nu}_\mathrm{m}$	fH^p/U_m^n	0	0.087	0.861	0.13	0.54	0.83
Present study	$\delta\mathsf{Nu}_\mathrm{M}$	fH^p/U_m^n	−1.264	0.054	0.190	−1.089	−0.627	0.68
Present study	$\delta\mathsf{Nu}_\mathrm{m}$	fH^p/U_m^n	−1.274	0.117	0.136	−1.355	−0.509	0.67

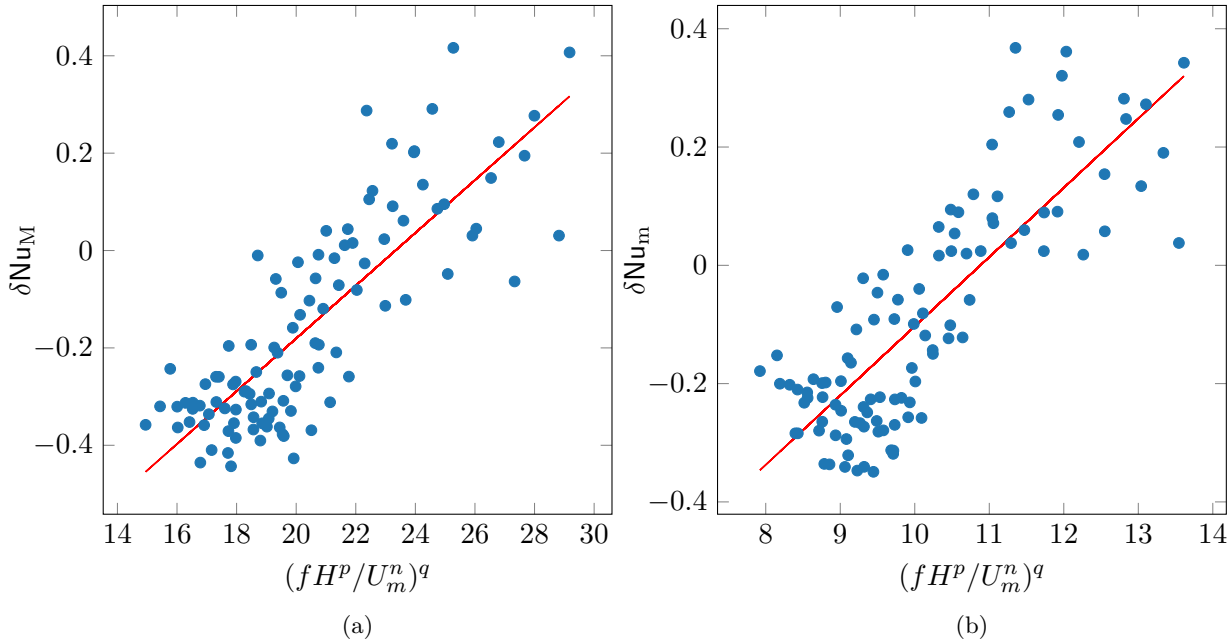

Figure 4.13: Scaling of (a) $\delta\mathsf{Nu}_\mathrm{M}$ and (b) $\delta\mathsf{Nu}_\mathrm{m}$ using Eqs. 4.20 and 4.19, respectively.

$$\delta\mathsf{Nu} = \left(\mathsf{Nu}_\mathrm{pulsed} - \mathsf{Nu}_\mathrm{steady}\right)/\mathsf{Nu}_\mathrm{steady} \tag{4.18}$$

By fitting the stagnation point enhancement ratios, they were able to find the general power law whose coefficients are presented in Table 4.2, which has a relatively high coefficient of determination R^2 of 0.81. Noticing that the exponents p and n are close to unity, the authors also used a modified Strouhal number defined as $fH/U_m = \mathsf{Sr}(H/w)$ (where $\mathsf{Sr} = fD/U_m$), to scale the results (Table 4.2, second row).

The present data were also fitted using the same general power law (Eq. 4.17). Although the results of this study are not a priori comparable to those of Persoons et al. (2013) due

to the difference in both geometry and operating parameters, the contrast between the results remains striking. As already noted in previous sections, improvement in peak heat transfer is achieved by reducing the standoff distance, and increasing the frequency. This enhancement is more noticeable for larger values of the Reynolds number. These three observations are reflected in the signs of the coefficients p, n and q. Of these three, p has the largest relative value, indicating that improvement due to pulsation is particularly sensitive to the distance between the jet and the target surface. Unlike Persoons et al. (2013), the frequency has a smaller influence on improvement than do the other parameters. Although, admittedly, this might be due to the range of frequencies used in the present study.

Turning to the enhancement parameter $\delta\mathsf{Nu}_\mathrm{m}$, the signs of the coefficients remain unchanged although the absolute value of p becomes noticeably larger, indicating a higher sensitivity of the mean Nusselt number to standoff distance. The two general power laws based on the current data have coefficients of determination of 68 and 67%, respectively.

In the same vein as Persoons et al. (2013), the coefficients were rounded, and the laws were rewritten to reveal a correlation between the enhancement ratio, and dimensionless groups Sr, Re_w and H/w:

$$\delta\mathsf{Nu}_\mathrm{m} = b_\mathrm{m} + a_\mathrm{m}\left(\mathsf{SrRe}_w^{3/2}\,(H/w)^{-3/2}\right)^{q_m} \tag{4.19}$$

$$\delta\mathsf{Nu}_\mathrm{M} = b_\mathrm{M} + a_\mathrm{M}\left(\mathsf{SrRe}_w^{5/3}\,(H/w)^{-1}\right)^{q_M} \tag{4.20}$$

where $[a_\mathrm{m}, b_\mathrm{m}, q_\mathrm{m}] = [0.130, -1.279, 0.124]$ for the mean Nusselt number and $[a_\mathrm{M}, b_\mathrm{M}, q_\mathrm{M}] = [0.035, -1.182, 0.218]$ for the peak with $R^2 = 0.671$ and 0.677, respectively (Figure 4.13).

4.4.4 Nusselt number distribution

Finally, the spatial distribution of the Nusselt number on the heated plate is considered. We focus our attention on cases with an impact distance between 2 and 5 jet widths and observe how the Nusselt profiles evolve with increasing mean jet Reynolds number. For the lowest impact velocity, corresponding to $\mathsf{Re}_w = 3200$ (Figure 4.14a), all of the distributions exhibit a clear peak at the impingement point $x/w = 11$, with no salient secondary features to be seen. The steady jet has the lowest performance for $x/w \geq 14$, i.e. in the wall jet region. In the intermediate region, $x/w \leq 9$, it slightly outperforms the L5 case, but remains short of the remaining pulsed cases. For $\mathsf{Re}_w = 5700$ (Figure 4.14b), the steady case shows a relative improvement in both the intermediate and stagnation regions. The heat transfer however quickly deteriorates in the wall jet region, performing worse than all the pulsed cases. For this value of the Reynolds number, secondary features become visible in the curves of the pulsed cases. In the stagnation region, the sharp peak observed for lower Re_w was replaced by either a relatively flat (e.g., L5) or slanted (Lg1) top, as if a local minimum occurs at the stagnation point. In some cases, another feature can be seen in the intermediate region (e.g., at $x/w = 8$ for Lg0 and $x/w = 5$ for L3) that resembles an inflection point or the beginning of a secondary peak. Increasing the Reynolds number one

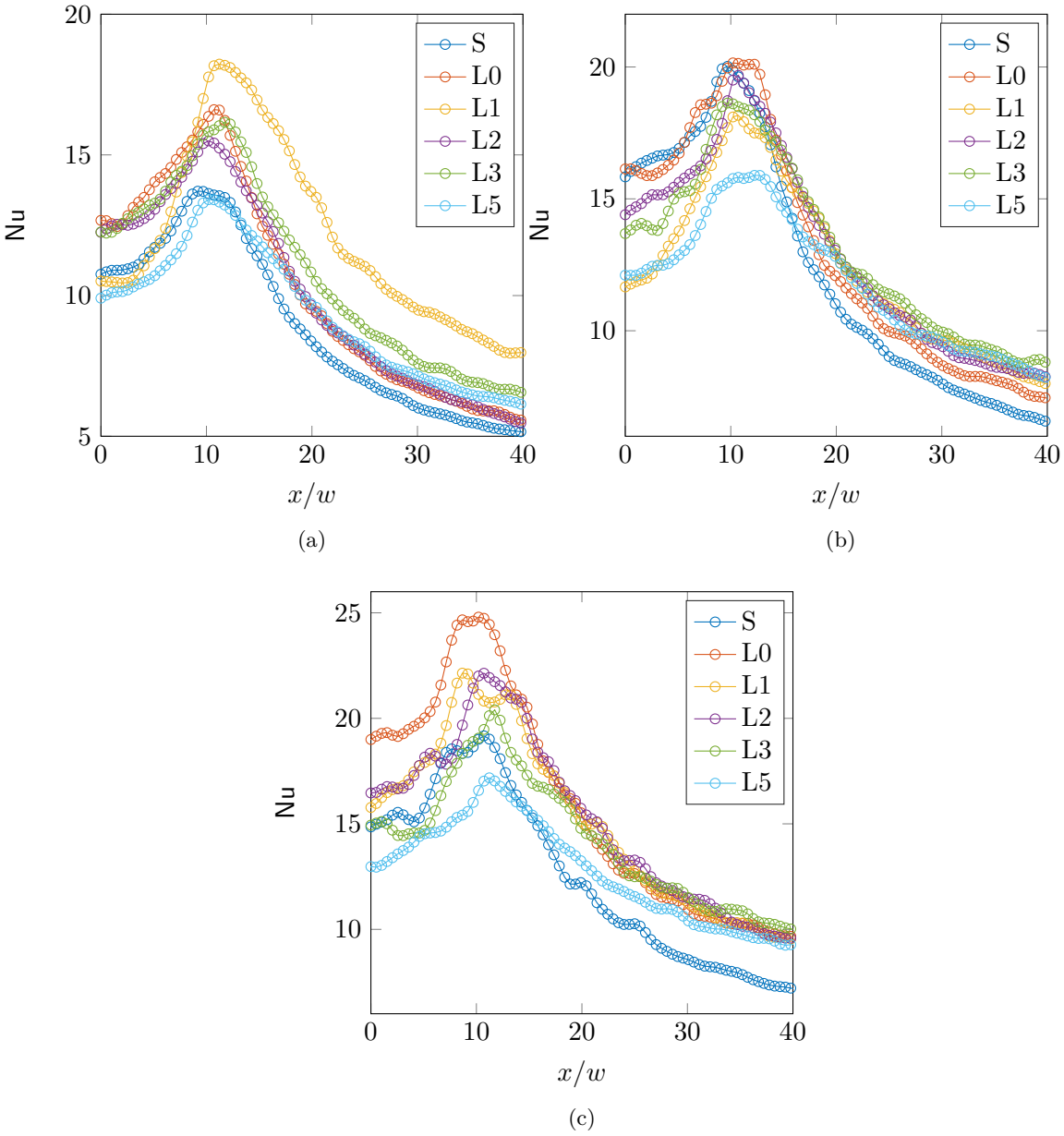

Figure 4.14: Nusselt number distribution over the plate for $H/w = 2$ and (a) $\mathsf{Re}_w = 3200$, (b) $\mathsf{Re}_w = 5700$ and (c) $\mathsf{Re}_w = 6700$.

more time made these features much more prominent for both the steady and pulsed cases (Figure 4.14c). A clear secondary peak can be observed in the intermediate region, whose location changes with pulsation frequency without following a clear trend. In certain cases, such as S and Lg1, the peak at the stagnation is replaced by a prominent local minimum surrounded by two peaks. As was noted for lower Reynolds numbers, the steady jets seemed particularly inefficient in the wall jet region and only consistently outperformed case L5 in the stagnation and intermediate zones.

The situation changes for the steady jet when the target plate was moved downstream

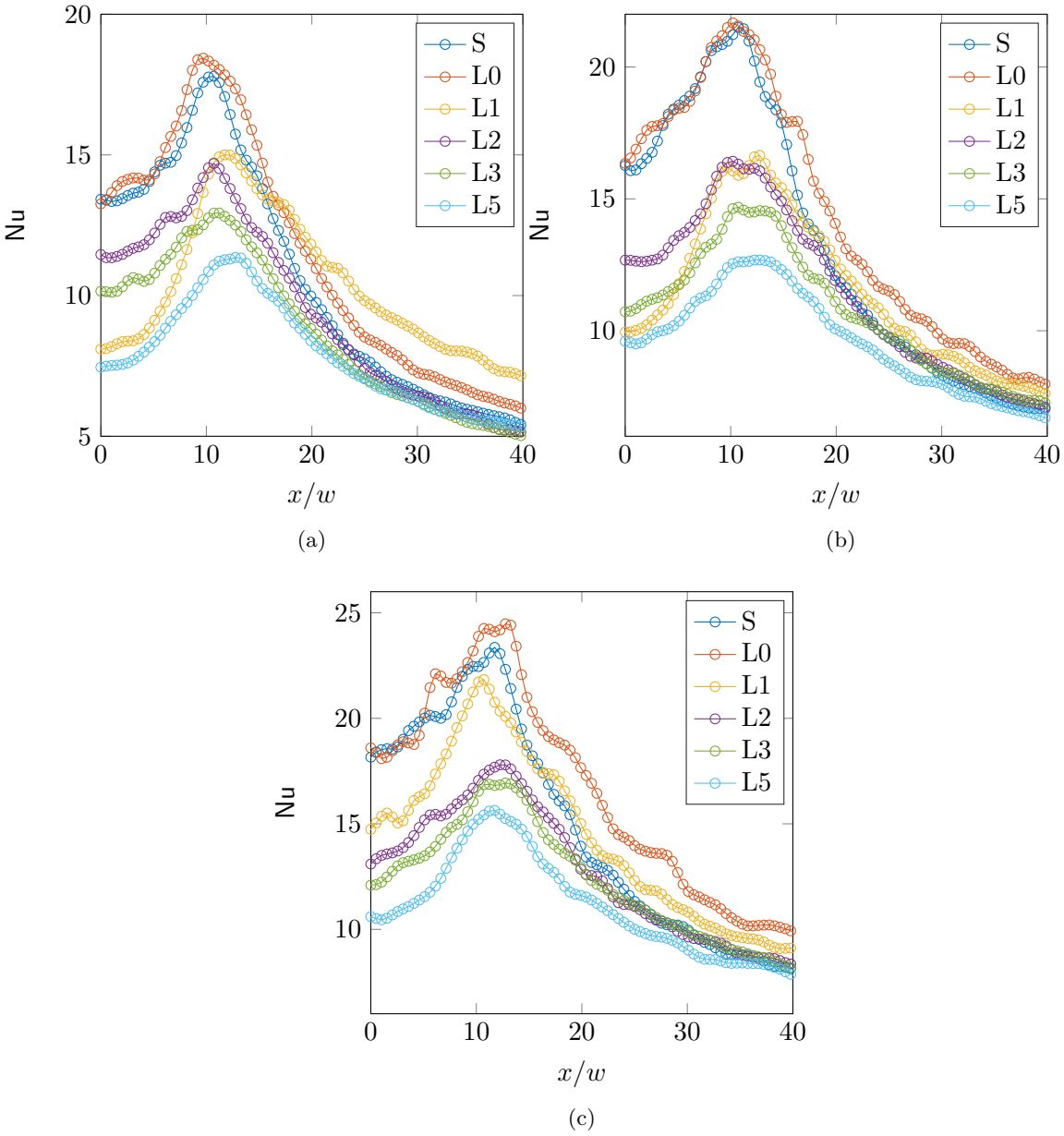

Figure 4.15: Nusselt number distribution over the plate for $H/w = 3$ and (a) $\mathsf{Re}_w = 3200$, (b) $\mathsf{Re}_w = 5700$ and (c) $\mathsf{Re}_w = 6700$.

to $H/w = 3$ (Figure 4.15). For the lowest Reynolds number considered (Figure 4.15a), the distribution of S and Lg0 are similar, although the Lg0 case has a marginal advantage over the entire range of x/w. For cases L2 through L5, overall performance seemed to decrease with pulsation frequency for all Reynolds numbers considered. The Lg1 curve had a particularly low performance in the intermediate region but compensate in the wall jet region where it outperforms all the other cases. For a Reynolds number of 5700, the curves seems to fall into two groups. On one hand, S and Lg0 that are similar except in the wall jet region where Lg0 performs better, and on the other the lower frequency curves

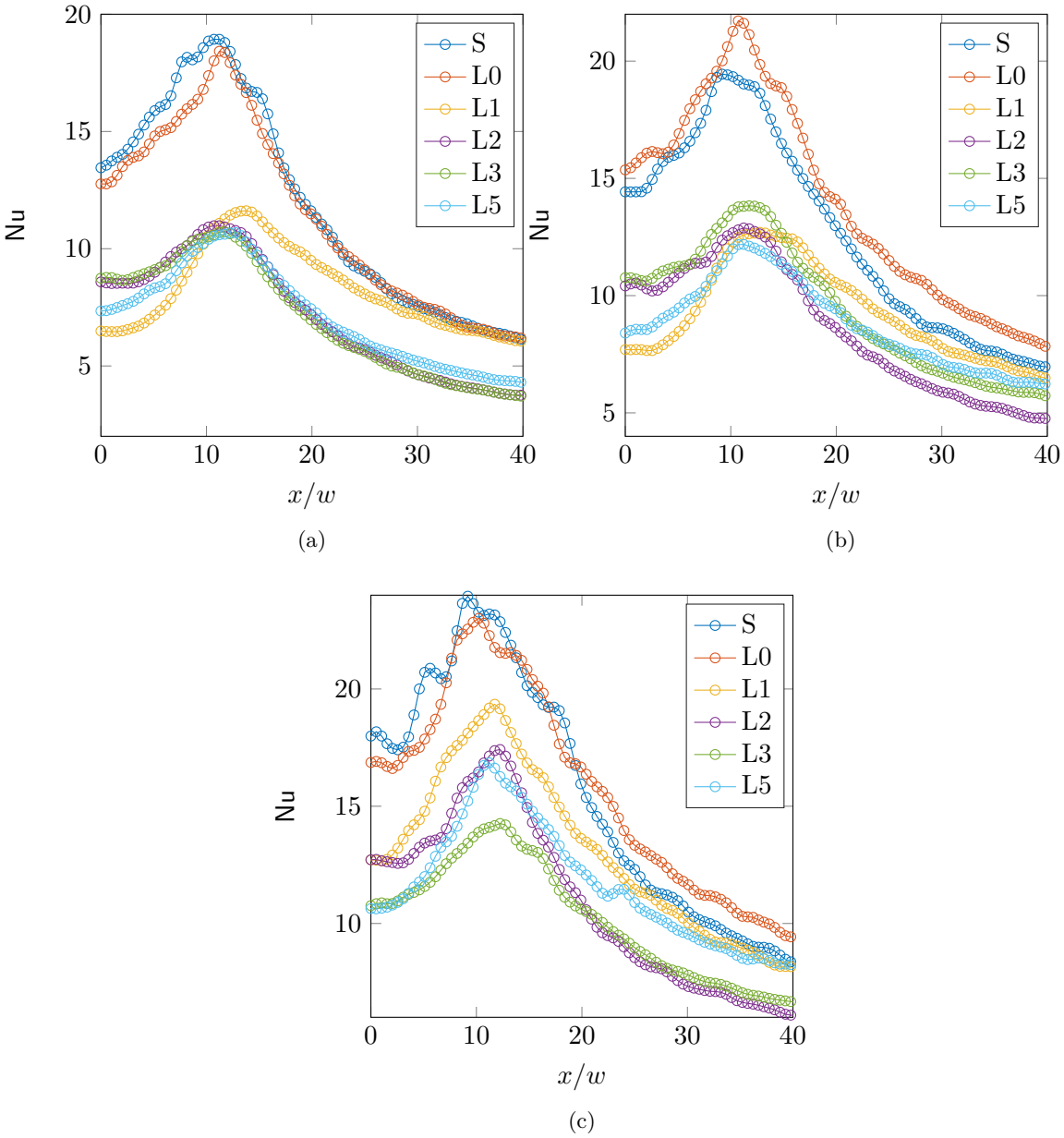

Figure 4.16: Nusselt number distribution over the plate for $H/w = 4$ and (a) $\mathsf{Re}_w = 3200$, (b) $\mathsf{Re}_w = 5700$ and (c) $\mathsf{Re}_w = 6700$.

whose efficiency decreases with frequency. For the highest Reynolds number (Figure 4.15c), the performance of Lg1 is improved, making it closer to S and Lg0. The remarks made earlier regarding the secondary features of the Nusselt distribution can also be made here.

For $H/w = 4$ (Figure 4.16), there is a distinct divide between the S and Lg0 and the remaining cases, as was noted in previous sections regarding the peak and average Nusselt numbers. The lower frequency cases do not seem to follow any particular trend, nearly overlapping in most situations and over larges ranges of x/w. The S and Lg0 cases can also be said to nearly overlap, with Lg0 outperforming S for some values of Re_w, and especially

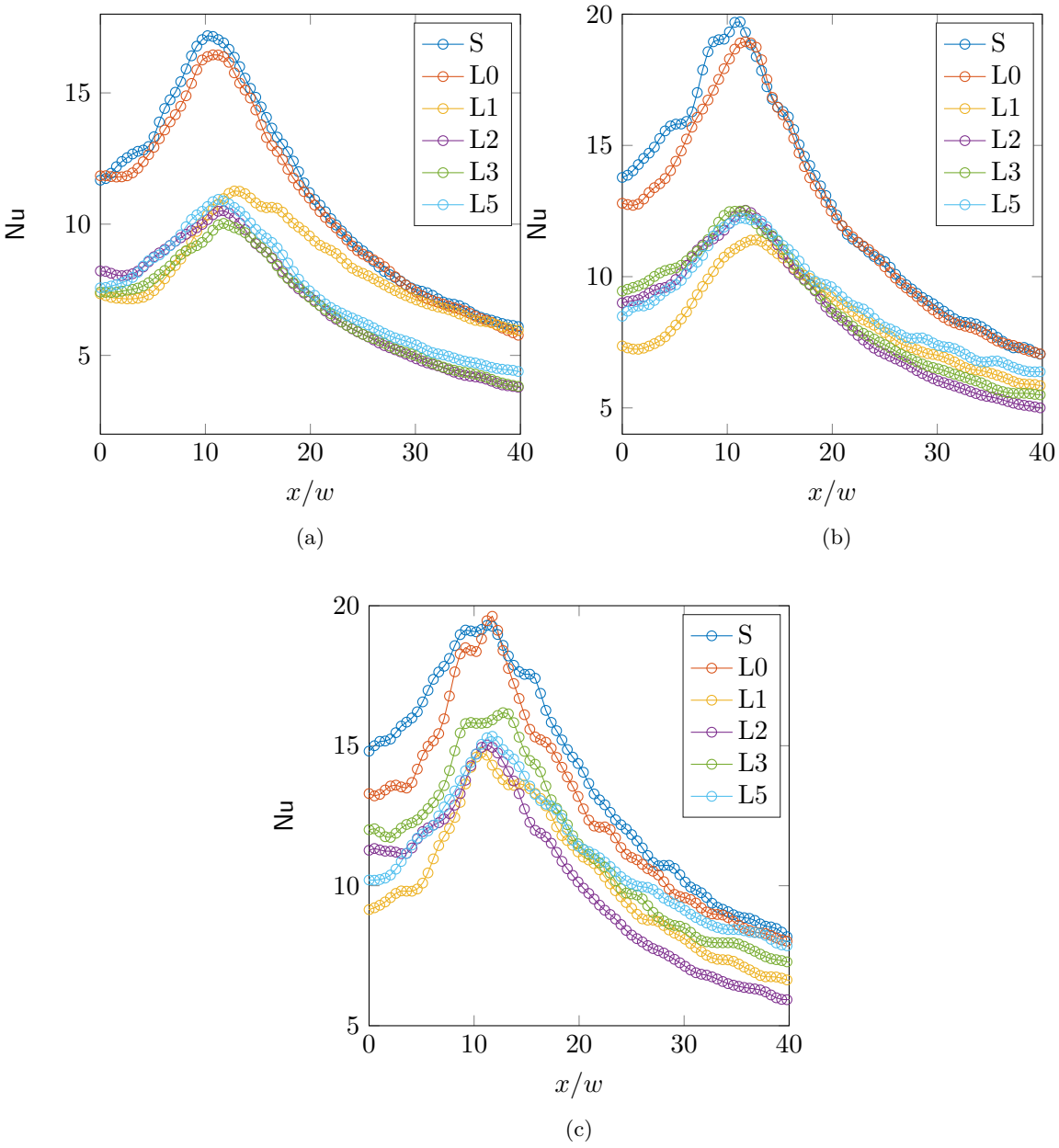

Figure 4.17: Nusselt number distribution over the plate for $H/w = 5$ and (a) $\mathsf{Re}_w = 3200$, (b) $\mathsf{Re}_w = 5700$ and (c) $\mathsf{Re}_w = 6700$.

in the wall jet region. Once more, increasing Re_w gives rise to secondary features for all the cases presented.

Finally, for $H/w = 5$ (Figure 4.17), the S and Lg0 remain nearly identical over the range of x/w for $\mathsf{Re}_w = 3200$ (Figure 4.17a) and 5700 (Figure 4.17b). Similarly, the lower frequency cases nearly overlap, the only exception being Lg1 which had higher efficiency in the wall jet region compared to L2-L5. For $\mathsf{Re}_w = 6700$ (Figure 4.17a) the gap between the different cases is reduced, especially in the wall jet region. In the stagnation region,

the S and Lg0 remain clearly ahead of the rest, with the S case having wider peak and performing better than Lg0 in the intermediate region.

4.5 Concluding Remarks

In this experimental study, fluidic oscillators were used to produce pulsed impinging jets that were compared to equivalent steady jets in terms of heat transfer performance. The aim was to find the values of average Reynolds number, impact distance and pulsation frequency that lead to an enhancement in heat transfer. An ITO-coated glass plate was used as a heating surface, and the Nusselt number was computed from IR temperature measurements in order to quantify performance. The different prototypes used to produce the steady and pulsed jets were made by stereolithography using a medical-grade 3D printer. The main findings can be summarized in four points:

- It is possible to enhance heat transfer by pulsating the jet, especially at high frequencies, by up to 42%, depending on the average Reynolds number and the impact distance.
- The Nusselt number behaves differently above a certain jet pulsation frequency. For low frequencies (Lg1-L5, $f \leq 900\,\mathrm{Hz}$), and with few exceptions, the peak and average Nusselt numbers decrease monotonically with standoff distance. For higher frequencies (Lg0, $f \approx 1100\,\mathrm{Hz}$), the peak and average Nusselt numbers exhibit a peak at around $H/w = 4$, which corresponds to the potential core length. The Nusselt curve is then similar to that of the steady case, but with higher values for $H/w \lesssim 4$ and lower values for $H/w \gtrsim 4$
- By fitting the data using a general power law, used previously for axisymmetric impinging jets, the sensitivity of the enhancement ratio to frequency, standoff distance and average jet velocity was shown. Unlike the previously studied axisymmetric jets, pulsating plane jets lead to significant enhancement for small impact distances, which is further amplified by increasing the Reynolds number of the jet.
- The effect of the impact distance is more prominent in the average Nusselt number enhancement ratio, leading us to believe that pulsating the jet in the range of frequencies considered has an extended spatial effect around the impact point especially for small values of H/w.

This last observation, coupled with the fact that these devices are compact and self-excited, can be advantageous in situations where the envisaged cooling solution must comply with stringent constraints on space and weight.

There is still a number of factors that need to be considered in order to understand how jet pulsation affects heat transfer, such as the waveform of the pulsation, the initial jet geometry and multiple jet interaction, just to name a few. Finally, on a more technical note, it is worth noting that the robust nature of fluidic oscillators, compared to other devices that produce pulsed flows, should be tempered with the knowledge that they induce large pressure drops and produce a lot of noise. So the question remains as to whether these cons are outweighed, in any given application, by the compactness, low-maintenance and independence of the oscillator.

"Dis-moi comment l'on te cherche, je te dirai qui tu es."

La Formation de l'esprit scientifique
Gaston Bachelard

5

Numerical Simulations

The fluid inside an oscillator evolves into a landscape of elementary flows that interact with one another giving rise to a periodic behavior. At the inlet, a sonic channel flow turns into a jet as the fluid enters the switching zone where it slowly develops into a channel flow, part of which goes through the feedback loops while the other exits the oscillator through the outlet channels. At the same time, pressure waves travel along the feedback loops, dictating the frequency of oscillation. Outside the oscillator, a pair of pulsating jets issue from the slot orifices and impinge onto a flat surface, producing a stagnation region followed by a wall jet, where laminar-to-turbulent transition can occur. The simulation models must be able to accurately take into account all of these phenomena in order to offer reasonable predictions of the oscillator's behavior and of the heat transfer performance of the pulsating jets that it produces. In this chapter, two approaches were taken: first, a series of two-dimensional simulations, based on RANS models are performed, verified then validated against experimental data. Both the internal and external flows are studied via pressure measurements inside the feedback loops and hot-wire measurements of the pulsating jets. Second, a series of three-dimensional simulations relying on Hybrid RANS/LES models were performed on part of the flow, namely the exit channels and the impinging jet. Data from experiments are used to set the pulsating inlet condition of this truncated system.

5.1 Introduction

The following set of equations underlie most, if not all of the problems in fluid dynamics:

$$\frac{\partial \rho}{\partial t} + \nabla \cdot (\rho \mathbf{U}) = 0 \tag{5.1}$$

$$\frac{\partial}{\partial t}(\rho \mathbf{U}) + \nabla \cdot (\rho \mathbf{U}\mathbf{U}) = -\nabla p + \nabla \cdot (\mu \nabla \mathbf{U}) + \nabla \cdot (\lambda (\nabla \cdot \mathbf{U})\mathbf{I}) + \rho \mathbf{f} \tag{5.2}$$

where ρ is the density of the fluid, $\mathbf{U}$ the Eulerian velocity vector, p the pressure, μ the dynamic viscosity, λ the bulk viscosity, $\mathbf{I}$ the identity tensor and $\mathbf{f}$ a body force (for instance, gravity). The first equation is the *continuity equation* while the second is the *Navier-Stokes equation for compressible flows.* Using the product rule and equation (5.1) it can be shown that:

$$\frac{\partial}{\partial t}(\rho \mathbf{U}) + \nabla \cdot (\rho \mathbf{U}\mathbf{U}) = \rho \frac{\partial \mathbf{U}}{\partial t} + \rho \mathbf{U} \cdot \nabla \mathbf{U} \tag{5.3}$$

Equation (5.2) is often simplified, manipulated or decomposed in order to meet the demands of a specific problem. For instance, incompressible flows have constant density in space and time which results in the following set of equations:

$$\frac{\partial \mathbf{U}}{\partial t} + (\mathbf{U} \cdot \nabla)\mathbf{U} = -\nabla p/\rho + \nabla \cdot (\nu \nabla \mathbf{U}) + \mathbf{f} \tag{5.4}$$

In the current study however, we will use the general form of the Navier-Stokes equations presented above since we are dealing with a compressible air flow that reaches sonic speeds at the throat of the oscillator. We also expect to reach a Reynolds number of around $7,000$ in certain sections, notably at the exit of the oscillator. In order to avoid the prohibitive cost of performing a direct numerical simulation, we will resort to two different approaches to simulating the flow: the first consists in using the Reynolds-Averaged Navier-Stokes (RANS) equations with corresponding wall functions and the second is the Improved Delayed Detached Eddy Simulation (IDDES) reformulation of the $k-\omega$ SST two equation model which is a hybrid method combining the Large Eddy Simulation (LES) and RANS approaches. The first approach is detailed next.

5.2 RANS Models of Turbulence

The fundamental idea behind all the models of turbulence discussed in this section is the decomposition of the relevant fields into an average component and a fluctuating component, i.e.:

$$\phi = \langle \phi \rangle + \phi' \tag{5.5}$$

Where ϕ is an arbitrary field variable. The averaging operator $\langle \square \rangle$ (sometimes denoted by $\overline{\square}$) used here represents an *ensemble-average* and obeys the following rules:

$$\langle \phi + \psi \rangle = \langle \phi \rangle + \langle \psi \rangle \tag{5.6}$$

$$\langle a\phi \rangle = a\langle \phi \rangle \qquad a = \text{constant} \tag{5.7}$$

$$\langle \langle \phi \rangle \psi \rangle = \langle \phi \rangle \langle \psi \rangle \tag{5.8}$$

$$\left\langle \frac{\partial \phi}{\partial \mathbf{x}} \right\rangle = \frac{\partial \langle \phi \rangle}{\partial \mathbf{x}} \qquad \text{and} \qquad \left\langle \frac{\partial \phi}{\partial t} \right\rangle = \frac{\partial \langle \phi \rangle}{\partial t} \tag{5.9}$$

Applying the above decomposition to velocity, pressure and the stress tensor, we can rewrite equation (5.2) (using Einstein notation) as:

$$\rho \frac{\partial}{\partial t}(\langle u_i \rangle + u_i') + (\langle u_j \rangle + u_j') \frac{\partial}{\partial x_j}(\langle u_i \rangle + u_i') = -\frac{1}{\rho} \frac{\partial}{\partial x_i} (\langle p \rangle + p') + \frac{\partial}{\partial x_j} \left(\langle \tau_{ij} \rangle + \tau_{ij}' \right) \tag{5.10}$$

5.2.1 Two-equation linear eddy-viscosity models

The Reynolds stress cannot be expressed in terms of the resolved quantities. A mathematical closure capable of reproducing the effects of the Reynolds stress on the flow needs to be formulated. A framework based on tensor representation, introduced by Lumley (2007), makes it possible to model terms such as the Reynolds stress tensor in a formal way. In this section, a quick overview [1] of the theoretical underpinnings of two-equation linear eddy-viscosity models is presented, from the point of of view of Lumley's formal approach, and emphasizing the assumptions made along the way. This goes a long way in elucidating some of these models' shortcomings when simulating complex flows.

The first step is to assume that the Reynolds stress R_{ij} tensor is a function of the mean strain rate tensor S_{ij} (which is a symmetric tensor, $S_{ij} = S_{ji}$):

$$R_{ij} = f(S_{ij}) \tag{5.11}$$

Lumley's approach is predicated on two main principles: first, an invariant can only be a function of other invariants, and second, a quantity that is multilinear in some arbitrary tensor B^i can only be equal to another quantity that is also multilinear in B^i. In the present case, the Reynolds stress tensor is first contracted with two arbitrary tensors B^i, C^j in order to obtain a mixed invariant, which is then a function of mixed invariants (e.g. of the form $\left(S_i^j\right)^n B^i C_j$) and the principal invariants I, II and III of the strain rate tensor.:

$$R_{ij} B^i C^j = f\left(\left(S_i^k\right)^n B^i C_j, \left(S_i^k\right)^n C^i B_j, \mathrm{I}, \mathrm{II}, \mathrm{III} \right) \qquad \text{for } n = 0, 1, 2 \tag{5.12}$$

where $\left(S_i^k\right)^n = S_i^m S_m^p \dots S_h^k$. Since the left-hand side of the equation is multilinear in B^i

[1] For a more detailed derivation, the reader is referred to specialized texts such as Schiestel (2008) or Lumley (2007)

and C^j then so must the right-hand side, which explains the exclusion of invariants of the form $\left(S_i^j\right)^n B^i B_j$. Writing out the terms, and assuming we are in a Cartesian coordinate system:

$$R_{ij} = A\left(S_{ij}\right)^0 + B\left(S_{ij}\right)^1 + C\left(S_{ij}\right)^2 \tag{5.13}$$

$$= A\delta_{ij} + BS_{ij} + CS_{im}S_{mj} \tag{5.14}$$

If $A = \frac{2}{3}k$, $B = -2\nu_t$ and $C = 0$ we obtain a linear eddy-viscosity model of the Reynolds stress, where k is the turbulent kinetic energy and ν_t the eddy viscosity. If the turbulent viscosity ν_t is a constant, we end up with the well-known Boussinesq hypothesis. In two-equation models, the turbulent viscosity is isotropic, and is given by the Prandtl-Kolmogoroff formula:

$$v_t = c_\mu l\sqrt{k} \tag{5.15}$$

where l is the length scale of the energy-carrying vortices and c_μ a model constant (typically set to 0.09). Although all models consist of a transport equation for k, the choice of the second transported quantity, which determines the length scale, is not unique. For instance, the viscous dissipation $\epsilon \approx k^{3/2}/l$ is a common choice that works well for free shear flows and is the basis for the $k-\varepsilon$ model and its variants. Although these models were widely used in engineering applications for a while, they fail to predict flow and heat transfer where the flow interacts with a solid boundary. The different two-equation linear eddy-viscosity models are presented in detail next to highlight their possible shortcomings. The complexity of the flow created by the oscillator requires a model that is able to handle both free shear and bounded flows at low and high speeds through a multitude of geometric features and with heat transfer.

5.3 RANS Simulations

5.3.1 Boundary conditions

The oscillator designs studied in Chapters 3 and 4 are used here to simulate the flow. Figure 5.1 illustrates the domain along with its main features and boundary conditions.

The same types of boundary conditions were applied for all the simulations. The inlet temperature was set at a fixed, uniform value of $T_{in} = 300\,\mathrm{K}$. Similarly the backflow temperature at the outlet was also set to 300 K. The outlet pressure was fixed at $p_{out} = 1\,\mathrm{bar}$ while the inlet was set to $p_{in} = 2.5\,\mathrm{bar}$ for the turbulence model validation study. Fixed, uniform values of $p_{in} = 1.5$ to $3.5\,\mathrm{bar}$ were then successively imposed at the inlet in order to gauge the effect of inlet pressure on the oscillator. The velocity at the inlet was calculated from the flux through the inlet cells and at the outlet a von Neumann (zero gradient) boundary condition was used. Furthermore, all solid surfaces were modeled as adiabatic boundaries except for the impact plate whose temperature was fixed at $T_p = 310\,\mathrm{K}$. Finally, the boundary conditions for the turbulence variables at the target plate

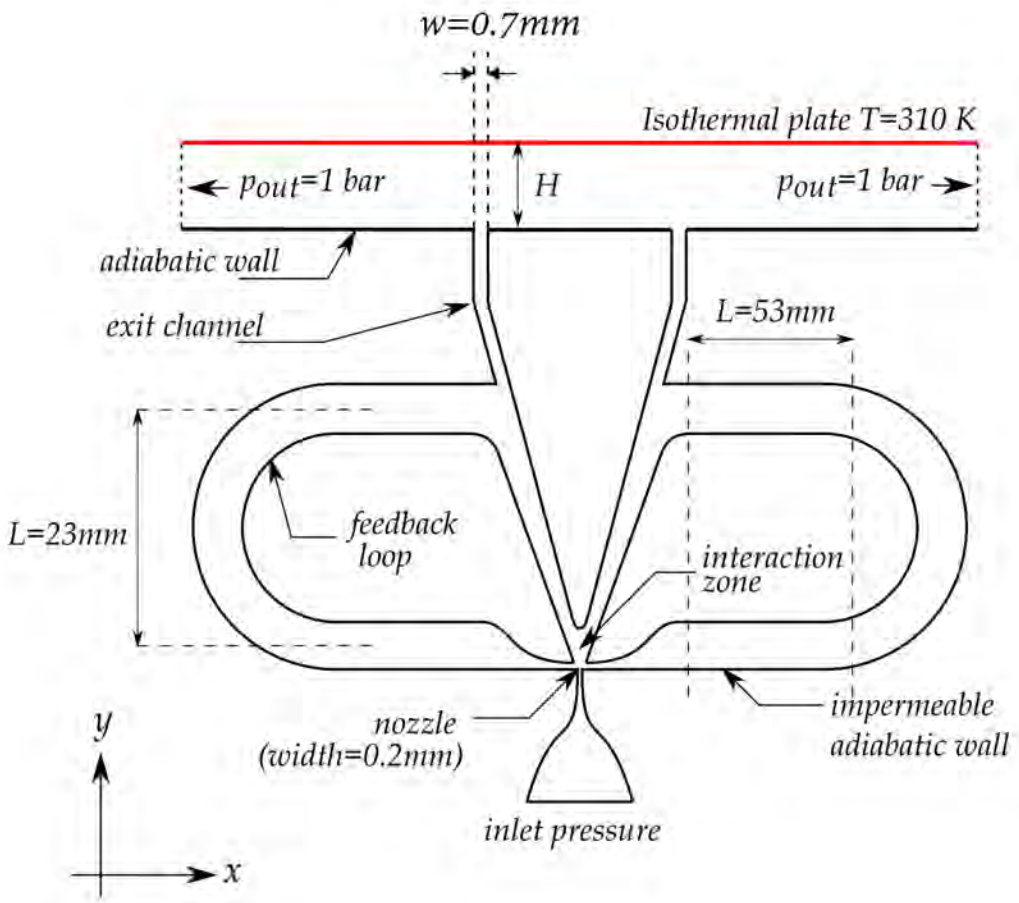

Figure 5.1: Illustration of the computational domain used for the 2D RANS simulations (the annotations corresponding to the dimensions of the feedback loop are taken from the Lg0 prototype, the remaining dimensions, i.e. the inlet and exit widths remain the same for all the simulated cases).

and solid boundaries are listed in Table 5.1.

5.3.2 Mesh Convergence

Considering the complexity of the computational domain, the mesh convergence study was done in two parts. First, the effects of mesh density inside the interaction zone on the exit velocity waveform and frequency was studied. A simulation using the $k-\omega$ SST model was run with an initial, relatively coarse mesh in the interaction zone. Then the mesh density in the wall normal direction was doubled and the simulation repeated. Aside from a few deviations, the velocity profiles at the exits remain unchanged as can be seen in Figure 5.2 for the left outlet; the coarse mesh in the interaction zone is then used for the rest of the study.

The mesh density near the impact wall was then tested. According to Gardon and

Table 5.1: Boundary conditions for turbulence variables at the heated wall and solid boundaries

OpenFOAM BC	Var.	Formula/Expression
nutKWallFunction	ν_t	$\nu_t = \nu \cdot \frac{\kappa y^+}{\ln(Ey^+) - 1}$
kqRWallFunction	k	Inherits from zeroGradient (von Neumann BC)
omegaWallFunction	ω	$\omega_{vis} = 6.0\frac{\nu}{\beta_1 y^2}$ $\omega_{log} = \frac{k^{1/2}}{C_\mu^{1/4}\kappa y}$
epsilonWallFunction	ϵ	$\epsilon_{vis} = 2wk\frac{\nu_w}{y^2}$ $\epsilon_{log} = wC_\mu\frac{k^{3/2}}{\nu_{t_w} y}$

Akfirat (1966), the highest stagnation Nusselt number for steady jets is obtained for $H/w = 4-6$. A standoff distance of $H/w = 5$ was then chosen as a representative case. An initial coarse mesh, with a maximum y^+ value of 4 (at the impact point, only when the jet velocity is at its peak) was used as a reference (referred to as "M"). The mesh density in the vicinity of the wall was then increased twice, once by a factor of 2 ("M $\times$ 2") then by a factor of 3 ("M $\times$ 3") with respect to the coarse mesh. Regardless of the mesh, the main peaks of the Nusselt profile remain at the same locations (Figure 5.3). However, there is a small but noticeable discrepancy between the values of these peaks between the "M" case and the remaining two meshes. Since the main features of the Nusselt distribution occur at the same locations for the three meshes and considering the number of cases that will be studied, the first mesh "M" is used for the rest of this study. The slight increase in accuracy for "M $\times$ 2" and "M $\times$ 3" does not justify the increase in computational cost incurred.

5.3.3 Turbulence Model Validation

Wang (2017), using a similar oscillator design but for active flow control, found that the Realizable $k-\varepsilon$ and SST $k-\omega$ models yielded accurate pulsation frequencies. However, in the present study, the $k-\varepsilon$ model and its variants may not accurately predict the heat transfer in an impinging jet (as noted early on by Viskanta (1993) for steady slot jets). Hofmann et al. (2007b) performed simulations of steady and pulsating submerged jets using some of the most commonly used Reynolds-Averaged Navier-Stokes (RANS) turbulence models. The authors noted that while most of the models gave accurate Nusselt number distributions in the wall jet regions, only the SST $k-\omega$ (with transitional flow option) yielded accurate enough results in the stagnation region. This turbulence model was able

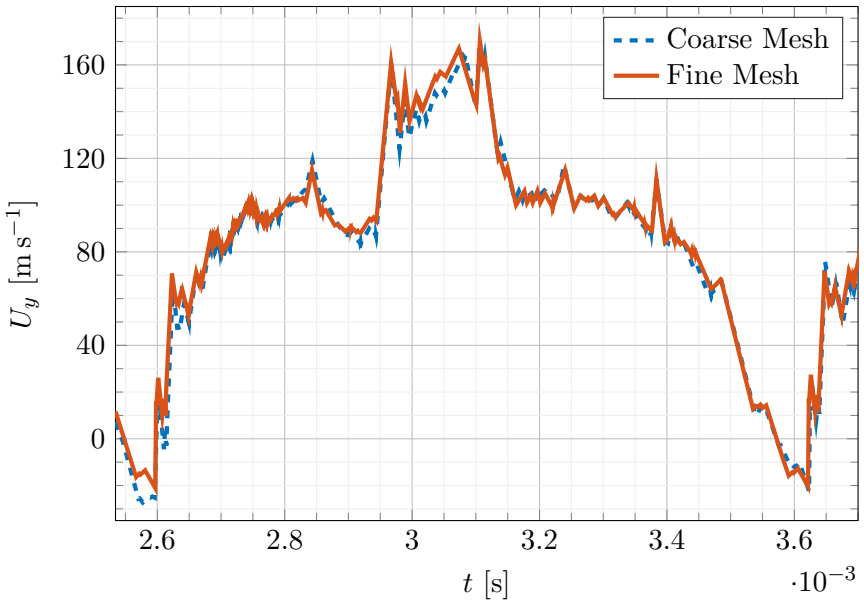

Figure 5.2: Comparison between the velocity waveform at the left outlet obtained for a coarse and a fine mesh in the interaction zone.

to correctly predict the secondary heat transfer peaks that were found in experiments at low stand-off distances. In light of this, it would seem that the SST $k-\omega$ is the most suited for our study since it accurately predicts the frequency of the oscillator and the heat transfer in the stagnation point of the impinging jet.

Nonetheless, the sparsity of studies in the literature on pulsating plane impinging jet warrants a turbulence model validation study. In what follows, two different stand-off distances $H/w = 2$ and 5 are considered for the same oscillator geometry and inlet pressure. The following models were tested:

- Standard $k-\varepsilon$: the stated purpose of this model (Launder and Spalding (1974)) was to predict a wide range of flows in a physically real manner at a low computational cost. In other words, the model has to be simple to develop and use and have extensive universality, in the sense that a single combination of model 'constants' should be enough to model a wide range of flows. Other models, such as $k-kl$ and $k-W$, although mathematically equivalent to $k-\varepsilon$, do not meet the requirements of universality. Their 'constants' must depend on certain flow characteristics, such as the turbulence length scale, in order to fit experimental data. According to Launder, at the time, the standard $k-\varepsilon$ model was only surpassed by Reynolds-stress models (RSM) in terms of accuracy. However, it fails to meet the universality criterion for axisymmetric jets. Some of the constants should then depend, among other things, on the centerline velocity of the jet and the radial width of the mixing region.
- RNG $k-\varepsilon$: in this approach, the effect of large scales on eddies falling in the inertial subrange is represented by a random force f_i that acts on the flow. The Renormalization Group (RNG) method (Yakhot and Orszag (1986)) consists in iterating a scale removal

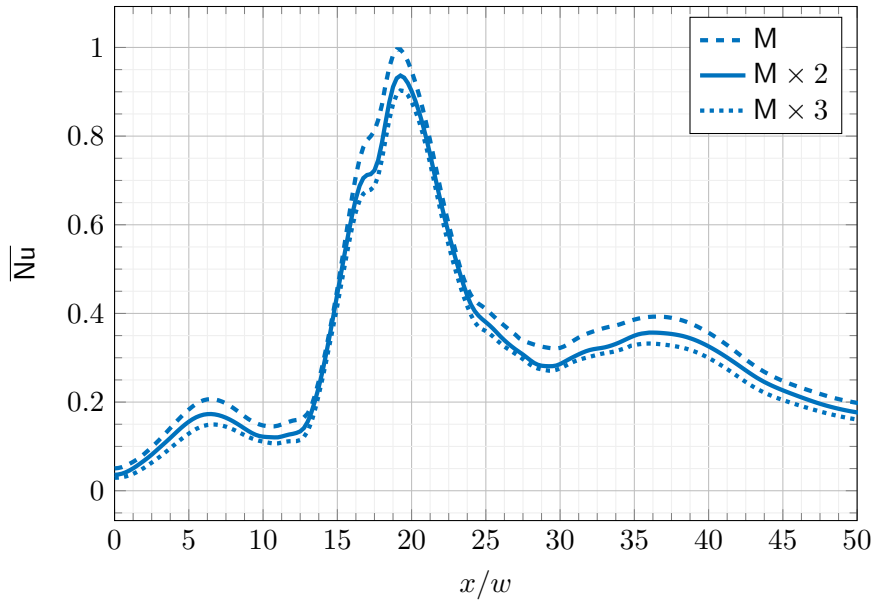

Figure 5.3: Average Nusselt number distribution along the impact surface for different mesh densities.

procedure, starting from the small scales up to the inertial range, whereby the dynamic equations are averaged over infinitesimal wavenumber bands $[k_c, k_c']$. At the end of this complex procedure, a model resembling the standard $k-\varepsilon$ model is found but with modifications to the model coefficients (some of which are no longer 'constants') and with additional terms that account for the effects of the discarded small scales.

- Realizable $k-\varepsilon$: realizability conditions (Schumann (1977)) are imposed on the Reynolds stress tensor, meaning that its diagonal elements $\overline{u_i u_i}$ (for $i = 1, 2$ and 3) are positive and its off-diagonal elements $\overline{u_i u_j}$ satisfy the Schwartz inequality $\overline{u_i u_j}^2 \leq \overline{u_i^2 u_j^2}$ (for $i, j = 1, 2$ and 3). This ends up changing the model coefficients and the production and destruction terms in the ϵ equation. The coefficient C_μ used in computing the turbulence viscosity μ_t is no longer a constant, but depends on flow quantities such as the strain-rate tensor S_{ij}, the rate of rotation tensor Ω_{ij}, k and ϵ.
- $k-\omega$ SST (Menter (1993): as mentioned earlier, the choice of the length-scale determining equation is not unique. It is then possible to replace the rate of dissipation of the turbulent kinetic energy TKE ϵ with the specific dissipation rate ω. Wilcox (1988) compared $k-\varepsilon$- and $k-\omega$-based models by studying the structure of the velocity defect layer with and without adverse pressure gradients. Unlike the $k-\varepsilon$ model, the $k-\omega$ model resulted in defect-layer structures that are in close agreement with experimental results. Furthermore, using ω instead of ϵ allows for the inclusion of roughness effects at solid boundaries since the value of ω can be specified arbitrarily at the wall. The major drawback of the original model is its sensitivity to the values of ω in the freestream. The SST variant combines both: in the freestream, the parameters of the $k-\varepsilon$ model are activated, while near the wall, the $k-\omega$ model takes over.

- Langtry-Menter 4-equation transitional SST model based on the $k-\omega$ SST model (Langtry and Menter (2009)): this model adds to the $k-\omega$ SST model two additional equations for the intermittency γ and the momentum thickness Reynolds number Re_θ, respectively. The transition phenomena are not modeled, as the name might suggest, but rather correlation-based equations are introduced into the already established CFD method.

The results from these simulations are compared to experimental data that were presented in previous chapters. The experimental data were obtained from pressure sensors integrated in the feedback loops, hot-wire measurements of the jets at the exit of the oscillator and infrared camera measurements of the impact plate. The validation is then performed on three levels:

1. the internal behavior of the jet via the pressure sensors and frequency response to different inlet pressures,
2. the velocity profiles and waveforms of the produced pulsating jets, and
3. the heat transfer performance of the pulsed impinging jets.

Inlet pressure

The inlet pressure, being the single control parameter of the fluidic oscillator, has a wide range of effects on the behavior of the oscillator, from the mass flow rate to the waveform of the velocity profiles at the exits. The system was simulated using the $k-\omega$ SST RANS model for five inlet pressures $p_{in} = 1.5, 2, 2.5, 3$ and 3.5 bar and the Langtry-Menter Transition SST model for $p_{in} = 2, 2.5, 3$ and 4 bar. The $k-\epsilon$ models were excluded since, as will show in the next section, the predictions they produce are far more inaccurate than those of the $k-\omega$ models. At large inlet pressures (usually exceeding 3 bar), the frequency of the bi-stable oscillator studied here becomes constant, unlike the sweeping jet or sonic oscillators whose frequencies increase with inlet pressure. This strong correlation

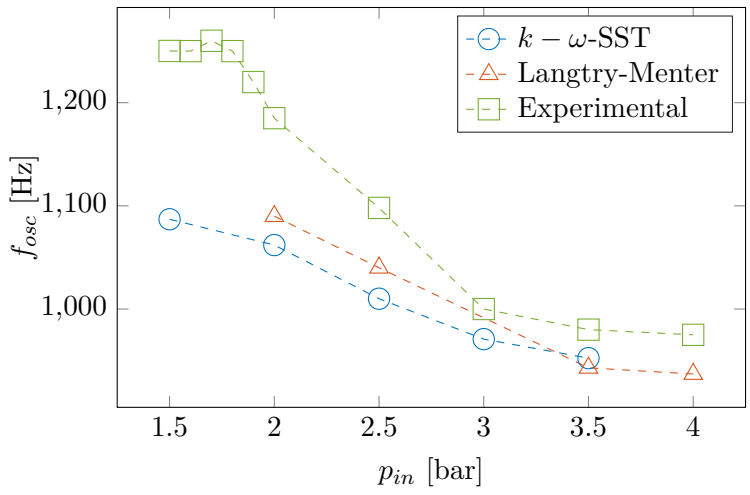

Figure 5.4: Frequency response of the oscillator from numerical results (2D $k-\omega$ SST and Langtry-Menter) and experimental results.

can obscure the effects of each of these two parameters on the flow. For the pulsating jet oscillator studied here, the frequency can reach up to 1270 Hz before decreasing to a constant value of 975 Hz (Figure 5.4). The frequency response using the $k-\omega$ SST model exhibits a similar behavior for low pressures ($p_{in} < 2.5$ bar) even though the frequency is significantly lower. The frequencies from the Langtry-Menter model are slightly closer to the experimental values. In both cases, the gap between experimental and numerical results eventually tightens as the inlet pressure is increased. Finally, for $p_{in} = 2.5$ bar, all the remaining $k-\varepsilon$ models result in a frequency of around 970 Hz, which is 13% lower than the experimental value for the same inlet pressure.

Pressure inside feedback loops

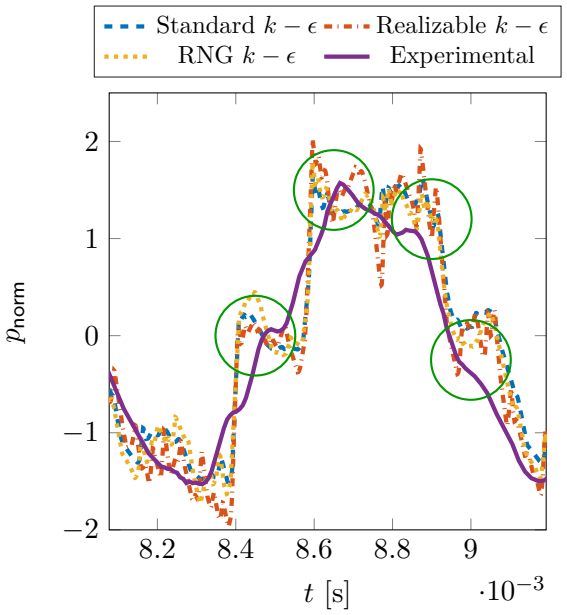

Figure 5.5: Normalized pressure inside the feedback loop during a single pulsation from experimental measurements and three $k-\varepsilon$ models.

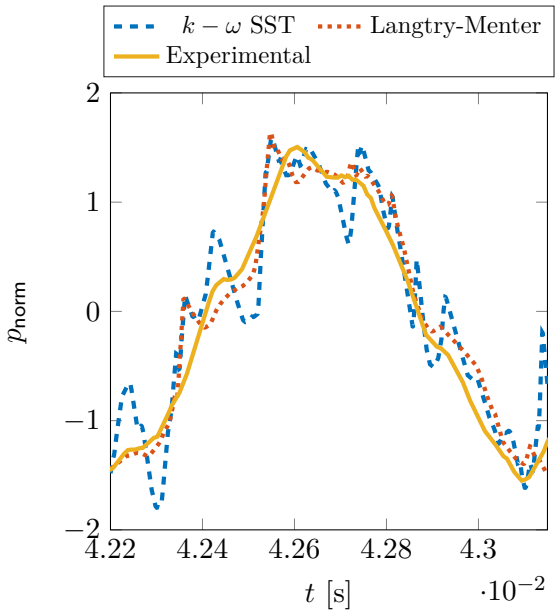

Figure 5.6: Normalized pressure inside the feedback loop from experimental measurements and the $k-\omega$ SST and Langtry-Menter models.

Since the behavior of the oscillator depends in part on the pressure waves traveling inside the feedback loops, pressure measurements are compared to numerical results (Figures 5.5 and 5.6). The numerical results were found by averaging the pressure over an area having the same dimensions and position as the pressure transducer used in the experiments. In spite of the slight difference in frequency between them, the pressure plots from the three different $k-\varepsilon$ models overlap over the oscillation period. When compared to the experimental measurements, some of the features of the pressure evolution (marked by a green circle) occur roughly at the same time, but are more prominent in the numerical results. A similar observation can be made for the $k-\omega$ model, where sudden pressure fluctuations can be seen (Figure 5.6). Finally, the Langtry-Menter transitional model offers

by far the best prediction of pressure fluctuations in the feedback loop. Except for a couple of offshoots, there is significant overlap between the experimental and numerical data for this transitional model.

Exit Velocity Profile

Another quantity of interest is the velocity at the exit slots. We begin by looking at the time-averaged velocity profile across the width of the slot (Figure 5.7). Measurements were performed at around $0.2w$ away from the exit slot along the jet axis using a hot-wire anemometer (w is the initial width of the jet/the width of the exit channel). The numerical results were sampled at the same axial distance. All of the turbulence models produce normalized velocity profiles that are in good agreement with experimental measurements. The profile is asymmetrical because of the bend in the exit channels that pushes the fluid away from its center of curvature. The straight portion of the channel downstream from the bend is not long enough for the channel flow to properly develop before reaching the exit slot. In terms of maximum velocity, the $k-\varepsilon$ RNG and $k-\omega$ SST models come within $1-2\%$ of the experimental value, while the remaining models underestimate its values by at least 15%.

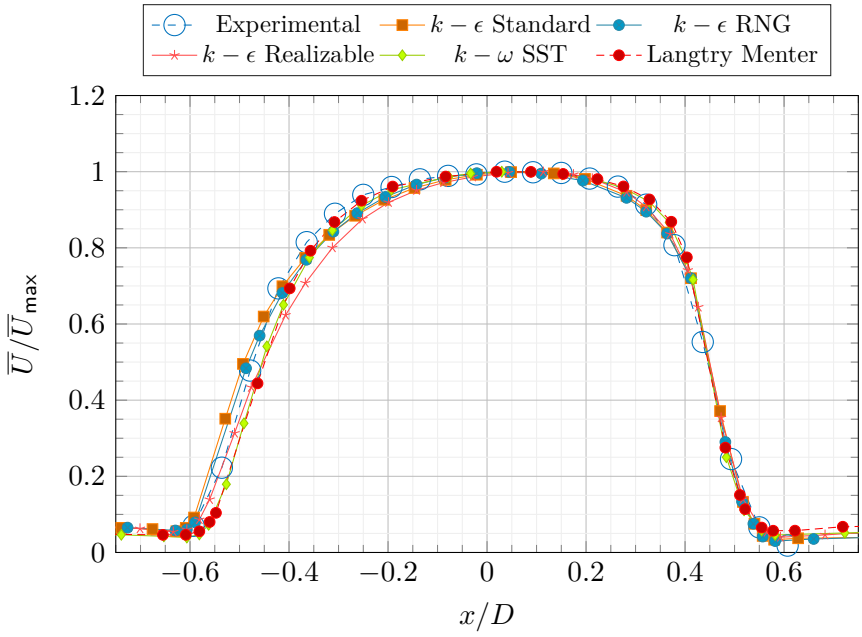

Figure 5.7: Time-averaged velocity profile of the jet across the center of the exit slot from experimental and numerical results. ($p_{\text{in}} = 2.5\,\text{bar}$)

5.3.4 Exit Velocity Waveform

Although their frequencies are not exactly the same, the experimental and numerical velocity waveforms were aligned in order to compare them (Figure 5.8). To facilitate the comparison, a single pulsation is subdivided into 5 phases, labeled with roman numerals.

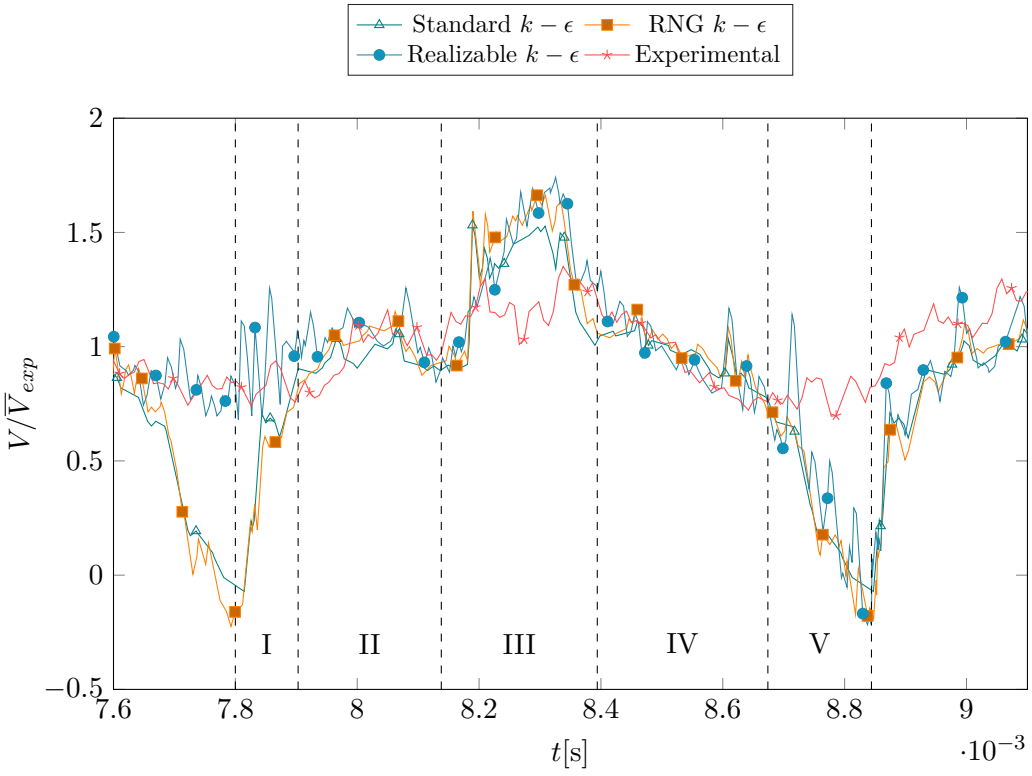

Figure 5.8: Velocity waveforms from experimental and numerical results ($k-\epsilon$), sampled at the center of the jet near the exit slot. ($p_{\text{in}} = 2.5\,\text{bar}$)

The three $k-\epsilon$ models show good agreement with the experimental results in phases (II) and (IV), in particular, the first local peak at around $t = 8\,\text{ms}$ in the experimental results can also be gleaned in the numerical waveforms. In phase (I) however, the standard and RNG variants predict significantly lower values of the velocity, even reaching negative values at the minimum ($t = 7.8\,\text{ms}$). The Realizable $k-\epsilon$ model seems to produce closer values in phase (I), however this is not consistent across all the pulsation. This can be seen in Phase (V) where the realizable variant is closer to the other models than it is to the experimental measurements. In phase (III), the experimental waveforms exhibits two main peaks, one at $t = 8.2\,\text{ms}$ and another at $t = 8.35\,\text{ms}$. This feature is not seen in the numerical results, where the velocity abruptly rises at $t = 8.17\,\text{ms}$, then slowly increases until it reaches its maximum value at $t = 8.35\,\text{ms}$.

The same approach is used to evaluate the $k-\omega$-based models (Figure 5.9). Large deviations are observed in phases (I) and (V), although, compared to all the other models, the Langtry-Menter model results in slightly higher values. In phases (II) and (IV) there is significant overlap between the three curves. In phase (III), the simulations overestimate the peak velocity. Nevertheless, the SST $k-\omega$ model has a 'two-peak' structure similar to that of the experimental waveform. The local minimal lying between those two peaks occurs roughly at $t = 18.85\,\text{s}$ (dashed red line) for both the experimental and SST $k-\omega$ curves.

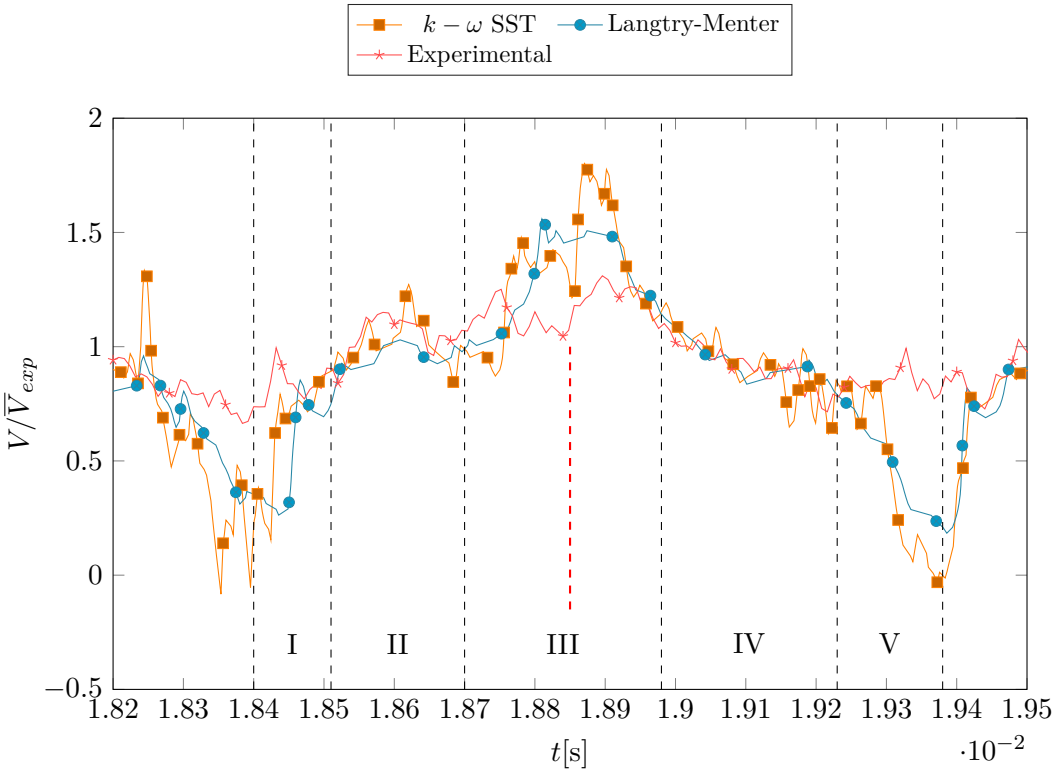

Figure 5.9: Velocity waveforms from experimental and numerical results ($k-\omega$), sampled at the center of the jet near the exit slot. ($p_{\mathsf{in}} = 2.5\,\mathrm{bar}$)

Without measurements from inside the switching zone, the discrepancies in phases (I), (III) and (V) cannot be directly explained. However, the difference in switching time, inferred from the response to different inlet pressures, could be a clue. If the jet is completely attached to one side of the switching zone, it would require more time to reach the other side upon the arrival of the pressure wave. On the other hand, if there is a large recirculation bubble between the inlet jet and the attachment surface, this may reduce the switching time, since the deviation angle required to move the jet from one branch to the other is reduced. In an extreme case, although most of the flow is going through one branch, some of it may escape through the other, feeding the second exit. This may explain why at the beginning of phase (I) the velocity remains relatively high in the experimental case, while being lower in phase (III): an incomplete switching of the jet to one side may lead to some leakage to the other, reducing the velocity's amplitude of pulsation at the exit.

Stagnation-point Nusselt number

Jet impingement cooling involves a complex flow structure that can be subdivided into three main parts: the developing jet zone (free-shear flow), the stagnation zone and the wall jet (wall-bounded flow). Models based on both $k-\varepsilon$ and $k-\omega$ transport equations were first designed and optimized to handle free-shear flows. Even though $k-\omega$ models have proven effective in predicting boundary-layer flows such as wall jets (Zuckerman and Lior

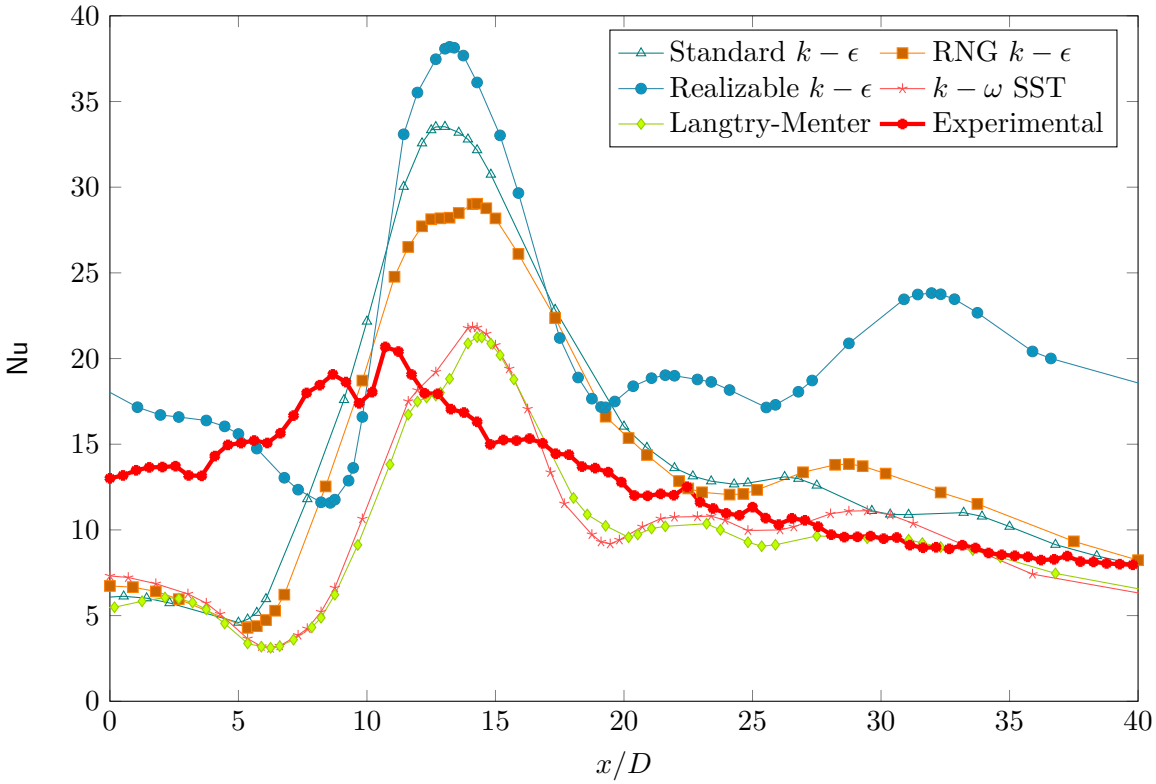

Figure 5.10: Nusselt number distribution around the stagnation point (at $x/w = 19$) for $p_{\text{in}} = 2.5\,\text{bar}$ and $H/w = 5$

(2005)), both types of models do not perform well in the stagnation region where normal strain and the rise in pressure play an important role. For instance, in $k-\varepsilon$ models, the pressure-strain correlation term

$$\Phi_{ij} = \overline{\frac{p}{\rho}\left(\frac{\partial u_i}{\partial x_j} + \frac{\partial u_j}{\partial x_i}\right)} \tag{5.16}$$

that appears in the $\overline{u_i u_j}$ (second moment) equation is of secondary importance, and is approximated by assuming that the flow is weakly anisotropic (Schiestel (2008)). Furthermore, $k-\varepsilon$ models suffer from two well-known problems: the "round jet anomaly" and the "stagnation-point anomaly". The first involves over-predicting the value of the spreading rate of a round jet, which should not be an issue in the present study. On the other hand, the stagnation-point anomaly (Durbin (1996)) refers to a spurious build-up of turbulence kinetic energy (TKE) k in the stagnation region. This phenomenon can upset the surrounding flow and it can lead to overestimating the boundary Nusselt number in situations where heat transfer is of interest. To curb this effect, the k and ω equations of SST models contain production limiters of the form $-\beta^*\rho k\omega$ and $-\beta\rho\omega^2$, respectively (Menter (2009)).

In light of this, it is not surprising that all of the $k-\varepsilon$ models over-predict the stagnation Nusselt number by up to 90% (Figure 5.10). The Realizable $k-\varepsilon$ offers the worst predictions

overall as it overestimates the peak Nusselt number and the heat transfer distribution is both quantitatively and qualitatively different from the experimental curve. In addition to the primary peak, two local maxima can be observed at $x/w = 22$ and $x/w = 32$, the second peak being more prominent than the first. The values of the Nusselt number remain higher than the other numerical and experimental curves even for large values of x/w. The peaks from the Standard and RNG variants, although lower than the previous case, remain significantly higher than in the $k-\omega$ and experimental results. Predictably, at larger distances from the peak, these two variants join the remaining cases. A weak secondary peak can be seen for the Standard and RNG models at $x/w = 26.5$ and 29, respectively.

There is stark difference between the $k-\varepsilon$ and $k-\omega$ models in the vicinity of the stagnation point. First, the peak ($x/w = 14.5$) is adjoined to the left by a secondary feature ($x/w = 11.5$) for $k-\omega$ models which can barely be discerned for the Realizable $k-\varepsilon$ model and is completely absent from the Standard and Realizable $k-\varepsilon$ models. This feature is also present in the experimental data as a secondary peak at $x/w = 9$, which is more prominent than in the numerical results. The double peak in the experimental curve is often attributed to a laminar-to-turbulent transition as the flow exits the stagnation region which leads to a peak in turbulence intensity at that point. The peak values from the $k-\omega$ simulations are close to the experimental values. However, the simulations place these peaks further downstream from the origin. This is because the axis of the jets is tilted during impingement as can be seen in the velocity contours of Figure 5.11. Since the simulations were performed in a 2D domain, the fluid can only escape in the $x-$direction, meaning that the fluid can accumulate in the space between the two jets, raising the pressure in that area. The difference in pressure between the intermediate space and the outlets of the domain causes the jets to tilt slightly outwards. For the $k-\omega$ cases, the Nusselt number decreases for $x/w < 10$ more rapidly than in the experimental case. This can also be attributed to the tilt of the jet: a large portion of the fluid is diverted directly towards the outlets, keeping the fluid in the space between the two jets *relatively* calm. In the experimental setup, the fluid in that area can easily escape in the $z-$direction, creating a wall jet that cools the heated surface. The choice of a 2D numerical domain is at fault here. As a consequency and although the $k-\omega$ models do not precisely capture the features of the stagnation region, they give a reasonably accurate distribution of the Nusselt number for this particular case.

In the present case, this secondary feature occurs farther downstream and can be attributed to the reattachment of the flow to the impact wall. In order to illustrate this, Figure 5.11 shows the average velocity field from the $k-\omega$ SST simulation in a part of the exit space surrounding the stagnation point. At around $x/w = 27$, the wall jet separates from the impact wall and attaches itself to the confining wall. This leads to a rapid decrease in wall shear stress and consequently to a decrease in Nusselt number. The reattachment of the jet further downstream causes a slight increase in Nusselt number, which explains the secondary peak at $x/w = 37$. In the experimental results, no such salient features were detected, which leads to the conclusion that none of these RANS models can accurately

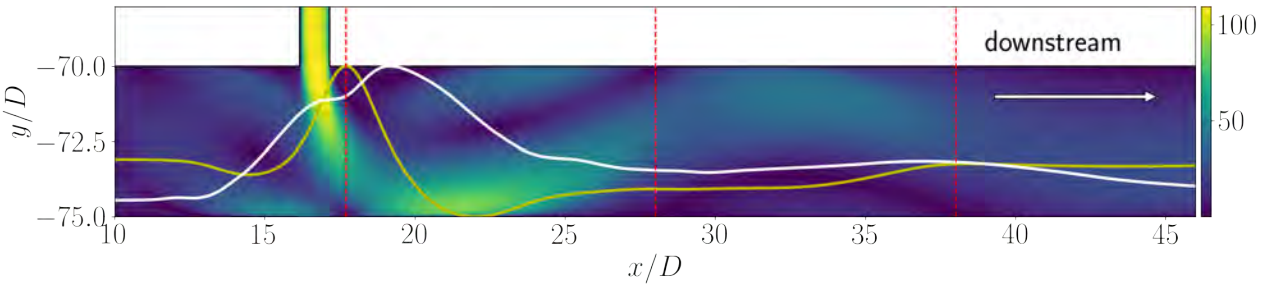

Figure 5.11: Average velocity field around one of the oscillator's exits, overlayed with normalized average pressure (yellow) and average Nusselt (white) profiles. The dashed lines (red) indicate, from left to right, the positions of the stagnation point, the first local minimum, and the secondary peak.

predict the behavior of the confined flow.

5.3.5 Effect of H/w

Since the $k-\omega$ SST model gives the best predictions in terms of pressure profiles in the feedback loops and stagnation-point Nusselt number, it was used to simulate the system for different standoff distances H/w. According to Gardon and Akfirat (1966), the stagnation Nusselt number reaches its peak value $H/w = 4-6$. Up to this distance, the potential

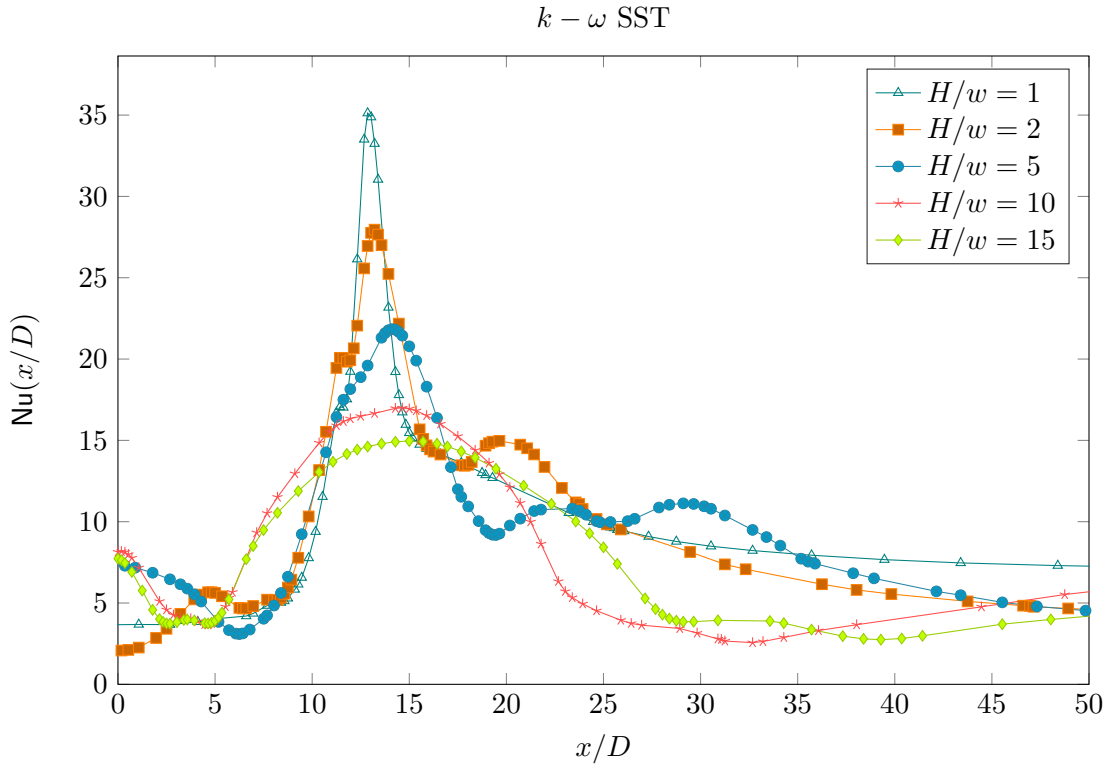

Figure 5.12: Nusselt number distribution around the stagnation-point for different standoff distances H/w ($k-\omega$ SST)

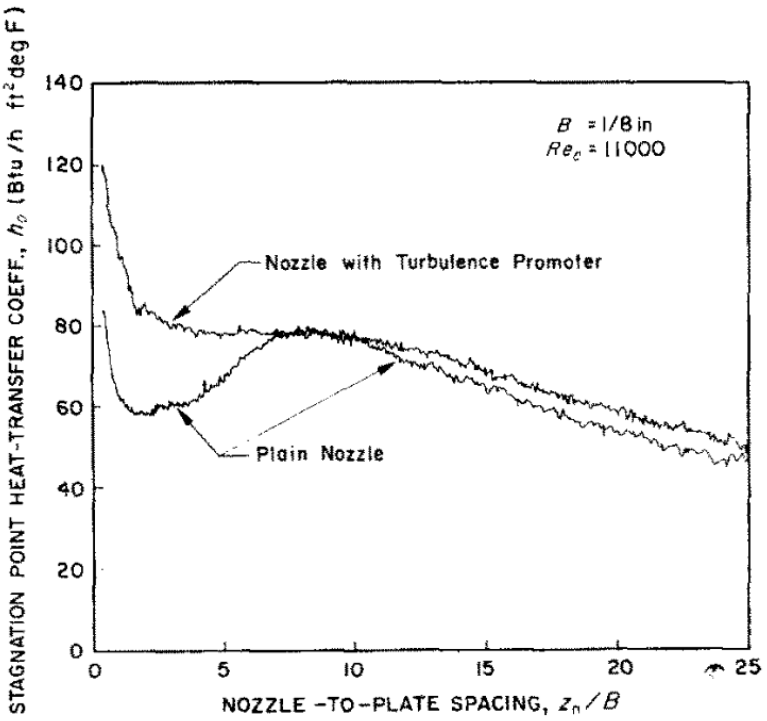

Figure 5.13: Effect of increasing the turbulence level of the jet on the stagnation point Nusselt number for a slot jet (Gardon and Akfirat, 1966).

core of the jet reaches the impact plate and so the average centerline velocity remains the same. At the same time, the turbulence intensity along the jet axis increases as we move downstream from the base of the jet. At the tip of the potential core, the centerline velocity starts to decay while the turbulence intensity continues to rise. However, the increase in turbulence intensity is not enough to offset the effects of a rapidly decreasing velocity before impact and so the stagnation-point Nusselt number plummets as the standoff distance increases. The effect of all this is to produce a peak in $\mathsf{Nu}_{\mathsf{max}}$ for H/w equal to the potential core length. If the initial turbulence intensity of the jet is increased, the authors observed a monotonic decrease in Nusselt number with increasing distance, from $H/w \approx 0$ onward as can be seen in Figure 5.13.

The experimental results from Chapter 4 (Figure 5.14) show a similar result in that heat transfer is improved for small impact distances by increasing turbulence levels at the jet nozzle by pulsating the flow. The $k-\omega$ SST model overestimates the values of the peak Nusselt number for $H/w < 5$. This could be an issue with the production limiters mentioned above which should limit the turbulent kinetic energy production in the jet, avoiding overshoots in heat transfer rates. Although the experimental and numerical curves for the pulsed jet approach one another around $H/w = 5$, the experimental data show a much steeper decline in performance for larger distances. The experimental values for the steady case seem to approach those of the numerical pulsed case in the range of H/w explored here.

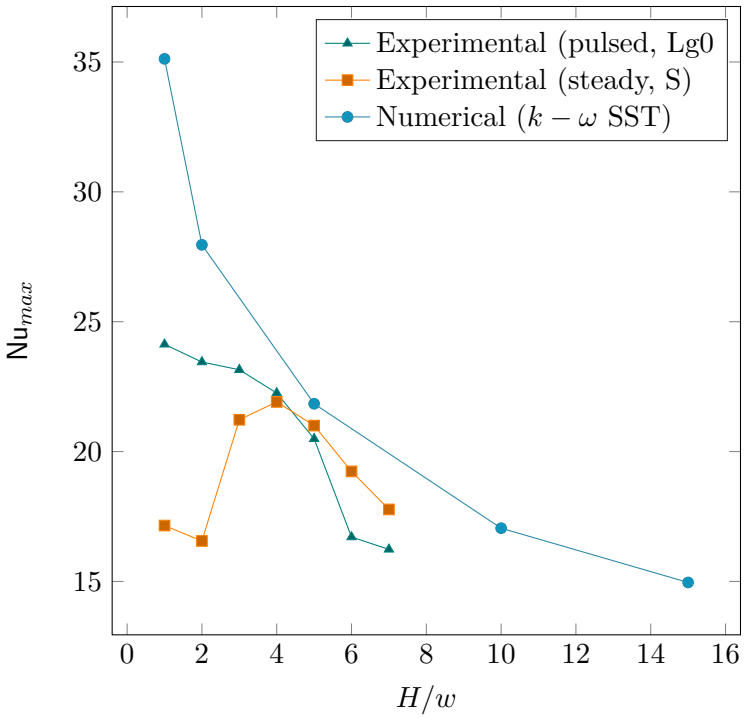

Figure 5.14: Experimental and numerical values of the peak Nusselt number versus standoff distance for $p_{\mathsf{in}} = 2.5\,\mathrm{bar}$.

Effect of inlet pressure/jet Reynolds number

The inlet pressure of the oscillator also determines the Reynolds number of the pulsating jets, which in turn affects the cooling rate on the impact surface. Higher Reynolds numbers not only improve heat transfer, but also alter the distribution of the Nusselt number (Figure 5.15). For $p_{\mathsf{in}} = 1.5\,\mathrm{bar}$, on the right side of the peak, the Nusselt number decreases up to $x/w = 25$ in the downstream direction, with a weak inflection point at around $x/w = 23$. This inflection point becomes more prominent as the jet Reynolds number increases, and eventually, for $p_{\mathsf{in}} = 3$ and $3.5\,\mathrm{bar}$, a secondary peak appears at $x/w = 25$ and $x/w = 26$ respectively.

Turning to the left side of the primary peak, the Nusselt number decreases monotonically for $p_{\mathsf{in}} = 1.5\,\mathrm{bar}$. As the inlet pressure is increased, an inflection point appears, followed by a secondary feature. As was pointed out before (Figure 5.11), this inflection point corresponds to the stagnation point of the impinging jet.

5.4 Concluding remarks: RANS Simulations

The present study attempts to assess the ability of five different turbulence models to predict the flow dynamics and heat transfer characteristics of a fluidic oscillator. The validation of the models was performed in several steps, beginning with the internal dynamics of the device and ending with the heat transfer characteristics of the impinging jets at their

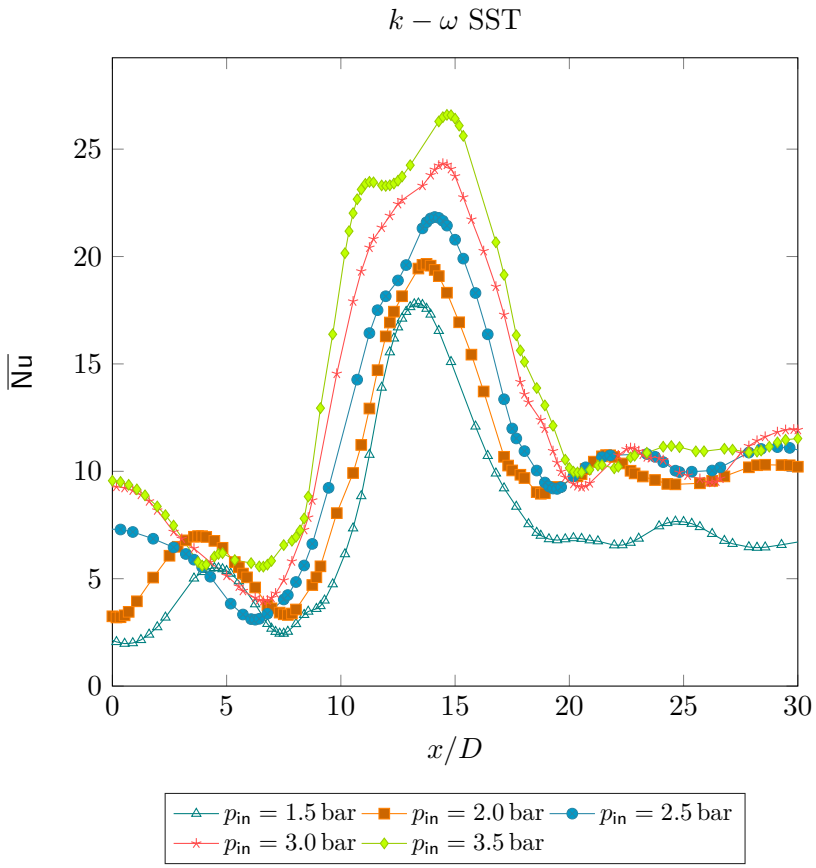

Figure 5.15: Nusselt number distribution around the stagnation-point for different inlet pressures p_{in} ($k-\omega$ SST)

exits. The $k-\omega$ models, with and without correlation-based transition modeling, clearly outperformed the $k-\epsilon$ models both in terms of internal dynamics of oscillator as well as the Nusselt number distribution on the impact plate. More specifically:

- The $k-\epsilon$ models all underestimate the oscillation frequency by 12% while the SST $k-\omega$ and the Langtry-Menter models resulte in frequencies that are only 8 and 5% lower than the experimental values for $p_{\mathrm{in}} = 2.5\,\mathrm{bar}$. For these two models, the errors decrease with increasing inlet pressure.
- The pressure evolution inside the feedback loops is more irregular for the $k-\epsilon$ models than for the experimental measurements and there is nearly no overlap. The SST $k-\omega$ model yields similar results since the pressure fluctuations are overpredicted. The Langtry-Menter model results in pressure fluctuations that agree remarkably well with experimental results. There is significant overlap between the numerical and experimental pressure evolutions during the entire pulsation.
- Although all the numerical models resulte in acceptable average velocity profiles at the exit of the oscillator, the velocity waveforms were less accurate. The numerical and experimental results are in good agreement during certain phases, as was shown in

Figures 5.8 and 5.9, but fail to predict the maximum and minimum velocities. The $k-\omega$ models are marginally better than the $k-\epsilon$ models, but the amplitude of pulsation is still largely overestimated.

- Finally, the heat transfer characteristics of the impinging jets were investigated. The RNG $k-\epsilon$ and both $k-\omega$ modes yield similar Nusselt distributions with peak Nusselt numbers that are close to the experimental value. However, downstream from the peak, all the numerical profiles exhibit a sharp decline, deviating from the experimental curve, before eventually catching up to it.

In short, the $k-\omega$ models are relatively better suited to predict both the internal dynamics of the oscillator and the heat transfer on the impact plate than the $k-\epsilon$ models. Although the Langtry-Menter model was shown to have a slight edge over the SST $k-\omega$ model, this comes at a higher computational cost and might not always be justified.

5.5 Hybrid RANS/LES Simulations

5.5.1 Basics of the Hybrid RANS/LES approach

Impinging jets can be seen as a combination of elementary flows: a free turbulent jet that reaches a solid boundary produces a stagnation flow, followed downstream by a wall jet. Each of these flows can be further subdivided into potential cores, shear layers, boundary layers and so on. As a consequence, impinging jets contain a number of different turbulence characteristic lengths. Problems like this are intractable for Direct Numerical Simulations (DNS) or even highly resolved Large Eddy Simulations (LES) in some cases. For DNS, all the turbulence scales, down to the Kolmogorov length η, must be resolved while LES require the resolution of the largest scales containing most of the turbulent kinetic energy of the system. These turbulence producing scales become comparable to the Kolmogorov scale near the wall making the LES grid resolution requirements comparable to those of a DNS. On the other hand, Reynolds-Averaged Navier-Stokes models based entirely on transport equations of statistical quantities are very widely used in industrial and engineering applications. These models drastically reduce grid resolution requirements compared to DNS and LES but are unable to accurately predict global coefficients (e.g., drag and lift coefficients) in strongly unsteady flows.

Since the late 1990's, hybrid models have been developed that switch between RANS and LES making it possible to resolve parts of the flow while modeling others. The transition between the two can be either sharp or dynamic (zonal methods) or smooth (non-zonal or global methods).

As pointed out by Chaouat (2017), the RANS and LES approaches can be bridged in the framework of spectral turbulence theory. In a nutshell, the Reynolds decomposition can be generalized by developing the fluctuating part, such that:

$$\phi = \langle\phi\rangle + \sum_{m=1}^{\infty} \phi'_{[\kappa_{m-1},\kappa_m]} \tag{5.17}$$

where the fluctuating components $\phi'_{[\kappa_{m-1},\kappa_m]}$ are obtained by averaging in Fourier space the total fluctuating component $\hat{\phi}'(\kappa)$ over the band $[\kappa_{m-1}, \kappa_m]$:

$$\phi'_{[\kappa_{m-1},\kappa_m]}(\xi) = \int_{\kappa_{m-1}<|\kappa|<\kappa_m} \hat{\phi}'(\kappa) \exp(j\kappa\xi) d\kappa \tag{5.18}$$

If only the term $m = 1$ is retained, the Reynolds decomposition is recovered. Keeping terms up to $m = 2$ leads to two components $\phi'_{[0,\kappa_c]}$, that contains the largest eddies down to the cut-off wavenumber κ_c, and $\phi'_{[\kappa_c,\kappa_d]}$, that contains the scales at the cut-off and down to the dissipation wavenumber κ_d. In the LES approach, the first component is resolved while the second is modeled.

5.5.2 Global Hybrid Models

The hybrid model used in the present study is a product of a series of modifications brought upon the original Detached Eddy Simulation (DES) model. It is based on the Spalart-Allmaras one-equation turbulence model in which wall distance d_w is replaced by a new length scale defined as:

$$\tilde{d} = \min\left(d_{wall}, C_{DES}\Delta\right) \tag{5.19}$$

where d_{wall} is the distance from the wall, C_{DES} is a model coefficient, and Δ the cut-off scale, defined as $\max(\Delta_1, \Delta_2, \Delta_3)$ (the Δ_i's are the dimensions of the cell). One of the main flaws in DES is the premature activation of LES in the boundary layer if the grid spacing is smaller than δ, the boundary layer thickness. When the premature switch from RANS to LES occurs, the modeled turbulence viscosity suddenly drops but no unsteady turbulent content is produced in order to balance it out. This results in a separation of the flow from the solid boundary. This issue was resolved by using shielding functions f_d in the following manner:

$$\tilde{d} = d_{wall} - f_d \max\left(0, d_{wall} - C_{DES}\Delta\right) \tag{5.20}$$

that delay the activation of LES in the boundary layer. For this reason, the model is called Delayed Detached Eddy Simulation (DDES). The shielding function needs to be calibrated for each RANS model in such a way as to protect the attached boundary layer, while favoring the production of unsteady turbulence scales in the transition region between the boundary layer and the free-stream. Otherwise, we would lose the scale resolving capabilities of DDES. The final step in refining the hybrid approach is the Improved DDES (IDDES) formulation that combines DDES with Wall-modeled LES (WMLES). This resolves the mismatch between the inner log layer, where the RANS model dominates, and the outer log layer where LES takes over. The length scale is then:

$$\tilde{d} = \tilde{f}_d(1 + f_e)d_{wall} + (1 - \tilde{f}_d)C_{DES}\Delta \tag{5.21}$$

The first hybrid formulation relied on a one-equation closure, the Spalart-Allmaras model. The approach was later generalized to two-equation models such as the $k-\omega$ SST model.

Hybrid models were originally conceived for applications involving flows around airfoils. To our knowledge, there are very few studies that have used these models to simulate plane impinging jets in heat transfer application. One of the first studies to do so can be found in Kubacki and Dick (2010). The authors observed in a previous work (Kubacki and Dick (2009)) that the $k-\omega$ model was not capable of predicting the Nusselt profile for large standoff distance ($H/w \approx 10$) mainly due to an underestimation of mixing in the free jet's mixing layer. A hybrid RANS/LES approach can overcome this difficulty by simulating the nascent vortices in the jet shear layer and their development further downstream. This hybridization is achieved by introducing the grid spacing Δ into the models in three ways: in the dissipation term D_k in the k transport equation (M1), in the eddy viscosity ν_t (M2), or in both simultaneously (M3). Two-dimensional RANS simulations were also performed for comparison. The hybrid models results in better agreement with the experimental Nusselt and skin friction coefficient profiled compared to the 2D RANS model, especially for larger standoff distances (in this case $H/w = 9.2$). The authors noted that the three models yielded similar results to one another because they all lead to a Smagorinsky model in the LES regions of the flow (although the constant in M1 is slightly higher than in the Smagorinsky model). A follow-up study by the same authors (Kubacki et al. (2013)) led to similar conclusions. A hybrid model akin to M2 was used, where the grid spacing is defined as the maximum distance between cell faces $\Delta = \max(\Delta_x, \Delta_y, \Delta_z)$ in D_k and $\Delta = (\Delta_x \Delta_y \Delta_z)^{1/3}$ in the turbulence viscosity.

In what follows, we will be using the Improved Delayed Detached Eddy Simulation model based on t he $k-\omega$ Shear Stress Transport model, whose formulation can be found in Gritskevich et al. (2012). In a nutshell, the IDDES model is similar to $k-\omega$ SST except for the dissipation term $D_k = \rho\beta^*\omega k$ that is replaced with $\rho k\sqrt{k}/l_{IDDES}$, where ρ is the fluid density, ω the specific rate of dissipation, k the turbulence kinetic energy, β^* a model constant, and l_{IDDES} the length scale. The introduction of the length scale l_{IDDES} (defined similarly to $\tilde{d}$ in Eq. 5.21, refer to the Appendix in Gritskevich et al. (2012) for the detailed formulation) makes it possible to switch between RANS and LES models depending on the LES length scale Δ, the local turbulence length scale and the distance to the closest wall.

5.6 Hybrid LES/RANS simulations: Setup

5.6.1 Computational domain

Even though the hybrid approach alleviates the meshing requirements near solid boundaries, it remains relatively expensive. To further cut down on computational costs, the computational domain was restricted to the gap between the exit plane of the oscillator and the heated surface. Pulsating velocity conditions are applied at the inlet and are based

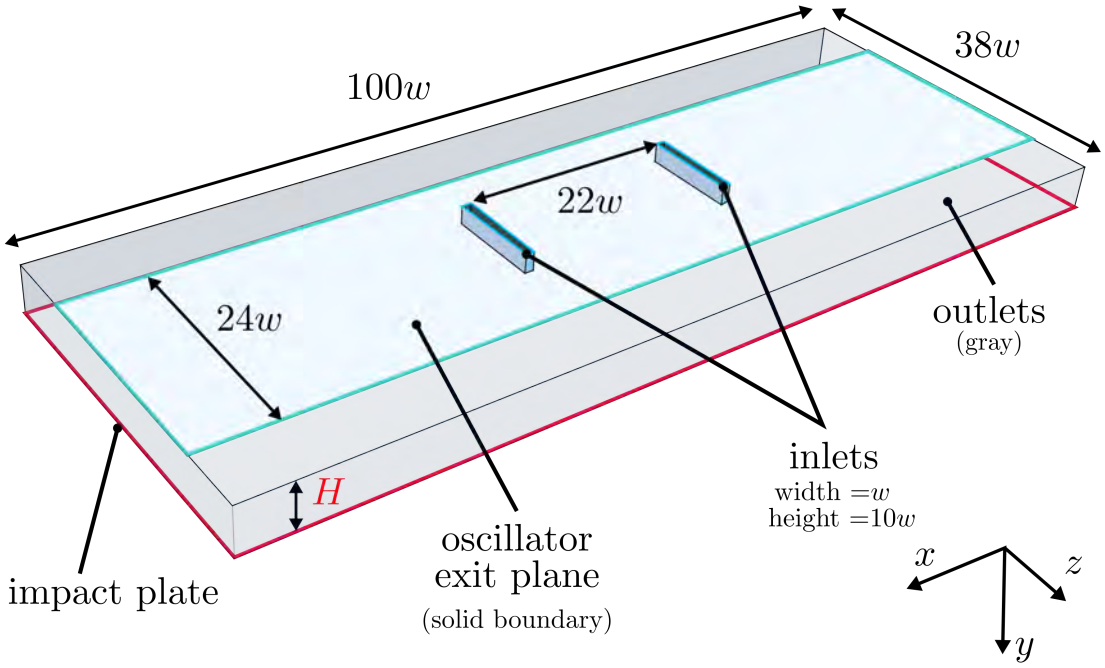

Figure 5.16: Computational domain and boundary conditions

on experimental measurements (see section 5.6.3). The exit face of the oscillator is also included in the domain as a $24w \times 100w$ solid boundary (see Figure 5.16). Beyond this area, the flow is only bounded by the heated plate from below (Figure 5.16, red contour). The inlet boundaries are connected to the exit slots via channels of length $2w$. The jets impact the heated surface along the y-axis then most of the flow deviates laterally along the x-axis. The centers of the two slots are placed 22 slot widths apart. Three impact distances of $H/w = 2, 5$ and 7 are investigated in this study.

5.6.2 Meshing strategy

The meshing constraints differ from one region to another in the domain. Near the solid boundary, in particular the heated surface, the meshing requirements are those of the $k-\omega$ Shear Stress Transport model, i.e., $y^+ = u^* y/\nu = 1$ (where u_* is the friction velocity at the nearest wall, y is the distance to the nearest wall and ν is the local kinematic viscosity of the fluid). In the shear layer of the jet, the mesh resolution depends on the vorticity thickness:

$$\delta_\omega = \frac{\Delta U}{\max\left(d\langle U\rangle/dx\right)} \tag{5.22}$$

that was estimated from hot-wire measurements. According to Sagaut et al. (2013),

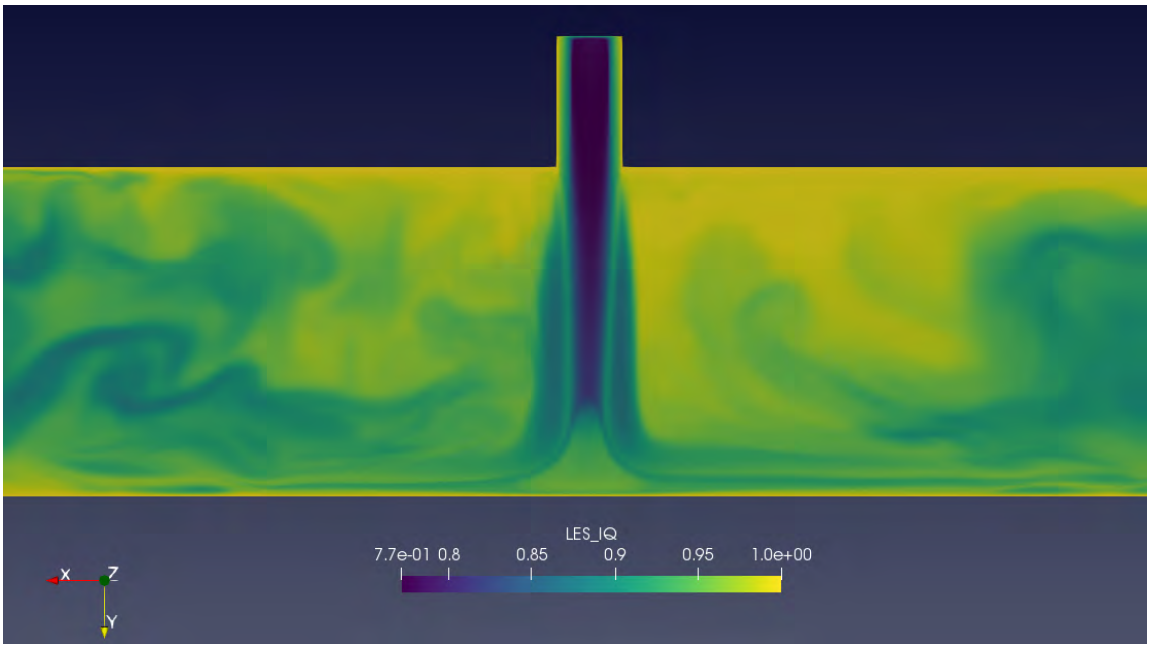

Figure 5.17: Contours of the LESIQ_ν quality index for the $H/w = 5$ case when the inlet velocity reaches its maximum value.

for a second-order accurate explicit centered scheme, about $25 - 30$ points are needed to discretize the vorticity thickness, i.e., $\Delta x \approx \delta_\omega/30$. Moreover, the streamwise and spanwise resolutions also depend on the vorticity thickness via $\Delta y \approx \delta_\omega/4$ and $\Delta z \approx \delta_\omega/6$, respectively.

With these constraints in mind, an initial mesh was produced and used to simulate the flow for a single pulsation period. The LES index of quality LESIQ_ν, which was proposed by Celik et al. (2005), was then computed using the effective turbulence viscosity $\nu_{t,\text{eff}}$. This index was conceived by the authors as a practical criterion that can be used to assess the quality of LES simulation in engineering applications. Whereas most LES studies resort to experimental or DNS data to validate their results, the LES index of quality offers a less costly alternative that restores the predictive quality of LES simulations. This index is defined as:

$$\text{LESIQ}_\nu = \frac{1}{1 + \alpha_\nu \left(\frac{\langle \nu_{t,\text{eff}} \rangle}{\nu} \right)^n} \tag{5.23}$$

where ν is the molecular viscosity, $\nu_{t,\text{eff}}$ the turbulence eddy viscosity, and α_ν and n are parameters determined from the criterion that a good LES simulation requires that 80% of the TKE must be resolved. Indeed, if we consider that $\text{LESIQ}_\nu \geq 0.8$ indicates a good quality LES, while a value of 0.95 and above means that we have reached the mesh resolution of a DNS, then the values of α_ν and n can be estimated to be 0.05 and 0.53, respectively.

The LESIQ_ν quality index reaches its lowest value around the center of the inlet channel

and in the initial part of the potential core of the jet. The minimum is equal to 0.77 and is reached when the inlet velocity reaches its peak value (Figure 5.17, for $H/w = 5$). It is worth noting that in these regions, the URANS length scale is activated, and so the index is not relevant here. However, the value of LESIQ_ν is above 0.87 in the shear layer surrounding the jet and in the rest of the domain during the entire period. This means that the regions in which the simulation switches to LES satisfy the condition that LESIQ_ν must be greater than 0.8 and no further refinement was performed on this mesh. The same meshing strategy was followed for the $H/w = 2$ and 7 cases.

5.6.3 Boundary conditions

The velocity fluctuations at the center of the slots were taken from experimental measurements performed using a hot wire probe. The velocity fluctuations were fitted using an eight-term Fourier model:

$$v_{\max}(t) = a_0 + \sum_{n=1}^{8} a_n \cos(2\pi n f t) + b_n \sin(2\pi n f t) \tag{5.24}$$

where a_0 is the average velocity and f is the fundamental frequency. The model was then implemented in OpenFOAM as part of a codedFixedValue boundary condition. A simplified spatial profile was chosen in both the x and z directions such that:

$$V(x, z, t) = v_{\max}(t) F_x F_z \tag{5.25}$$

with:

$$F_x = 1 - \left(\frac{2x}{D}\right)^8 \tag{5.26}$$

$$F_z = 1 - \left(\frac{2z}{D}\right)^{14} \tag{5.27}$$

(here, the center of a given slot was at $x = 0$ and $z = 0$). A uniform and constant temperature distribution $T = 310\,\text{K}$ was set at the impact surface, whereas the inlet channel and confinement walls were modeled as adiabatic boundaries. A wave transmissive outflow boundary condition was applied to the pressure field to avoid wave reflection at the boundaries of the domain. When applied to a field ϕ, this boundary condition solves the following advection equation:

$$\frac{\partial \phi}{\partial t} + \mathbf{U} \cdot \nabla \phi = 0 \tag{5.28}$$

If the advection velocity $\mathbf{U}$ was assumed to be normal to the boundary[2], the above

[2]This is a fair assumption in this case, since the outlet of the main flow is about 40 jet widths away from the stagnation point.

equation becomes:

$$\frac{d\phi}{dt} + (u_n + c) \cdot \frac{\partial \phi}{\partial n} = 0 \tag{5.29}$$

where u_n is the velocity of the outflow and c the speed of sound.

5.6.4 Solver and numerical schemes

A transient compressible solver called *rhoPimpleFoam* was used in these simulations, even though, at any given moment, the maximum velocity never exceeds $100\,\mathrm{m\,s^{-1}}$. It uses the PIMPLE algorithm for the pressure-velocity coupling, which is a combination of the PISO (pressure-implicit with splitting of operators) and SIMPLE (semi-implicit method for pressure-linked equation) methods. The diffusive and convection terms were both discretized using second-order central differencing schemes. The generalised geometric algebraic multigrid (GAMG) solver were used with a *GaussSeidel* smoother for the pressure equation, as it is recommended on large grids. The preconditioned conjugate gradient (PCG) and the preconditioned bi-conjugate gradient (PBiCGStab) algorithms were used for solving the density and momentum equations, respectively. The PBiCGStab algorithm was also used for the turbulence variables k and ω and the energy equation. Thermal effects on the physical properties of air were neglected seeing as temperature variations did not exceed $20\,^{\circ}\mathrm{C}$. Finally, the tolerance for all physical quantities was set to 1×10^{-6} or less.

5.6.5 Simulated physical time

The flow was first simulated for about 5 complete jet pulsations to avoid polluting the statistical quantities with transient data. After that, the averaging was performed for 5 pulsations.

5.6.6 Sampling

Considering the size of the grid, the entire data for each physical quantity is only written out once every millisecond of physical simulated time. However, some data is sampled at a higher rate across a number of planes:

- a plane normal to the $z-$axis and passing through the center of the domain
- a plane formed by the $x-$axis and the central axis of the left slot
- a series of planes normal to the $y-$axis separated by a constant gap of one slot width w. For example, for the $H/w = 7$ case, there are 7 such planes at $y = w, 2w, \ldots, 7w$ from the jet exit plane.

  These samples are written out every $1/400\,\mathrm{ms}$ of physical simulated time.

5.7 Results: Hybrid LES/RANS Simulations

5.7.1 Vortex dynamics

By looking at data sampled from a number of surfaces in the domain, we attempt to describe the features that arise in the pulsating flow. More specifically, the dynamics of nascent and developing vortices are deduced from the velocity $\mathbf{u}$ and vorticity $\mathbf{\Omega}$ fields with the help of the Q-criterion. Although there is no universally accepted definition of what a *vortex* is (Jeong and Hussain (1995)), the Q-criterion offers a relatively simple way of identifying large coherent structures. The Q-criterion belongs to a class of vortex identification methods based on the velocity gradient tensor $\mathbf{D} = \nabla\mathbf{u}$ (or $D_{ij} = \partial u_i/\partial x_j = u_{i,j}$ in tensor notation). It can be decomposed into a symmetric and a skew-symmetric part $D_{ij} = S_{ij} + \Omega_{ij}$, where

$$S_{ij} = \frac{1}{2}\left(\frac{\partial u_i}{\partial x_j} + \frac{\partial u_j}{\partial x_i}\right) \tag{5.30}$$

$$\Omega_{ij} = \frac{1}{2}\left(\frac{\partial u_i}{\partial x_j} - \frac{\partial u_j}{\partial x_i}\right) \tag{5.31}$$

are known as the strain rate and vorticity tensors, respectively. In an incompressible flow, Hunt et al. (1988) defines a vortex as a connected fluid region where the second invariant Q of the velocity gradient tensor is positive:

$$Q \equiv \frac{1}{2}\left(u_{i,i}u_{i,i} - u_{i,j}u_{j,i}\right) = \frac{1}{2}\left(\Omega^2 - S^2\right) > 0 \tag{5.32}$$

where Ω and S are the magnitude of vorticity and strain rate, respectively [3]. Put differently, a vortex is where the magnitude of vorticity prevails over that of strain rate. In practice, the condition stated in Eq. 5.32 is not enough to clearly demarcate coherent structures from smaller, incoherent vortices. An arbitrary threshold is typically chosen to pinpoint regions where vorticity strongly predominates over the strain rate. The arbitrariness of this threshold is one of the pitfalls of this method. Other identification techniques exist and are tailored to specific applications (Kolář (2007)), however, the Q-criterion serves the purposes of the present study, namely, to find nascent vortices and track their evolution during each pulsation period. The instantaneous flow fields are presented here in different regions of the domain, namely the free jet region, the outbound flow and the intermediate zone

[3] the summation is carried out on both indices i and j in Eq. 5.32

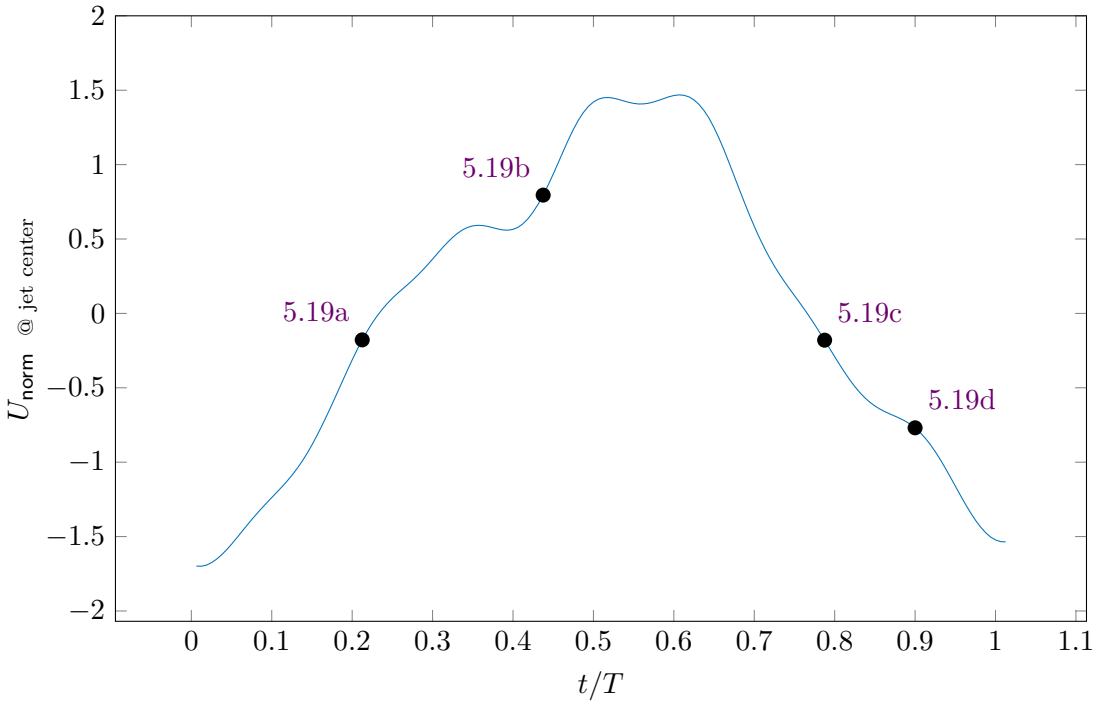

Figure 5.18: Normalized velocity waveform at the center of the jet exit slot.

5.7.2 Outbound flow

Standoff distance $x/w = 2$, midplane $z = 0$ As mentioned earlier, the vorticity field along with the detected edges of the regions where Q is large are used to describe the vortex dynamics in the flow (Figure 5.19a). The origin of the $x-$axis coincides with the center of the jet exit slot. The different phases described next are indicated on the velocity waveform shown in Figure 5.18. As the velocity of the jet increases, trail of vortex dipoles appear in the shear layer of the wall jet (Figure 5.19a). The distance between the jet exit plane and the target surface is too short for vortices to develop in the shear layer of the impinging jet. As velocity continues to increase, the nascent vortices appear farther downstream (Figure 5.19b). The adverse pressure gradient produced by the vortices becomes strong enough that the dipole is ejected from wall. The wall jet separates from the boundary and turns into a channel flow downstream. The ejected dipole eventually causes the wall jet to roll-up backwards. This continues even as the flow begins to slow down (Figure 5.19c). Finally, as the velocity approaches its minimum value, a regular trail of vortex pairs are shed directly from the stagnation region (Figure 5.19d).

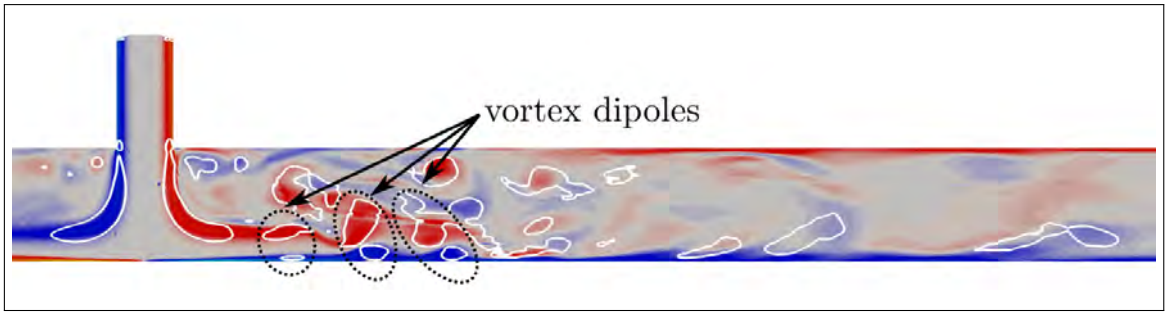

(a)

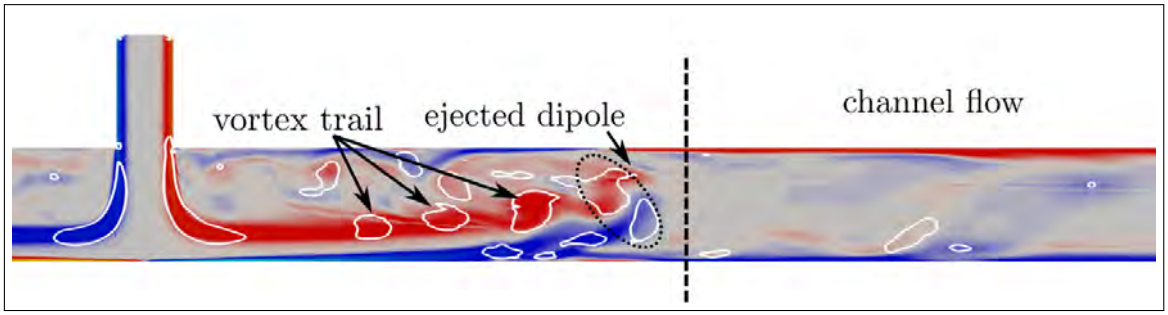

(b)

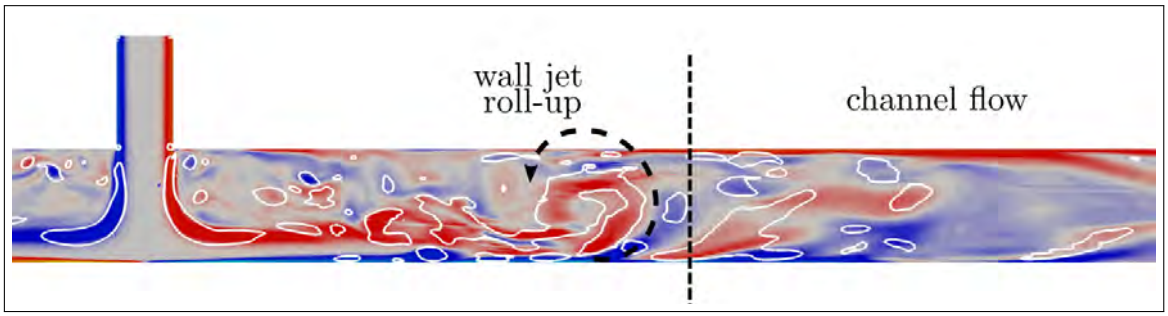

(c)

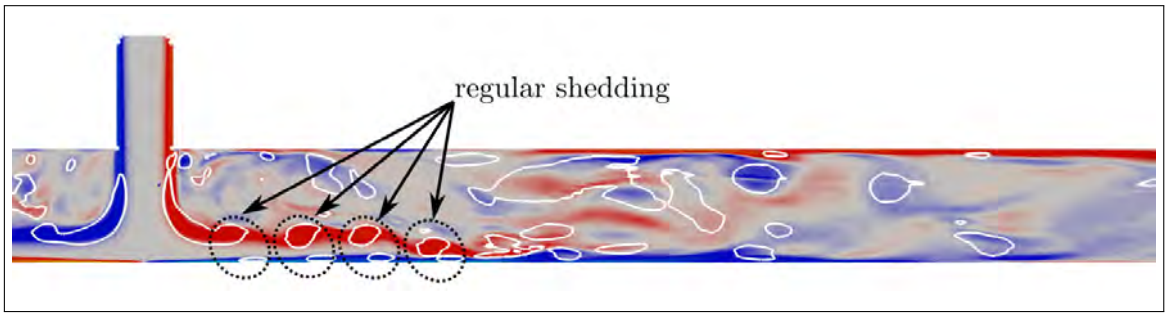

(d)

Figure 5.19: Vorticity ω_z contours (red: counterclockwise CCW, blue: clockwise CW) and boundaries of fluid regions where $Q \geq 1 \times 10^9\,\mathrm{s}^{-1}$ (white) for $H/w = 2$ at different times of the pulsation as shown in Figure 5.18.

Standoff distance $x/w = 5$, midplane $z = 0$ As the velocity starts to increase in the jet exit plane (Figure 5.21b), small, clockwise rotating vortices (red) are shed downstream from the stagnation zone at a regular interval, each accompanied by a counterclockwise (blue) vortex near the wall. At this point during the pulsation, the wall jet remains attached to the impingement surface. As the velocity continues to increase (Figure 5.21c), a larger vortex dipole (VD1) is shed from the stagnation region and is eventually ejected away from the surface, leading to wall jet separation (Figure 5.21d). This process then repeats itself (Figure 5.20e) until the jet reaches peak velocity, with the ejected dipoles breaking up and following a large orbital motion around each other leading to a roll up of the wall jet. As the velocity begins to decrease, the rolled up wall jet starts to unwind (Figure 5.20f), and the separation point moves downstream (Figure 5.20g). Finally, regular vortex shedding resumes (Figure 5.20h, just as at the beginning of the cycle. These vortex dipoles remain close to the surface, slightly undulating the wall jet without causing separation. As a side note, the jet is deflected to the right from 5.21a to (d) and then again at 5.20h because of the influence of the second jet. Around peak velocity from 5.20e to (g), the jet impinges normally onto the surface.

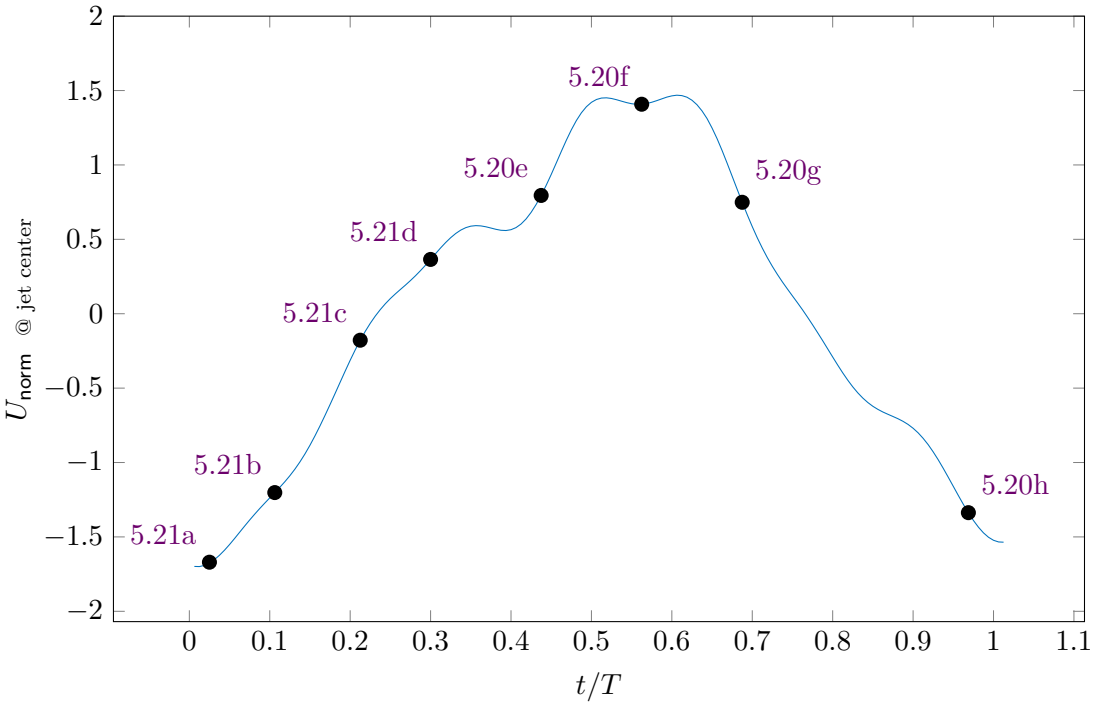

Figure 5.20: Normalized velocity waveform at the center of the jet exit slot.

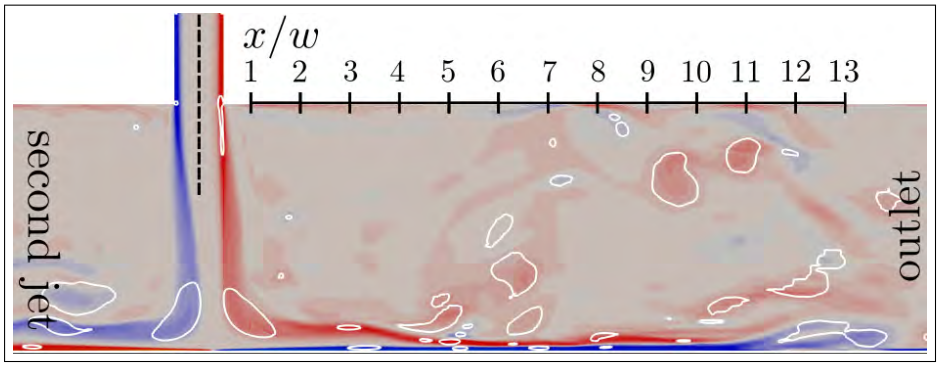
x/w
1 2 3 4 5 6 7 8 9 10 11 12 13
second jet
outlet

(a)

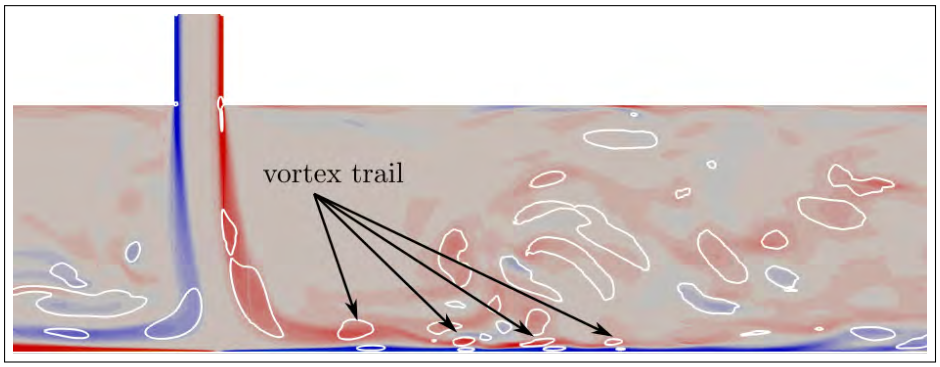
vortex trail

(b)

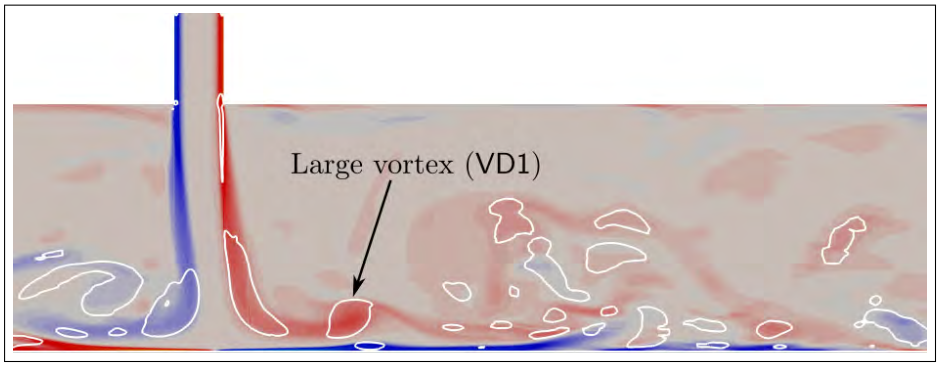
Large vortex (VD1)

(c)

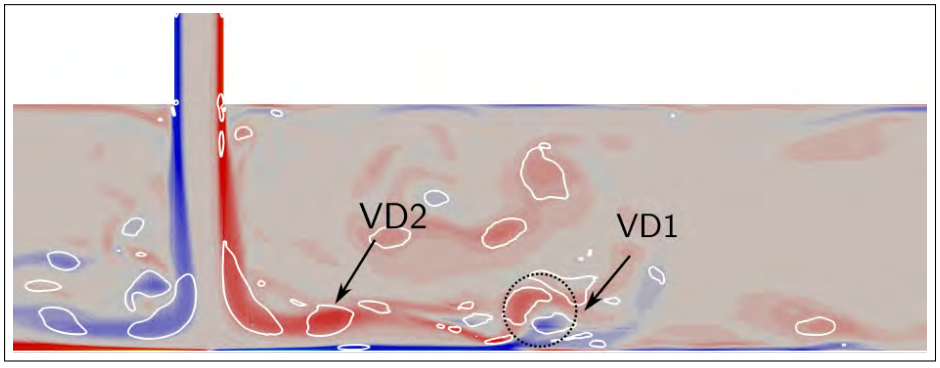
VD2
VD1

(d)

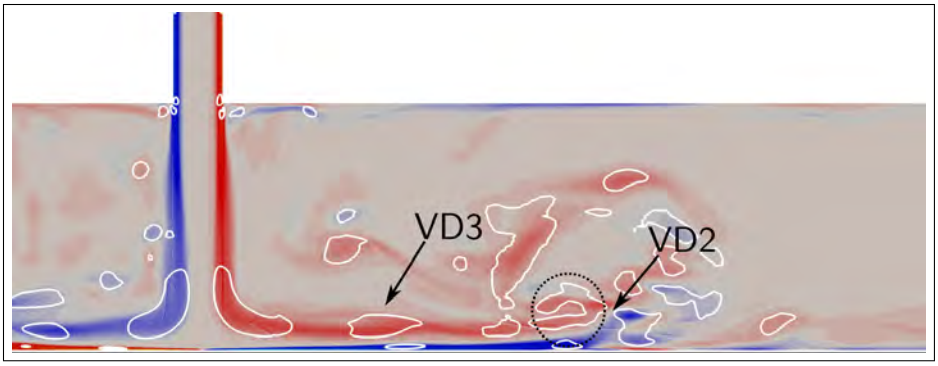

(e)

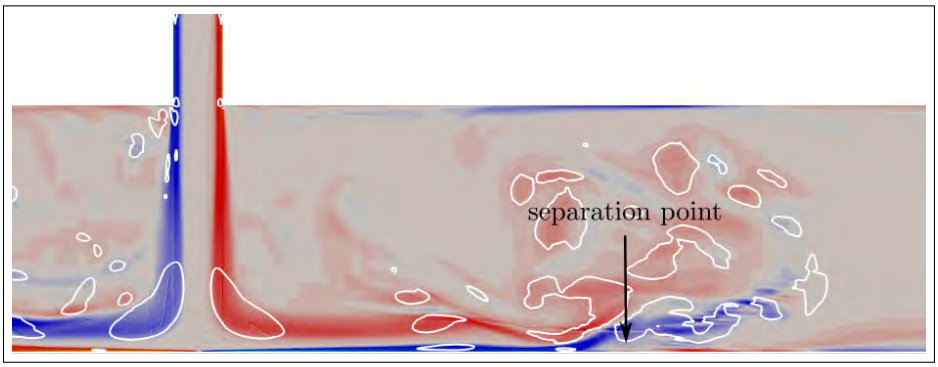

(f)

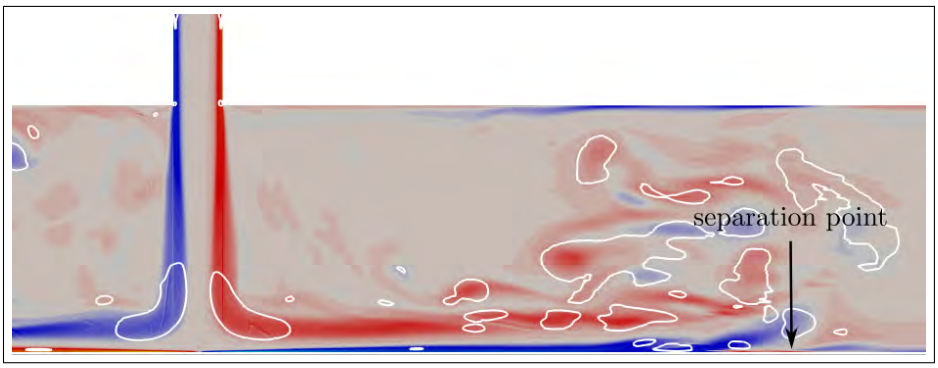

(g)

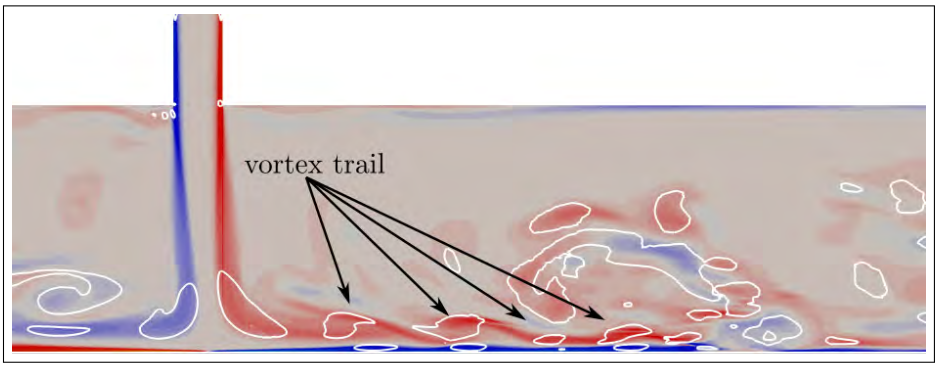

(h)

Figure 5.20: Vorticity ω_z contours (red: counterclockwise CCW, blue: clockwise CW) and boundaries of fluid regions where $Q \geq 1 \times 10^9\,\mathrm{s}^{-1}$ (white) for $H/w = 5$ at different times of the pulsation as shown in Figure 5.20.

Standoff distance $x/w = 7$, midplane $z = 0$ Similarly to the previous case, a trail of vortices appear in the wall jet region and are transported downstream by the flow during the off-phase of the jet pulsation (Figure 5.22a). However, unlike the two cases described earlier, the jet begins to decay before reaching the heated surface since the impact distance $x/w = 7$ is greater than the length of the potential core. The jet becomes unstable, taking on a flapping motion which leads to a back and forth motion of the stagnation point on the heated target plane. The instability grows as the velocity of the jet starts increasing during the on-phase and eventually leads to a roll-up of a series of vortex pairs that are asymmetrical with respect to the jet axis (Figure 5.22b). Unlike the previous cases, these vortices appear in the free jet region, before reaching the target surface. As the jet reaches peak velocity, the flapping motion ceases and the flow hits the plate perpendicularly. Nevertheless, the stagnation point continues to oscillate about the jet axis, albeit at a smaller amplitude than during the preceding phase (Figure 5.22c then 5.22d). Finally, as the velocity begins to decrease, the flapping motion resumes and the process repeats itself.

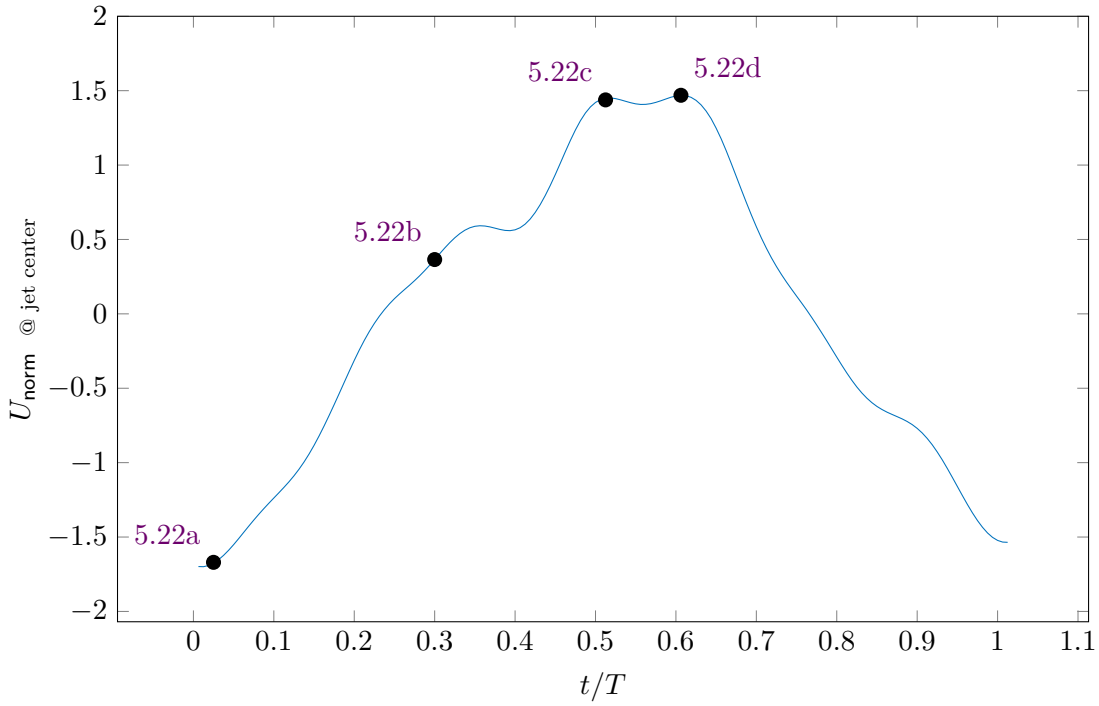

Figure 5.21: Normalized velocity waveform at the center of the jet exit slot.

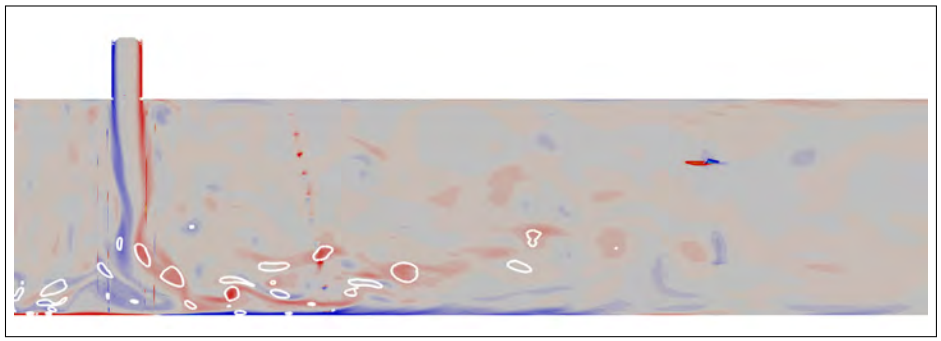

(a)

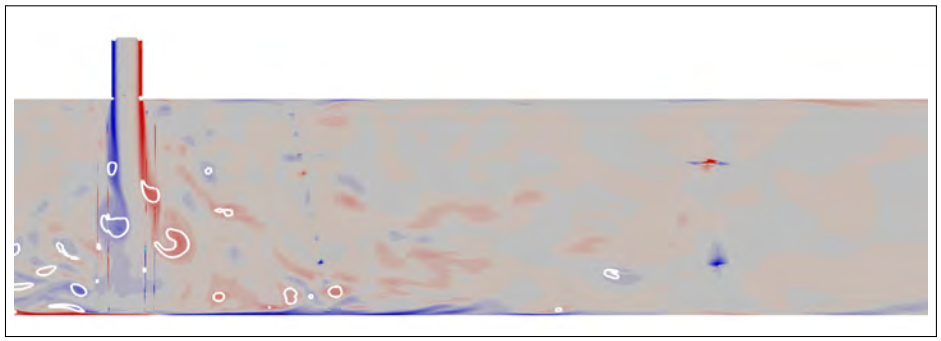

(b)

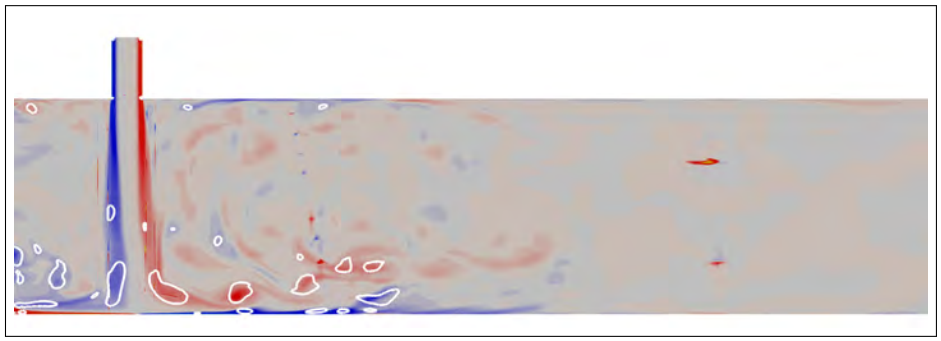

(c)

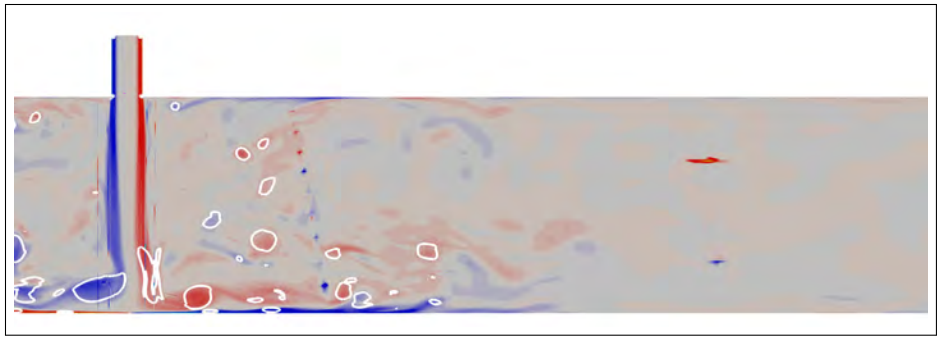

(d)

Figure 5.22: Vorticity ω_z contours (red: counterclockwise CCW, blue: clockwise CW) and boundaries of fluid regions where $Q \geq 1 \times 10^9\,\mathrm{s}^{-1}$ (white) for $H/w = 7$ at different times of the pulsation as shown in Figure 5.21.

5.7.3 Intermediate region

Standoff distance $x/w = 2$, midplane $z = 0$ Moving on to the intermediate region, the vortex dipole ejection induces separation of the wall jet at around seven initial width from the axis of the jet (Figure 5.23a). The jet on the right is approaching its maximum velocity. Seeing as the gap between the target (bottom) and confinement (top) plates is narrow, the separated flow impinges on the former. Shortly thereafter, the flow departs from the top plate and re-impinges on the target plate (Figure 5.23b). On the other side, the jet is in the off-phase, and a weak wall jet can be seen that dissipates before reaches the other wall jet. No significant interaction between the two wall jets can be seen.

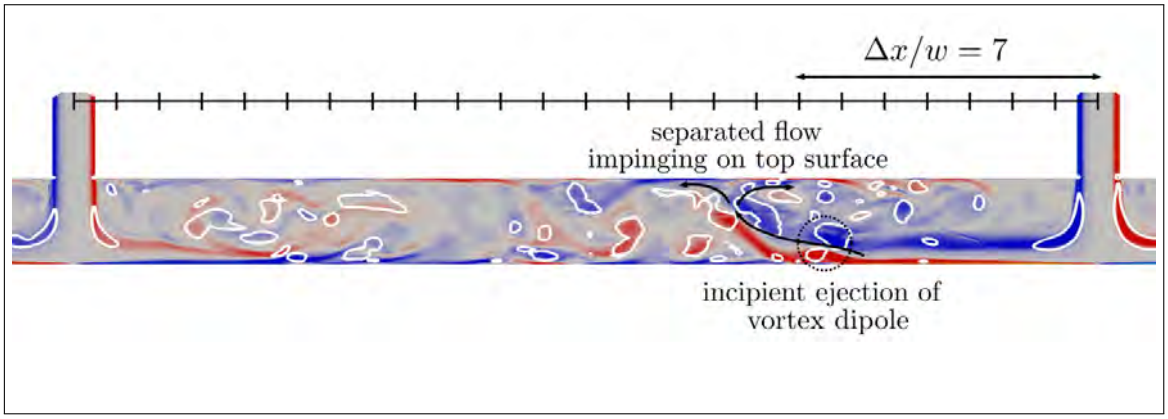

(a)

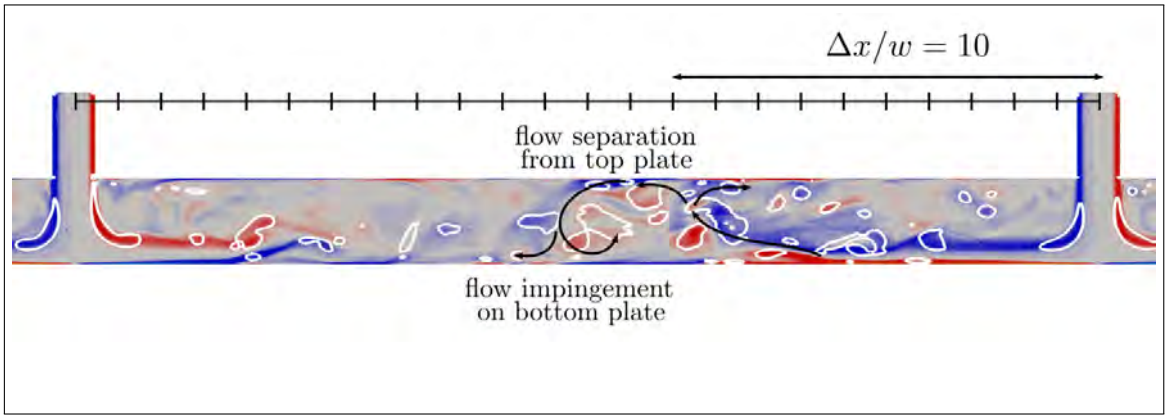

(b)

Figure 5.23: Vorticity ω_z contours (red: CCW, blue: CW) and boundaries of fluid regions where $Q \geq 2 \times 10^9\,\mathrm{s}^{-1}$ (white) for $H/w = 2$.

Standoff distance $x/w = 5$, midplane $z = 0$ The formation, development and ejection of vortex structures described earlier also occur in this part of the domain. The main difference is that the structures do not propagate towards the exits, but remain in this region. This results in a higher turbulence activity. Seeing as the jet velocity never reaches zero during the cycle, the inbound wall jets collide and flow upwards, away from the wall.

This upwash is referred to as the 'fountain flow'. Its position changes during each cycle. The wall jet with the higher velocity pushes the fountain flow toward the other jet, causing its wall jet to roll up on itself. Figures 5.24a and 5.24b show both cases where the right or left wall jet rolls up, respectively.

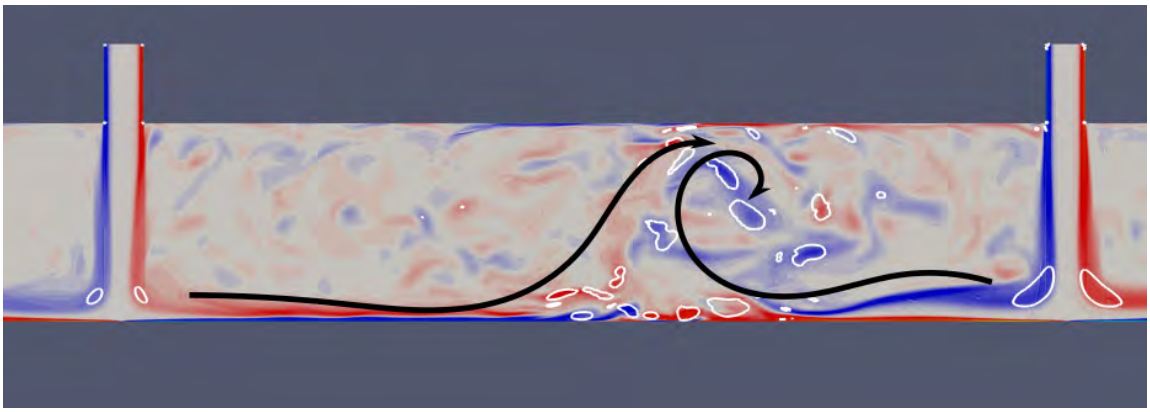

(a)

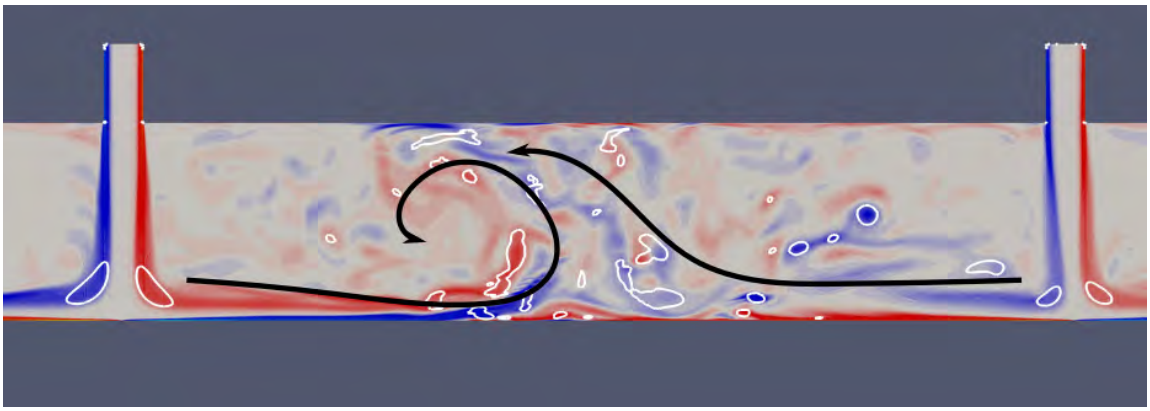

(b)

Figure 5.24: Vorticity ω_z contours (red: CCW, blue: CW) and boundaries of fluid regions where $Q \geq 5 \times 10^9\,\mathrm{s}^{-1}$ (white) $H/w = 5$. The black lines roughly indicate the flow direction of the two wall jets.

Standoff distance $x/w = 7$, midplane $z = 0$ In this last case, although the inbound wall jet does separate due to vortex dipole ejection, the distance between the top and bottom walls is broad large enough that the flow does not reach the top plate. The ejected vortices, that formed in the shear layer of the free jet region, simply 'float' away from the target plate and dissipate into the intermediate region.

5.7.4 Heat Transfer

Just as in the RANS part of the study, the Nusselt number was computed from the vertical temperature gradient across the target plate. Unlike the RANS simulations, it was not possible to run the calculations for the hybrid model for tens of pulsation periods in order

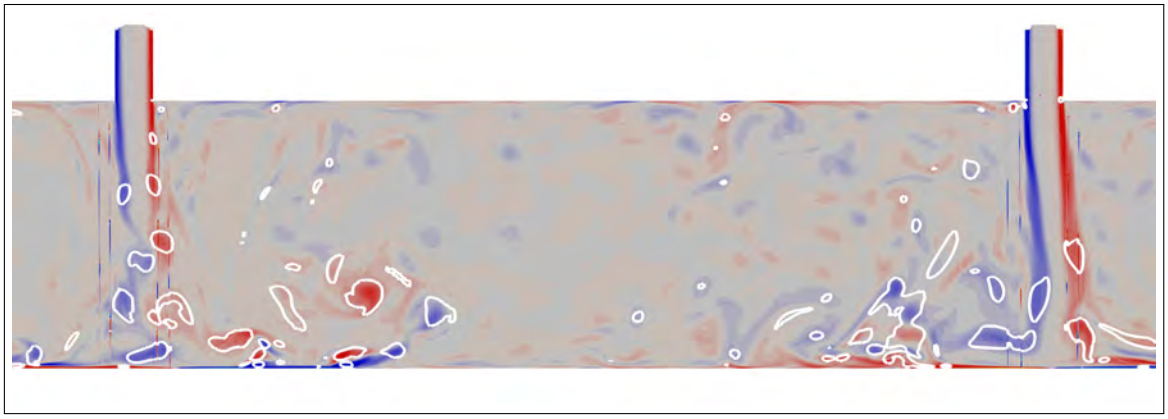

Figure 5.25: Vorticity ω_z contours (red: CCW, blue: CW) and boundaries of fluid regions where $Q \geq 5 \times 10^9\,\mathrm{s}^{-1}$ (white) $H/w = 7$.

for the temperature gradients to completely converge. The hybrid simulations were run for at least 8 pulsation periods in order for the flow to develop, then the average temperature gradients were obtained after only 3 pulsation periods. Accordingly, as can be seen in Figure 5.26, the Nusselt number distribution is not sufficiently symmetrical in the wall jet region where the flow is typically more incoherent than around the impact point of the two jets, and so the average quantities take longer to converge. However, several features of these distributions can be highlighted in view of the description of the flow given earlier. For instance, for $H/w = 7$, the ejection of the dipoles from the wall and the absence of any significant interaction between the two wall jets is reflected in the absence of any salient features in the Nusselt number distribution for this region. For $H/w = 2$ and 5 however, the dynamics of the flow produce a number of local maxima. For instance, when $H/w = 2$, two adjoined peaks can be seen in the center of the distribution and are associated with the re-impingement of the flow onto the bottom plate near the center of the intermediate region (Figure 5.23b). For $H/w = 5$, the point of collision of the two wall jets in the intermediate regions moves about the center of domain depending on the relative velocities of the two pulsed jets, which might explain the relatively distinct peaks near the center.

Turning to the impact region, a standoff distance of $H/w = 5$ leads to the highest value of the peak Nusselt number, followed closely by $H/w = 2$. Performance quickly deteriorates when $H/w = 7$. This is in sharp contrast with the RANS results, where a steep, monotonic decrease of the maximum Nusselt number was observed for increasing impact distance. Although a quantitative comparison cannot reasonably be done between the hybrid and experimental results, the overall behavior seems comparable (see Figure 4.9 in Chapter 3). In the experimental results, the peak Nusselt number changed very little, compared to the steady case, for standoff distances of up to 4 to 5 initial jet widths, which corresponds to the length of the potential core, sometimes even reaching a maximum near $H/w = 4$. Likewise, the peak Nusselt number for $H/w = 2$ and 5 are relatively close to one another, and whereas it is much lower for $H/w = 7$.

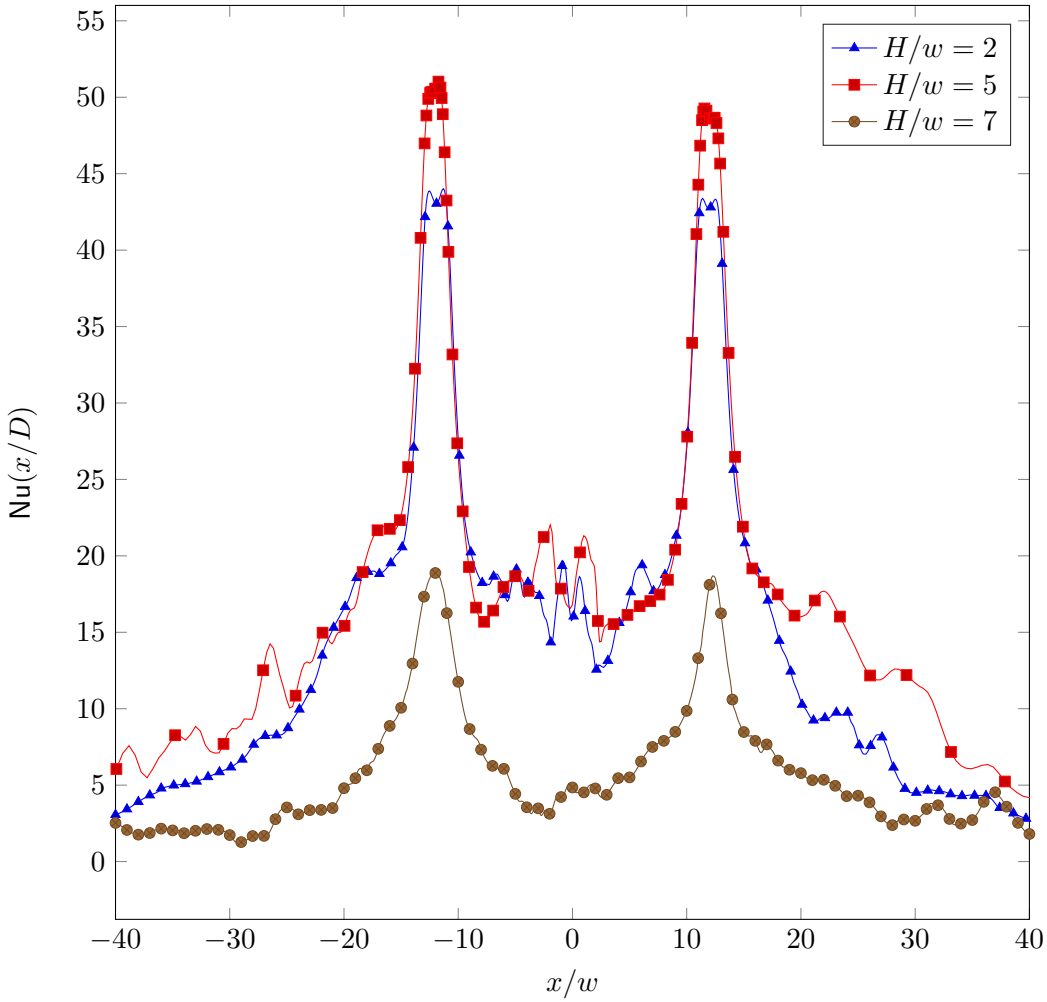

Figure 5.26: Nusselt number distribution on the constant temperature surface from the hybrid LES/RANS simulations with three standoff distances $H/w = 2, 5$ and 7.

5.8 Conclusion

In the first part of this numerical study, several of the most popular RANS models were used to simulate the Lg0 prototype along with the pulsed impinging flow it produces in order to assess heat transfer performance. All of these models felt short on many accounts, and the main conclusions were summarized in Section 5.4.

In order to have a glimpse of the phenomena taking place in the impingement flow, we turned to a hybrid LES/RANS approach that is capable of simulating the large, energy containing parts of the flow while modeling the rest. This is a compromise between the LES or DNS, whose computational costs are often prohibitive, and RANS which is unable to predict the flow structures that affect heat transfer. Although it was not possible to simulate the flow long enough for the average temperature gradients to converge, we were able to observed the dynamics of vortex structures in the flow as well as the interaction between the two out-of-phase jets. The preliminary heat transfer results show a convincing,

albeit qualitative, resemblance to the experimental results. The same could not be said of the RANS results.

Having studied the internal behavior of the oscillator as well as the pulsed flow that it produces, using both experimental and numerical approaches and having shown that fluidic oscillators can, under certain conditions, outdo steady impinging jets in terms of heat transfer performance, we now move on to the second part of the study which involves miniaturizing the device. As mentioned at the end of the literature review, little interest has been given to pulsed impinging jets in microfluidic cooling applications. A recent study by Huang et al. (2022) has shown that pulsed sub-millimetric jets can significantly improve heat transfer in microchannel heat sinks. However, since the study was purely numerical, the pulsed microjets were produced by imposing periodically fluctuating boundary conditions. In what follows, we present the development and instrumentation of microfluidic oscillators that can be used in new heat transfer applications such as in Huang et al. (2022).

Part II

Microscopic Design

"There are no small parts, only small act[uat]ors."

Attributed to Konstantin Stanislavski

6

Dry-Film Lamination and Initial Diagnosis

Having studied the behavior of the fluidic oscillator in response to operating and design conditions as well as its performance as a cooling device, we now turn to the production, instrumentation and testing of a miniaturized version. Compared to the original prototype, the dimensions were reduced along the x and y axes by a factor of ten. The depth of the channels is either 25 or 50 µm. These result in aspect ratios of the main jet of 1.25 and 2.5, respectively.

Before embarking on the complicated task of producing microfluidic channels with integrated temperature sensors, a number of prototypes were produced without sensors to make sure that they could function at this scale. Previous work by Yang et al. (2007) on oscillators having roughly the same throat width (16 µm) and using a liquid as a working fluid showed that the oscillator would only work if the feedback loops were asymmetrical. The high relative viscosity at this scale and the use of liquid inhibits the initial instability of the jet that sets off the switching mechanism. This was not an issue here, where a symmetric design seems to produce consistent oscillations with air as the working fluid. This was verified at first by measuring the audible frequency of the device when it was supplied with pressurized air. As will be presented in the following chapters, a more accurate assessment will be possible once sensors are implemented inside the device.

6.1 From stereolithography (SLA) to dry-film deposition

As a segue between the two parts of the study, we begin by looking back at the fabrication methods that were at our disposal when producing the 'macroscopic' version of the oscillator and why we landed on stereolithography in lieu of more conventional methods that use CNC machines and require mechanical assembly.

The aspect ratio of the most critical features in the oscillator is in the range of 1 : 35 [width:height]: for a typical throat width of 200 µm, this led to a channel height of 7 mm, something that cannot be achieved easily with conventional machining. Hence, the prototype previously produced by Wang (2017) consisted of several parts that had to be mechanically assembled. This led to several issues, namely misalignment, causing geometric asymmetry, and leakage, both of which strongly affect the functioning of the oscillator. To avoid dealing with the same issues, we opted to use a 3D-printer to manufacture our first prototype at the nearby Laboratory for Analysis and Architecture of Systems (LAAS). The available 3D-printer that could produce the best prototype in terms of accuracy and surface quality was the DW 029J+ from DWS Systems. Unfortunately, due to the limited working area of the printer ($150 \times 150 \times 100$ mm) we had to reduce the length of the feedback loops. The printer produces the models by stereo-lithography (SLA) which consists in hardening successive layers of a polymer onto a plate using UV light.

Judging by the complexity and scale of the model that we are studying it is almost inconceivable to produce it using conventional methods, i.e. methods that involve taking away material from a part to obtain the required shape. The modern alternative is using 3D-printing, or, in more technical terms, *additive manufacturing* **(AM)** (or even *layer manufacturing processes*). As its name indicates, additive manufacturing is the process of producing three dimensional objects by adding successive layers of material, most commonly a polymer. The main benefits of AM is the ability to produce highly sophisticated shapes and parts that normally require assembling several pieces together (keep in mind that assembly points usually constitute the primary source of weakness) relatively fast and without the need to define production steps like in CNC manufacturing.

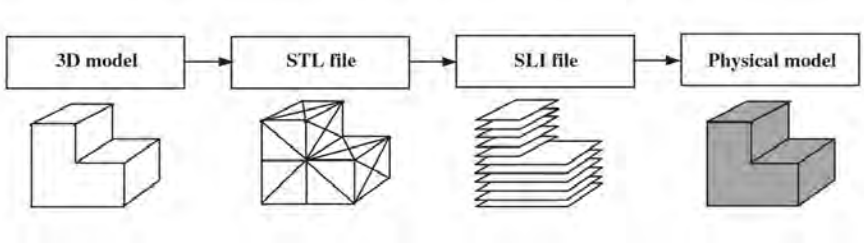

Figure 6.1: Key steps to produce a physical model Alves and Bártolo (2006)

Our prototype was made using a specific type of additive manufacturing called *stereolithography* (**SLA**). As can be seen in figure 6.2, SLA requires a polymer in liquid state that is progressively solidified using a moving laser beam. The steps leading up to the actual manufacturing (Figure 6.1) are as follow (Corbel et al., 2011):

1. Solid model generation
2. STL file generation (3D meshes of triangular elements)
3. SLI file generation (model slicing)
4. Physical model production

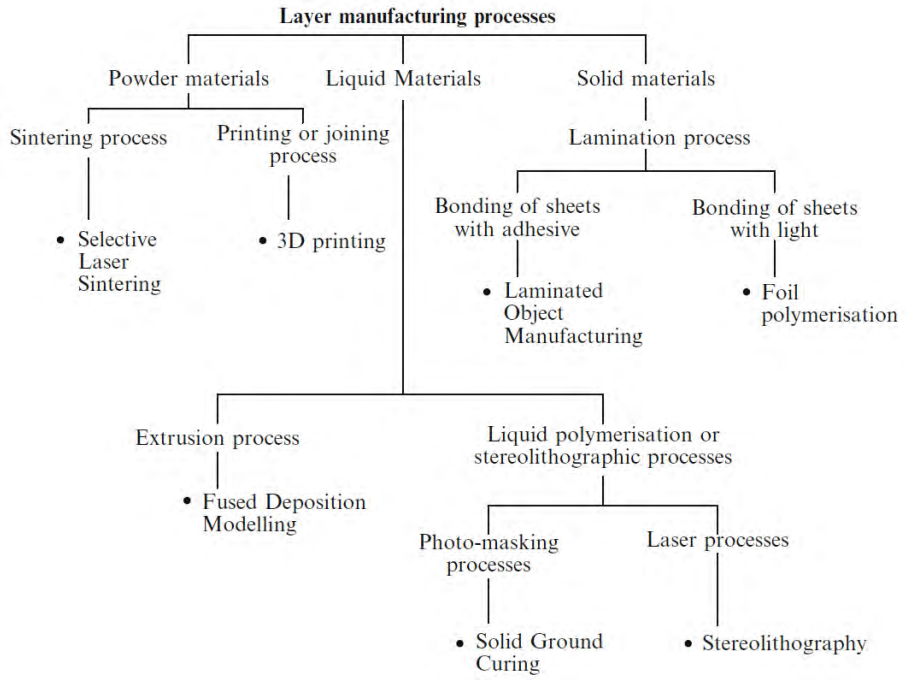

Figure 6.2: Classification of additive manufacturing processes. Corbel et al. (2011)

The solid model can be generated using any software (in our case, we started by producing a 3D model of the oscillator using a CAD software, then modified it to include fittings for the pressure inlet and reduced the size to fit the working area. The STL file basically defines a set of triangular facets that approximate the surface of the object. This process of triangulation is subject to a set of rules: the adjacency rule and the orientation rule [1].

Tessellating a surface is equivalent to producing a first-order approximation of it and that can lead to issues with regards to complex shapes. Furthermore, an adequate chordal tolerance (maximum distance between the actual surface and a given edge) has to be chosen in order to obtain a smooth enough surface which may lead to larger data files.

The next step is to prepare the 3D print files from the STL file, which includes print support structures placement and size optimization, as well as object orientation: this is done within Nauta, a software from DWS. The next step is slicing the CAD model as to obtain layer by layer contours. The thickness of the layers can either be constant or adaptive. With the latter, the layers become thinner where the surface presents high curvature.

[1] the specifics of this process are of no particular interest for this study, see Chen et al. (1999) for further details

While slicing is the spacing along the $Z-$axis (thickness), the hatching represents the X/Y spacing between two adjacent laser passes. A small hatching has been favored to obtain significant overlap between adjacent laser passes and a more cohesive, solid layer in spite of the longer printing time. The contour number was kept minimal to maximize absolute dimension accuracy of the microchannels.

Now that we are done with the preliminary steps, we can focus on the manufacturing process itself. We start with a vat filled with the liquid polymer (DS3000 by DWS in our case) and containing a movable surface. A set of actuated mirrors (figure 6.3) are used to deflect the laser beam in order to harden the polymer layer by layer based on the sections produced during slicing. Each layer is created by hardening a set of *voxels* (the three-dimensional version of *pixel*), the part is then dipped deep enough into the liquid to recoat the surface and to produce, after a wait period, the next layer.

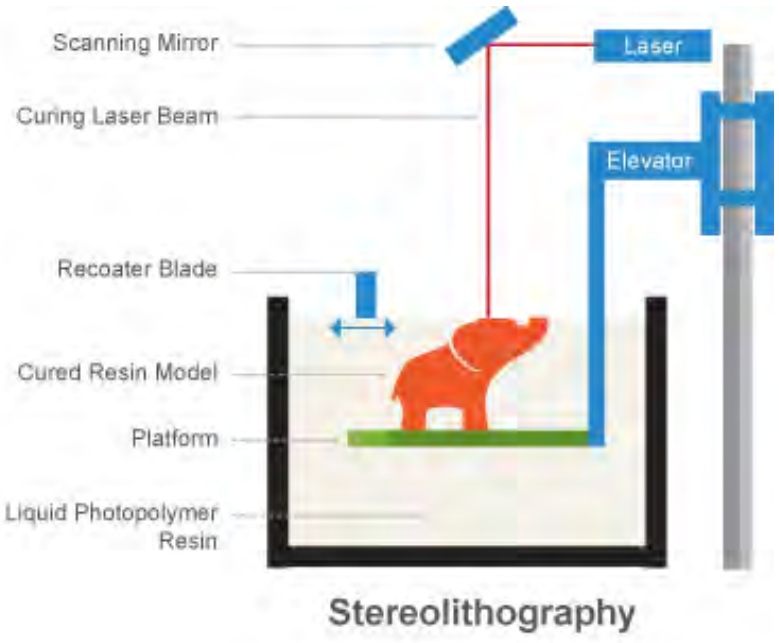

Figure 6.3: Direct focused beam-writing method

Keeping in mind that the smallest dimension in the geometry is 200 µm, the 3D printer used was able to accurately produce the prototype thanks to a $30-40\,\mu m$ resolution in the XY plane, and a $10-100\,\mu m$ resolution along Z. Comparing our prototype with the one used by Shiqi Wang Wang (2017), we can easily observe the advantage of using stereolithography. First of all, no assembly is needed. The previous prototype was machined out of metal blocks and sandwiched between two plates and fasted at several points. The two main issues with this configuration are the high possibility of air leakage between the plates as well as misalignment of the different shapes that constitute the oscillator when it is assembled (see figure 6.4). In addition, the left wall of the oscillator's throat, which is supposed to be rectilinear, is slightly curved due to machining error.

Having only changed the loop length to account for the limited working area of the

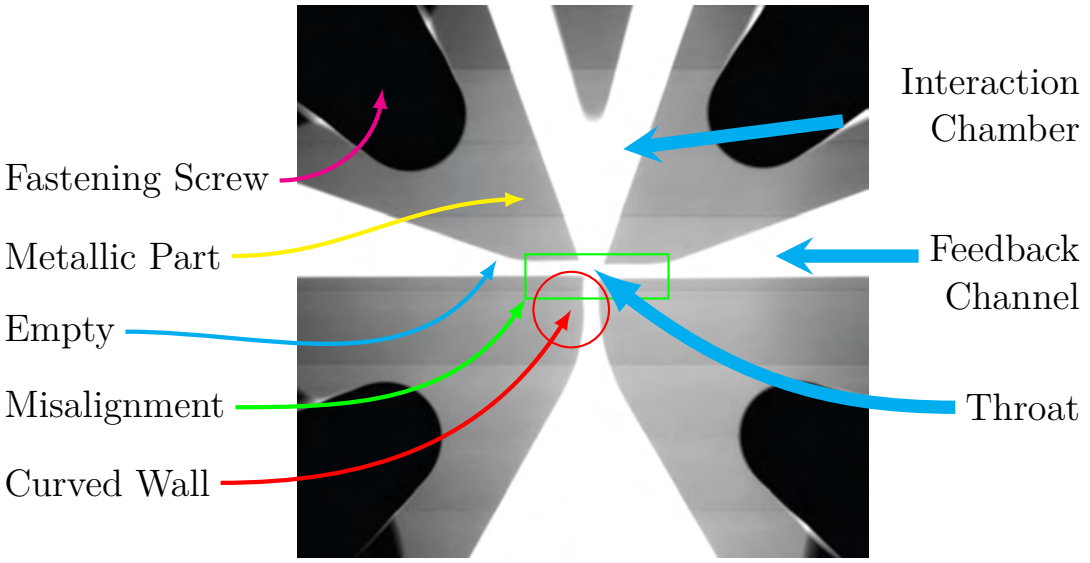

Figure 6.4: Throat, Interaction Chamber and Feedback channels of the prototype used by Shiqi Wang in Wang (2017)

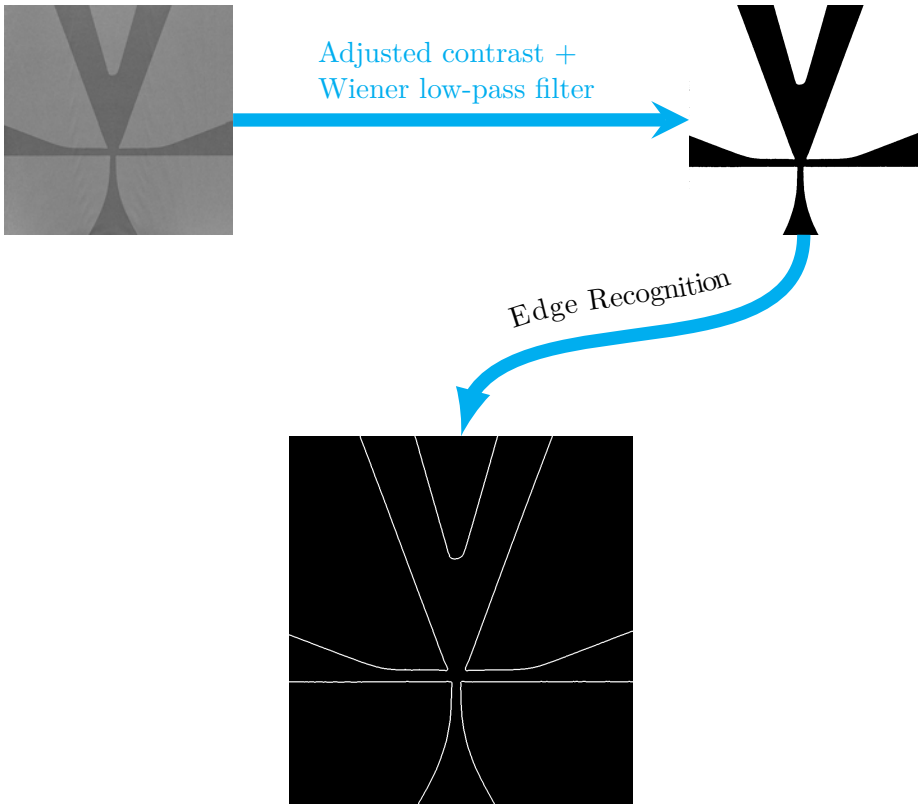

Figure 6.5: Tomography of throat/interaction chamber zone of the new oscillator along with the processed images. (Throat width= 200 µm)

printer, we can still compare the quality of our new prototype with that of the old prototype, specifically at the throat. The new prototype is entirely made out of a patented resin called DS3000 and does not require assembly. The only constraint on the choice of resin was the

high pressure at the inlet which it can effectively withstand. As can be seen in figure 6.5, the feedback channels are perfectly aligned, and the form of the lateral surfaces correspond well to the numerical drawing. Also worth noting is the low cost of production of these prototypes when compared to conventional methods. Moving on, reducing the scale of the model by a factor of ten requires an entirely different approach. For the dimensions that we are looking to achieve, the 3D printers are simply not accurate enough. We must resort to microfabrication techniques. There are a number of approaches at our disposal to create microchannels, such as PDMS molds, spin-coated liquid photoresists or laminated dry-film that we will present next.

6.2 Microfluidic oscillators without temperature sensors

The development of complex microfluidic devices was first made possible by the use of polydimethylsiloxane (PDMS) soft-lithography (Xia and Whitesides, 1998), which is a relatively simple tool for rapid prototyping. A master mold is made using photolithography into which the PDMS is poured and polymerized. The resulting PDMS chips are then bonded over the substrate. The master mold is typically made from a negative photoresist, patented by IBM in 1989, called SU-8 which is adapted for thick-film applications and has a low absorbance in the near ultra-violet (UV) range. Molding techniques have since gained ground for their ability to produce three-dimensional stacked structures and to be integrated in silicon-based devices. The process of producing the SU-8 mold can be divided into the following main steps:

1. **Wafer preparation:** The wafer is cleaned using a piranha solution, which is a mixture of sulfuric acid (H_2SO_4) and hydrogen peroxide (H_2O_2). The wafer is then heated in order to remove any residual moisture on the surface. Plasma treatment (O_2) of the wafer can be used in order to improve the adhesion as well as spin-coating an adhesion promoter before depositing the SU-8.
2. **Spin-coating of the photoresist:** the resin is poured onto the rotating wafer. The puddle of resin spreads in the radial direction, until it coats the entire wafer. The rotation speed, acceleration and the viscosity of the resin will determine the thickness of the coating.
3. **Soft bake:** in this step, the wafer is heated in order to evaporate the solvent and make the photoresist layer more solid. The heating is done gradually and in steps in order to avoid creating residual stresses inside the photoresist.
4. **UV exposure:** the photoresist is exposed to UV light through a photomask. The parts exposed to the light are hardened while the other parts will remain soluble in the developer fluid.
5. **Post Exposure Bake (PEB):** Heating the photoresist after exposure further drives the polymerization reaction already activated by the UV radiation. The heating is done gradually to reduce residual stresses in the photoresist.
6. **Development:** the non-polymerized parts of the photoresist are dissolved by a developer fluid. The patterns can now be seen on the wafer.

For the present application, this technique is not appropriate for a number of reasons. First, PDMS is porous to gases while we aim at using air as the working fluid. Second, obtaining aspect ratios of 1:5 or more is challenging (Hoelzle et al., 2014); although the maximum aspect ratios of the channels in the prototypes presented in this chapter are only 1:1.25 and 1:2.5, larger aspect ratios are desirable because jet switching occurs more readily when the flow is two-dimensional which was pointed out early on during the Fluidics era in the 1960's (e.g. Muller (1964)). As we will show at the end of Chapter 7, prototypes with an inlet aspect ratio of 1:5 seem to function better than the ones presented in this

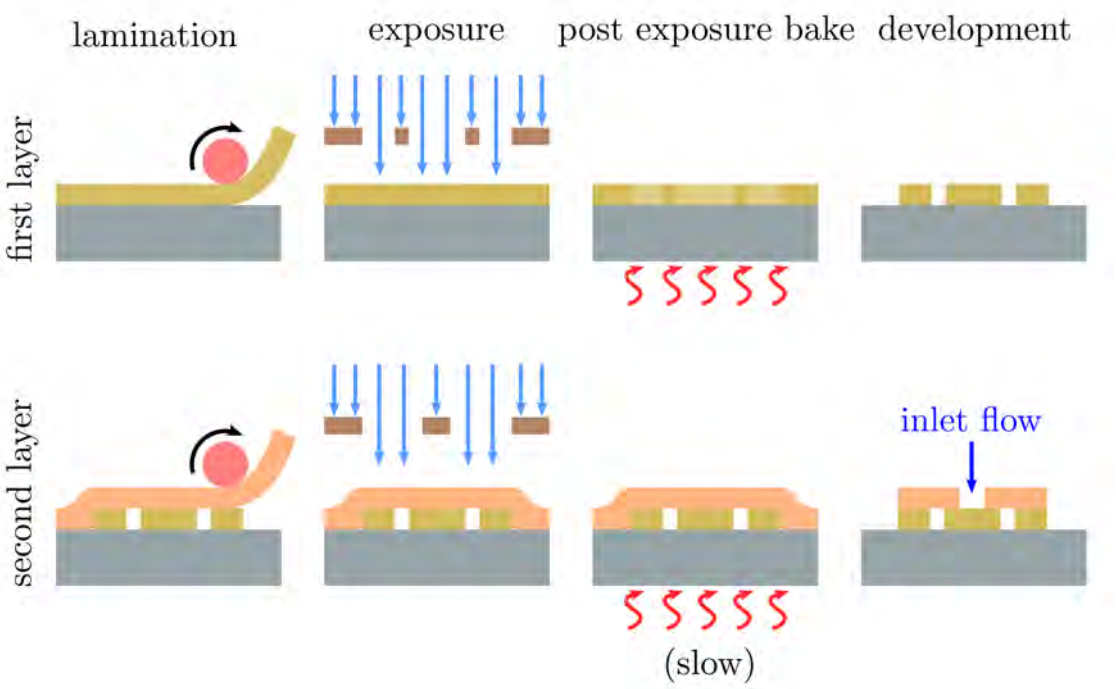

Figure 6.6: Dry film deposition and patterning process used to produce the microfluidic oscillators. The channels are patterned into the first layer whereas the second layer serves as an enclosure with inlet ports.

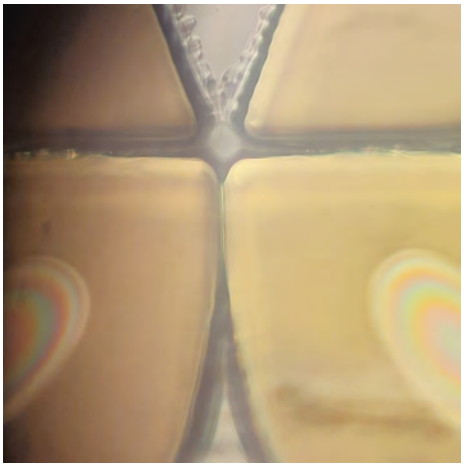

Figure 6.7: Inlet throat of the microfluidic oscillator. The obstruction of the inlet is explained by an over-exposure of the photoresist.

chapter. Third, the PDMS chip has to be bonded to the wafer, and aligning it with the sensors that would have been implemented beforehand is not a trivial task.

An alternative to PDMS chips is spin-coating SU-8 onto the substrate and patterning the channels via photolithography. However, it is not possible to enclose the channels, i.e., multilayer structures with free-standing features cannot be done with spin-coated liquid

films.

A different approach altogether consists in using a permanent epoxy dry film that is laminated onto the substrate, in lieu of the spin-coated liquid resin. Stöhr et al. (2008) used TMMF S2000 dry film to produce 2D microchannels which showed a good adhesion between the layers of TMMF and between the dry film and the silicon or glass substrate. Unlike liquid photoresists such as SU-8, dry films do not require a soft bake after lamination, substantially reducing the process duration. The thicker the layers are, the more substantial the process speed-up is. In addition, dry-film lamination offers a better homogeneity than does SU-8. In the present work, DF-1000 series dry-film is used which is around ten times less expensive than both SU-8 and TMMF S2000 for the same layer thickness, and three times faster to process than SU-8. Courson et al. (2014) showed that using DF-1000 can accurately produce the desired patterns, with residual stresses and optical properties comparable to those of SU-8 photoresist.

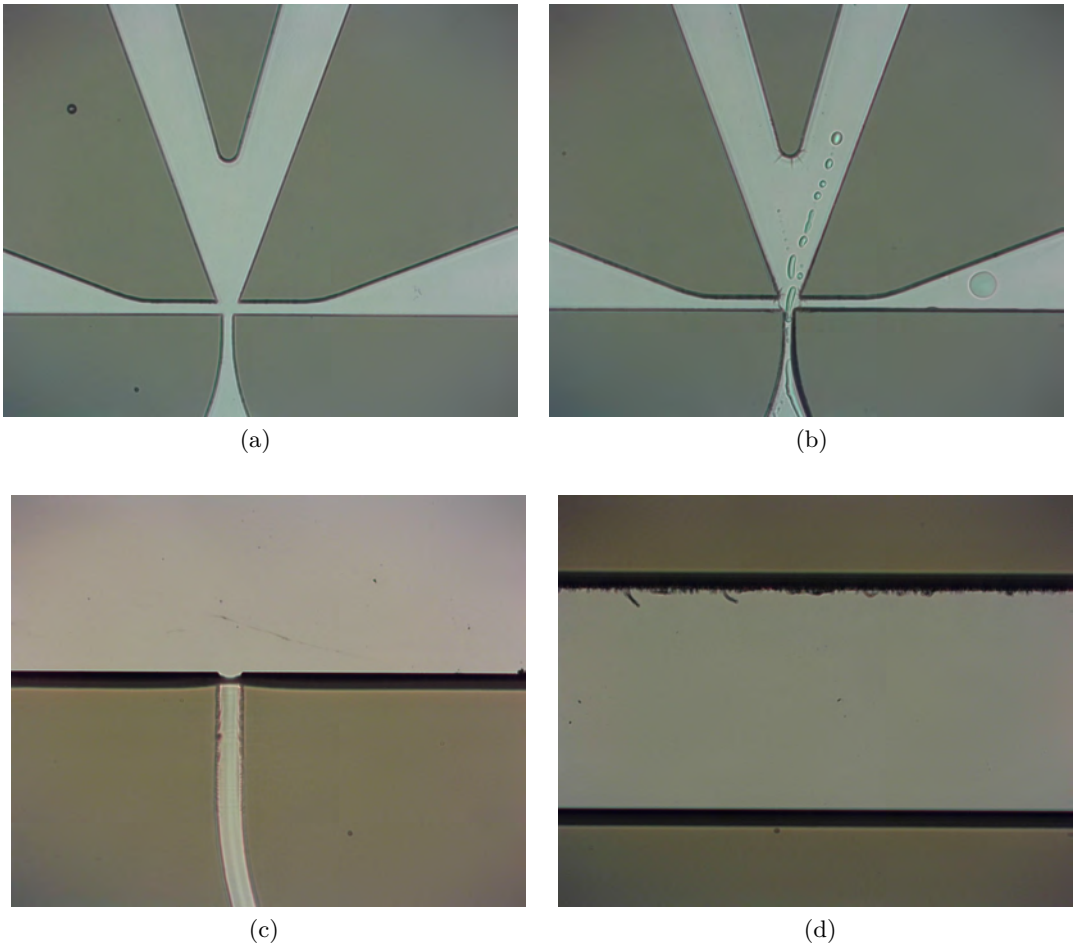

(a) (b)

(c) (d)

Figure 6.8: Microscope images of (a) the critical part of the oscillator design (throat width = 20 µm), (b) isopropanol droplets going through the throat and into the switching area, (c) an exit channel and (d) part of a feedback loop.

The microfluidic oscillators were produced by deposition of DF-1000 series dry-film

layers onto a silicon wafer (SiP 1701). For the prototypes having a channel depth of 50 µm, we begin by laminating a layer of DF1050 (50 µm) onto the substrate. The desired pattern is transferred from the mask to the dry film layer by exposing it to UV radiation. The dry-film in this case is a negative photoresist, meaning that the part exposed to the UV-light becomes insoluble in the developer fluid. The exposure dose, measured in $\mathrm{W\,m^{-2}}$, is crucial in obtaining a quality resolution. After baking, and development using cyclohexanone, the same process is repeated in order to close off the channels with another DF-1050 film (50 µm) keeping only a circular orifice at the inlet. The lamination and patterning process for both the first layer containing the microchannels and the second layer which acts as an enclosure are illustrated in Figure 6.6. Unlike the original prototypes, the fluid first enters the system in a direction parallel to the channel depth. A first run produced a poorly resolved pattern, especially around the throat area that was nearly blocked (Figure 6.7). This severe loss in resolution was attributed to a too high exposure dose of $340\,\mathrm{W\,m^{-2}}$.

A second iteration with an exposure dose reduced to around $240\,\mathrm{W\,m^{-2}}$ significantly improved the resolution (Figure 6.8a). Figure 6.8b was also included because it shows droplets of isopropryl (cleaning fluid) going through the inlet and into the switching zone, indicating that the critical channel is clear. Similarly, the 50 µm-wide exits were well-resolved (Figure 6.8c) as well as the 320 µm-wide feedback channels (Figure 6.8d).

The enclosure, whose schematics are shown in Figure 6.9, was made using a CNC machine. A rubber O-ring is used to connect the oscillator to the inlet of the casing. For wider prototypes, two additional O-rings are added to hold the oscillator in place. A push-in pneumatic fitting connects the device to the service air.

6.3 Prototype designs

Five different designs were implemented (mask drawings of the channel patterns in Figure 6.10), with the aim of producing pulsed microjets with a range of frequencies. The first design, dubbed 'butterfly' (Figure 6.10a) has the shortest feedback loops of the five designs, and, based on dimensional arguments, should have a frequency roughly ten times that of its large-scale counterpart, Lg0, i.e., around 10 kHz. This assumes that both the pressure wave travel time and the switching time are proportional to the dimensions of the device. For the pressure wave travel time this should be the case if the speed of sound remain relatively the same. For the switching time, this has not yet been proven, but for most of the designs used here, the switching time is short compared to the wave travel time because of the length of the feedback loops, and so the scaling argument should give good estimations. Seeing as the effects of scale reduction on the switching mechanism are currently unknown, this value merely serves as a rough estimate. To our knowledge, there are no studies reported in the literature on the characteristics of a microfluidic oscillator with air as working fluid and a choked inlet throat.

The second design, 'butterfly 2' (Figure 6.10b), is identical to the first except for its longer feedback loops that should bring the frequency down to around 2.5 kHz. The geometry of each feedback loop remains simple and consists of straight channels and a single

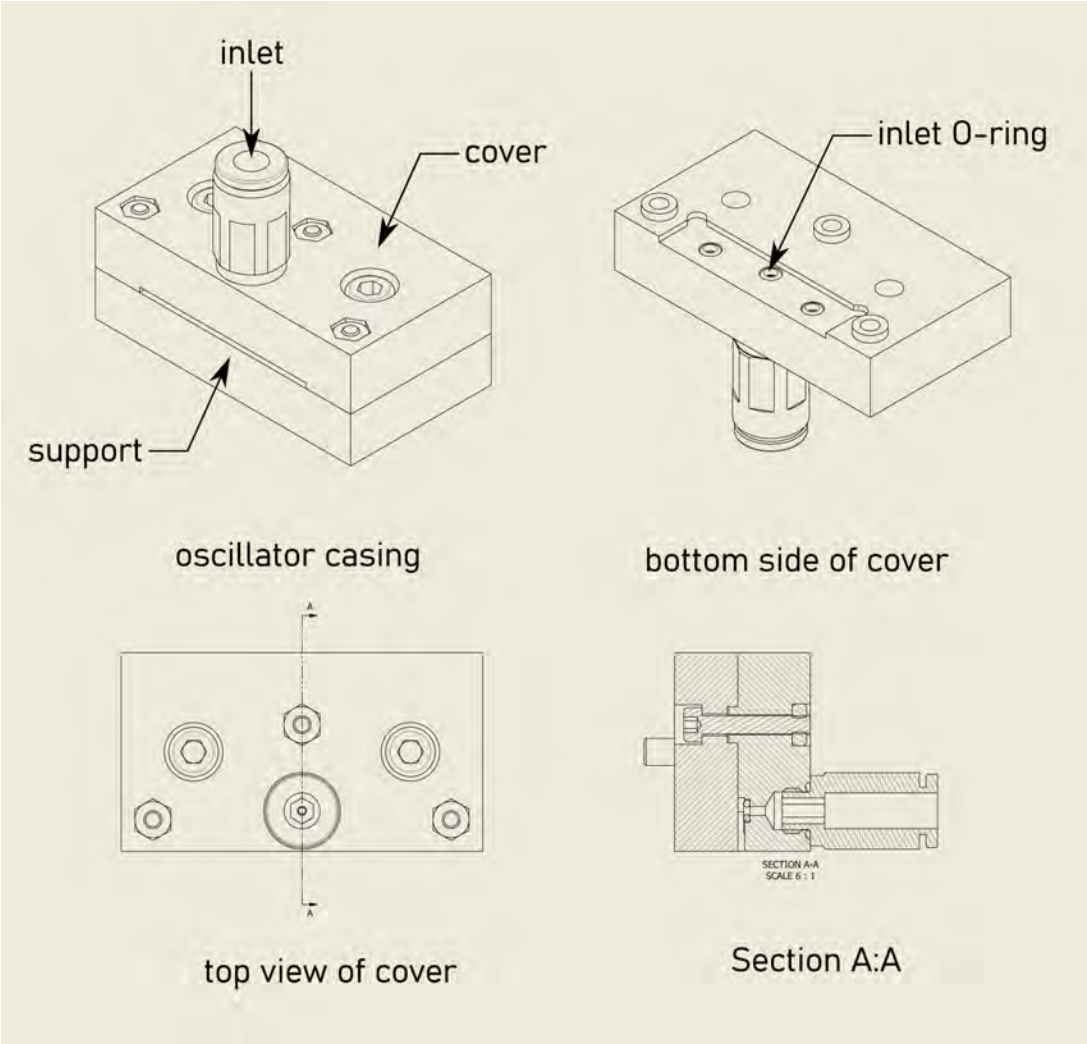

Figure 6.9: Schematics of the enclosure used for the dry-film oscillators.

wide bend. The 'dragonfly' (Figure 6.10c) has an overall size similar to that of 'butterfly 2', but with twice the feedback loop length and a different geometry consisting of the three bends on each side. Its frequency is expected to be around 1.4 kHz. The feedback loops of the next design, 'eagle 1' (Figure 6.10d) have the same length as those of 'dragonfly', but with a geometry having more bends connecting shorter straight channels. Comparing how these two designs behave would allow us to figure out the effect of feedback line geometry on the characteristics of the devices.

A final design was considered which is similar to 'eagle 1', where the straight sections of the feedback loop were extended vertically ('eagle 2', Figure 6.10e). Assuming that this model works, and that the pressure waves propagate without excessive attenuation in the feedback line, 'eagle 2' should have a frequency of around 700 Hz.

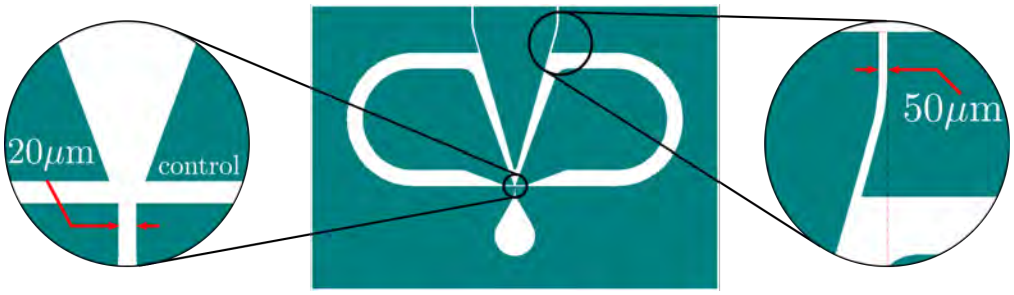

(a) Butterfly (B1): $L_f = 11\,000\,\mu\text{m}$

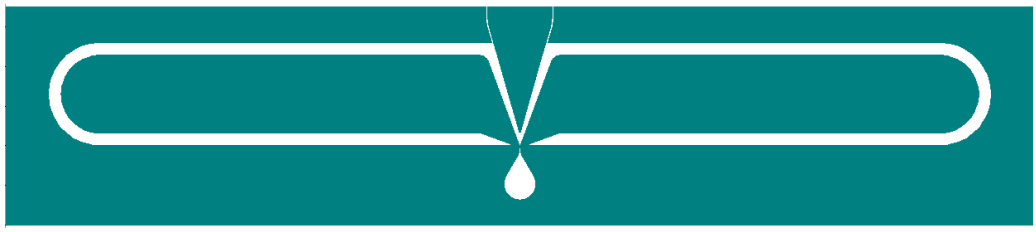

(b) Butterfly 2 (B2): $L_f = 45\,000\,\mu\text{m}$

(c) Dragonfly (D): $L_f = 83\,000\,\mu\text{m}$

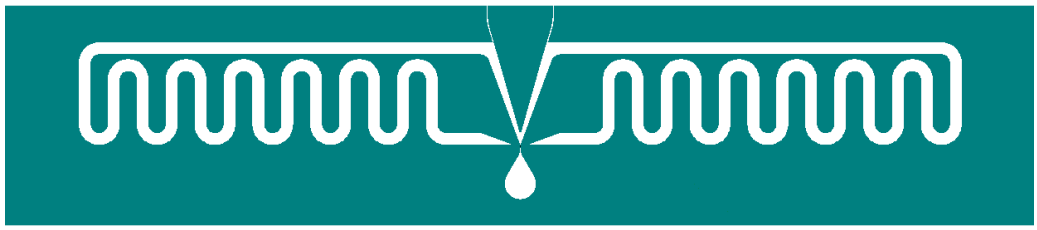

(d) Eagle 1 (E1): $L_f = 81\,000\,\mu\text{m}$

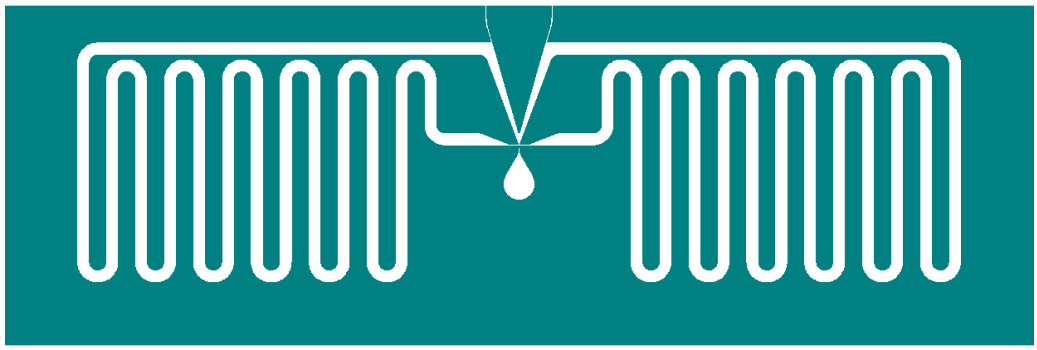

(e) Eagle 2 (E2): $L_f = 172\,000\,\mu\text{m}$

Figure 6.10: Different oscillator designs used for producing pulsed microjets. The total length of the feedback loops (both sides) is included for each design.

6.4 Preliminary diagnosis

In the next chapter, the working principle and microstructuring process of a rapid thermal sensor are presented, whose role will be to give us some information on the internal mechanisms of the oscillator. Similar sensors will also be implemented on a heated external surface in order to assess the heat transfer due to the pulsed impinging micro-jets. Before delving into this long process, we will present a rough assessment of the micro-oscillators. We begin by checking that air flows through both exits of the device by filling a beaker with water and placing the oscillator exits just above the surface of the water. As can be seen in Figure 6.11, the surface of the water is deformed in two places coinciding with the positions of the exits. The same was observed for all the designs presented earlier.

Figure 6.11: View of the oscillator in its casing placed in water (left) with a detail showing the deformation of the surface of the water which is due to the two microjets (right). A drawing of the oscillator is superimposed over the image.

The second step is to make sure that the oscillators are working properly. Using a microphone placed near the exit plane of the device, it was possible to pick up the frequency of the pulsed microjets. The capacity of the microphone to detect high frequencies was checked using a digital tone generator. It provided accurate readings up to 15 kHz. For the prototypes having a channel depth of 25 µm, no distinct tone could be detected for any of the designs. Moving on to the prototypes with a channel depth of 50 µm, for Oscillator B1, a faint but distinct tone can be heard and was well defined on the spectrogram for inlet pressures of $p_{\text{in}} = 2$ to 2.9 bar (Figure 6.12). The frequency first increases with pressure from 9094 to a peak of 9938 Hz before decreasing to 8344 Hz. Beyond this point, it is not clear whether or not the pulsations persist, as the noise from the jet itself seems to cover the tone. The frequencies are roughly an order of magnitude higher than in the original design which was 10 times larger in width and length. The frequency peak is not in itself surprising, since we had already noted in Chapter 3 that the switching time is a function of inlet pressure. The difference here is that the frequency peak occurs at a

pressure $p_{\text{in}} = 2.3\,\text{bar}$ instead of $p_{\text{in}} = 1.5\,\text{bar}$ as in the original design.

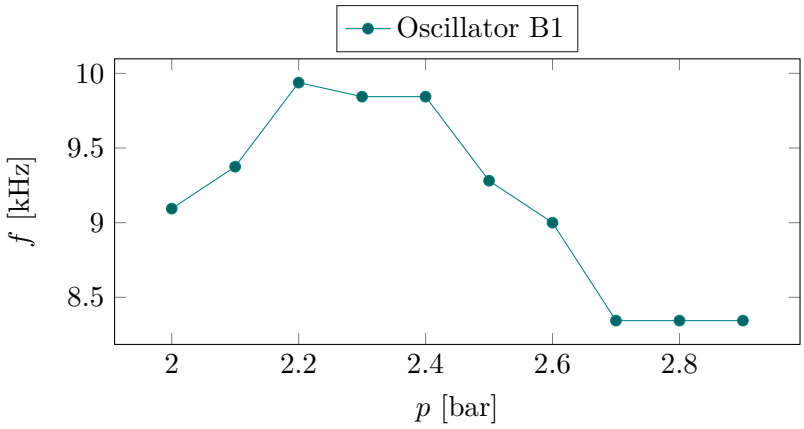

Figure 6.12: Detected frequency of Oscillator B1 for different inlet pressures.

For Oscillator B2 (Figure 6.13), the tone becomes distinct at $p_{\text{in}} \geq 3.3\,\text{bar}$, and its frequency decreases slightly in the range of pressures considered, but remains close to 4300 Hz. Here again, above a certain pressure, the tone becomes difficult to distinguish from the noise. For the remaining designs, no tone was detected in the range of pressures available to us. The frequency changes very little with pressure compared to the first design. Although these preliminary observations are merely qualitative, they give a rough idea of what to expect when sensors will be included inside the microchannels. These sensors will need to have response times short enough to detect pulsations of at least 5 kHz. As we will see in the following chapter, sensors are placed strategically inside the device so as to allow us to compute the switching time of the main jet inside the oscillator as well as the travel time of the pressure waves in the feedback loops.

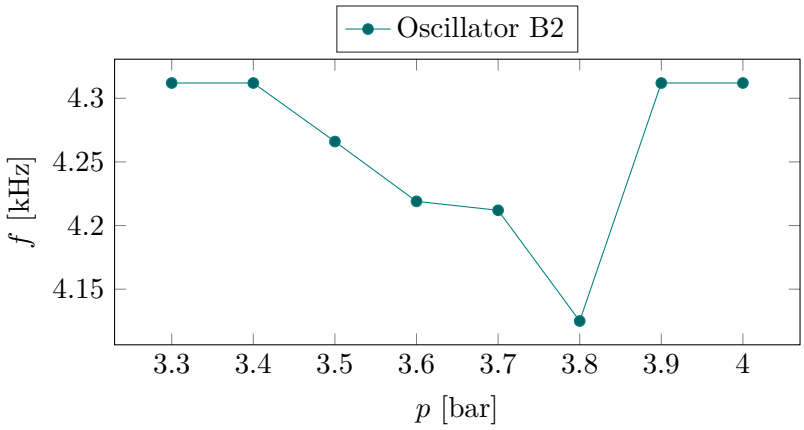

Figure 6.13: Detected frequency of Oscillator B2 for different inlet pressures.

During the final production cycle, a set of prototypes having a depth of 100 µm were also produced on the wafers with temperature sensors. As will be detailed in the final sections of the forthcoming chapter, all the prototypes that are 100 µm-deep actually work.

"When you want to know how things really work, study them when they are coming apart."

Zero History, William Gibson

7 PolySi-based Temperature Sensors

An array of temperature sensors are implanted on the silicon substrate before setting the microfluidic channels. This will allow us to monitor the passage of pressure waves and transient phenomena inside the oscillator in a non-intrusive way. Other types of micro-sensors, such as pressure sensors, are more prone to damage and have a significantly slower response. The temperature sensors used here were developed at the Laboratory for Analysis and Architecture of Systems (LAAS) and have high thermal sensitivity and small response times. Their originality lies in the fact that the sensing element is partially suspended over the substrate, so that their response time is no longer limited by the conductivity of the substrate. The same sensors are also integrated onto a target plate in order to measure the instantaneous temperature. An illustration of the planned is shown in Figure 7.1. Other thermal measurement methods exist such as resistance thermometers or thermal imaging. Resistance thermometers such as PT100 or polysilicon-based resistors (such as the one used by Chang et al. (2013)) are prone to self-heating and even though the measurements can be corrected, the dissipated heat can have an effect on the flow. Thermal imaging is also used for liquid flows in microchannels (Kakuta et al. (2011)) but is not adapted for gas flows. The polysilicon sensors presented next are more suited to the present application since they have a high thermal resistivity, low self-heating for a specific range of currents and are non-intrusive.

7.1 Working principle

Although differing in design, all the sensors implemented in this study are built around a $P^{+}N^{++}-$junction. These junctions are created in a polycrystalline silicon (polysilicon) film deposited on a prepared high-resistivity SiP wafer. In broad terms, the junctions are

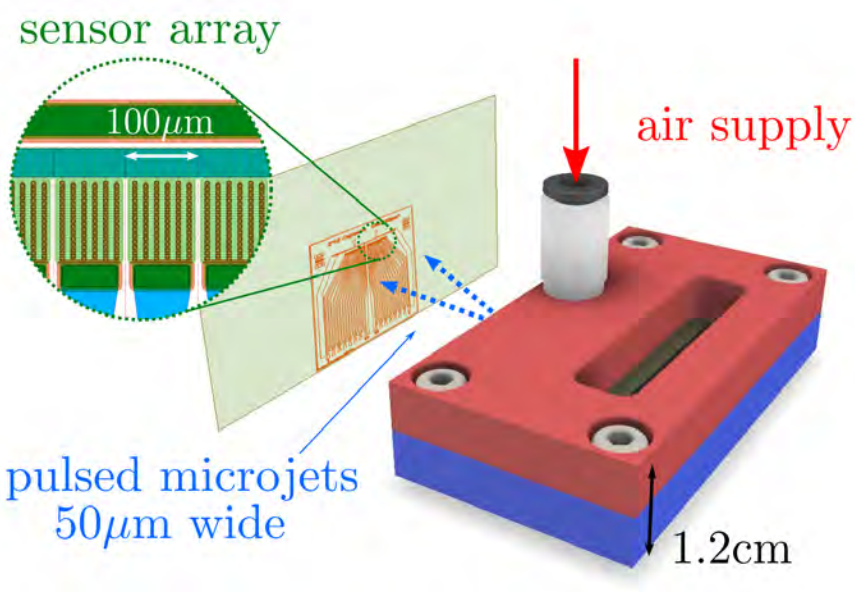

Figure 7.1: Illustration of the setup for testing the pulsed impinging microjets. The setup includes the casing (blue and red part), which holds the instrumented microfluidic chip and the heated impact surface which includes an array of 30 temperature sensors shown in detail.

made by first implanting Boron ions ($p-$type) into the entire polysilicon film. The $n-$type regions are then patterned by ion implantation of Phosphorus into the $p-$type region. This requires that the donor concentration N_D be much larger than the acceptor concentration N_A. With this condition ($N_D \gg N_A$) in mind, the following approximation of the width of the depletion region can be made:

$$W = \sqrt{\frac{2\varepsilon V_{bi}}{q}\left(\frac{N_A + N_D}{N_A N_D}\right)} \approx \sqrt{\frac{2\epsilon V_{bi}}{qN_A}} = w_p \tag{7.1}$$

where ε is the permittivity of the film, V_{bi} the potential barrier of the junction, q the elementary charge and w_p the width of the depletion region on the $p-$type side. As a result, the depletion region extends almost entirely into the $p-$region. The properties of this $P^+N^{++}-$junction, which acts as a Zener diode (Figure 7.2), are then determined to a large degree by the concentration of the $p-$type dopant N_A. Experimental results demonstrating the sensitivity of the Zener voltage to N_A can be found in a thesis by Bertrand Marty (2009).

Depending on the applied current, this Zener diode, in reverse bias, can function as either a thermal actuator or sensor. An element whose $p-$type dopant dose [1] is $D \approx 3 \times 10^{13}\,\mathrm{cm}^{-2}$ is used to illustrate the different modes of operation (Figure 7.3):

[1] For ion implantation, the dopant concentration is related to the dopant dose via $N = D/L$ where L is the thickness of the film.

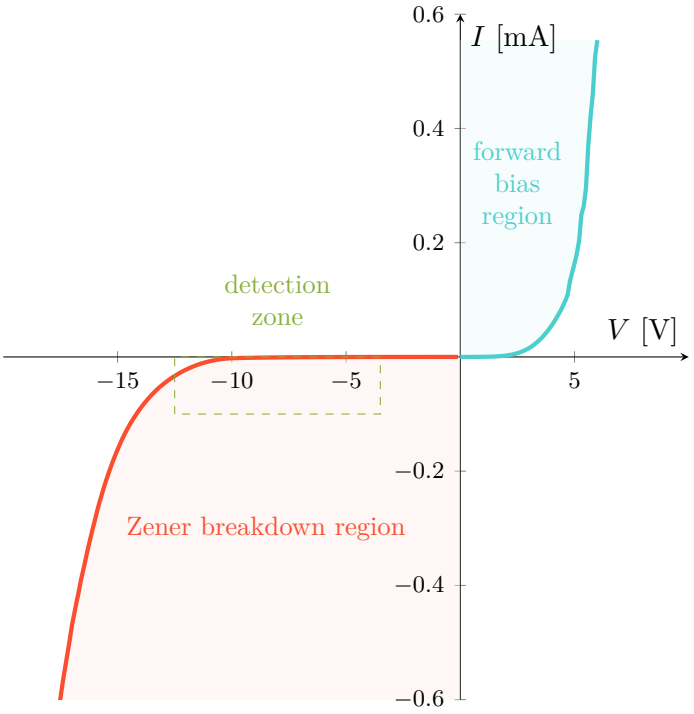

Figure 7.2: Current-voltage characteristic measured for one of the oscillator sensors; as the plot shows, these elements behave like Zener diodes. The dashed green rectangle indicates the detection zone shown later in Figure 7.3.

1. **Leakage current:** below a current of around 100 nA, the electrons cannot overcome the barrier potential of the $P^+N^{++}-$junction. As a consequence, a leakage current goes through the layers surrounding the polysilicon (e.g., the substrate beneath the PolySi film).
2. **Thermal sensor:** for intermediate values of the current, the thickness of the depletion region is of the order of a few nanometers. In this case, the wavefunction of an electron can propagate through the potential barrier, allowing it to cross it. This phenomenon is called quantum tunneling and occurs at the surface of the polySi film. This mode is referred to as the "surface conduction mode". The characteristic curve is particularly sensitive to temperature variations in this mode and reaches a peak sensitivity $S_V \approx -75\,\mathrm{mV\,°C^{-1}}$ (Figure 7.3, blue curve). In comparison, K-type thermocouples can only reach a sensitivity of about $40\,\mu\mathrm{V\,°C^{-1}}$.
3. **Thermal actuator:** Above a current of around 20 µA, the electric field is strong enough that the electrons can cross the junction. The electrons flow through the entire volume of the polySi film. The voltage across the element is then greater than the Zener voltage. This conduction mode is dubbed the "volume conduction mode" (LUBIN2012). The element dissipates heat with a resistance R_S. Surface and stray conduction still occur, but are negligible compared to volume conduction. Although the voltage remains sensitive to temperature changes, the dissipation of heat would hinder temperature measurements and so the element cannot be used as a sensor in this mode.

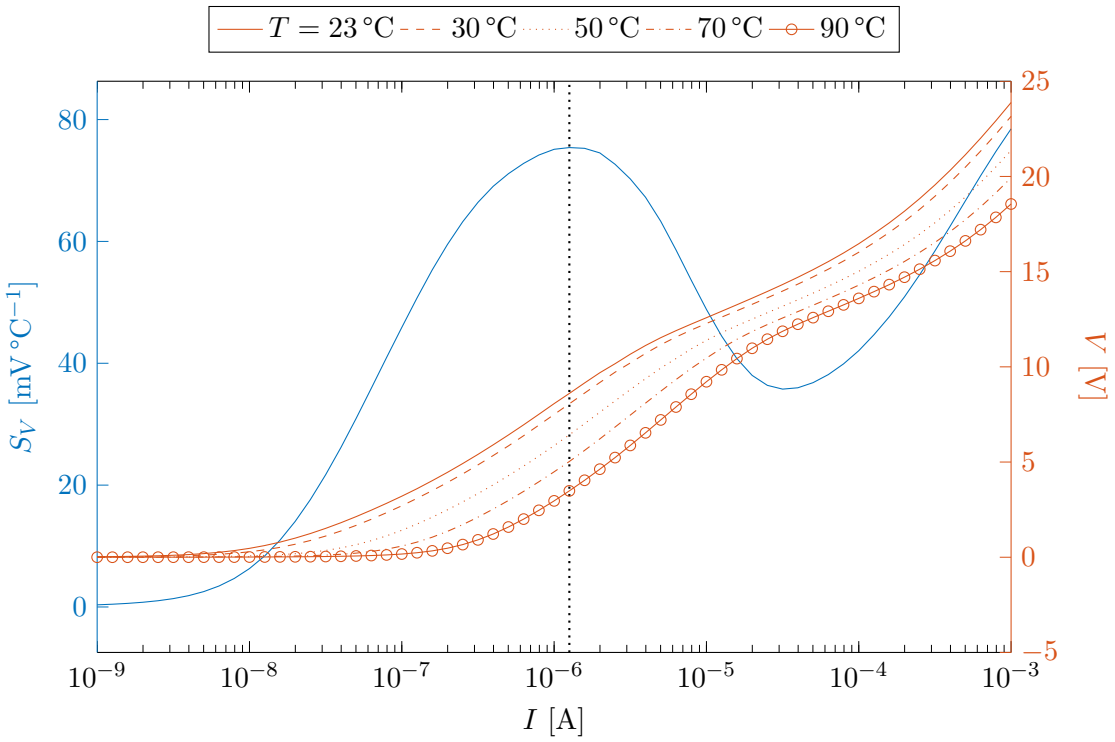

Figure 7.3: Characteristic curve for $D \approx 3 \times 10^{13}\,\mathrm{cm}^{-2}$

Camps et al. (2013) proposed an electrical model where surface and bulk conduction are assimilated to two diodes D_S and D_V, respectively, placed in parallel and with a forward bias V_a(the leakage current is neglected). The resistance of the entire element is modeled by a resistor R_S (Figure 7.4).

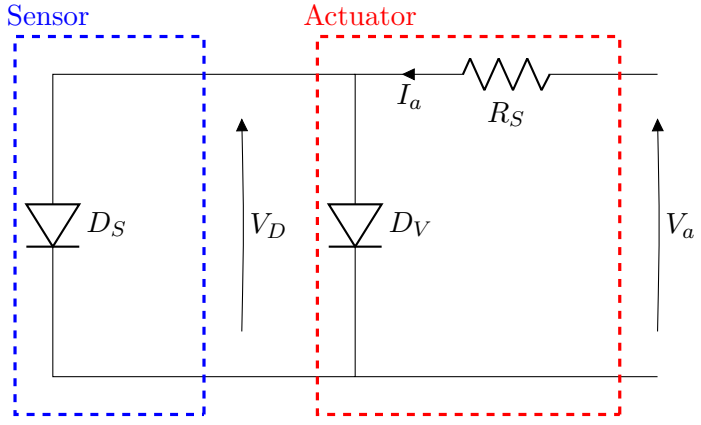

Figure 7.4: Electrical model of the sensor.

In addition to thermal sensitivity, the unsteady nature of the flow, either inside the oscillator or near the heated impingement surface, requires a sensor with a short response time. The limiting factor in this regard is the thermal inertia of the substrate on which the sensors are manufactured. Even with silicon wafers, the thermal inertia remains high. In

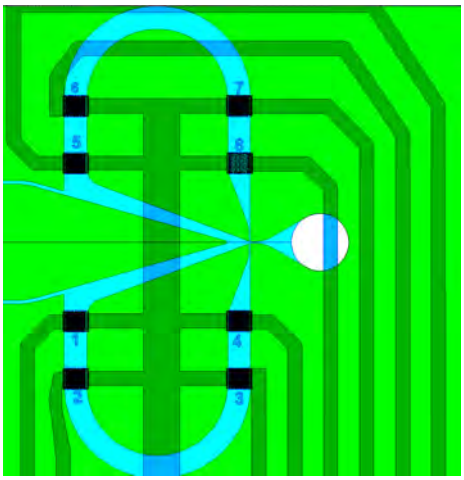

Figure 7.5: Superimposed mask drawings used for the process showing the temperature sensors (numbered $1-8$) and the fluidic microchannels for oscillator 1.

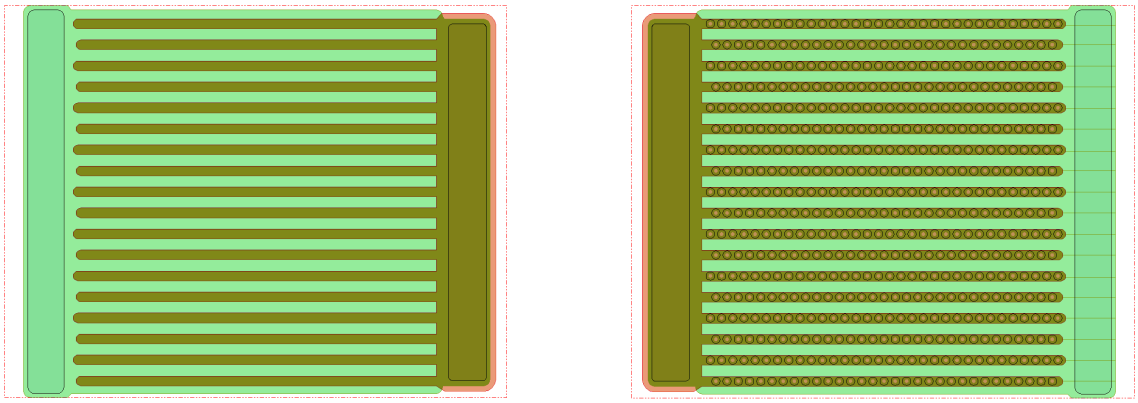

(a) (b)

Figure 7.6: Mask drawings of the sensors used to instrument the microfluidic oscillator (a) original design without holes, (b) new design with holes in the $n-$regions used to partially etch the silicon oxide layer underneath the sensor.

order to overcome this, the junctions, where temperature detection occurs, can be partial 'suspended' over the substrate. This is done by removing parts of a silicon oxide layer placed between the high resistivity silicon substrate and the sensing elements. Openings are incorporated into the design of the successive layers that will allow us to etch the SiO_2 layer at the end of the process.

The novelty of the present iteration of the sensor is the wet-etching of a sacrificial layer underneath the element so that the junctions are no longer in contact with the substrate. This has the effect of reducing the thermal inertia of the sensors enabling faster thermal measurements.

7.2 Sensor design

The temperature sensors described earlier are going to be used to either measure temperature fluctuations due to the pulsating flow inside the device or to evaluate the heat transfer from the impinging jets on a heated surface.

In the first case (Figure 7.5), the sensors are placed symmetrically along both feedback loops of each device. If the response time is short enough, these sensors will allow us to measure the frequency of the devices and get a sense of how the pressure waves are moving along the channels. The detection area of these sensors have a roughly square shape with sides equal to the channel width $W_{\mathrm{FBL}} = 320\,\mu\mathrm{m}$. The $p-$type (green) and $n-$type (brown) regions are interdigitated to increase the measurable current during detection.

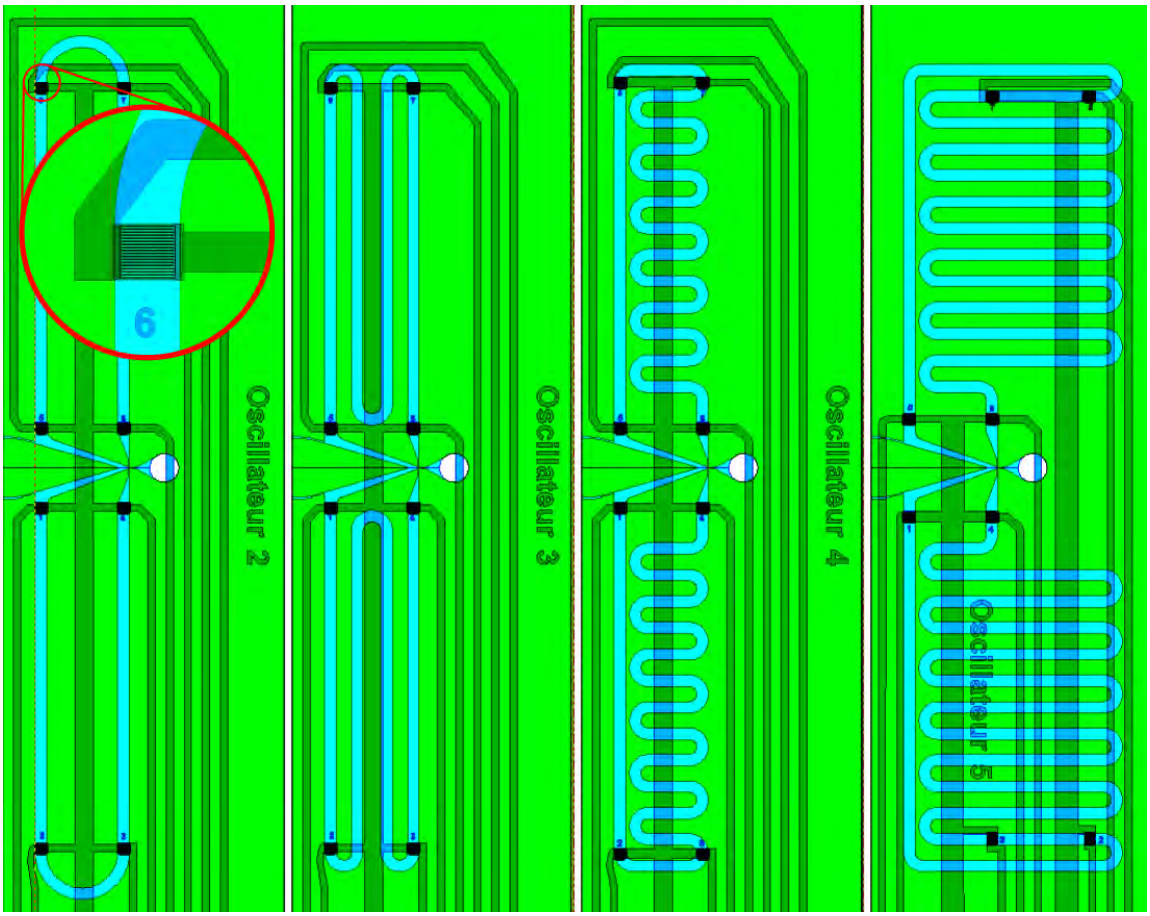

Figure 7.7: Superimposed mask drawings used for the process showing the temperature sensors (zoom on sensor 6 for B2) and the fluidic microchannels for oscillators 2 (B2) through 5 (E2).

In the first design (Figure 7.6a), the $pn-$junction is in contact with the underlying layer. The second design (Figure 7.6b) includes holes in the polysilicon film and passivation layers through which the initial oxide layer can be attacked using buffered HF. The remaining parts of this sacrificial layer act as pillars that hold up the polysilicon layer. The $pn-$junctions are suspended over the substrate. The remaining oscillator designs also

include 8 sensors placed at the inlets of the feedback loops, near the control ports and along the feedback channels (Figure 7.7).

Thermal chips were implemented on the same wafers as the oscillator, and consisted of a doped polysilicon band which acts as a heater, and an array of 30 sensors similar in design to the ones presented earlier. Two versions of the thermal chip were produced with sensors having dimensions of 100 µm × 100 µm and 100 µm × 1000 µm, respectively (Figure 7.8).

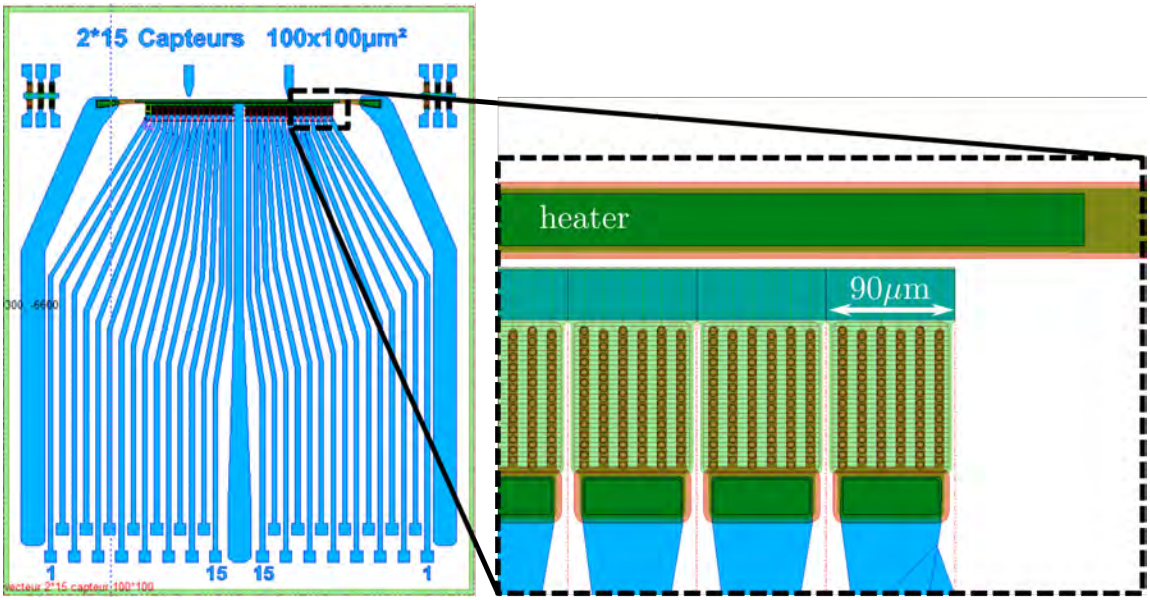

(a)

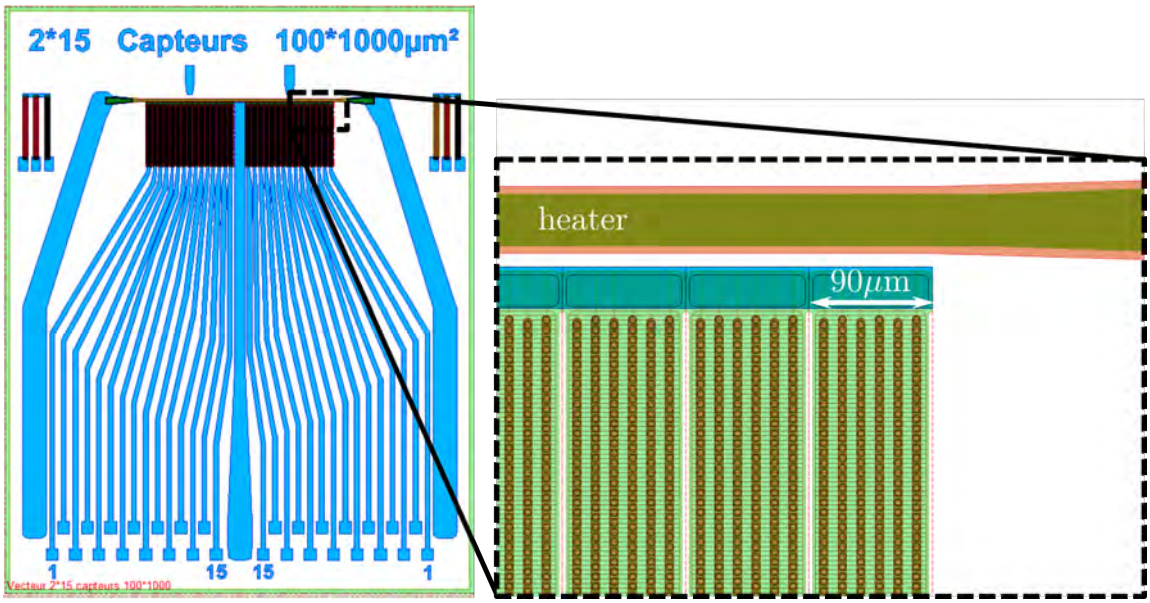

(b)

Figure 7.8: Thermal chip design with (a) 100 µm × 100 µm and (a) 100 µm × 1000 µm sensors.

The size of the sensors on the thermal chip must be sufficiently large to accommodate a $pn-$junction that is long enough to produce easily measurable currents and small enough to resolve the features of the temperature profile on the chip due to the impinging microjets. The first design (Figure 7.8a), which has an effective area of roughly $100\,\mu m \times 100\,\mu m$, only averages the temperature in the vertical direction over $100\,\mu m$ whereas the second design (Figure 7.8b) is ten times longer in the vertical direction, which should increase the measurable current all while averaging the temperature over an area ten times larger.

7.3 Manufacturing process

In addition to the basic layering, patterning, doping and heating operations that constitute most fabrication processes, the current process ends with a wet etching step that removes parts of the initial oxide layer from underneath the polysilicon layer. The duration of the etching is a crucial factor. Long etching times result in an excessive consumption of the silicon oxide pillars that become too weak to anchor the overhanging polysilicon film. At the other extreme, the $pn-$junctions are not sufficiently detached and so their thermal inertia remains important. A compromise between mechanical strength of the sensor and low thermal inertia must be found. In the following, the description of the process is broken down into three parts: substrate preparation, implementation of the sensor and finally the wet etching.

7.3.1 Preparing the substrate

The process is done on a 4" Silicon (Si) wafer that is 400 µm thick and has high resistivity (HR) of 4000 Ω cm. High resistivity wafer were chosen to limit parasitic currents between the sensor and the substrate. We begin by four layering steps that lay the foundations for building the sensor. These preliminary steps are as follows:

1. Deposition of a 2 µm-thick layer of silicon oxide SiO_2 by Plasma-enhanced chemical vapor deposition (PECVD) at 300 °C. This layer will be etched at the very end of the entire process in order to suspend the junctions.
2. Low pressure chemical vapor deposition (LPCVD) of 100 nm of Si_3N_4 which will serve as a protective layer during HF etching at the end.
3. LPCVD of 300 nm of polysilicon at 605 °C.
4. Ion implantation of Boron (P doping) with an ion energy of $E = 30\,\text{keV}$. Three sets of two wafers each were implanted with the following dopant doses :
   - $N_A = 1.5 \times 10^{18}\,\text{cm}^{-3}$ (dose $D = 5 \times 10^{13}\,\text{cm}^{-3}$)
   - $N_A = 2.1 \times 10^{18}\,\text{cm}^{-3}$ (dose $D = 7 \times 10^{13}\,\text{cm}^{-3}$)
   - $N_A = 3 \times 10^{18}\,\text{cm}^{-3}$ (dose $D = 1 \times 10^{14}\,\text{cm}^{-3}$)

   in order to consider the effect of different dopant concentrations on the sensitivity of the sensing elements.
5. Finally, a silicon dioxide mask for high temperature diffusion is deposited by PECVD at 300 °C (250 nm).

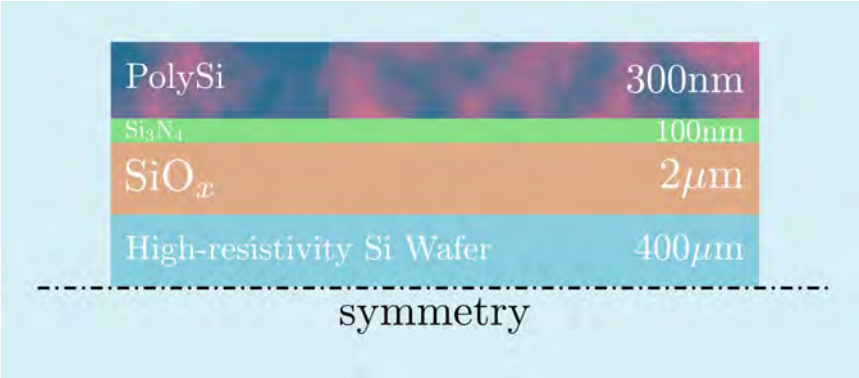

Figure 7.9: Illustration of the upper-half of the prepared wafer.

An illustration of the prepared wafers is shown in Figure 7.9. Steps 1-4 are done on both sides of the wafer in order to balance out the thermo-mechanical stresses inside the layers and reduce deformation.

7.3.2 Building the sensor

The next part of the process is structured around 5 photolithography steps, the first four of which will allow us to pattern the P^+, N^{++}, Polysilicon and metallic regions of the sensors. The fifth photolithography is done on some of the wafers, as it will allow us to remove part of the SiO_2 sacrificial layer that was deposited at the beginning of the preparation of the

substrate. This way, we will end up with two versions of sensor: one where the sensing elements are suspended over the substrate and another where they are in contact with it.

The remaining steps of the process are as follows:

6. **Photolithography 1, etching out the sensors**: Patterning of the polysilicon and silicon nitride layers by photolithography of a 1.1 µm sacrificial ECI resin layer, followed by reactive ion etching. The resin is then removed using acetone and water followed by a plasma cleaning.

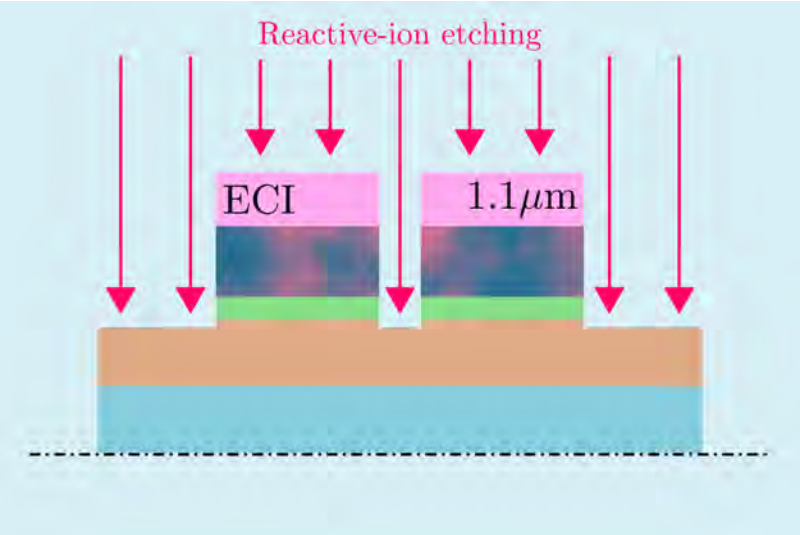

Figure 7.10: Step 6

7. **Photolithography 2, N^{++} ion implantation**: the N^{++} are patterned into a 2.5 µm ECI layer. Ion implantation of Phosphorus.

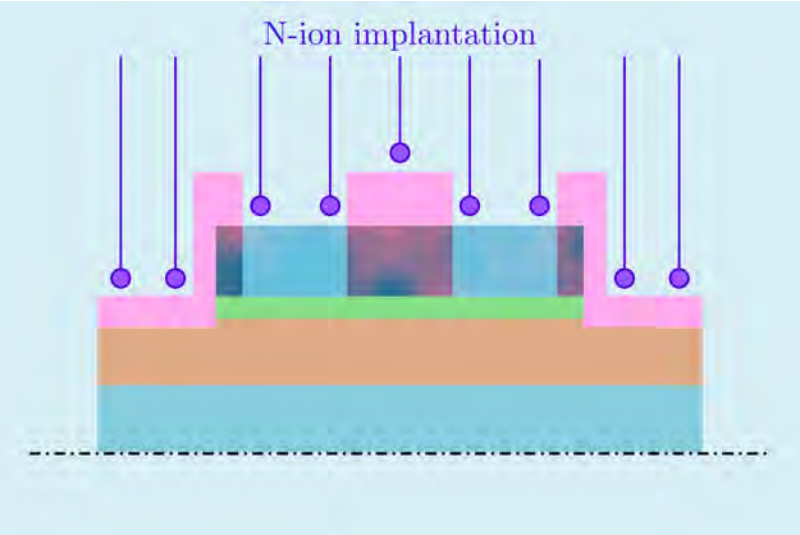

Figure 7.11: Step 7

8. **Passivation layer**: LPCVD of an 80 nm silicon nitride (Si_3N_4) passivation layer at

700 °C.

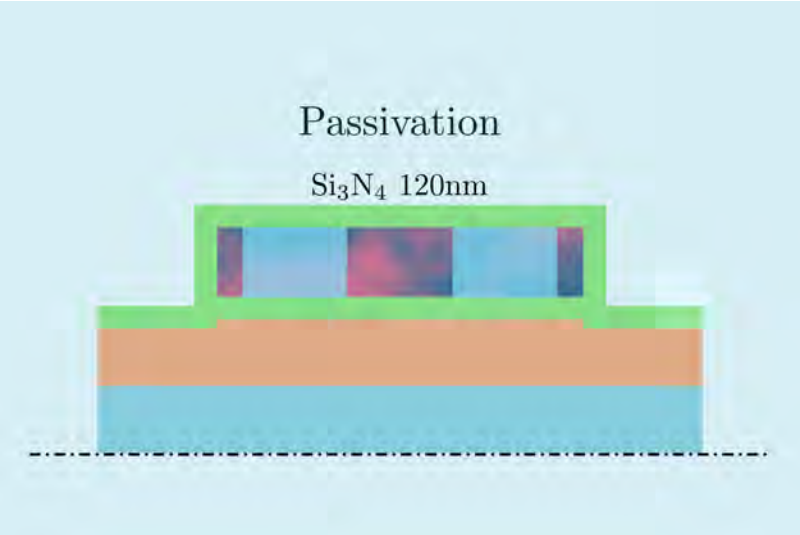

Figure 7.12: Step 8

9. **Annealing and dopant activation:** Baking at 1000 °C for 30 minutes with N_2
10. **Photolithography 3, opening of contact holes**: Deposition of a 1.1 µm sacrificial ECI layer. Patterning of the contact holes areas by photolithograpy followed by reactive ion etching of the silicon nitride layer and entering slightly into the polysilicon layer to ensure contact in the next step.

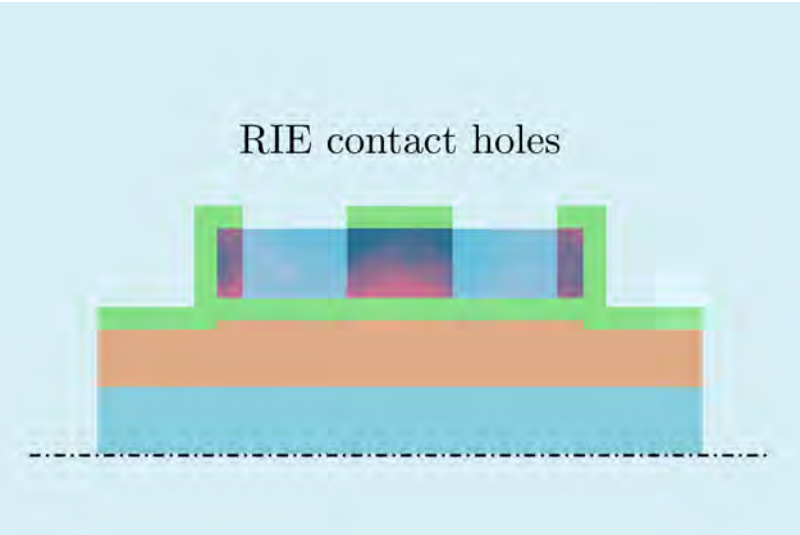

Figure 7.13: Step 10

11. **Photolithography 4, metallization patterns**: Chromium/Gold (Cr 50 nm, Au 300 nm) metallization patterned by lift-off to create interconnections.

12. **Alloying:** Baking at 250 °C for 1 hour with N_2H_2 to enhance the adherence of the metallic layer.

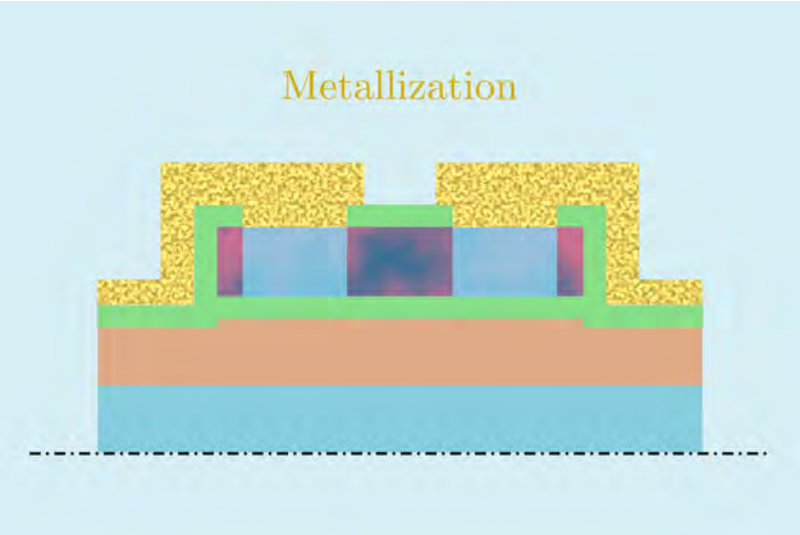

Figure 7.14: Step 11

13. **Photolithography 5, wet etch**: A 2.5 µm layer of ECI is deposited to protect the sensors from the final etch using a buffered etchant in an ultrasonic vessel. The etching time determines the size of the holes inside the sacrificial SiO_x layer.

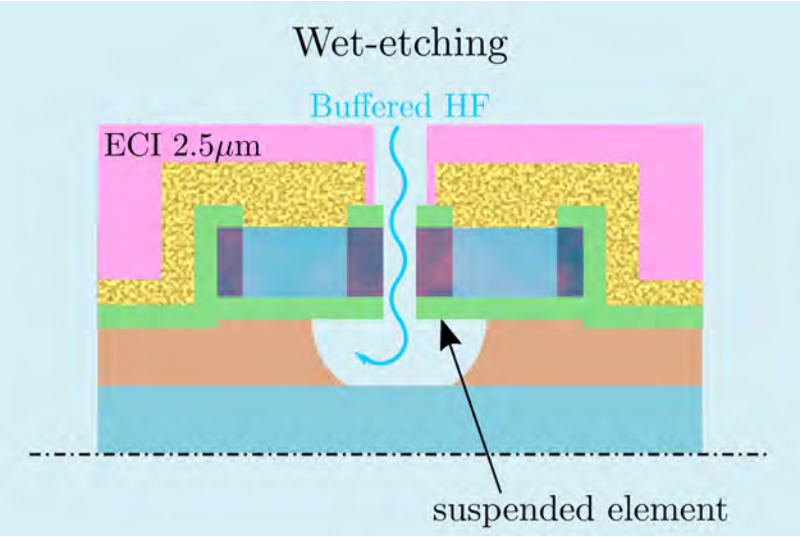

Figure 7.15: Step 13

Images of the 300 µm × 300 µm sensor with openings for the final Buffered Oxide Etch (BOE) step are presented in Figure 7.16. Six of the aforementioned steps were chosen to show the progression of the building process. A more comprehensive picture gallery of the process can be found in the appendix to this chapter.

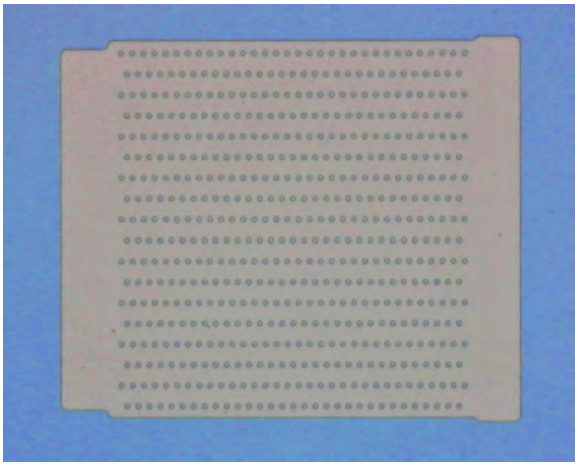

(a) Reactive-ion etching of the polysilicon layer (step 6)

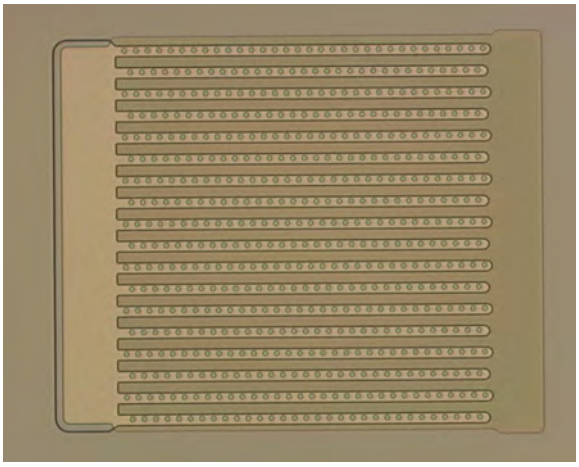

(b) Opening in the ECI layer just before N-ion implantation (step 7)

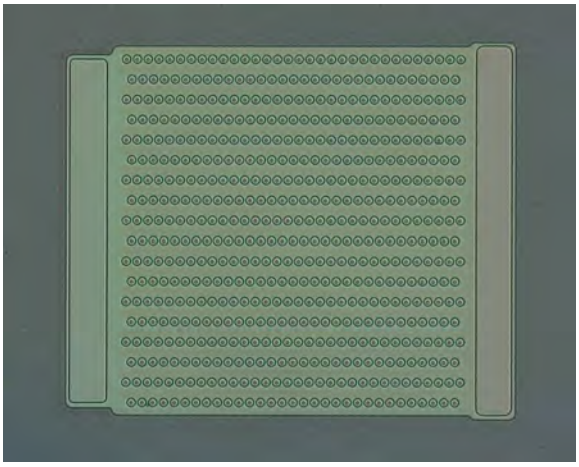

(c) Opening holes for contact and final wet-etching (step 10)

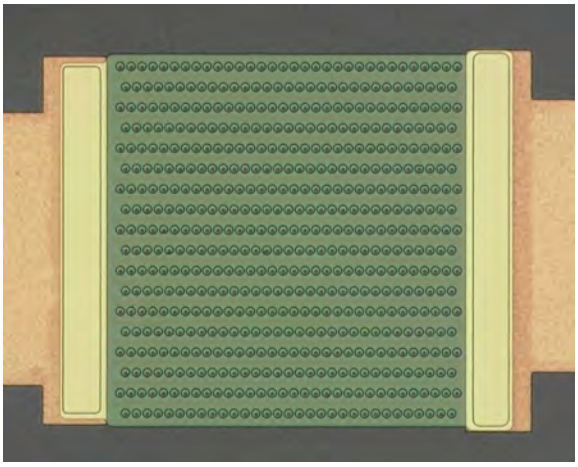

(d) Metallization and lift-off (step 11)

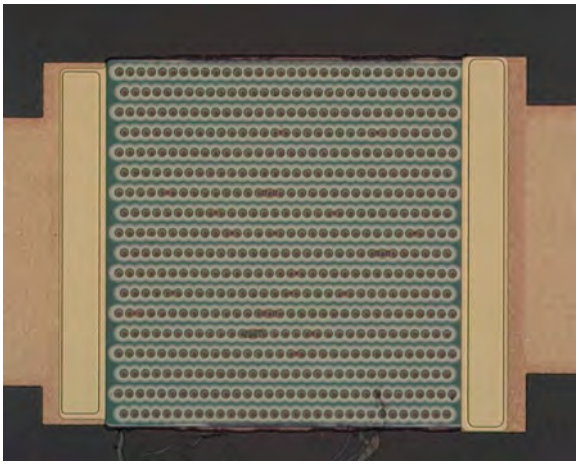

(e) Opening holes for contact and final wet-etching (step 13)

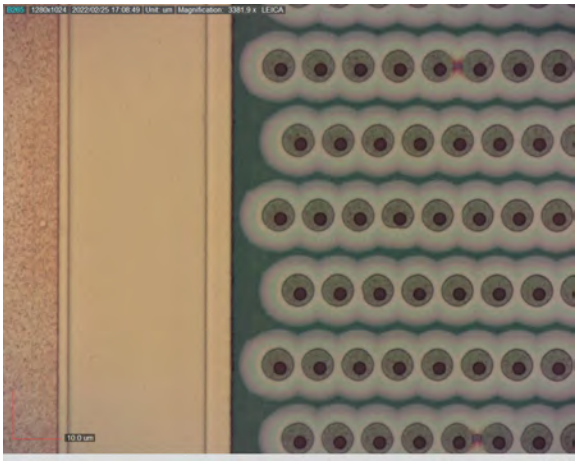

(f) Detailed view of the suspensed zone

Figure 7.16: Microstructuring process of the temperature sensors that will be embedded in the microfluidic oscillator. This version of the sensor has holes in the polysilicon and silicon nitride layers that will enable us to partially remove the initial SiO_x layer and suspend the PN−junctions.

7.3.3 PN−junction suspension via wet-etching

As mentioned earlier, the distinctive feature of the current iteration of these polysilicon sensors is the partial removal of the sacrificial layer underneath the PN−junctions to lower their thermal inertia. Hydrofluoric acid HF can attack the silicon oxide without damaging the silicon substrate. However, the etch rate of full strength HF is too fast to control during a process (typically 300 $\text{Å}\,\text{s}^{-1}$ at room temperature). For this reason, HF is usually mixed with water and ammonium fluoride NH_4F, which acts as a buffer to the generation of hydrogen ions that accelerate the etch. These solutions are called buffered oxide etches (BOE) and are mixed in different strengths to change the etch rate, which is also dependent on temperature (Figure 7.17). An increase in temperature of only a few degrees during the etch can lead to over-etching the silicon oxide layer, making the sensors more fragile. Prior to etching, the wafer undergoes a UV-ozone treatment to enhance the wetting characteristics of its surface which allows the BOE to uniformly penetrate the small openings (as in Figure 7.16f). The beaker containing the wafer and the solution are placed in an ultrasonic water tank. When the ultrasounds are turned on, the tank starts to heat up, slightly raising the temperature of the water. The temperature was monitored during the etch to make sure it does not exceed 28 °C.

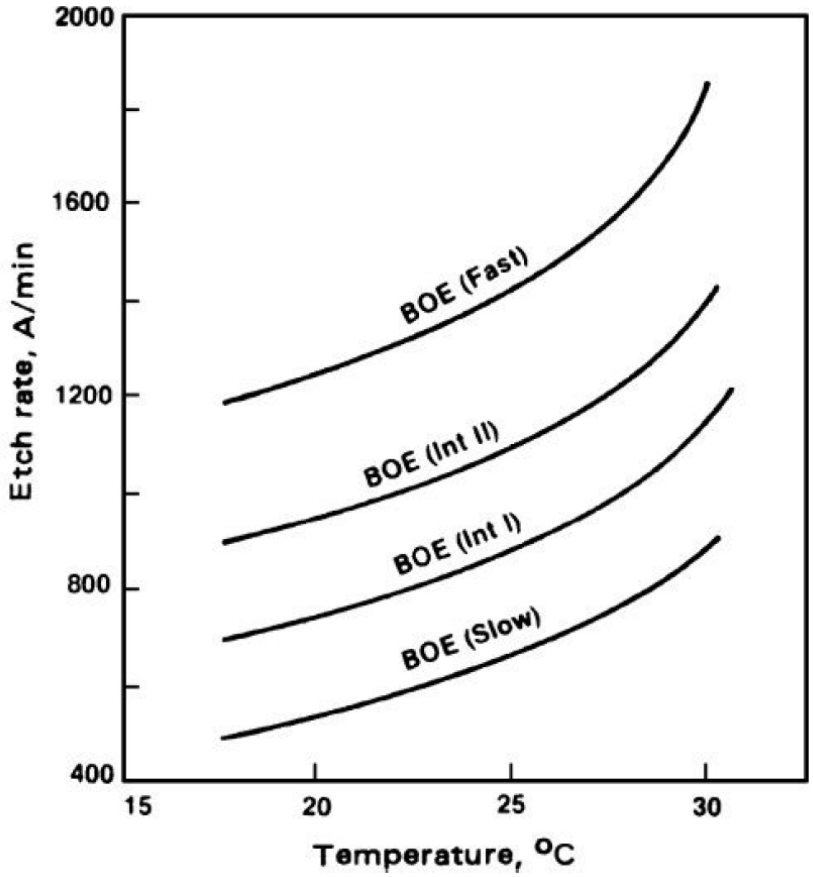

Figure 7.17: Etch rate versus temperature for buffered oxide solutions van Zant (2014).

The buffered-HF solution reaches the sacrificial SiO_x layer through holes in the polysilicon and silicon nitride layers opened in step 6 (section 7.3.2, Figures 7.10 and 7.16a) and in the passivation layer in step 10 (Figures 7.13 and 7.16e). Over-etching can occur in a matter of minutes, and can weaken the sensing area or cause it to break off of the polysilicon layer. In order to estimate the etching rate, one of the wafers is placed in the BOE for 20 min. The solution having a higher wetting on the silicon nitride layer covering the oxide than on the silicon surface underneath, the etching is quicker on the top side of the oxide layer as can be seen in Figure 7.18. The etching rate is approximately 1100 Å min^{-1}. The annular shape in the etched region is likely silicon nitride residue from the RIE in step 10, but does not have an effect on the wet etch.

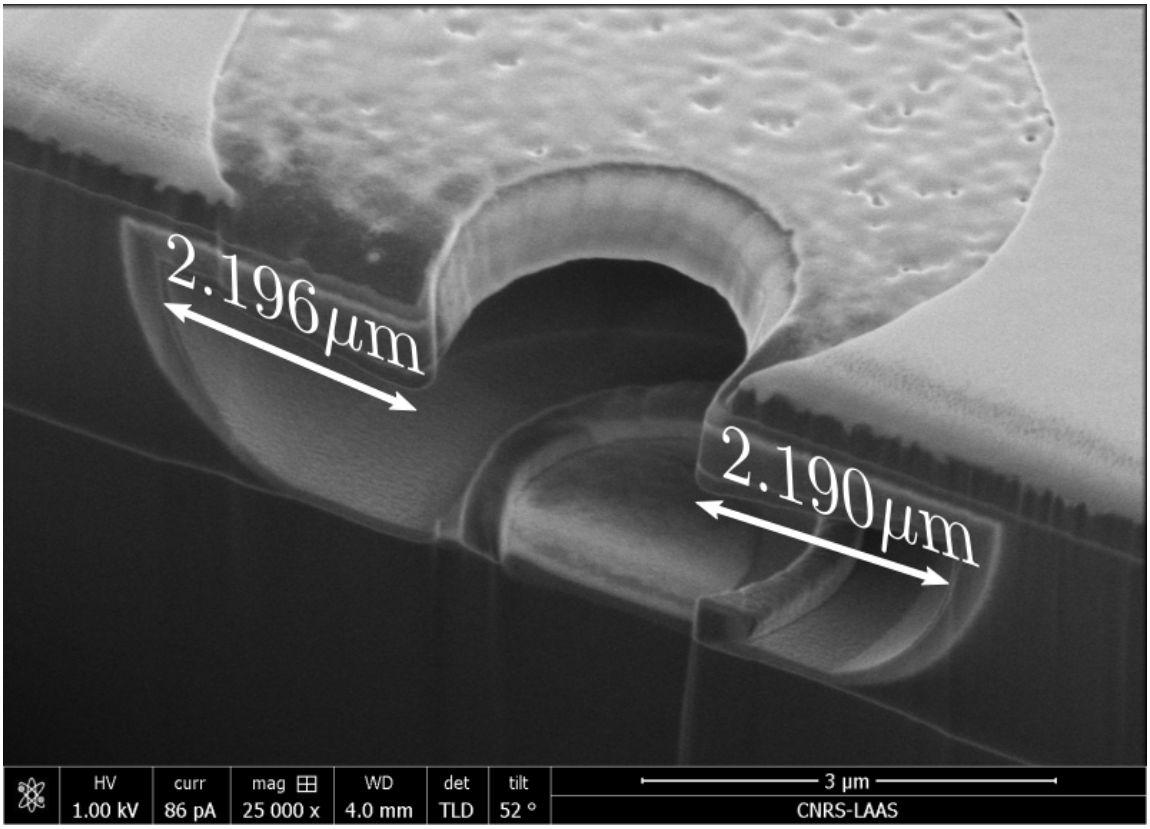

Figure 7.18: SEM of partially suspended sensor

The remaining samples were etched for 40 min so that the $pn-$junction is completely suspended. Again, using a focused ion beam (FIB) parts of the circuit were gradually removed (Figure 7.19) to reveal the different layers and assess the final wet etch. As can be seen in Figure 7.20, the remaining sections of the oxide layer are uneven, being larger at the bottom than the top. As mentioned before, this is due to the different wetting of the silicon nitride surface above the oxide and the silicon surface below. Worth noting is the rougher surface of the polysilicon layer, compared to Figure 7.18, which shows that in spite of the high selectivity of the wet-etch, the polysilicon layer is not completely impervious to the attack. A closer look of one of the openings is presented in Figure 7.21. The image

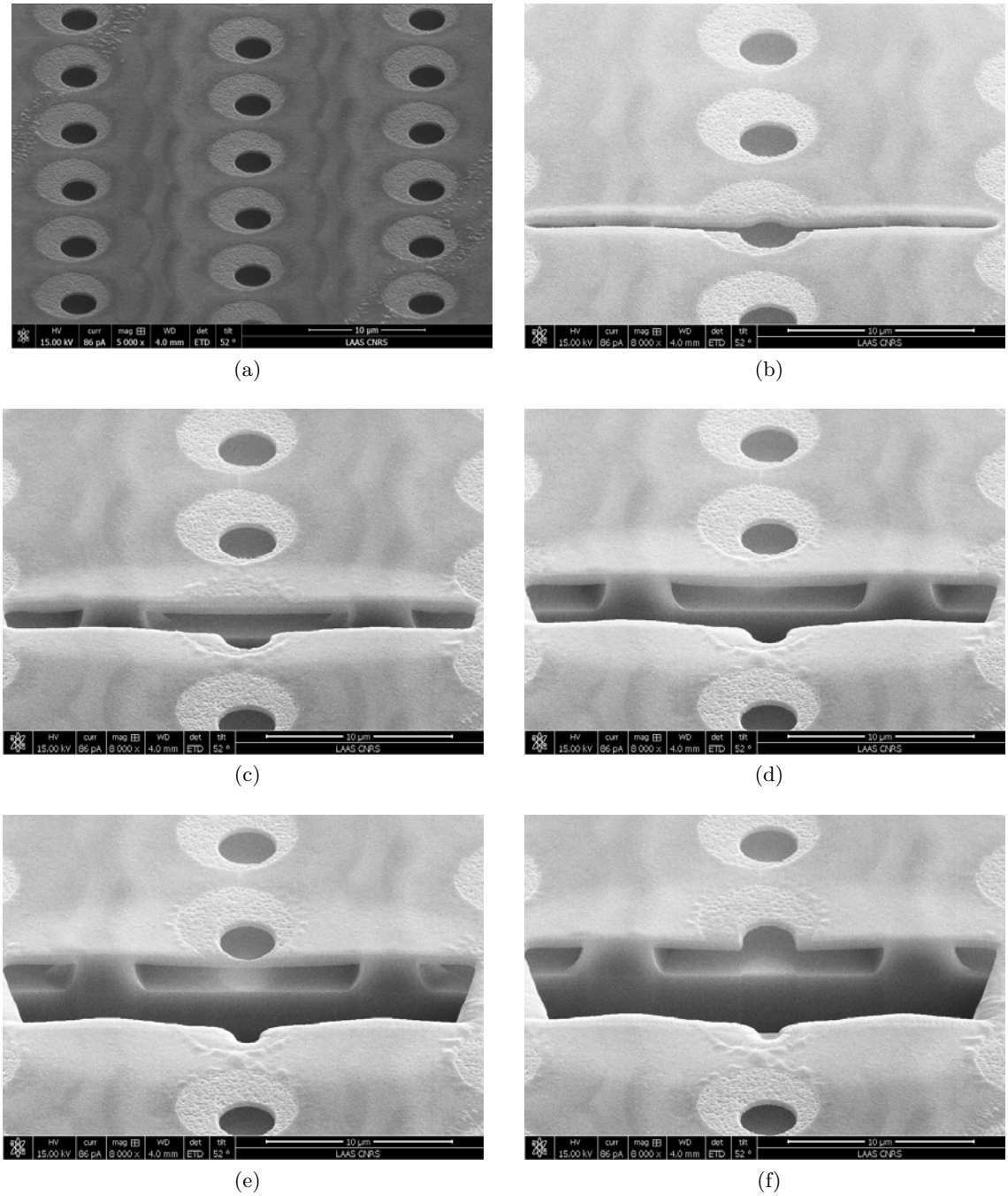

Figure 7.19: Portions of the circuit are gradually removed using a focused ion beam in order to reveal the structure of the suspended sensors.

was colorized to roughly indicate the $p-$ (blue) and $n-$regions (red). The junctions are clearly suspended. The total width of the emptied region at the cross section shown in these figures is roughly 9.30 µm

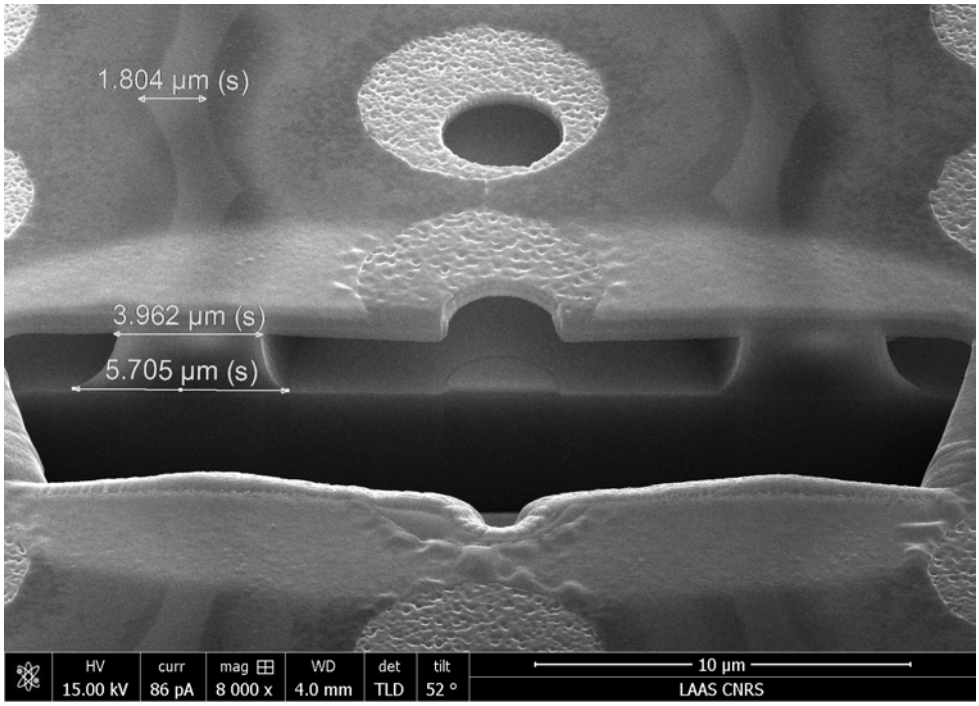

Figure 7.20: SEM of the suspended regions after removal of parts of the sensor using a focused ion beam (FIB).

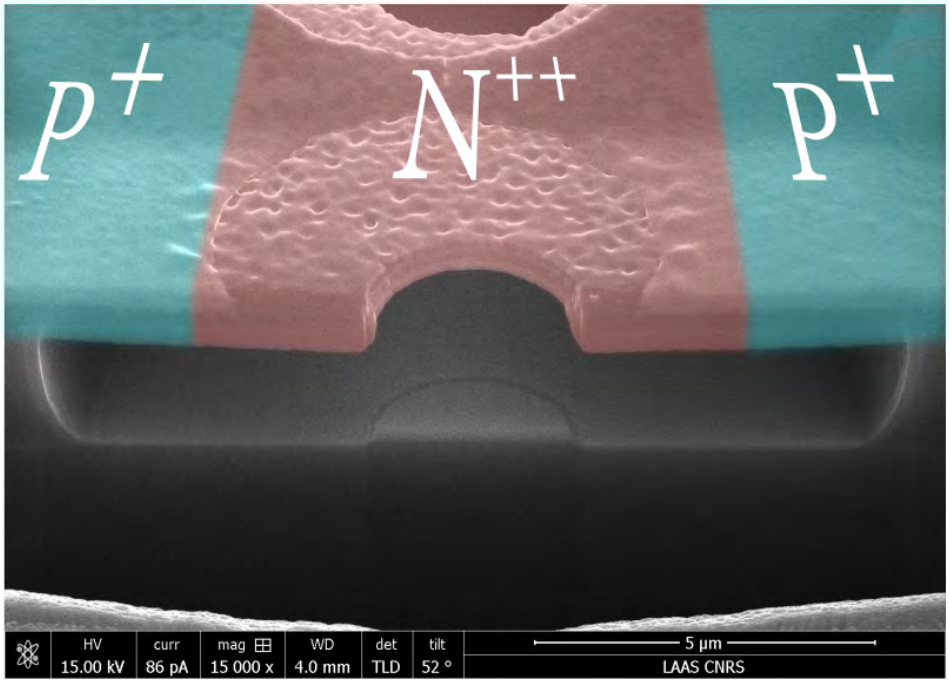

Figure 7.21: A close-up of the sensor which was colorized to show the position of the $pn-$junction

7.4 V/I characteristics and temperature sensitivity

The doping level of the P regions plays an important role in determining the measurable current passing through the sensors. Another factor is the length of the junction which is related to the size and geometry of the element. Three different designs were needed for the purposes of this study: one for detecting the periodic flow at different points inside the oscillator and is 320 µm × 320 µm in size, and two designs for measuring the temperature distribution on the impact plate at 100 µm × 100 µm and 100 µm × 1000 µm, respectively.

7.4.1 Before Buffered Oxide Etching (BOE)

Before finally removing parts of the sacrificial layer beneath the junctions, the current-voltage characteristics of the different sensors were first measured and plotted. In addition to the length of the junction, which depends on the geometry of the $n-$ and $p-$regions, and the acceptor concentration N_A, light sensitivity, the presence of the BOE holes in the polysilicon layer and the uniformity of the deposited layers can affect the characteristics of the sensors. The first set of tests consist in measuring the current-voltage characteristic of a number of identical sensors on the same wafer, under the same operating conditions (room temperature, absence of light, etc.). The dispersion of the data around the mean curve does not exceed 3% in the detection ($I = 0.1$ to 10 µA, Figure 7.22) and actuation ($I \geq 10$ µA) modes. The dispersion reaches 12% or more for current less than 10 nA.

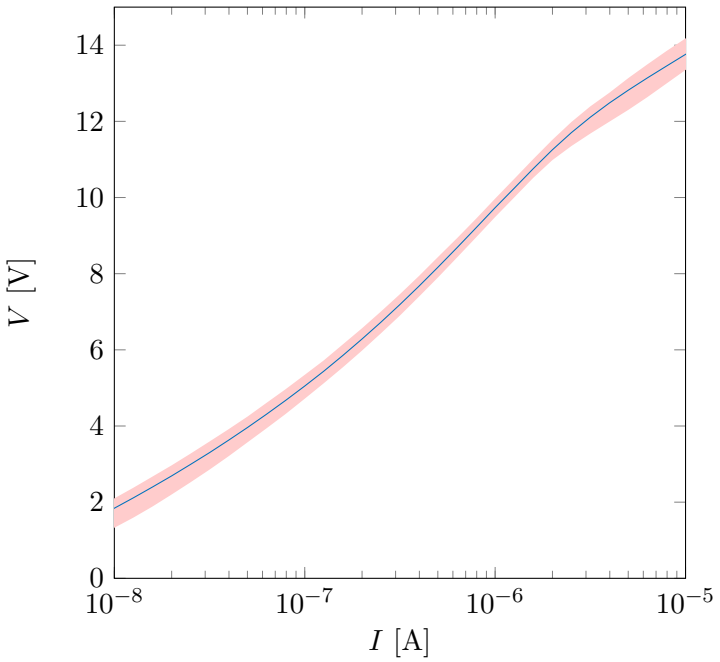

Figure 7.22: Mean characteristic curve with dispersion bands (red) from 14 300 µm × 300 µm- sensors from the same wafer ($D \approx 7 \times 10^{13}\,\mathrm{cm}^{-2}$) with BOE openings.

When a reverse voltage is applied on a diode, a photon hitting the depletion region can be absorbed, producing a new electron-hole pair. This in turn increases the current

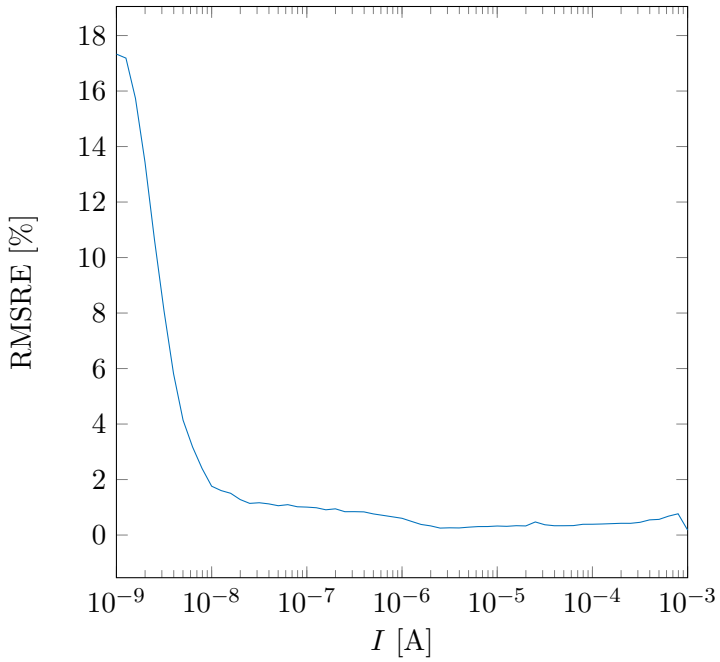

Figure 7.23: Root-mean-square relative error for fourteen 300 µm × 300 µm- sensors from the same wafer ($D \approx 7 \times 10^{13}\,\mathrm{cm}^{-2}$) between the measured characteristic curves with and without exposure to light.

going through the diode and alters the current-voltage curve. In light of this, the effect of photon exposure is considered for 8 sensors. The current-voltage characteristic curves where measured when the microscope light was on and off. The root-mean-square relative error was then computed to assess the sensitivity of the diodes to light (Figure 7.23). It is

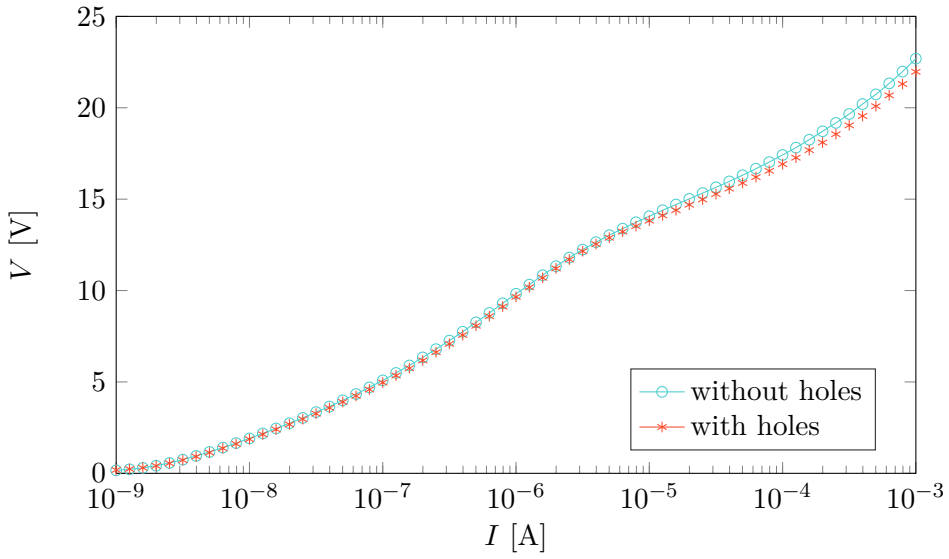

Figure 7.24: Current-voltage characteristics of two sensors with and without openings for the final wet-etching step.

clear that the effect of light produced by an ordinary lamp is negligible since it is less than 2% in both the detection and actuation regions although it is significant in the leakage current area.

As was shown in section 7.1, the depletion region extends almost entirely into the $p-$region because of the high levels of acceptor concentration. The holes in the polysilicon layer, whose sole purpose is to provide a path for the final wet-etching step, were intentionally place in the $n-$region to avoid interference with the depletion layer. In addition, these

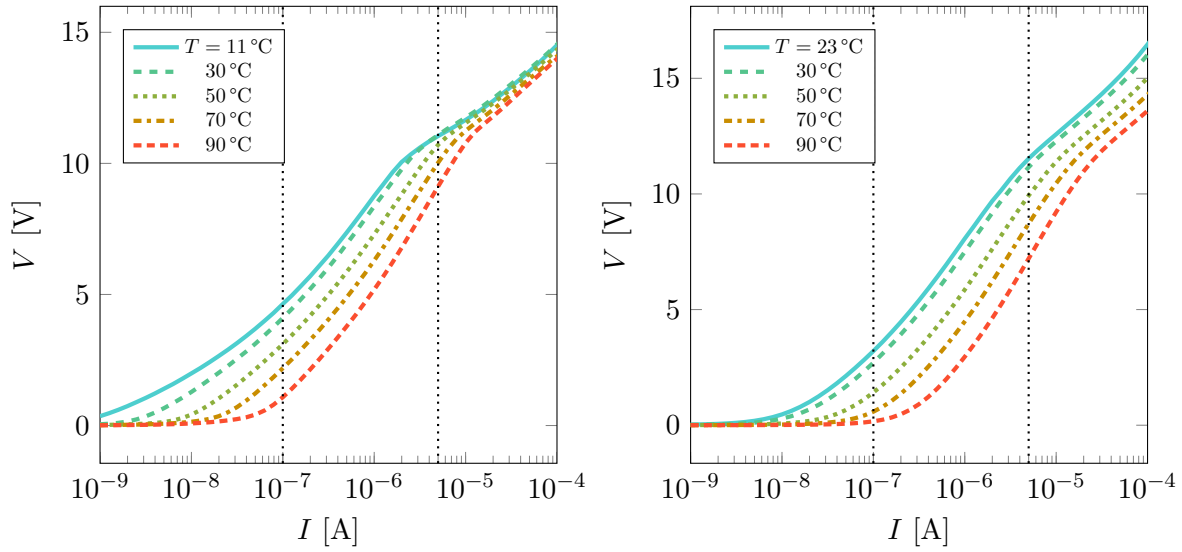

(a) $D \approx 5 \times 10^{13}\,\mathrm{cm}^{-3}$

(b) $D \approx 6 \times 10^{13}\,\mathrm{cm}^{-3}$

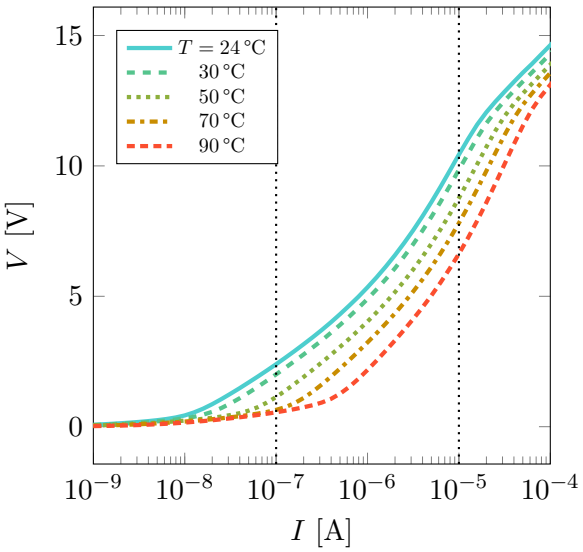

(c) $D \approx 7 \times 10^{13}\,\mathrm{cm}^{-3}$

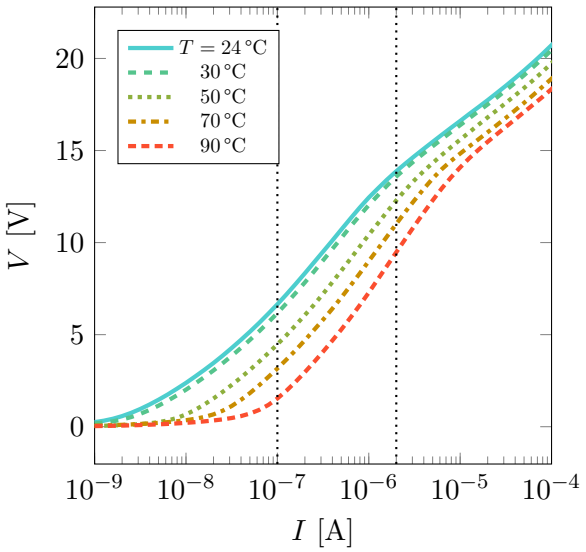

(d) $D \approx 1 \times 10^{14}\,\mathrm{cm}^{-3}$

Figure 7.25: V/I characteristic curves for the 300µm × 300µm sensor at different temperatures and for different dopant concentrations. The detection zone lies between the dotted lines in each plot.

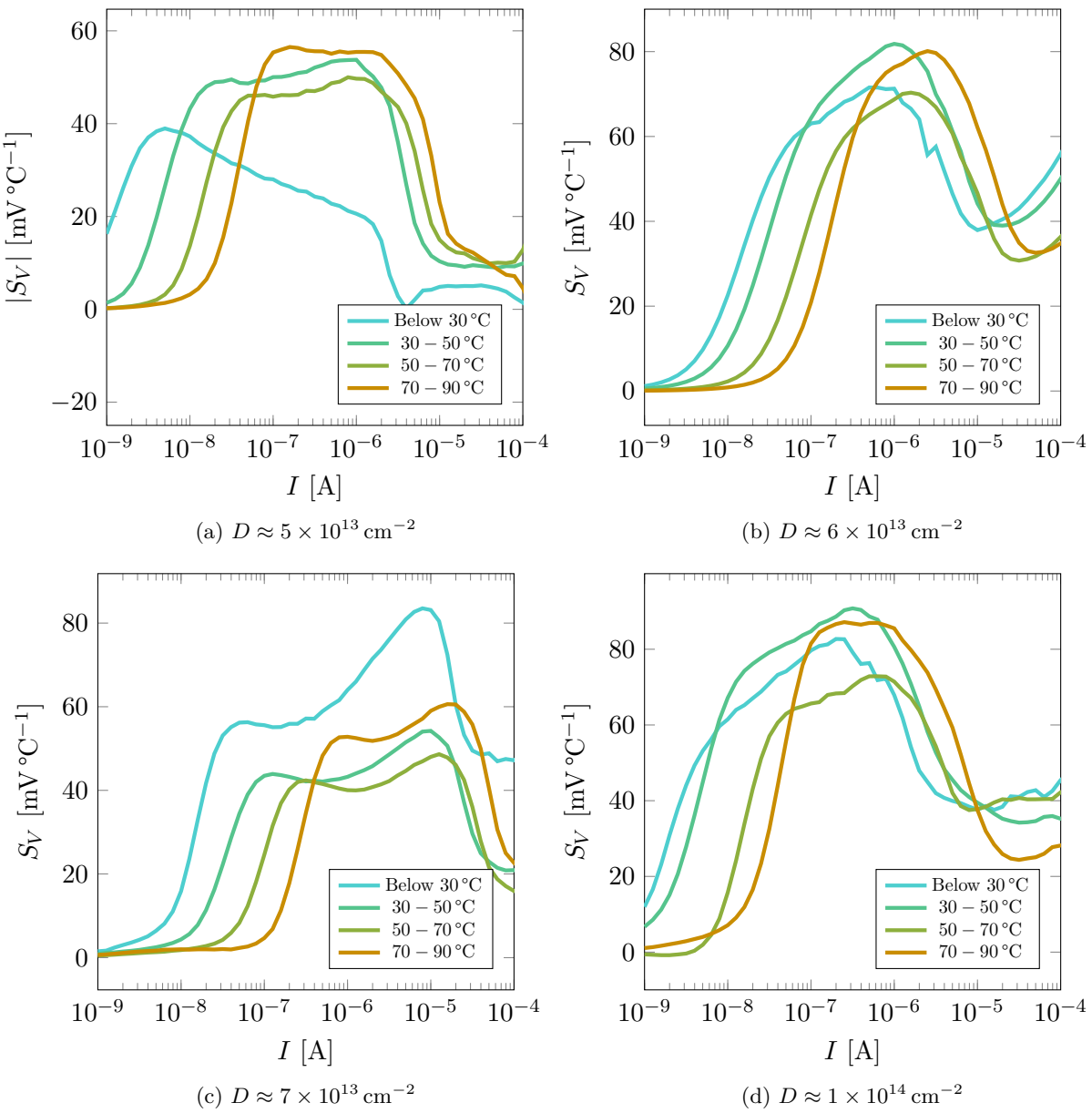

(a) $D \approx 5 \times 10^{13}\,\mathrm{cm}^{-2}$

(b) $D \approx 6 \times 10^{13}\,\mathrm{cm}^{-2}$

(c) $D \approx 7 \times 10^{13}\,\mathrm{cm}^{-2}$

(d) $D \approx 1 \times 10^{14}\,\mathrm{cm}^{-2}$

Figure 7.26: V/I characteristic curves for the 300µm × 300µm sensor at different temperatures and for different dopant concentrations.

holes do not alter the charge density, the cross section or the length of the $pn-$junction. So in principle, placing the openings in the $n-$region should not have an effect on the current-voltage characteristic in the detection region. This is not necessarily the case for the volume conduction region, since the holes alter the resistance of the $n-$region. This was verified for a number of sensor-pairs and an example is shown in Figure 7.24

To sum up, these diodes can be produced consistently and are not affected in any significant way by either light or openings in the $n-$doped regions. However, they are highly sensitive to temperature variations. For a given voltage level, the current increases with

temperature, leading to a noticeable change in the current-voltage characteristic, especially in the detection range (Figure 7.25). In the volume conduction range, the junction switches to a thermal actuation mode whereby it produces enough heat to alter its own temperature, making it unsuitable as a sensing element. The transition between the surface and volume conduction modes occurs when the slopes of the V/I characteristic changes. The highest current level at which the transition happens was obtained for $D \approx 7 \times 10^{13}\,\mathrm{cm}^{-2}$ (Figure 7.25c) and is equal to approximately $I = 10\,\mu\mathrm{A}$. In the remaining cases, the detection range extends to around $I = 2\,\mu\mathrm{A}$.

Using these V/I characteristics, the sensors' thermal sensitivity can be estimated for each temperature range (Figure 7.26). The sensitivity curves for the different doping levels all exhibit the same behavior. For low currents, the sensitivity is nearly zero but begins to rapidly rise as surface conduction starts to take over. In the detection zone, where the leakage current becomes relatively negligible but volume conduction is not yet predominant, the increase in sensibility slows down, sometimes reaching a plateau as in Figure 7.26a. The peak sensitivity is achieved in this range and has a typical value of -60 to $-80\,\mathrm{mV\,°C^{-1}}$. To put these values into perspective, type K thermocouples (Chromel/Alumel) usually have a thermal sensitivity of only $40\,\mu\mathrm{V\,°C^{-1}}$ which is three orders of magnitude lower than the sensors produced here.

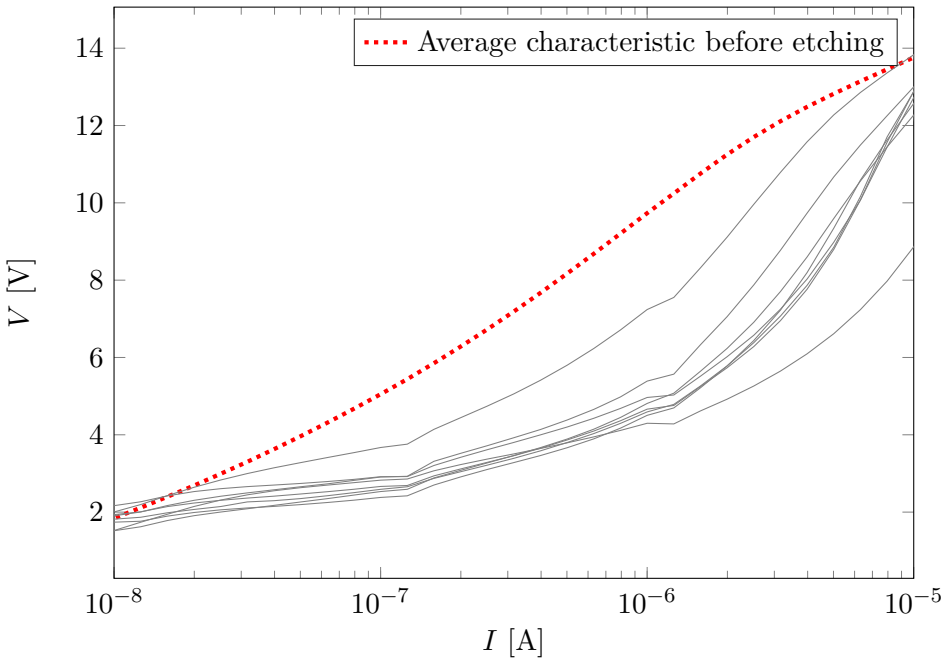

Figure 7.27: V/I characteristics of 8 sensors doped at $300\,\mu\mathrm{m} \times 300\,\mu\mathrm{m}$ from the same wafer ($D \approx 7 \times 10^{13}\,\mathrm{cm}^{-2}$) after wet-etching.

7.4.2 Post-BOE

The final, and arguably the most crucial step of the microstructuring process is the wet-etching. After several tests, it was determined that an etching time of 40 min at around 27 °C was needed to remove all but 2 µm wide strips of the SiO_2 layer. These strips, or anchors, carry the polysilicon layer. Compared to measurements from before the BOE (Figure 7.22), the sensors exhibit a slightly higher dispersion in current-voltage characteristics (Figure 7.27). Furthermore, for a given current, the voltage in the detection region

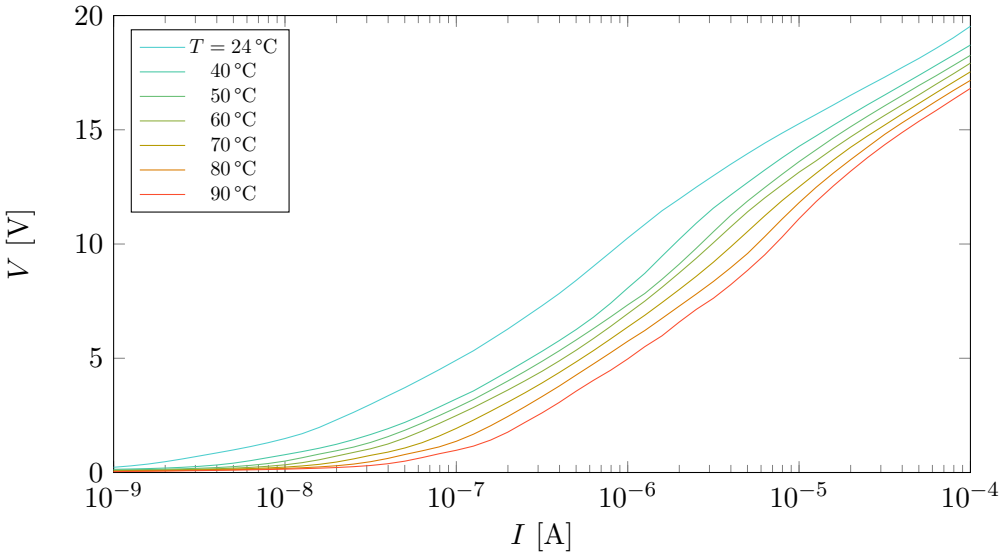

(a)

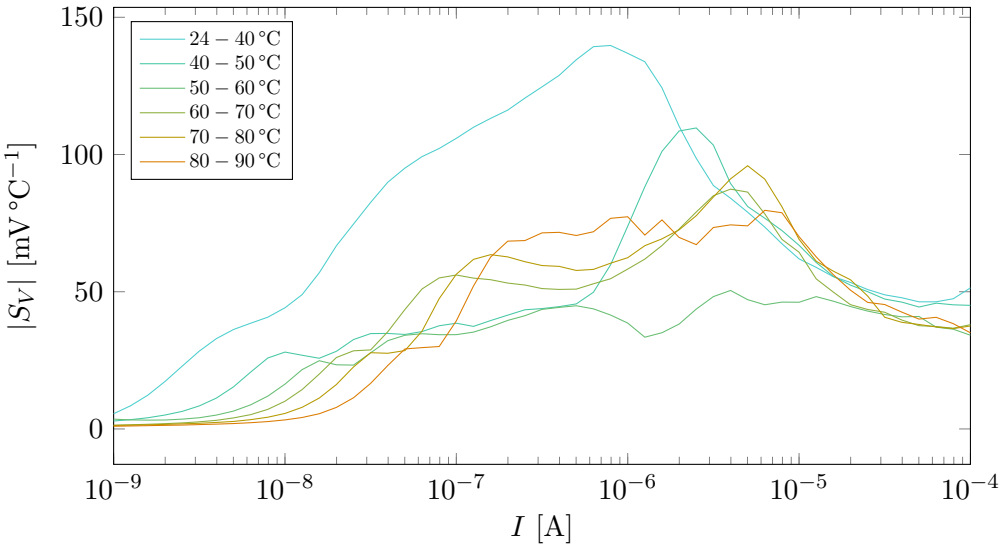

(b)

Figure 7.28: (a) Voltage/current characteristic of the sensors after the wet etch for different temperatures and (b) thermal sensitivity of the sensors after the wet etch in different temperature ranges ($D \approx 1 \times 10^{14}\,\mathrm{cm}^{-2}$).

is consistently lower for the suspended sensors.

The characteristics were again measured at different temperatures in order to assess the thermal sensitivity of the post-BOE sensors (Figure 7.28a). A clear shift in the curve can be noticed as the temperature is increased. The temperature sensitivity in each temperature range was then computed (Figure 7.28b). The results show that the peak sensitivity is the same as or even higher than it was prior to the etch. In the low temperature range, the sensitivity is particularly high, peaking at around $140\,\mathrm{mV\,°C^{-1}}$ for $I \approx 1\,\mu\mathrm{A}$.

7.5 Dry-film lamination

Prior to the lamination step in the previous chapter, an adhesion promoter, GPTMS (3-Glycidoxypropyltrimethoxysilane, 1% in isopropanol), was first deposited on the empty wafer. Now that the sensors have been built onto the wafer and partially suspended, using the adhesion promoter is no longer an option since it risks contaminating the openings in the polysilicon layer. In lieu of this, only a plasma descum step is performed before the lamination in order to remove any thin, difficult to detect residue from previous steps and thus improve adhesion of the dry-film. The wafers are placed in an oxygen-rich plasma chamber for 2 min at 200 W. Having etched a large part of the sacrificial layer, the main concern was that the suspended structures would collapse under the pressure of lamination. However, it seems that the structures are sturdy enough to survive the first lamination step as can be seen in Figure 7.28. The scanning electron microscope images presented earlier (Figures 7.19 to 7.21), were taken after lamination. No sign of bending or deterioration of the polysilicon layer were detected.

Having forgone the adhesion promoter, to avoid clogging up the cavities, local delamination was observed, especially near the suspended sensors and metallizations. Even when GPTMS was used, there was slight delamination around the metal patterns that are ad-

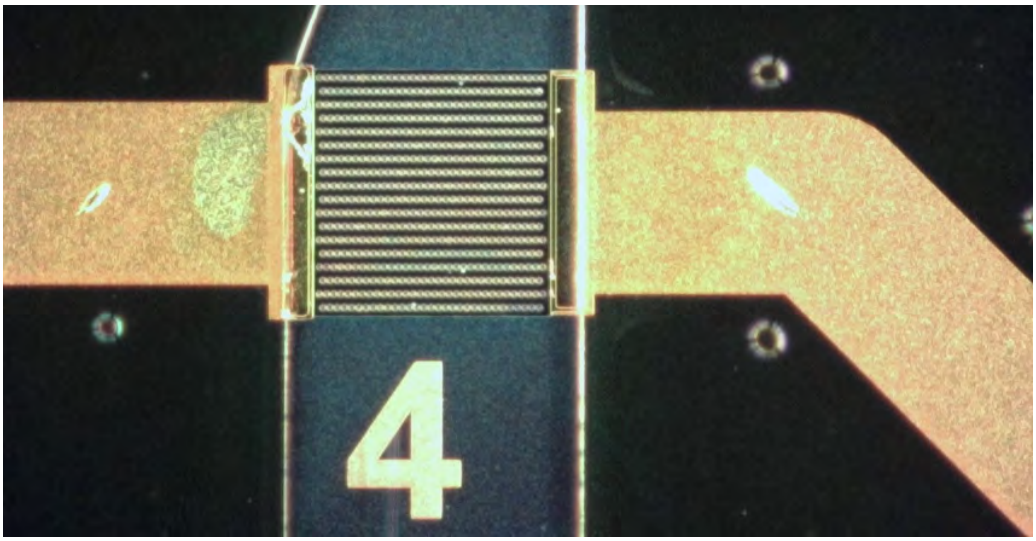

(a)

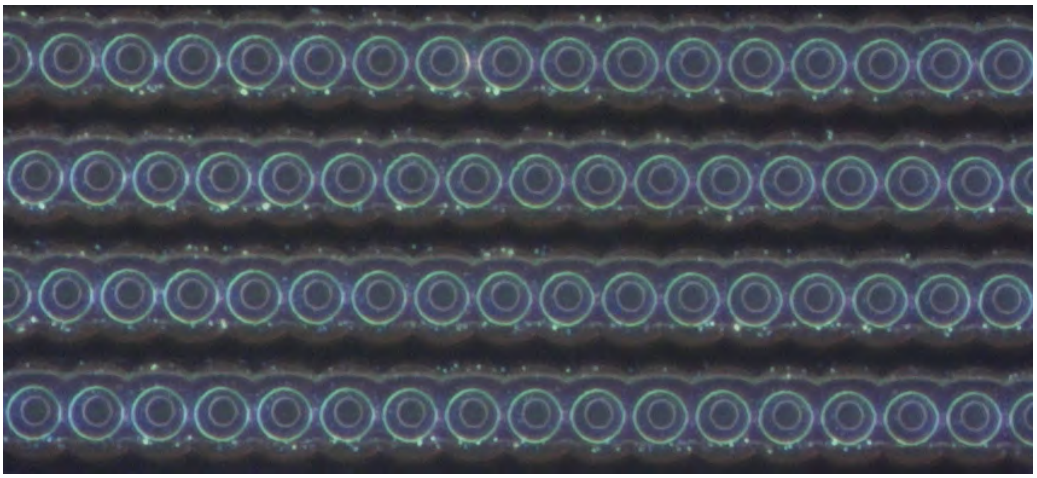

(b)

Figure 7.28: (a) Sensor after lamination of a layer of 100 µm thick dry-film and (b) a close up of the openings (dark field). The grayish halos surrounding the openings are the emptied parts of the oxide layer that can be seen through the silicon nitride and polysilicon layers.

jacent to the opened channels, but it did not occur often. An example is shown in Figure 7.29, which was taken from sensors that were suspended but did not function properly because of insufficient doping levels.

With the functioning sensors, only a plasma descum step was performed before building the microfluidic devices, so local delamination was more pervasive. Furthermore, we had observed that thin films of ECI from step 13 sometimes remained attached to the sensors even after several rounds of cleaning using a Piranha solution. These films seemed to be anchored to the openings in the polysilicon layer. No such issue was noted near the sensors without openings. These residues could also prevent the dry-film from adhering to the substrate. Local delamination is not necessarily a problem unless the flow in the channels has a high pressure, in which case it could propagate and detach the entire dry-film layer.

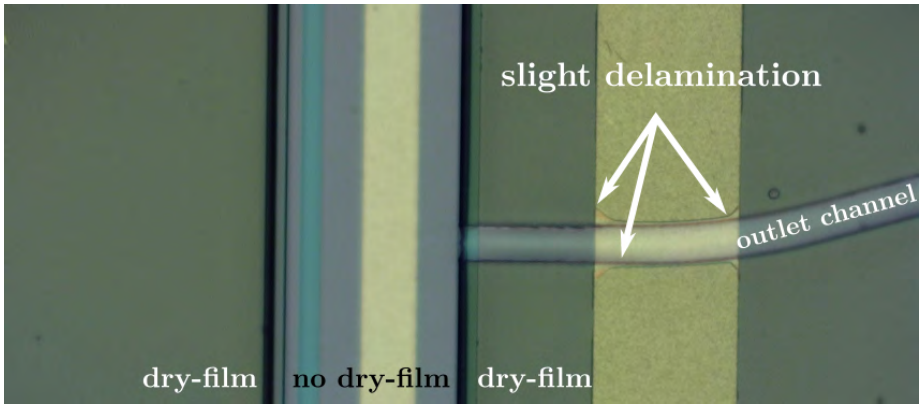

Figure 7.29: Slight delamination around the metal patterns even when using an adhesion promoter.

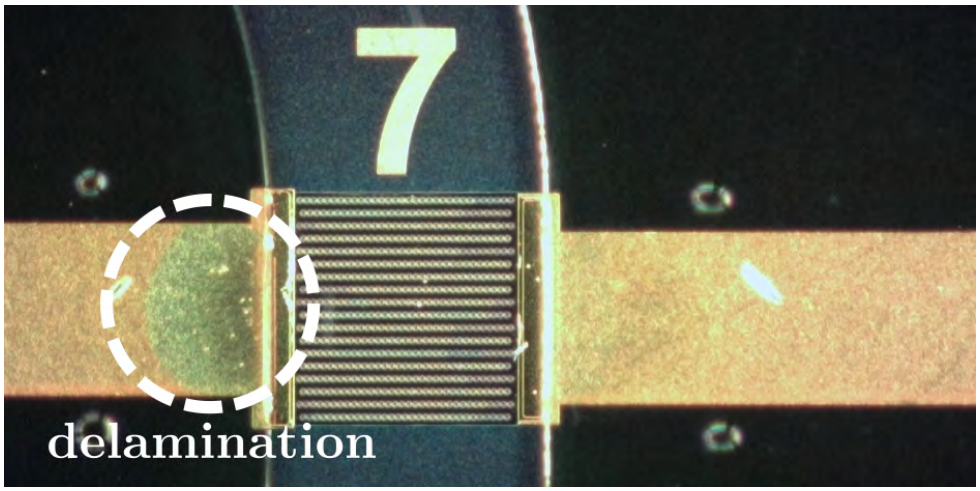

(a)

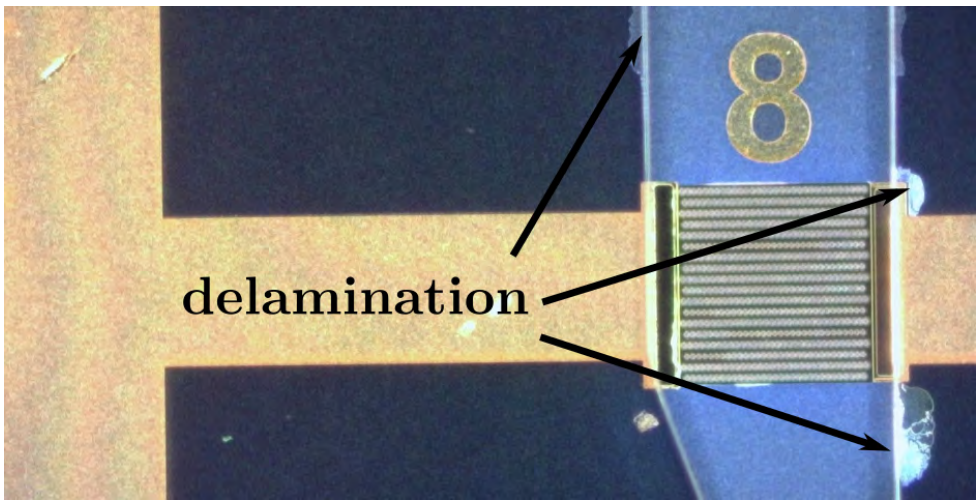

(b)

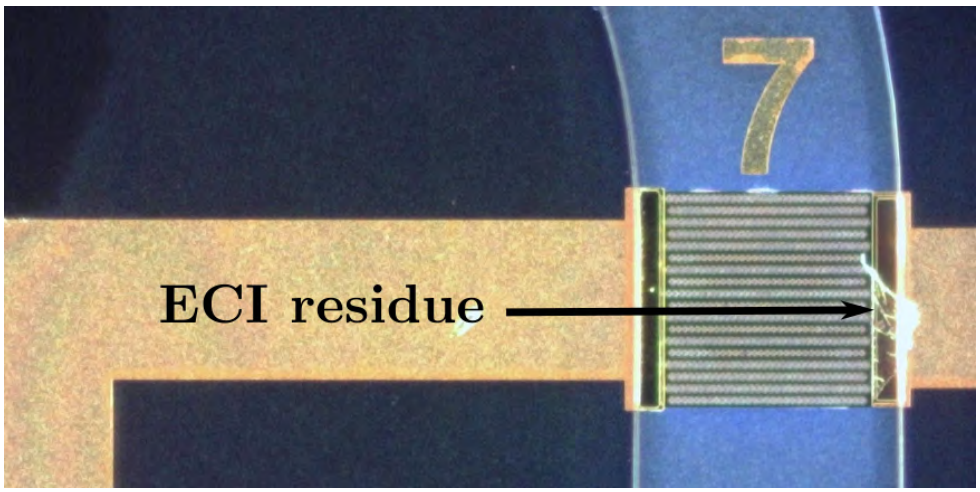

(c)

Figure 7.30: Images of different wafers after dry-film lamination showing issues such as local delamination and persistent residue from step 13.

7.6 Response time

7.6.1 Chip assembly

The silicon wafers on which the sensors and microfluidic channels were implemented were cut using a dicing saw fitted with a diamond blade and then glued onto individual PCBs. To avoid damaging the dry film layers, a space must be left between the sawed edge of the silicon substrate and the edge of the dry film. At the same time, we need to cut the wafer as close as possible to the outlet of the oscillator to reduce the interaction between the microjets exiting the channels and the part of the wafer that outflanks the dry-film layers. A margin of less than 50 µm was chosen as a reasonable compromise (Figure 7.31, blue). The chip is then connected to the PCB via wire bonding (Figure 7.31, red). Finally, the wires are protected with conformal coating which is cured by UV light. This coating shields the wires from any external damage, and prevents them from touching the metallic patterns on the PCB and creating a short-circuit.

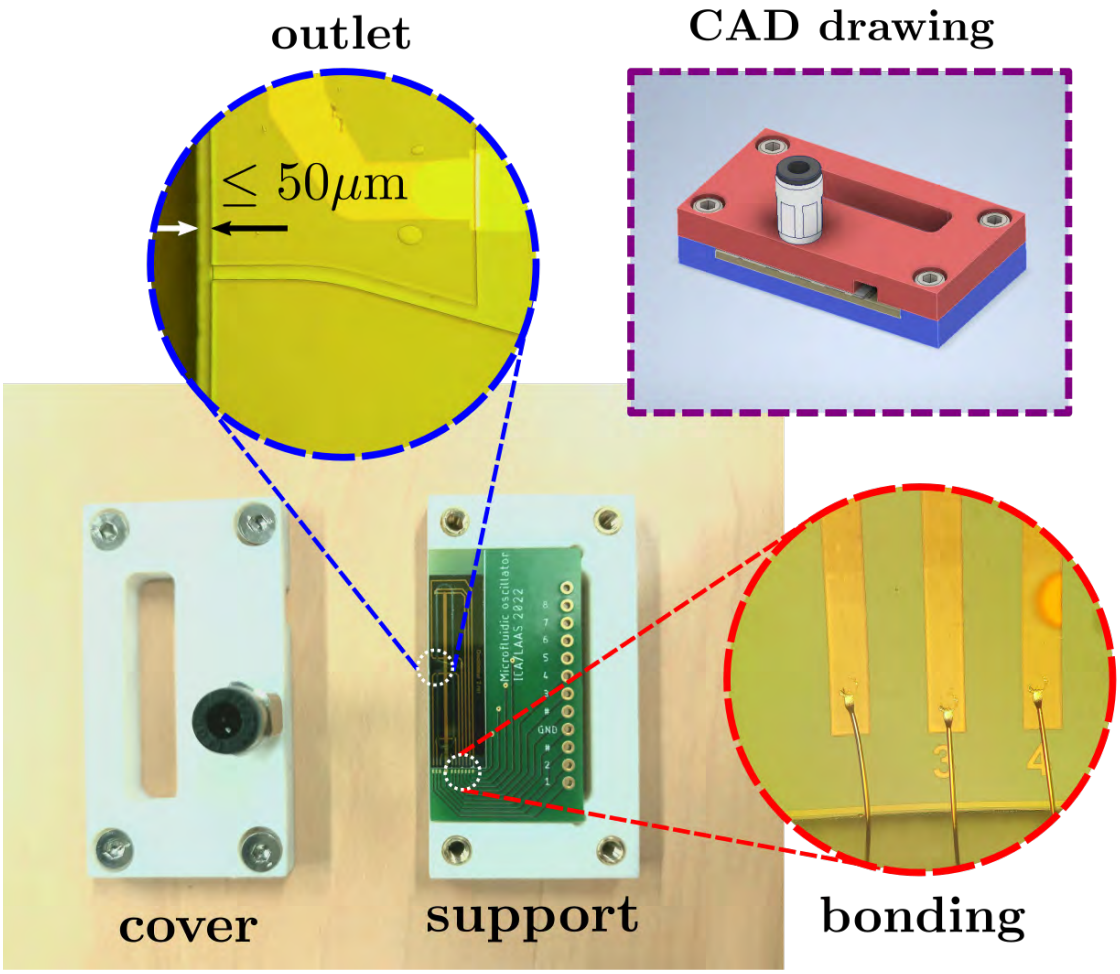

Figure 7.31: Chip/PCB/casing assembly with details of the chip-to-PCB bonding wires (red) and of the diced edge of the wafer in front of the micro-oscillator's exit (blue).

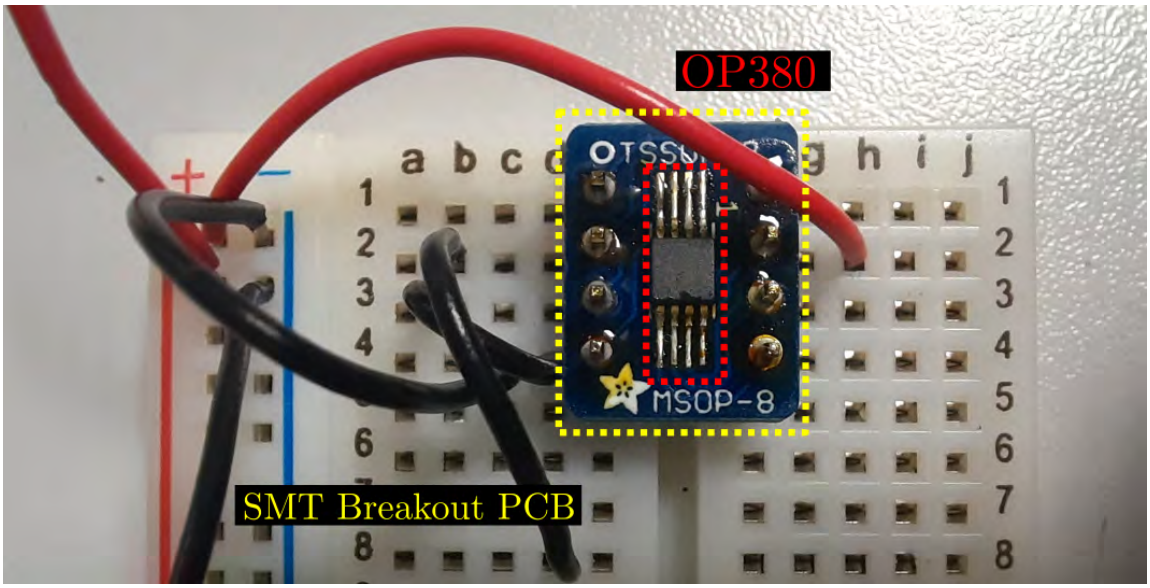

Figure 7.32: Transimpedance amplifier (OP380) mounted on an SMT Breakout PCB which is used to condition the measured signal from the thermal sensors.

7.6.2 Signal amplification and acquisition

A transimpedance amplifier (TIA) is used to amplify the signal coming from the thermal sensors. The particular model used here is the OP380 which was soldered onto an SMT Breakout PCB as shown in Figure 7.32

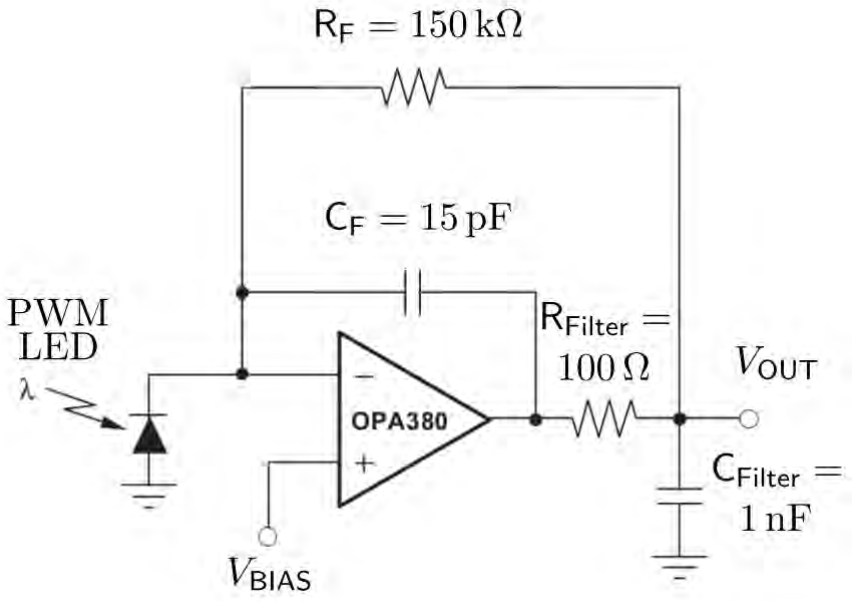

Figure 7.33: Circuit used to test the response time of the TIA with the filter resistance and capacitance.

The circuit was first tested with a photodiode as shown in the schematics of Figure 7.33. A pulsed light was produced using an LED connected to a micro-controller and the response of the photodiode was measured. A screen capture from the oscilloscope is presented in Figure 7.34. The rise time for a pulsed signal at $f = 9.5\,\text{kHz}$ is only $2.928\,\mu\text{s}$

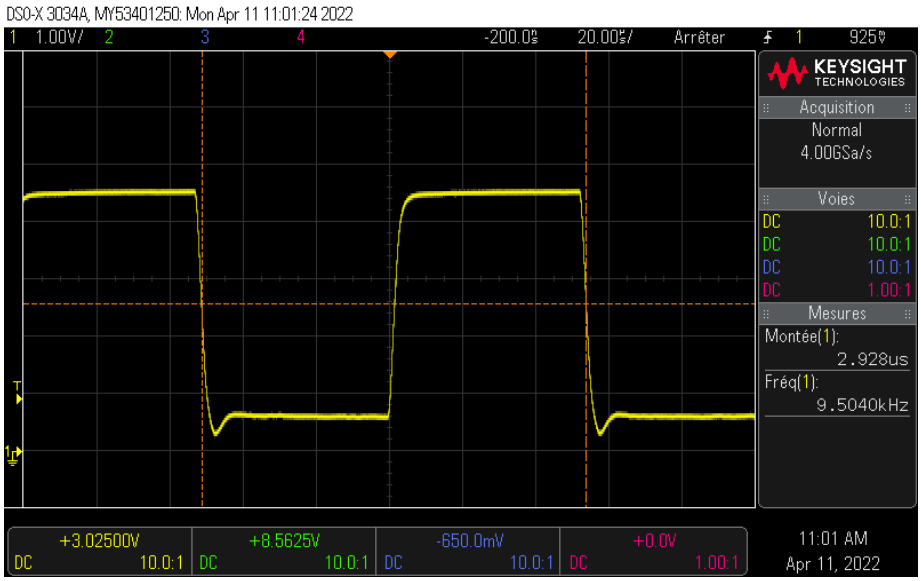

Figure 7.34: Voltage of the photodiode in response to a pulsed light source.

An illustration of the circuit is shown in Figure 7.35, where the sensor is represented as a Zener diode.

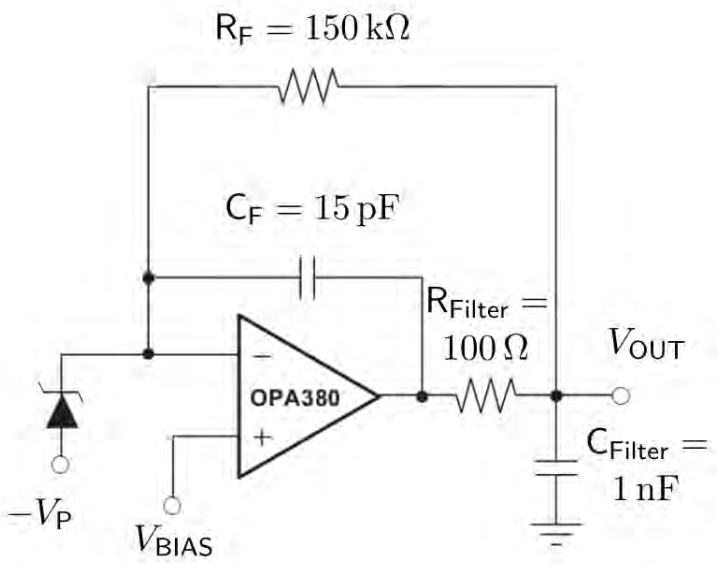

Figure 7.35: Circuit used to convert the current produced by the thermal sensor to a voltage and amplify and filter it.

7.6.3 Additional oscillator having a depth of 100 µm

In the previous chapter, five prototypes having constant depths of 25 and 50 µm were produced and their frequency was estimated as that of the tones they emit. The 25-micron-deep designs did not seem to function at all. This is unsurprising seeing as the aspect ratio of the inlet section is less than 2. On the other hand, oscillators B1 and B2 with a depth of 50 microns emit a clear sound that was easily picked up by the microphone. As was already noted, their frequencies are around ten times higher than their large scale equivalents. Seeing as the deeper channels showed more promise, and after the sensor arrays were produced, an additional series of oscillator were made with a depth of 100 microns. In this case, all of the designs produced clear, measurable tones. Some exceptions notwithstanding, the frequency tends to decrease with inlet pressure. Most prototypes start to oscillate at around $p_{\text{in}} = 2\,\text{bar}$, except the one with the longest feedback loops, E2, which starts at $p_{\text{in}} = 2.7\,\text{bar}$.

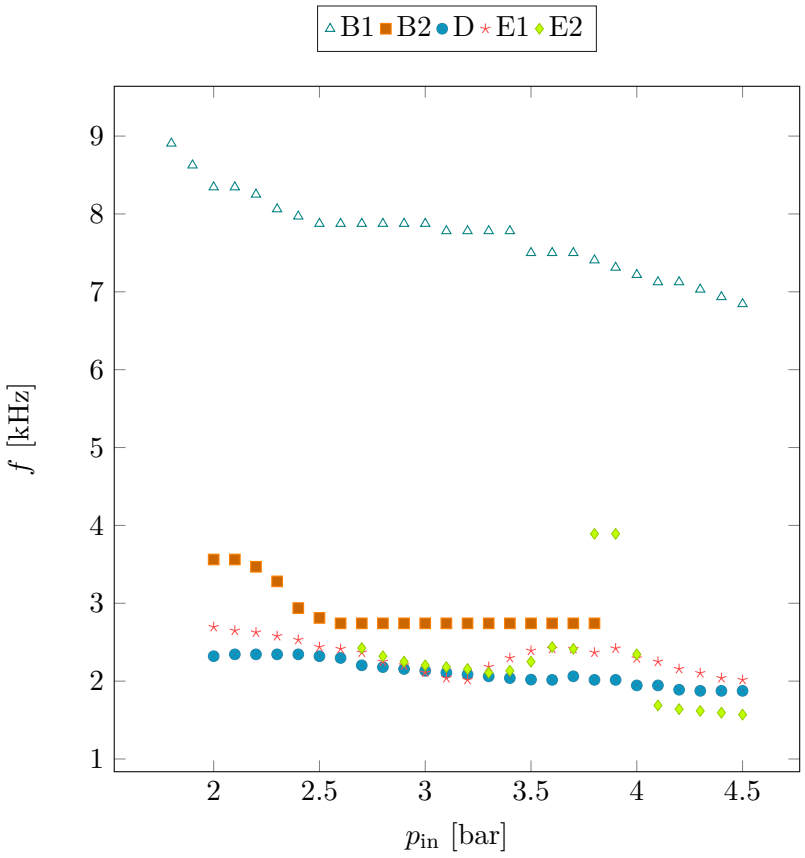

Figure 7.36: Frequency detected using a microphone versus inlet pressure for the five oscillator designs.

Comparing the frequency curves for B1 with a depth of 50 µm (Figure 6.12) and 100 µm (Figure 7.36), a striking difference between the shape of the curves and the values of the frequency can be observed. Whereas the frequency of the 50 µm-deep version peaks at around $p_{\text{in}} = 2.3\,\text{bar}$ before reaching a nearly constant value for higher pressures, the fre-

quency for 100 µm decreases monotonically across the entire range of pressures. Similarly, the frequency of B2 when its depth is 100 µm is lower than had been noted in the previous chapter. Prototypes D and E1, having nearly the same feedback loop lengths, have similar frequency responses, with a slight departure for $p_{\text{in}} = 3.5 - 4\,\text{bar}$, where E1 exhibits a slight peak. Oddly enough, the last case, E2, having the longest feedback loop, has a comparable response to those of D and E1. The frequency suddenly switches from 2.4 to 3.9 kHz for $p_{\text{in}} = 3.8 - 3.9\,\text{bar}$. This may be due to a passing change in pulsation mode, as was observed in Chapter 3 for the large scale device.

The following table summarizes the results from the preliminary measurements performed at the end of the previous chapter along with the additional cases presented here.

Table 7.1: Frequency ranges detected using a microphone for different oscillator designs and channel depths.

		Channel depth		
Prototype	L_f	25 µm	50 µm	100 µm
B1	11 000 µm	–	8.41 – 9.92 kHz	6.85 – 8.9 kHz
B2	45 000 µm	–	4.12 – 4.31 kHz	2.74 – 3.56 kHz
D	83 000 µm	–	–	1.88 – 2.32 kHz
E1	81 000 µm	–	–	2.02 – 2.70 kHz
E2	172 000 µm	–	–	1.57 – 2.44 kHz

Using the same model for frequency that was adopted in Chapter 3, namely:

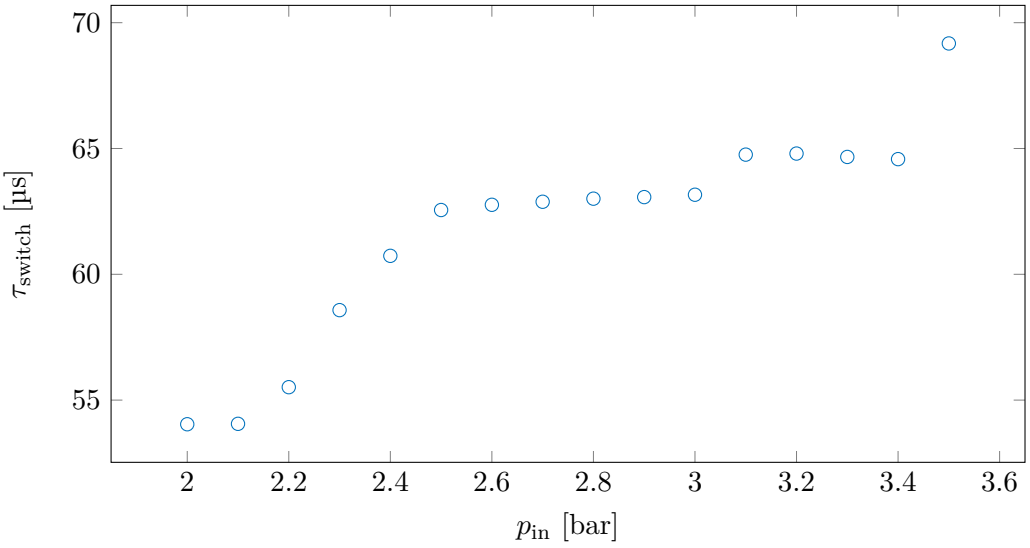

Figure 7.37: Total switching time found by fitting the frequency results for B1, B2, D and E1 for $p_{\text{in}} = 2 - 3.5\,\text{bar}$ using Eq. 7.2.

$$f = \frac{1}{2L_f/c + \tau_{\text{switch}}} \tag{7.2}$$

the frequency results for B1, B2, D and E1 were fitted in order to deduce the behavior of switching time τ_{switch} with increasing inlet pressure p_{in}. Unlike the macroscale prototypes, the switching time seemed to increase with pressure and then level off for $p_{\text{in}} \approx 2.5\,\text{bar}$. A slight jump in switching time can be seen at $p_{\text{in}} \approx 3\,\text{bar}$. The integrated temperature sensors may give us more information in order to better interpret these results.

7.7 Proof of concept: preliminary measurements using the integrated sensors

Having proven the mechanical strength of the sensors as well as the reproducibility by performing extensive electrical tests, it is time to use them to measure fluctuations inside an oscillator. In Figure 7.38, the plot of the Fast Fourier Transform (FFT) of the amplified signal from one of the sensors inside the 'D' oscillator at $p_{\text{in}} = 2.5\,\text{bar}$ exhibits three distinct peaks that stand out from the surrounding noise. The first peak corresponds to the fundamental frequency of the oscillator and the two others its harmonics. Similar results within the same range of inlet pressures were also obtained but are not shown here for the sake of brevity. However, the range of frequencies detected corresponds to what was presented in the preceding section.

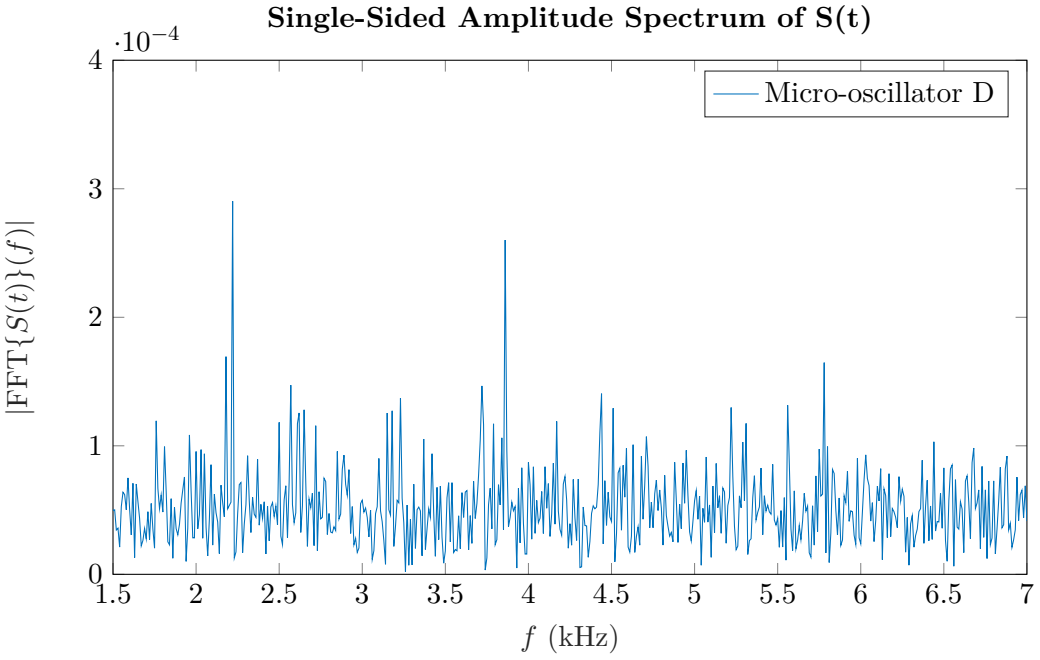

Figure 7.38: Single-sided FFT of the amplified signal from one microsensor inside of the 100 µm-deep 'D' oscillator (see Table 7.1).

This plot demonstrates that the fluctuations inside the oscillator, which stem from pressure variations, can be clearly detected using the micro-sensors that were produced from scratch, and thus the goal that was set at the beginning of this endeavour has been reached. What remains is to use these sensors to characterize the oscillators in more detail. Measuring the signals simultaneously from different sensors within the same oscillator would help achieve a better understanding of how they function at this scale. Moving forward, using PCB's which contains the amplification circuit could help further reduce the noise in the signal. However, at this stage of development, this hybrid microfluidic/electronic chip was shown to work sufficiently well to perform meaningful measurements.

7.8 Summary and conclusion

In this chapter, the entire process of developing, producing and testing microfluidic oscillators with integrated, custom-built instrumentation was presented. Of particular interest was the attempt to reduce the thermal inertia of a polysilicon based thermal sensor by suspending its temperature-sensitive regions over the substrate via wet-etching. We managed to show that this step is not only feasible and controllable, but that the suspended structures are not damaged during the following steps which included applying high pressures and temperatures on the wafer in order to laminate layers of dry-film. A number of oscillators, having different channel depths, were tested. It was shown that the aspect ratio of the inlet cross section plays a crucial role in determining whether or not the oscillators could function and has an effect on the frequency of pulsation. The final assembly includes the chip with the suspended sensors and microfluidic channels, the casing used to encapsulate the chip and to connect pneumatic fittings for the inlet supply and finally the circuitry used to condition the signal from the sensors. This highly compact system only requires compressed air and an oscilloscope to run. Preliminary tests have shown that it is possible to detect rapid fluctuations, clearly distinguishable from noise, using these sensors, thus providing a proof of concept of these instrumented fluidic/electronic chips.

"La lutte elle-même vers les sommets suffit à remplir un coeur d'homme. Il faut imaginer Sisyphe heureux."

Le Mythe de Sisyphe, Albert Camus

8

Summary and Conclusion

8.1 New contributions

Pulsed impinging jets have the potential to improve heat transfer compared to steady jets having the same mass flow rate. This dissertation investigated the use of fluidic oscillators to produce these pulsed jets. The advantage of using these devices is the absence of moving parts which makes them more robust in harsh environments and lower-maintenance compared to typical electro-mechanical solutions. A number of variations on the original design were implemented which showed that the oscillator may function in different modes of pulsation, the main actors of these modes being the switching mechanism of the main jet and the traveling waves in the feedback loops. The heat transfer performance of the pulsed jet was assessed for a range of pulsation frequencies, standoff distances and Reynolds numbers in an attempt to pinpoint the optimal operating conditions. Simulations were then performed to further understand the fluid and thermal phenomena taking place inside the oscillator itself and in the flow produced by the pulsed impinging jet.

In the second part of the thesis, oscillators at one tenth the scale of the original design were fabricated along with integrated sensors. The sensors used are based on temperature sensitive $pn-$junctions. The current iteration of these sensing elements is particular in that the junctions are suspended over the substrate by partially removing an underlying sacrificial layer. This has the effect of reducing the thermal inertia of the sensors, allowing for rapid thermal sensing. The main findings of the thesis are detailed next.

8.1.1 Pulsation modes of a pulsed jet fluidic actuator (PJFA)

An interplay between two phenomena gives rise to the bi-stable behavior of the oscillator: the switching mechanism of the main jet and the pressure wave traveling along the feedback loops. Early work, such as Simões et al. (2005), estimated the duration of an oscillation to be equal to the time needed by a pressure wave to travel once across each feedback loop. This duration is then roughly proportional to twice the length of the feedback loop, by assuming that the speed of wave propagation is constant, and that the jet switching time is negligible. Wang (2017) showed that for their design, the pressure waves had to travel back and forth across both feedback loops, so that the duration of each pulsation is proportional to four times the feedback loop length. On the other hand, Löffler et al. (2021) showed that the main jet can switch in two ways, either by attaching alternatively to the side walls of the interaction chamber or through an edge tone instability around the splitter edge. In the present work, it was shown that by slightly contracting the section of the feedback loops of the design used by Wang (2017), it was possible to provoke switching with a single wave travel along the each feedback loop. By further decreasing the width of the feedback loops, and increasing the supply pressure, the oscillator switches to high frequency mode in which switching in the interaction chamber is due to the edge tone instability rather than the Coanda effect. Furthermore, it was shown that the switching time decreases with inlet pressure. The decrease seems to be exponential when the inlet is at subsonic conditions. When the inlet section becomes choked, the switching time declines linearly. The way switching time is affected by inlet pressure requires a deeper study. Most of the early works on the topic, such as Muller (1964) or Epstein (1971), only consider subsonic incompressible conditions. In recent times, little attention has been given to this aspect of the device.

8.1.2 Flow field models using POD, DMD and DNN

Through conditional sampling, the velocity field was reconstructed from hot-wire measurements along with pressure signals from inside the feedback loop. Both 2D and 3D reconstructions were performed and were used to identify vortex dipoles in the flow. The data set thus produced was then used to construct a model based on data-driven methods. Two modal decomposition techniques, Proper Orthogonal Decomposition (POD) and Dynamic Mode Decomposition (DMD) were used first, with moderate success. A Deep Neural Network (DNN) with only three layers was then trained on the data. A rarely used, sinusoidal activation function was used and resulted in much shorter training times and a much more accurate representation of the flow than neural networks having the same structure but with more commonly used activation functions. Being able to construct a representation of the flow produced by a fluidic oscillator may be of interest in those applications where it is only part of a much larger system. In addition, such a representation can be useful when numerical simulations are performed as it always one to forgo simulating the entire oscillator when only the flow that it produces is of interest.

8.1.3 Heat transfer improvement using PJFAs

The pulsed jets produced by the oscillators were used to cool a heated surface. A reference steady case was also considered for comparison. Pulsed jets consistently outperform steady jets having the same average mass flow rate for small impact distances. However, unlike steady jets whose performance peaks when the standoff distance is equal to the potential core length, pulsed jets with low frequencies showed a monotonic decline in performance with standoff distance. The jet with the highest frequency had a distinctive behavior as it performed better than the steady jet for greater impact distances. A general power law was used to fit the improvement factor relative to the steady cases which confirmed that pulsed jets enhance heat transfer for higher frequencies and lower impact distances.

8.1.4 Simulating the complex flow inside and outside the PJFAs

Simulations were then performed to better explain certain experimental observations. It was shown that the URANS models fail to accurately predict both the behavior of the oscillator and the heat transfer performance. Worth noting however that the $k-\omega$ models were significantly better than the $k-\epsilon$ models on both accounts. A hybrid LES/URANS was then used to simulate the pulsating flow. To our knowledge, there has yet to be a study in the literature that uses the hybrid approach to simulate a pulsating impinging rectangular jet. We were able to visualize the nascent vortices in the shear layers of the jet and the wall jet and how they evolve over time, sometimes leading to flow separation from the heated wall. The heat transfer results, although incomplete, seemed to show a qualitative agreement with the experimental results. More simulations must be carried out in the future where additional parameters, such as pulsation frequency, are explored.

8.1.5 Proof of concept for Micro-PJFAs

Few studies have used microjets to cool electronic devices (Chen et al., 2005). To our knowledge, pulsed microjets have yet to be studied, specifically in heat transfer applications. Moreover, no study could be found in the literature that study oscillators at this scale, where the inlet section is only 20 µm-wide. The present work has shown that microfluidic oscillators can work with air as the working fluid and that that their frequency scales inversely with size. Tens of thousands of patents were granted since the late 1950's that are related to the term 'fluidic oscillator'. These inventions include sensors, actuators, control system and logic components. Could it be possible to replicate these complex devices, all based around the self-excited fluidic amplifier, at a scale of only a few tens of micrometers?

8.1.6 Suspension of thermal sensors

The present iteration of the tunnel junction sensors (studied previously by Camps et al. (2013)) is different in that the sensing areas are not in contact with the substrate. We

were able to elaborate an entire process that starts with microstructuring arrays of thermal sensors then partially suspending them via wet-etching and ends with laminating microchannels over them without incurring any damage to the structural integrity of the device. The ability to perform measurements *in situ* and also heat the flow (since the elements can act as thermal actuators for higher supply currents) can prove useful in many other microfluidic applications such as thermal transpiration experiments. During the fabrication runs, we also produced thermal transpiration chips for another project that will be tested soon.

8.2 Continuing experiments on pulsed impinging microjets

The entire experiment on pulsed impinging microjets produced by no-moving-parts microfluidic oscillators has been set up, from the development and fabrication of miniaturized, sensitive and rapid temperature sensors, to a proof of concept of truly micro-scale PJFA's and the design and structuring of an instrumented heated plate. Many questions were raised regarding how the device's behavior is affected by the design of the feedback loops and the inlet pressure. A very short term goal consists in assessing the cooling performance of the pulsed microjets on the heated plate. Depending on the results, integrating these microfluidic oscillators into an actual cooling system would be the next step.

8.3 Future work on oscillator design

One of the main drawbacks of using fluidic oscillator is the inability to control certain operating conditions. For instance, the average Reynolds number of the produced pulsed jets, the frequency and waveform of the pulsation are closely related and cannot be modulated individually. The only parameter that can be controlled during operation is the supply pressure. However, one can find a number of patents, starting from the early days of fluidics and up to the present, of fluidic oscillators whose output can be more readily controlled. For instance, Sowers (1964) proposed an oscillator that can provide a number of stable frequencies depending on the feedback passageway which is selected via external control (Fig. 8.1a).

Another design by O'Neill (1969) achieved frequency modulation by changing the volume of the feedback loops. This is done by connecting them to a U-shaped tube filled with water and applying a pressure on the open end in order to change the water level, effectively changing the capacitance of the feedback loops. Another parameter of interest is the waveform of the exit velocity. Neradka (1971) patented a device that can produce a constant frequency velocity signal but with a modulated amplitude (Fig. 8.2).

These and many other designs patented over the years, could be used to better control the pulsed jet and to test more experimental configurations. The unexplored topics mentioned in the literature review, such as polychromatic forcing or even controlling vortex size and shedding frequency become within reach with more sophisticated oscillator designs.

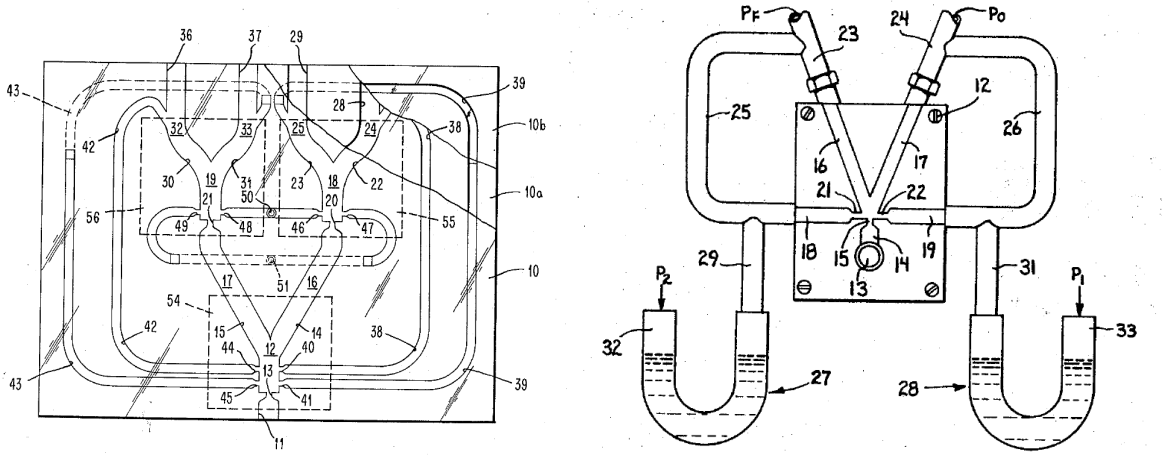

(a) (b)

Figure 8.1: Fluidic oscillator designs with variable frequency by (a) Sowers (1964) and (b) O'Neill (1969).

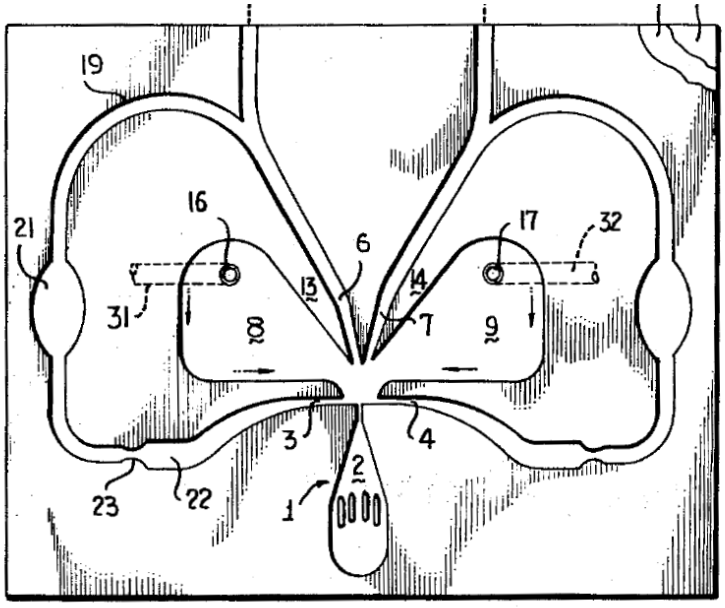

Figure 8.2: Oscillator design by Neradka (1971) capable of producing amplitude-modulated velocity signals.

Appendices

A

POD, DMD and DNN

A.1 Proper Orthogonal Decomposition

The Proper Orthogonal Decomposition (POD) [1] attempts to extract, in a way, structures that typify the behavior of the flow as a whole. If k is a deterministic function that has such a structure, then we want to maximize the magnitude of its projection $(u,k)/(k,k)^{1/2}$ onto our data u. This must be done in a statistical sense, otherwise we would be led to the trivial solution $k = u$. Lumley proposes maximizing the following quantity:

$$E\{(u,k)(u,k)^*\}/(k,k)^{1/2} = \lambda \geq 0 \tag{A.1}$$

It can be proven that the above optimization problem is equivalent to the following eigenvalue problem:

$$(R(t,t'),k^*(t')) = \lambda k(t) \tag{A.2}$$

where $R(t,t') = E\{u(t) \times u^*(t')\}$ is the correlation function, k and u are generalized functions, and $(^*)$ is the complex conjugate (the reader is referred to Lumley's book for a detailed proof). By solving this eigenvalue problem, what we find is an infinite number of orthogonal functions $k_n(t)$ (eigenfunctions), each one having the maximum amount of energy possible λ_n (eigenvalues). Knowing this, we can decompose u into 'modes' as follows:

$$u = \sum_{n=1}^{\infty} (u,k_n)\, k_n \tag{A.3}$$

[1] It is also known as principal component analysis (PCA) in statistics, empirical orthogonal functions (EOF) in climate and meteorology, the discrete Karhunen–Loeve transform, and the Hotelling transform

where the coefficients (u, k_n) are uncorrelated since for any p, q:

$$E\{(u, k_p)(u, k_q)^*\} = \Big(R(t, t'), k_p(t)k_q^*(t')\Big) \tag{A.4}$$

$$= \lambda_p(k_p(t), k_q(t) = \lambda_p \delta_p^q \tag{A.5}$$

Although in Lumley (2007) these modes are referred to as 'characteristic eddies', the procedure in itself, as described above, does not attach any a priori physical interpretation to each modes. In other words, these modes do not necessarily correspond one-by-one to the phenomena underlying the physical data. So we cannot directly jump to conclusions based on the modes alone. In what follows, we will be using the now commonly used variant called Snapshot POD. Instead of having a single point measurement $u(t)$ as was implied before, we have a field of data $\mathbf{U}(\mathbf{x}, t)$. The POD is done on the fluctuating field $\mathbf{U}_f(\mathbf{x}, t) = \mathbf{U}(\mathbf{x}, t) - \overline{\mathbf{U}}$:

$$\mathbf{U}_f(\mathbf{x}, t) = \sum_{n=1}^{\infty} \mathbf{A}_n(t)\mathbf{\Phi}_n(\mathbf{x}) \tag{A.6}$$

The data matrix $\mathbf{U}$ is constructed by filling each row with the p samples measured at each of the q grid points. We begin by constructing the $q \times q$ correlation matrix:

$$\mathbf{C} = \frac{1}{p-1}\mathbf{U}_f\mathbf{U}_f^T \tag{A.7}$$

The eigenvectors $\mathbf{\Phi}_n(\mathbf{x})$ and eigenvalues λ_n of the above correlation matrix represent the spatial functions and the energy contained in the corresponding mode. The time coefficients can be found by projecting the data matrix onto the corresponding spatial function:

$$\mathbf{A}_n(t) = \mathbf{\Phi}_n(\mathbf{x})\mathbf{U}_f \tag{A.8}$$

Finally, as mentioned before, each mode is the product of the time coefficient and the spatial mode:

$$\tilde{\mathbf{U}}_n = \mathbf{A}_n(t)\mathbf{\Phi}_n(\mathbf{x})^T \tag{A.9}$$

The eigenvalues are sorted in descending order, so that the fluctuations associated with the first modes are more significant than the rest from an energy standpoint. In other words, the eigenvectors we found represent the principal components of the data, or the directions of maximum variance.

A.2 Dynamic Mode Decomposition

A more recent decomposition technique was proposed by Schmid (2010), and is similar in many respects to POD. This technique, called Dynamic Mode Decomposition (DMD), assumes that there is a single, linear mapping $\mathbf{A}$ between successive snapshots of the flow:

$$v_{i+1} = \mathbf{A}v_i \tag{A.10}$$

where v_i is a snapshot of the data at a given instant. This means that the data matrix containing all the snapshots, can be written as:

$$\mathbf{V}_1^N = \left\{v_1, \mathbf{A}v_1, \mathbf{A}^2v_1, \ldots, \mathbf{A}^{N-1}v_1\right\} \tag{A.11}$$

turning the sequence of flow fields into a Krylov sequence. The system matrix $\mathbf{A}$ that underlies the flow fields is not available in an experiment. Its dynamic characteristics have to be extracted from the experimental data $\mathbf{V}_1^N$. In order to proceed, we assume that v_N becomes linearly dependent on the $N-1$ previous snapshots for a large enough N, in other words:

$$v_N = a_1v_1 + a_2v_2 + \cdots + a_{N-1}v_{N-1} + r \tag{A.12}$$

or

$$v_N = \mathbf{V}_1^{N-1}\mathbf{a} + r \tag{A.13}$$

where r is the residual vector. After some manipulation, it can be shown that:

$$\mathbf{A}\mathbf{V}_1^{N-1} = \mathbf{V}_2^N = \mathbf{V}_1^{N-1}\mathbf{S} + re_{N-1}^T \tag{A.14}$$

where e_{N-1}^T is a unit vector and $\mathbf{S}$ is the companion matrix of $-\mathbf{a}$. According to Schmid (2010), this decomposition based on $\mathbf{S}$ is ill-conditioned and proposes a pre-processing step based on a singular value decomposition (SVD) of $\mathbf{V}_1^{N-1} = \mathbf{U}\Sigma\mathbf{W}^H$. Substituting in the above equation, and rearranging yields $\mathbf{U}^H\mathbf{A}\mathbf{U} = \mathbf{U}\mathbf{V}_2^N\mathbf{W}\Sigma^{-1} \equiv \tilde{\mathbf{S}}$ which is related to $\mathbf{S}$ by a similarity transformation. The projected modes are extracted from $\tilde{\mathbf{S}}$ via:

$$\phi_i = \mathbf{U}y_i \tag{A.15}$$

where y_i are the eigenvectors of $\tilde{\mathbf{S}}$. The exact DMD modes, that are the exact eigenvectors of the system matrix $\mathbf{A}$ can be found via (Tu et al. (2014)):

$$\phi_i = \mathbf{V}_2^N\mathbf{W}\Sigma^{-1}y_i \tag{A.16}$$

The corresponding eigenvalues μ_i can be used to compute the energy content of the corresponding modes (Leask and McDonell (2019)):

$$p_i = \mu_i^{N-1}\|\phi_i\| \tag{A.17}$$

where $\|\mathbf{\Phi}_i\|$ is the $L2$-norm of a given mode. The field can be reconstructed from these eigenvectors and eigenvalues as follows:

$$v(\mathbf{x},t) \approx \sum_k \phi_k(\mathbf{x}) \exp(\omega_k t) b_k \tag{A.18}$$

where $\omega_k \equiv \ln(\mu_k)/\Delta t$ and the vector of b_k's is $\mathbf{b} = \mathbf{\Phi}^\dagger v_0$ (the columns of $\mathbf{\Phi}$ are ϕ_i, and $\mathbf{\Phi}^\dagger$ is its pseudo-inverse). The frequency and growth/decay rate of a given mode are given by $f_k = \Im(\omega_k)/2\pi$ and $\gamma_k = \Re(\omega_k)$, respectively.

One of the main hurdles of DMD is its sensitivity to noise in experimental data. Noise-corrupted data are not necessarily amenable to partition using DMD since the noise may be more predominant than some of the dynamical features of the flow. According to Dawson et al. (2016), the standard DMD algorithm is biased to noise present in the data because it implicitly assumes that the vector $\mathbf{V}_2$ contains all the noise while the data in $\mathbf{V}_1$ is noise-free. This is obviously not the case since both vectors are constructed from the same data set. In order to remove this bias, several methods are proposed, namely the noise-corrected, forward-backward and total least-squares variants (*ncDMD*, *fbDMD* and *tlsDMD* respectively). In the present work the *tlsDMD* and fbDMD variants were chosen along with the standard formulation presented above since the *ncDMD* requires knowledge of the characteristics of the noise. However, the same authors argue that sensor noise has a marginal effect on the DMD modes and their corresponding frequencies and that the choice of DMD algorithm is only important if the growth/decay rates are of interest.

The *fbDMD* formulation consists in finding the state matrix $\tilde{\mathbf{S}}_b$ in the same way $\tilde{\mathbf{S}}$ was found but by switching $\mathbf{V}_1$ and $\mathbf{V}_2$. Dawson et al. (2016) showed that it was possible to obtain a de-biased estimate of $\mathbf{A}$ via:

$$\tilde{\mathbf{A}} \approx \left(\tilde{\mathbf{S}}\tilde{\mathbf{S}}_b\right)^{1/2} \tag{A.19}$$

The eigenvalues and eigenvectors of $\tilde{\mathbf{A}}$ are computed and the DMD modes are found just as in the standard formulation.

The *tlsDMD* variant begins by projecting the original data onto r POD modes. The projected vectors $\tilde{\mathbf{V}}_1$ and $\tilde{\mathbf{V}}_2$ are stacked into a single matrix and a single-value decomposition is performed:

$$\begin{bmatrix} \tilde{\mathbf{V}}_1 \\ \tilde{\mathbf{V}}_2 \end{bmatrix} = U\Sigma W^H \tag{A.20}$$

Then, U, which is a $2r \times 2r$ matrix, is partitioned into $r \times r$ submatrices

$$U = \begin{bmatrix} U_{11} & U_{12} \\ U_{21} & U_{22} \end{bmatrix} \tag{A.21}$$

The new system matrix is then given by $\tilde{\mathbf{A}} = U_{21}U_{11}^{-1}$. The eigenvalues and eigenvectors of $\tilde{\mathbf{A}}$ are then used to find the DMD modes just as in the standard DMD algorithm.

A.3 Deep Neural Networks (DNN)

Machine Learning is finding evermore practical applications in physical sciences. Although usually associated with image processing and voice recognition, it has been used to model physical phenomena and is being driven by unprecedented amounts of experimental data. According to Brunton et al. (2019), a neural network is a "computational architecture, based loosely on biological networks of neurons, for nonlinear regression". Ott et al. (2021) used a neural network with 3 hidden layers containing 15, 11 and 9 neurons, respectively to estimate the phase-averaged velocity field of a pulsed jet. The activation function used was the sigmoid function with a SGD optimizer. However, neural networks using the sigmoid function can be difficult to train due to the possibility of vanishing gradients: the sigmoid function reaches saturation for large enough inputs and so produces gradients that are nearly zero. These vanishing gradients can hinder back-propagation.

In the present study, four activation functions were tested: the sigmoid function, the Rectified Linear Unit (ReLU), the Exponential Linear Unit (ELU) and the sine function. The ELU function (Djork Arne Clevert et al.) combines an exponential function for negative inputs with a linear function for positive ones and avoids the vanishing gradient problem. It is more costly to compute than the Rectified Linear Unit (ReLU) activation function, but leads to faster convergence. Finally, the sinusoidal function introduces a more complex non-linearity into the system and may be more adapted to the periodic flow studied here.

The Adaptive Momentum Estimation (Adam) optimization was used instead of SGD in order to accelerate convergence. Adam optimization combines the advantages of momentum optimization and RMSProp optimization by keeping track of past gradients and squares of gradients. Although Adam optimization is an adaptive learning rate algorithm, the learning rate was still progressively reduced every time the error drop slowed down. The neural networks used have 3 hidden layers with a different number of total neurons (Table A.1). The input layer comprises the spatial coordinates $\mathbf{x}$ and time t while the output layer has a single neuron for the velocity. All of the neural networks were implemented using the Keras API.

The sinusoidal representation networks (SIREN) (Sitzmann et al. (2020)) must be properly initialized in order to accelerate the training and outperform the rest. The weights matrix is given by $\mathbf{W} = \omega_0\hat{\mathbf{W}}$ where $\hat{\mathbf{W}}$ is initialized according to a random uniform distribution $\mathcal{U}\left(-\sqrt{c/n\omega_0^2}, \sqrt{c/n\omega_0^2}\right)$. This ensures that the input of each successive hidden layer is normally distributed, i.e. $\mathbf{W}^T \cdot \mathbf{x} \sim \mathcal{N}(0,1)$. The authors of Sitzmann et al. (2020) recommend setting $\omega_0 = 30.0$ for the first hidden layer, and $\omega_0 = 1.0$ for the rest. For the present data set, these values of ω_0 were not changed and yielded good results.

In order to accelerate convergence, a custom learning rate scheduler, elaborated through

trial and error, was used. The learning rate changes in three steps. For the first three epochs, the learning rate is constant at $\eta = 0.02$, and then decreases exponentially by a constant factor $\exp(-0.05)$. In the final step, when the exponentially decreasing learning rate reaches 5×10^{-4}, it is held constant at this value until the end of the training. The training is interrupted if no improvement in the loss function is seen for 50 consecutive epochs or if the number of epochs exceeds 1500.

	Number of neurons			
Neural Network	1st layer	2nd layer	3rd layer	Activation function
SIG-3 $\times$ 20	20	20	20	sigmoid
ReLU-3 $\times$ 20	20	20	20	ReLU
ELU-3 $\times$ 20	20	20	20	ELU
SINE-3 $\times$ 20	20	20	20	sinusoidal
SIG-3 $\times$ 40	40	40	40	sigmoid
ReLU-3 $\times$ 40	40	40	40	ReLU
ELU-3 $\times$ 40	40	40	40	ELU
SINE-3 $\times$ 40	40	40	40	sinusoidal
ELU-3 $\times$ 60	60	60	60	ELU
SINE-3 $\times$ 60	60	60	60	sinusoidal

Table A.1: Deep Neural network structures and activation functions tested.

B

FLIR SC235 Data Sheet

B.1 FLIR SC235 Data Sheet

The data sheet of the FLIR SC235 camera used to perform the thermal measurements of Chapter 4 is reproduced below.

FLIR SC325

Speed up your design cycle with infrared

The SC325 is designed from the ground-up to deliver the accurate thermographic imaging and repeatable temperature measurement necessary in demanding science and R&D applications. Each crisp thermal image is built from over 76,000 individual picture elements that are sampled by the camera's on-board electronics and firmware. SC325 features include:

Key features and Benefits:

- **Uncooled Microbolometer Detector** – Maintenance-free and provides excellent long wave imaging performance
- **Optics and Focus** – standard built-in 25° lens with optional 6°, 15°, 45°, and 90° lenses available to achieve other fields of view; manual and auto focus standard
- **Microscopy and Close-up Measurement** – Optional 100 µm, 50 µm, and 25 µm microscope optics and microscope stand are available for small target imaging and measurement
- **Precise Timing and Control** – Optically-isolated digital I/O connections eliminate communication latencies with digital in and out for shutter disable and program control along with a V-sync connector for triggering and synchronization
- **Plug-and-Play Compatibility** – Ideal system integration solution with universal plug and play and GigE Vision Control protocols. The camera can be fully configured from the PC, allowing command, control, and collection of full frame data from the camera in real time.
- **Versatility** – Compact, rugged, and lightweight with straightforward 3-sided mounting feature that permits quick installation and easy movement for new application requirements
- **Fast Data Transfer** – Equipped with an RJ-45 gigabit Ethernet connection that supplies a 16-bit 320 x 240 images at rates as high as 60 Hz along with linear temperature data; GenICam and GigE Vision Compliant
- **Tailored to Your Application** – FLIR Systems offers a complete line of accessories including optics, enclosures, data systems, and software tools to suit the most demanding applications.

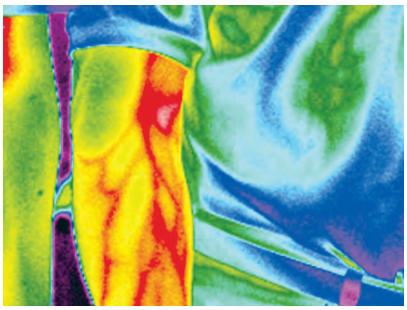

320 x 240 pixels IR resolution and thermal sensitivity of 50mK provides optimized image details and temperate difference information.

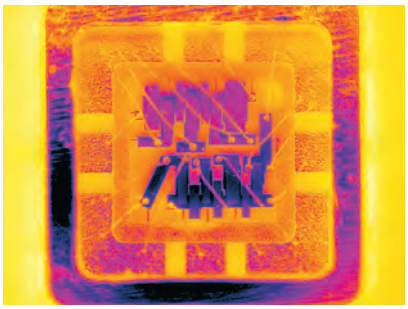

Infrared measurement allows you to see a thermal problem and measure temperature over surfaces accurately.

Typical applications:

The FLIR SC325 camera is an excellent choice for those who want to work in R&D and need high frame rates but for whom 320 x 240 pixels resolution is sufficient. For those who need to use camera in R&D, it is highly recommended to use the FLIR ResearchIR software.

FLIR SC325 Technical Specifications

Imaging and optical data	
Field of view (FOV)	25° x 18.8°
Minimum focus distance	0.4 m
Focal length	18 mm
Spatial resolution (IFOV)	1.36 mrad
Lens identification	Automatic
F-number	1.3
Thermal sensitivity / NETD	<0.05°C @ + 30°C / 50 mK
Image frequency	60 Hz
Focus	Automatic or manual (built in motor)
Detector data	
Detector type	Focal Plane Array (FPA), uncooled microbolometer
Spectral range	7.5-13 µm
IR resolution	320 x 240 pixels
Detector pitch	25 µm
Detector time constant	Typical 12 ms
Measurement	
Object temperature range	-20°C to +120°C 0 °C to +350°C
Accuracy	±2°C or ±2% of reading
Measurement analysis	
Atmosphere transmission correction	Automatic, based on inputs for distance, atmospheric temperature and relative humidity
Optics transmission correction	Automatic, based on signals from internal sensors
Emissivity correction	Variable from 0.01 to 1.0
Reflected apparent temperature correction	Automatic, based on input of reflected temperature
External optics / windows correction	Automatic, based on input of optics / windowtransmission and temperature
Measurement corrections	Global object parameters
Ethernet	
Ethernet	Control and image
Ethernet, type	Gigabit Ethernet
Ethernet, standard	IEEE 802.3
Ethernet, connector type	RJ-45
Ethernet, communication	TCP/IP socket-based FLIR proprietary and GenICam protocol
Ethernet, image streaming	16-bit 320 x 240 pixels @ 60 Hz - Signal linear - Temperature linear - Radiometric GigE Vision and GenICam compatible
Ethernet, protocols	TCP, UDP, SNTP, RTSP, RTP, HTTP, ICMP, IGMP, ftp, SMTP, SMB (CIFS), DHCP, MDNS (Bonjour), uPnP
Digital input / output	
Digital input, purpose	Image tag (start, stop, general), Image flow ctrl. (Stream on/off), Input ext. device (programmatically read)
Digital input	2 opto-isolated, 10-30 VDC
Digital output, purpose	Output to ext. device (programmatically set)
Digital output	2 opto-isolated, 10-30 VDC, max 100 mA
Digital I/O, isolation voltage	500 VRMS
Digital I/O, supply voltage	12/24 VDC, max 200 mA
Digital I/O, connector type	6-pole jackable screw terminal
Power system	
External power operation	12/24 VDC, 24W absolute max
External power, connector type	2-pole jackable screw terminal
Voltage	Allowed range 10-30 VDC

Environmental data	
Operating temperature range	-15°C to +50°C
Storage temperature range	-40°C to +70°C
Humidity (operating and storage)	IEC 60068-2-30/24 h 95% relative humidity +25°C to +40°C
EMC	• EN 61000-6-2:2001 (Immunity) • EN 61000-6-3:2001 (Emission) • FCC 47 CFR Part 15 Class B (Emission)
Encapsulation	IP 40 (IEC 60529)
Bump	25 g (IEC 60068-2-29)
Vibration	2 g (IEC 60068-2-6)
Physical data	
Weight	0.7 kg
Camera size (L x W x H)	170 x 70 x 70 mm
Tripod mounting	UNC1/4"-20 (on three sides)
Base mounting	2 x M4 thread mounting holes (on three sides)
Housing material	Aluminium

Scope of delivery
Hard transport case or cardboard box
Infrared camera with lens
Calibration certificate
Ethernet™ cable
Mains cable
Power cable, pig-tailed
Power supply
Printed Getting Started Guide
Printed Important Information Guide
User documentation CD-ROM
Utility CD-ROM
Warranty extension card or Registration card
Optional Accessories
IR lens f = 30 mm, 15° incl. case
IR lens f = 10 mm, 45° incl. case
Close-up 4× (100 µm) incl. case
Close-up 2× (50 µm) incl. case
Lens 76 mm (6°) with case and mounting support for A/SC3XX
Lens 4 mm (90°) with case and mounting support for A/SC3XX
Close-up 1× (25 µm) incl. case and mounting support for A/SC3XX
High temp. option +1200°C/+2192°F for FLIR T/B2XX to T/B4XX and A/SC3XX Series
Power supply for A/SC3XX and A/SC6XX
Power cord EU
Power cord US
Power cord UK
Ethernet cable CAT-6, 2m/6.6 ft.
Power cable, pig-tailed
Hard transport case for A/SC3XX and A/SC6XX series
Delivery Box for A/SC3XX

Recommended softwares for documentation and analysis:
- ThermoVision(TM) System Developers Kit
- FLIR ResearcherIR
- FLIR QuickPlot

Asia Pacific Headquarter
Hong Kong
FLIR Systems Co Ltd.
Room 1613 – 16, Tower 2
Grand Central Plaza
138 Shatin Rural Committee
Road, N.T, Hong Kong
Tel: +852 2792 8955
Fax: +852 2792 8952
Email: flir@flir.com.hk

China Head Office - Shanghai
FLIR Systems (Shanghai) Co., Ltd
Tel: +86 21 5169 7628
Fax: +86 21 5466 0289
e-mail: info@flir.cn

Japan Office - Tokyo
FLIR Systems Japan K.K.
Tel: +81 3 6277 5681
Fax: +81 3 6277 5682
e-mail: info@flir.jp

Korea Office - Seoul
FLIR Systems Korea Co., Ltd
Tel: +82 2 565 2714
Fax: +82 2 565 2718
e-mail: sales@flirkorea.com

Taiwan Representative Office
Tel: +886 2 27579662
Fax: +886 2 27576723
e-Mail: flir@flir.com.hk

India Representative Office
Tel: +91 11 4606 7100
Fax: +91 11 4606 7110
e-mail: flir@flir.com.hk

FLIR®

www.flir.com/thg

100930 SC325 datasheet_en

Bibliography

Afanasyev, Y. D. (2006). Formation of vortex dipoles. *Phys. Fluids*, 18(3).

Alimohammadi, S., Dinneen, P., Persoons, T., and Murray, D. B. (2014). Thermal management using pulsating jet cooling technology. *J. Phys. Conf. Ser.*, 525(1).

Alm, B., Imke, U., Knitter, R., Schygulla, U., and Zimmermann, S. (2008). Testing and simulation of ceramic micro heat exchangers. *Chem. Eng. J.*, 135(SUPPL. 1).

Alves, N. M. and Bártolo, P. J. (2006). Integrated computational tools for virtual and physical automatic construction. *Autom. Constr.*, 15(3):257–271.

Arshad, A., Jabbal, M., and Yan, Y. (2020). Synthetic jet actuators for heat transfer enhancement – A critical review. *Int. J. Heat Mass Transf.*, 146:118815.

Azevedo, L. F. A., Webb, B. W., and Queiroz, M. (2015). *Vortex Rings and Jets*, volume 111 of *Fluid Mechanics and Its Applications*. Springer Singapore, Singapore.

Behera, R. C., Dutta, P., and Srinivasan, K. (2007). Numerical study of interrupted impinging jets for cooling of electronics. *IEEE Trans. Components Packag. Technol.*, 30(2):275–284.

Béra, J. C., Michard, M., Grosjean, N., and Comte-Bellot, G. (2001). Flow analysis of two-dimensional pulsed jets by particle image velocimetry. *Exp. Fluids*, 31(5):519–532.

Berthold, A. and Haucke, F. (2020). Influence of Excitation Frequency, Phase Shift, and Duty Cycle on Cooling Ratio in a Dynamically Forced Impingement Jet Array. *J. Turbomach.*, 142(5).

Berthold, A., Haucke, F., and Weiss, J. (2020). Flow Field Analysis of a Dynamically Forced Impingement Jet Array. (January):1–16.

Bourdon, J., Asfaux, P., and Etayo, A. M. (2015). Review fo Power Electronics Opportunities to Integrate in the More Electrical Aircraft. In *2015 Int. Conf. Electr. Syst. Aircraft, Railw. Sh. Propuls. Road Veh.*, pages 1–6, Aachen, Germany.

Bradshaw, P. (1977). Effect of external disturbances on the spreading rate of a plane turbulent jet. *J. Fluid Mech.*, 80(4):795–797.

Browne, E. A., Michna, G. J., Jensen, M. K., and Peles, Y. (2010). Experimental Investigation of Single-Phase Microjet Array Heat Transfer. *J. Heat Transfer*, 132(4):041013.

Brunton, S. L., Noack, B. R., and Koumoutsakos, P. (2019). Machine Learning for Fluid Mechanics. *arXiv*.

Burmeister, L. C. (1959). Heat transfer between a plane surface and a pulsating, perpendicularly impinging air jet.

Camci, C. and Herr, F. (2002). Forced Convection Heat Transfer Enhancement Using a Self-Oscillating Impinging Planar Jet. *J. Heat Transfer*, 124(4):770.

Camps, T., Tasselli, J., Lubin, J., Lagrange, D., Bouscayrol, L., and Marty, A. (2013). Development of polysilicon devices for microfluidic thermal instrumentation. *Sensors Actuators, A Phys.*, 189:67–73.

Celik, I. B., Cehreli, Z. N., and Yavuz, I. (2005). Index of resolution quality for large eddy simulations. *J. Fluids Eng. Trans. ASME*, 127(5):949–958.

Chang, C. J., Chen, H. T., and Gau, C. (2013). Flow and heat transfer of a microjet impinging on a heated chip: Part II - Heat transfer. *Nanoscale Microscale Thermophys. Eng.*, 17(2):92–111.

Chang, S. W., Su, L. M., and Zheng, Y. (2000). Reciprocating impingement jet heat transfer with surface ribs. *Exp. Heat Transf.*, 13:275–297.

Chaniotis, A. K., Poulikakos, D., and Ventikos, Y. (2003). Dual Pulsating or Steady Slot Jet Cooling of a Constant Heat Flux Surface. *J. Heat Transfer*, 125(4):575.

Chaouat, B. (2017). The State of the Art of Hybrid RANS/LES Modeling for the Simulation of Turbulent Flows. *Flow, Turbul. Combust.*, 99(2):279–327.

Chen, Y., Ng, C., and Wang, Y. (1999). Data Reduction in integrated reverse engineering and rapid prototyping. *Int. J. Comput. Integr. Manuf.*, 12:97–103.

Chen, Y. C., Ma, C. F., Qin, M., and Li, Y. X. (2005). Theoretical study on impingement heat transfer with single-phase free-surface slot jets. *Int. J. Heat Mass Transf.*, 48(16):3381–3386.

Choi, J. J., Annaswamy, A. M., Lou, H., and Alvi, F. S. (2006). Active control of supersonic impingement tones using steady and pulsed microjets. *Exp. Fluids*, 41(6):841–855.

Cochrane, G. F. and Nevins, R. G. (1962). Paper N–5: Photographic Investigation of a Pulsating Air Jet Impinging on a Heated Plate. *J. SMPTE*, 71(1A):510–512.

Conlon, B. P. and Lichter, S. (1995). Dipole formation in the transient planar wall jet. *Phys. Fluids*, 7(5):999–1014.

Corbel, S., Dufaud, O., and Roques-Carmes, T. (2011). *Stereolithography*.

Courson, R., Cargou, S., Conédéra, V., Fouet, M., and Gué, A. M. (2014). Low cost integration of multilevel lab-on-a-chip using a new generation of dry film photoresists. *Smart Syst. Integr. - 8th Int. Conf. Exhib. Integr. Issues Miniaturized Syst. - MEMS, NEMS, ICs Electron. Components, SSI 2014*, pages 139–146.

Crow, S. C. and Champagne, F. H. (1971). Orderly structure in jet turbulence. *J. Fluid Mech.*, 48(3):547–591.

Dawson, S. T., Hemati, M. S., Williams, M. O., and Rowley, C. W. (2016). Characterizing and correcting for the effect of sensor noise in the dynamic mode decomposition. *Exp. Fluids*, 57(3):1–19.

Deo, R. C., Mi, J., and Nathan, G. J. (2008). The influence of Reynolds number on a plane jet. *Phys. Fluids*, 20(7).

Didden, N. and Ho, C. M. (1985). Unsteady separation in a boundary layer produced by an impinging jet. *J. Fluid Mech.*, 160:235–256.

Doty, J., Yerkes, K., Byrd, L., Murthy, J., Alleyne, A., Wolff, M., Heister, S., and Fisher, T. S. (2015). Dynamic Thermal Management for Aerospace Technology: Review and Outlook. *J. Thermophys. Heat Transf.*, 31(1):86–98.

Durbin, P. A. (1996). On the k-3 stagnation point anomaly. *Int. J. Heat Fluid Flow*, 17(1):89–90.

Epstein, M. (1971). Theoretical Investigation of the Switching Mechanism in a Bistable Wall Attachment Fluid Amplifier. *J. Basic Eng.*, 93(1):55–62.

Eschmann, G., Kuntze, A., Uffrecht, W., Kaiser, E., and Odenbach, S. (2015). Experimental and numerical investigation of heat transfer coefficients in gaseous impinging jets – First test of a recent sensor concept for steady and unsteady flow. *Int. J. Therm. Sci.*, 96:290–304.

Esmailpour, K., Hosseinalipour, M., Bozorgmehr, B., and Mujumdar, A. S. (2015). A numerical study of heat transfer in a turbulent pulsating impinging jet. *Can. J. Chem. Eng.*, 93(5):959–969.

Farrington, R. B. and Claunch, S. D. (1994). Infrared imaging of large-amplitude, low-frequency disturbances on a planar jet. *AIAA J.*, 32(2):317–323.

Gardon, R. and Akfirat, J. C. (1966). Heat Transfer Characteristics of Impinging Two-Dimensional Air Jets. *J. Heat Transfer*, 88:101.

Geng, L., Zheng, C., and Zhou, J. (2015). Heat transfer characteristics of impinging jets: The influence of unsteadiness with different waveforms. *Int. Commun. Heat Mass Transf.*, 66:105–113.

Ghadi, S., Esmailpour, K., Hosseinalipour, M., and Kalantar, M. (2016a). Dynamical Study of Pulsed Impinging Jet with Time Varying Heat Flux Boundary Condition. *Heat Transf. - Asian Res.*, 45(1):85–100.

Ghadi, S., Esmailpour, K., Hosseinalipour, S. M., and Mujumdar, A. (2016b). Experimental study of formation and development of coherent vortical structures in pulsed turbulent impinging jet. *Exp. Therm. Fluid Sci.*, 74:382–389.

Goldschmidt, V. W. and Bradshaw, P. (1973). Flapping of a plane jet. *Phys. Fluids*, 16(3):354–355.

Gritskevich, M. S., Garbaruk, A. V., Schütze, J., and Menter, F. R. (2012). Development of DDES and IDDES formulations for the k-ω shear stress transport model. *Flow, Turbul. Combust.*, 88(3):431–449.

Haneda, Y., Tsuchiya, Y., Nakabe, K., and Suzuki, K. (1998). Enhancement of impinging jet heat transfer by making use of mechano-fluid interactive flow oscillation. *Int. J. Heat Fluid Flow*, 19(2):115–124.

Herwig, H. and Middelberg, G. (2008). The physics of unsteady jet impingement and its heat transfer performance. *Acta Mech.*, 201(1-4):171–184.

Herwig, H., Mocikat, H., Gürtler, T., and Göppert, S. (2004). Heat transfer due to unsteadily impinging jets. *Int. J. Therm. Sci.*, 43(8 SPEC. ISS.):733–741.

Hewakandamby, B. N. (2009). A numerical study of heat transfer performance of oscillatory impinging jets. *Int. J. Heat Mass Transf.*, 52(1-2):396–406.

Hoelzle, D. J., Varghese, B. A., Chan, C. K., and Rowat, A. C. (2014). A microfluidic technique to probe cell deformability. *J. Vis. Exp.*, (91):7–9.

Hofmann, H. M., Kaiser, R., Kind, M., and Martin, H. (2007a). Calculations of steady and pulsating impinging jets - An assessment of 13 widely used turbulence models. *Numer. Heat Transf. Part B Fundam.*, 51(6):565–583.

Hofmann, H. M., Movileanu, D. L., Kind, M., and Martin, H. (2007b). Influence of a pulsation on heat transfer and flow structure in submerged impinging jets. *Int. J. Heat Mass Transf.*, 50(17-18):3638–3648.

Hsu, C. M., Jhan, W. C., and Chang, Y. Y. (2019). Flow and heat transfer characteristics of a pulsed jet impinging on a flat plate. *Heat Mass Transf. und Stoffuebertragung.*

Huang, X., Li, P., and Tan, Y. (2022). Analysis of time-dependent heat transfer of ellipsoidal protruded microchannel with multiple pulsating jets. *Appl. Therm. Eng.*, 210(March):118348.

Hubble, D. O., Vlachos, P. P., and Diller, T. E. (2013). The role of large-scale vortical structures in transient convective heat transfer augmentation. *J. Fluid Mech.*, 718:89–115.

Hunt, J. C. R., Wray, a. a., and Moin, P. (1988). Eddies, streams, and convergence zones in turbulent flows. *Cent. Turbul. Res. Proc. Summer Progr.*, (1970):193–208.

Hwang, S. D. and Cho, H. H. (2003). Effects of acoustic excitation positions on heat transfer and flow in axisymmetric impinging jet: Main jet excitation and shear layer excitation. *Int. J. Heat Fluid Flow*, 24(2):199–209.

Hwang, S. D., Lee, C. H., and Cho, H. H. (2001). Heat transfer and flow structures in axisymmetric impinging jet controlled by vortex pairing. *Int. J. Heat Fluid Flow*, 22(3):293–300.

Incropera, F. P., DeWitt, D. P., Bergman, T. L., and Lavine, A. S. (2007). *Fundamentals of Heat and Mass Transfer*.

Janetzke, T., Nitsche, W., and Tage, J. (2008). Experimental investigations of flow field and heat transfer characteristics due to periodically pulsating impinging air jets. *Heat Mass Transf. und Stoffuebertragung*, 45:193–206.

Jeong, J. and Hussain, F. (1995). On the identification of a vortex. *J. Fluid Mech.*, 285:69–94.

Kakuta, N., Fukuhara, Y., Kondo, K., Arimoto, H., and Yamada, Y. (2011). Temperature imaging of water in a microchannel using thermal sensitivity of near-infrared absorption. *Lab Chip*, 11(20):3479–3486.

Kataoka, K., Suguro, M., Degawa, H., Maruo, K., and Mihata, I. (1987). The effect of surface renewal due to large- scale eddies on jet impingement heat transfer. 30:559–567.

Kharoua, N., Khezzar, L., Nemouchi, Z., and Alshehhi, M. (2017). LES study of the combined effects of groups of vortices generated by a pulsating turbulent plane jet impinging on a semi-cylinder. *Appl. Therm. Eng.*, 114:948–960.

Kim, D. J., Jeong, S., Park, T., and Kim, D. (2019). Impinging sweeping jet and convective heat transfer on curved surfaces. *Int. J. Heat Fluid Flow*, 79(July):108458.

Klein, D. and Hetsroni, G. (2012). Enhancement of heat transfer coefficients by actuation against an impinging jet. *Int. J. Heat Mass Transf.*, 55(15-16):4183–4194.

Kline, S. and McClintock, F. (1953). Describing uncertainities in single sample. *Mech. Eng.*, 75:3–8.

Kolář, V. (2007). Vortex identification: New requirements and limitations. *Int. J. Heat Fluid Flow*, 28(4):638–652.

Kotsovinos, N. E. (1976). A note on the spreading rate and virtual origin of a plane turbulent jet. *J. Fluid Mech.*, 77(2):305–311.

Koyama, K. and Asako, Y. (2010). Experimental investigation of heat transfer characteristics on a gas-to-gas parallel flow microchannel heat exchanger. *Open Transp. Phenom. J.*, 2(1):1–8.

Kubacki, S. and Dick, E. (2009). Convective heat transfer prediction for an axisymmetric jet impinging onto a flat plate with an improved k- ω model. *Int. J. Numer. Methods Heat Fluid Flow*, 19(8):960–981.

Kubacki, S. and Dick, E. (2010). Simulation of plane impinging jets with k-ω based hybrid RANS/LES models. *Int. J. Heat Fluid Flow*, 31(5):862–878.

Kubacki, S., Rokicki, J., and Dick, E. (2013). Hybrid RANS/LES computations of plane impinging jets with DES and PANS models. *Int. J. Heat Fluid Flow*, 44:596–609.

Langtry, R. B. and Menter, F. R. (2009). Correlation-based transition modeling for unstructured parallelized computational fluid dynamics codes. *AIAA J.*, 47(12):2894–2906.

Launder, B. and Spalding, D. (1974). The numerical computation of turbulent flows. *Comput. Methods Appl. Mech. Eng.*, 3(2):269–289.

Leask, S. B. and McDonell, V. G. (2019). On the Physical Interpretation of Proper Orthogonal Decomposition and Dynamic Mode Decomposition for Liquid Injection. pages 1–26.

Leconte, J. (1858). On the influence of musical sounds on the flame of a jet of coal-gas. *London, Edinburgh, Dublin Philos. Mag. J. Sci.*, 15(99):235–239.

Lee, J. H.-w. and Chu, V. (2003). *Turbulent Jets and Plumes: a Lagrangian approach*. Springer.

Li, P., Guo, D., and Liu, R. (2019). Mechanism analysis of heat transfer and flow structure of periodic pulsating nanofluids slot-jet impingement with different waveforms. *Appl. Therm. Eng.*, 152(January):937–945.

Liu, S., Meneveau, C., and Katz, J. (1994). On the properties of similarity SGS models as deduced from measurements in a turbulent jet. *J. Fluid Mech.*, 275:83–119.

Liu, T. and Sullivan, J. P. (1996). Heat transfer and flow structures in an excited circular impinging jet. *Int. J. Heat Mass Transf.*, 39(17):3695–3706.

Löffler, S., Ebert, C., and Weiss, J. (2021). Fluidic-Oscillator-Based Pulsed Jet Actuators for Flow Separation Control. *Fluids*, 6(4):166.

Lumley, J. L. (2007). *Stochastic Tools in Turbulence*. Dover Publications, Mineola, New York, dover book edition.

Mahefkey, T., Yerkes, K., Donovan, B., and Ramalingam, M. L. (2004). Thermal Management Challenges For Future Military Aircraft Power Systems. Technical report.

Manca, O., Mesolella, P., Nardini, S., and Ricci, D. (2011). Numerical study of a confined slot impinging jet with nanofluids. *Nanoscale Res. Lett.*, 6(1):1–16.

Marcum, W. R., Cadell, S. R., and Ward, C. (2015). The effect of jet location and duty cycle on the fluid mechanics of an unconfined free jet and its heat transfer on an impinging plate. *Int. J. Heat Mass Transf.*, 88:470–480.

McKetta Jr, J. J. (1997). *Encyclopedia of chemical processing and design*. CRC press.

Menter, F. R. (1993). AIAA 93 · 2906 Zonal Two Equation k · co Turbulence Models for Aerodynamic Flows . Mailing Address : 24th Fluid Dynamics Conference FOR AERODYNAMIC FLOWS.

Menter, F. R. (2009). Review of the shear-stress transport turbulence model experience from an industrial perspective. *Int. J. Comut. Fluid Dyn.*, 23(4):305–316.

Michalke, A. (1984). Survey on jet instability theory. *Prog. Aerosp. Sci.*, 21(C):159–199.

Middelberg, G. and Herwig, H. (2009). Convective heat transfer under unsteady impinging jets: The effect of the shape of the unsteadiness. *Heat Mass Transf. und Stoffuebertragung*, 45(12):1519–1532.

Mladin, E. and Zumbrunnen, D. (1994). Nonlinear dynamics of laminar boundary layers in pulsatile stagnation flows. *J. Thermophys. Heat Transf.*, 8(3):514–523.

Mladin, E. C. and Zumbrunnen, D. A. (1995). Dependence of Heat Transfer to a Pulsating Stagnation Flow on Pulse Characteristics. *J. Thermophys. Heat Transf.*, 9(1):181–192.

Mladin, E. C. and Zumbrunnen, D. A. (1997). Local convective heat transfer to submerged pulsating jets. *Int. J. Heat Mass Transf.*, 40(14):3305–3321.

Mladin, E. C. and Zumbrunnen, D. A. (2000). Alterations to coherent flow structures and heat transfer due to pulsations in an impinging air-jet. *Int. J. Therm. Sci.*, 39(2):236–248.

Mohammadpour, J., Rajabi-Zargarabadi, M., Mujumdar, A. S., and Ahmadi, H. (2014a). Effect of intermittent and sinusoidal pulsed flows on impingement heat transfer from a concave surface. *Int. J. Therm. Sci.*, 76:118–127.

Mohammadpour, J., Zolfagharian, M. M., Mujumdar, A. S., Zargarabadi, M. R., and Abdulahzadeh, M. (2014b). Heat transfer under composite arrangement of pulsed and steady turbulent submerged multiple jets impinging on a flat surface. *Int. J. Therm. Sci.*, 86:139–147.

Morioka, N. and Oyori, H. (2014). All electric system architecture for aircraft and propulsion. *52nd Aerosp. Sci. Meet.*, (January):1–7.

Morioka, N., Saito, H., Takahashi, N., Seta, M., and Oyori, H. (2014). Thermal management system concept with an autonomous air-cooled system. *SAE Tech. Pap.*, 2014-Septe(September).

Morkovin, M. V. (1956). Fluctuations and hot-wire anemometry in compressible flows. *AGARDograph*, 24:1–102.

Muller, H. R. (1964). A Study of the Dynamic Features of a Wall-Reattachment Fluid Amplifier. *J. Basic Eng.*, 86(4):819–826.

Müller, H. R. (1964). Wall Reattachment Device with Pulsed Control Flow. In *Proc. Fluid Amplif. Symp.*, volume 1, page 179. Diamond Ordnance Fuze Laboratories, Ordnance Corps, Department of the Army.

Narumanchi, S., Kelly, K., Mihalic, M., Gopalan, S., Hester, R., and Vlahinos, A. (2008). Single-phase self-oscillating jets for enhanced heat transfer. *Annu. IEEE Semicond. Therm. Meas. Manag. Symp.*, pages 154–162.

Neradka, V. F. (1971). Modulated Pure Fluid Oscillator.

Nevins, R. G. and Ball, H. D. (1961). Heat transfer between a flat plate and a pulsating impinging jet. In *Proc. Natl. Heat Transf. Conf.*, volume 60, pages 510–516.

O'Donovan, T. S. and Murray, D. B. (2007a). Effect of acoustic excitation on the heat transfer to an impinging air jet. *2007 Proc. ASME/JSME Therm. Eng. Summer Heat Transf. Conf. - HT 2007*, 3:183–191.

O'Donovan, T. S. and Murray, D. B. (2007b). Jet impingement heat transfer - Part I: Mean and root-mean-square heat transfer and velocity distributions. *Int. J. Heat Mass Transf.*, 50(17-18):3291–3301.

O'Donovan, T. S. and Murray, D. B. (2007c). Jet impingement heat transfer - Part II: A temporal investigation of heat transfer and local fluid velocities. *Int. J. Heat Mass Transf.*, 50(17-18):3302–3314.

O'Donovan, T. S. and Murray, D. B. (2008). Fluctuating fluid flow and heat transfer of an obliquely impinging air jet. *Int. J. Heat Mass Transf.*, 51(25-26):6169–6179.

Olsson, M. and Fuchs, L. (1998). Large eddy simulations of a forced semiconfined circular impinging jet. *Phys. Fluids*, 10(2):476–486.

O'Neill, W. C. (1969). Fluid Oscillator Having Variable Volume Feedback Loops.

Ostermann, F., Woszidlo, R., Nayeri, C. N., and Paschereit, C. O. (2019). The interaction between a spatially oscillating jet emitted by a fluidic oscillator and a cross-flow. *J. Fluid Mech.*, 863:215–241.

Ott, C., Pivot, C., Dubois, P., Gallas, Q., Delva, J., Lippert, M., and Keirsbulck, L. (2021). Pulsed jet phase-averaged flow field estimation based on neural network approach. *Exp. Fluids*, 62(4):1–16.

Pakhomov, M. A. and Terekhov, V. I. (2010). Enhancement of an impingement heat transfer between turbulent mist jet and flat surface. *Int. J. Heat Mass Transf.*, 53(15-16):3156–3165.

Pakhomov, M. A. and Terekhov, V. I. (2013). Effect of pulse frequency on heat transfer at the stagnation point of an impinging turbulent jet. *High Temp.*, 51(2):256–261.

Pakhomov, M. A. and Terekhov, V. I. (2015). Numerical study of fluid flow and heat transfer characteristics in an intermittent turbulent impinging round jet. *Int. J. Therm. Sci.*, 87:85–93.

Persoons, T., Balgazin, K., Brown, K., and Murray, D. B. (2013). Scaling of convective heat transfer enhancement due to flow pulsation in an axisymmetric impinging jet. *J. Heat Transfer*, 135(11).

Peszynski, K., Smyk, E., Wawrzyniak, S., and Perczynski, D. (2016). Research of vibration asymmetry of fluidic oscillator with vortex chambers. *EPJ Web Conf.*, 49:02149.

Plateau, J. (1857). I. Experimental and theoretical researches on the figures of equilibrium of a liquid mass withdrawn from the action of gravity. –Third series . *London, Edinburgh, Dublin Philos. Mag. J. Sci.*, 14(90):1–22.

Popiel, C. O. and Trass, O. (1991). Visualization of a free and impinging round jet. *Exp. Therm. Fluid Sci.*, 4(3):253–264.

Quigley, R. E. (1993). More Electric Aircraft. In *Proc. Eighth Annu. Appl. Power Electron. Conf. Expo.* IEEE.

Rajabi Zargarabadi, M., Rezaei, E., and Yousefi-Lafouraki, B. (2018). Numerical analysis of turbulent flow and heat transfer of sinusoidal pulsed jet impinging on an asymmetrical concave surface. *Appl. Therm. Eng.*, 128:578–585.

Rajaratnam, N. (1976). *Turbulent Jets*, volume 5. Elsevier, New York.

Rakhsha, S., Rajabi Zargarabadi, M., and Saedodin, S. (2020). Experimental and numerical study of flow and heat transfer from a pulsed jet impinging on a pinned surface. *Exp. Heat Transf.*, 00(00):1–16.

Reynolds, W. and Hussain, A. (1972). The mechanics of an organized wave in turbulent shear flow. Part 3. Theoretical models and comparisons with experiments. *J. Fluid Mech.*, 54:263–288.

Ribeiro, M. M. and Whitelaw, J. H. (1980). The Structure of Turbulent Jets. *Proc. R. Soc. Lond. A. Math. Phys. Sci.*, 370(1742):281–301.

Rizk, M. H. and Menon, S. (1988). Large-eddy simulations of axisymmetric excitation effects on a row of impinging jets. *Phys. Fluids*, 31(7 , Jul. 1988):1892–1903.

Roux, S., Brizzi, L.-E., Dorignac, E., and Fenot, M. (2011a). Impinging jet heat transfer improvement using acoustic forcing. (September):E–0212.

Roux, S., Fénot, M., Lalizel, G., Brizzi, L. E., and Dorignac, E. (2011b). Experimental investigation of the flow and heat transfer of an impinging jet under acoustic excitation. *Int. J. Heat Mass Transf.*, 54(15-16):3277–3290.

Sagaut, P., Deck, S., and Terracol, M. (2013). *Multiscale and Multiresolution Approaches in Turbulence*, volume 52. IMPERIAL COLLEGE PRESS.

Sailor, D. J., Rohli, D. J., and Fu, Q. (1999). Effect of variable duty cycle flow pulsations on heat transfer enhancement for an impinging air jet. *Int. J. Heat Fluid Flow*, 20(6):574–580.

Sakanova, A., Tong, C. F., Nawawi, A., Simanjorang, R., Tseng, K. J., and Gupta, A. K. (2016). Investigation on weight consideration of liquid coolant system for power electronics converter in future aircraft. *Appl. Therm. Eng.*, 104:603–615.

Saltzman, D., Bichnevicius, M., Lynch, S., Simpson, T. W., Reutzel, E. W., Dickman, C., and Martukanitz, R. (2018). Design and evaluation of an additively manufactured aircraft heat exchanger. *Appl. Therm. Eng.*, 138(April):254–263.

Sanyal, A., Srinivasan, K., and Dutta, P. (2009). Numerical study of heat transfer from pin-fin heat sink using steady and pulsated impinging jets. *IEEE Trans. Components Packag. Technol.*, 32(4):859–867.

Schiestel, R. (2008). *Modeling and Simulation of Turbulent Flows*. Wiley-ISTE, 1st edition.

Schlichting, H. (2017). *Boundary layer theory*.

Schmid, P. J. (2010). Dynamic mode decomposition of numerical and experimental data. *J. Fluid Mech.*, 656:5–28.

Schumann, U. (1977). Realizability of Reynolds-stress turbulence models. *Phys. Fluids*, 20(5):721–725.

Selimefendigil, F. and Öztop, H. F. (2014). Pulsating nanofluids jet impingement cooling of a heated horizontal surface. *Int. J. Heat Mass Transf.*, 69:54–65.

Sharif, M. A. and Ramirez, N. M. (2013). Surface roughness effects on the heat transfer due to turbulent round jet impingement on convex hemispherical surfaces. *Appl. Therm. Eng.*, 51(1-2):1026–1037.

Shariff, K. and Leonard, A. (1992). Vortex Rings. *Annu. Rev. Fluid Mech.*, 24(1):235–279.

Sheriff, H. S. and Zumbrunnen, D. A. (1999). Local and instantaneous heat transfer characteristics of arrays of pulsating jets. *J. Heat Transfer*, 121(2):341–348.

Simões, E. W., Furlan, R., Bruzetti Leminski, R. E., Gongora-Rubio, M. R., Pereira, M. T., Morimoto, N. I., and Santiago Avilés, J. J. (2005). Microfluidic oscillator for gas flow control and measurement. *Flow Meas. Instrum.*, 16(1):7–12.

Sitzmann, V., Martel, J. N. P., Bergman, A. W., Lindell, D. B., and Wetzstein, G. (2020). Implicit Neural Representations with Periodic Activation Functions.

Sowers, E. U. (1964). Multi-frequency fluid oscillator.

Spyropoulos, C. (1964). A Sonic Oscillator. *Proc. Fluid. Amplif. Symp.*, pages 27–52.

Steinfurth, B. and Weiss, J. (2020). Vortex rings produced by non-parallel planar starting jets. *J. Fluid Mech.*

Stöhr, U., Vulto, P., Hoppe, P., Urban, G., and Reinecke, H. (2008). High-resolution permanent photoresist laminate for microsystem applications. *J. Micro/Nanolithography, MEMS, MOEMS*, 7(3):033009.

Swiderski, V. and Guenzel, P.-O. (2006). Thrust Reverser Unlocked. *Saf. First, Airbus S.A.S.*, (December):2–6.

Taira, K., Brunton, S. L., Dawson, S. T., Rowley, C. W., Colonius, T., McKeon, B. J., Schmidt, O. T., Gordeyev, S., Theofilis, V., and Ukeiley, L. S. (2017). Modal analysis of fluid flows: An overview. *AIAA J.*, 55(12):4013–4041.

Tang, C., Zhang, J. Z., Lyu, Y. W., and Tan, X. M. (2019). Convective heat transfer on a flat target surface impinged by pulsating jet with an additional transmission chamber. *Heat Mass Transf. und Stoffuebertragung*, 56(1):183–205.

Ten, J. S. and Povey, T. (2019). Self-excited fluidic oscillators for gas turbines cooling enhancement: Experimental and computational study. *J. Thermophys. Heat Transf.*, 33(2):536–547.

Tennekes, H. and Lumley, J. L. (1972). A First Course in Turbulence.

Tesař, V. (2009). Enhancing impinging jet heat or mass transfer by fluidically generated flow pulsation. *Chem. Eng. Res. Des.*, 87(2):181–192.

Tesař, V. (2017). Taxonomic trees of fluidic oscillators. *EPJ Web Conf.*, 143:1–10.

Tsubokura, M., Kobayashi, T., Taniguchi, N., and Jones, W. P. (2003). A numerical study on the eddy structures of impinging jets excited at the inlet. *Int. J. Heat Fluid Flow*, 24(4):500–511.

Tu, J. H., Rowley, C. W., Luchtenburg, D. M., Brunton, S. L., and Kutz, J. N. (2014). On dynamic mode decomposition: Theory and applications. *J. Comput. Dyn.*, 1(2):391–421.

Uddin, N., Neumann, S. O., and Weigand, B. (2013). LES simulations of an impinging jet: On the origin of the second peak in the Nusselt number distribution. *Int. J. Heat Mass Transf.*, 57(1):356–368.

Uddin, N., Neumann, S. O., and Weigand, B. (2016). Heat transfer enhancement by velocity field excitation for an impinging round jet. *Numer. Heat Transf. Part A Appl.*, 69(8):811–824.

van Zant, P. (2014). *Microchip Fabrication: A Practical Guide to Semiconductor Processing*. McGrawhill, New York.

Varieras, D., Brancher, P., and Giovannini, A. (2007). Self-sustained oscillations of a confined impinging jet. *Flow, Turbul. Combust.*, 78(1):1–15.

Vejrazka, J., Tihon, J., Mart, P., and Sobolík, V. (2005). Effect of an external excitation on the flow structure in a circular impinging jet. *Phys. Fluids*, 17(10).

Viskanta, R. (1993). Heat transfer to impinging isothermal gas and flame jets. *Exp. Therm. Fluid Sci.*, 6(2):111–134.

Walters, E. A., Iden, S., McCarthy, K., Amrhein, M., O'Connell, T., Raczkowski, B., Wells, J., Lamm, P., Wolff, M., Yerkes, K., Borger, W., and Wampler, B. (2010). INVENT modeling, simulation, analysis and optimization. *48th AIAA Aerosp. Sci. Meet. Incl. New Horizons Forum Aerosp. Expo.*, (November 2015).

Wang, B., Ni, J., Litvin, Y., Pfaff, D. W., and Lin, Q. (2012). A microfluidic approach to pulsatile delivery of drugs for neurobiological studies. *J. Microelectromechanical Syst.*, 21(1):53–61.

Wang, J., Li, Y., Liu, X., Shen, C., Zhang, H., and Xiong, K. (2020). Recent active thermal management technologies for the development of energy-optimized aerospace vehicles in China. *Chinese J. Aeronaut.*

Wang, S. (2017). *Experimental and Numerical Study of Micro-Fluidic Oscillators for Flow Separation Control*. PhD thesis, Université de Toulouse.

Wang, S., Baldas, L., Colin, S., Orieux, S., Kourta, A., and Mazellier, N. (2016). Experimental and Numerical Study of the Frequency Response of a Fluidic Oscillator for Active Flow Control. (June):1–15.

Warren, R. (1960). US Patent 3,016,066.

Warren, R. W. (1964). Negative Feedback Oscillator.

Wen, X., Liu, J., Li, Z., Peng, D., Zhou, W., Kim, K. C., and Liu, Y. (2020). Jet impingement using an adjustable spreading-angle sweeping jet. *Aerosp. Sci. Technol.*, 105:105956.

Wheeler, P. and Bozhko, S. (2014). The More Electric Aircraft. *IEEE Electrif. Mag.*, 44:6–12.

Wilcox, D. C. (1988). Reassessment of the scale-determining equation for advanced turbulence models. *AIAA J.*, 26(11):1299–1310.

Williams, M., Muley, A., Bolla, J., and Strumpf, H. (2008). Advanced heat exchanger technology for aerospace applications. *SAE Tech. Pap.*

Woszidlo, R., Ostermann, F., and Schmidt, H. J. (2019). Fundamental properties of fluidic oscillators for flow control applications. *AIAA J.*, 57(3):978–992.

Xia, Y. and Whitesides, G. M. (1998). Soft lithography. *Angew. Chemie - Int. Ed.*, 37(5):550–575.

Xu, B. P., Wen, J. X., and Volkov, K. N. (2013). Large-eddy simulation of vortical structures in a forced plane impinging jet. *Eur. J. Mech. B/Fluids*, 42:104–120.

Xu, P., Sasmito, A., and Mujumdar, A. (2016). A computational study of heat transfer under twin turbulent slot jets impinging on planar smooth and rough surfaces. *Therm. Sci.*, 20(suppl. 1):47–57.

Xu, P., Yu, B., Qiu, S., Poh, H. J., and Mujumdar, A. S. (2010). Turbulent impinging jet heat transfer enhancement due to intermittent pulsation. *Int. J. Therm. Sci.*, 49(7):1247–1252.

Yakhot, V. and Orszag, S. A. (1986). Renormalization group analysis of turbulence. I. Basic theory. *J. Sci. Comput.*, 1(1):3–51.

Yang, J. T., Chen, C. K., Hu, I. C., and Lyu, P. C. (2007). Design of a self-flapping microfluidic oscillator and diagnosis with fluorescence methods. *J. Microelectromechanical Syst.*, 16(4):826–835.

Yule, A. (1978). Large-scale structure in the mixing layer of a round jet. *J. Fluid Mech.*, 89(1978).

Zhang, Y., Li, P., and Xie, Y. (2018). Numerical investigation of heat transfer characteristics of impinging synthetic jets with different waveforms. *Int. J. Heat Mass Transf.*, 125:1017–1027.

Zhou, J. W., Wang, Y. G., Middelberg, G., and Herwig, H. (2009). Unsteady jet impingement: Heat transfer on smooth and non-smooth surfaces. *Int. Commun. Heat Mass Transf.*, 36(2):103–110.

Zhou, W., Yuan, L., Liu, Y., Peng, D., and Wen, X. (2019). Heat transfer of a sweeping jet impinging at narrow spacings. *Exp. Therm. Fluid Sci.*, 103(November 2018):89–98.

Zuckerman, N. and Lior, N. (2005). Impingement heat transfer: Correlations and numerical modeling. *J. Heat Transfer*, 127(5):544–552.

Zulkifli, R., Benard, E., Raghunathan, S., and Linton, A. (2004). Effect of pulse jet frequency on impingement heat transfer. *AIAA Pap.*, (January):10983–10992.

Zumbrunnen, D. A. (1992). Transient Convective Heat Transfer in Planar Stagnation Flows With Time-Varying Surface Heat Flux and Temperature. *J. Heat Transfer*, 114(1):85.

Zumbrunnen, D. A. and Aziz, M. (1993). Convective Heat Transfer Enhancement Due to Intermittency in an Impinging Jet. *J. Heat Transfer*, 115(1):91.